Secondary Natural Gas Recovery in the Appalachian Basin: Application of Advanced Technologies in a Field Demonstration Site, Henderson Dome, Western Pennsylvania

by
**Bob A. Hardage, Eloise Doherty,
Stephen E. Laubach,
and Tucker F. Hentz**


Bureau of Economic Geology
Noel Tyler, Director
The University of Texas at Austin
Austin, TX 78713-8924

in cooperation with industry partner
Atlas Resources, Inc.
311 Rouser Road
Moon Township, PA 15108

under Subcontract No. 97-305-TBEG

Submitted to
DOE
U.S. Department of Energy
Federal Energy Technology Center
Morgantown, WV 26507-0880

Submitted by
West Virginia University Research Corporation
Morgantown, WV 26506

FINAL REPORT
August 14, 1998

QAe7925

CONTENTS

Figures

Tables

Appendices

EXECUTIVE SUMMARY

The principal objectives of this project were to test and evaluate technologies that would result in improved characterization of fractured natural-gas reservoirs in the Appalachian Basin. The Bureau of Economic Geology (Bureau) worked jointly with industry partner Atlas Resources, Inc. to design, execute, and evaluate several experimental tests toward this end.

The experimental tests were of two types: (1) tests leading to a low-cost methodology whereby small-scale microfractures observed in matrix grains of sidewall cores can be used to deduce critical properties of large-scale fractures that control natural-gas production and (2) tests that verify methods whereby robust seismic shear (S) waves can be generated to detect and map fractured reservoir facies.

The grain-scale microfracture approach to characterizing rock facies was developed in an ongoing Bureau research program that started before this Appalachian Basin study began. However, the method had not been tested in a wide variety of fracture systems, and the tectonic setting of rocks in the Appalachian Basin composed an ideal laboratory for perfecting the methodology. As a result of this Appalachian study, a low-cost commercial procedure now exists that will allow Appalachian operators to use scanning electron microscope (SEM) images of thin sections extracted from oriented sidewall cores to infer the spatial orientation, relative geologic timing, and population density of large-scale fracture systems in reservoir sandstones. These attributes are difficult to assess using conventional techniques. In the Henderson Dome area, large quartz-lined regional fractures having N20E strikes, and a subsidiary set of fractures having N70W strikes, are prevalent.

An innovative method was also developed for obtaining the stratigraphic and geographic tops of sidewall cores. With currently deployed sidewall coring devices, no markings from which top orientation can be obtained are made on the sidewall core itself during drilling. The method developed in this study involves analysis of the surface morphology of the broken end of the core as a top indicator. Together with information on the working of the tool (rotation direction),

fracture-surface features, such as arrest lines and plume structures, not only give a top direction for the cores but also indicate the direction of fracture propagation in the tough, fine-grained Cataract/Medina sandstones. The study determined that microresistivity logs or other image logs can be used to obtain accurate sidewall core azimuths and to determine the precise depths of the sidewall cores.

Two seismic S-wave technologies were developed in this study. The first was a special explosive package that, when detonated in a conventional seismic shot hole, produces more robust S-waves than do standard seismic explosives. The importance of this source development is that it allows S-wave seismic data to be generated across all of the Appalachian Basin. Previously, Appalachian operators have not been able to use S-wave seismic technology to detect fractured reservoirs because the industry-standard S-wave energy source, the horizontal vibrator, is not a practical source option in the heavy timber cover that extends across most of the basin.

The second S-wave seismic technology that was investigated was used to verify that standard P-wave seismic sources can create robust downgoing S-waves by P-to-S mode conversion in the shallow stratigraphic layering in the Appalachian Basin. This verification was done by recording and analyzing a 3-component vertical seismic profile (VSP) in the Atlas Montgomery No. 4 well at Henderson Dome, Mercer County, Pennsylvania. The VSP data confirmed that robust S-waves are generated by P-to-S mode conversion at the basinwide Onondaga stratigraphic level. Appalachian operators can thus use converted-mode seismic technology to create S-wave images of fractured and unfractured rock systems throughout the basin.

INTRODUCTION

The Lower Silurian Cataract/Medina Group sandstone is one of the largest and most significant natural gas plays in the Appalachian Basin, with proved gas reserves of 9.1 Tcf from more than 76,000 total wells (McCormac and others, 1996). Additional estimated undiscovered resources range from 3.9 to 4.3 Tcf in this major U.S. gas play. The Cataract/Medina Group sandstones and other target formations have historically provided low-risk and low-cost opportunities for many Appalachian operators. However, after aggressive drilling and extension of this play, operators are currently facing critical economic limitations to production from the play. For example, Atlas Resources, Inc., the project's industry partner, has drilled more than 700 wells in the play area but is now encountering a significant decrease in undifferentiated-Cataract/Medina and Whirlpool natural-gas production both south and west of Henderson Dome in Mercer and Venango Counties, northwest Pennsylvania (fig. 1). The economic limitations for all operators include locally poor production, which has been encountered in expanded undifferentiated-Cataract/Medina and Whirlpool intervals within an arcuate trend of small grabens on the south and west flanks of Henderson Dome (fig. 2). In contrast, unusually good production is found on the structurally high sides adjacent to these grabens, suggesting that permeability has been enhanced by fracturing associated with the faulting. Atlas Resources, Inc. has demonstrated the existence of numerous faults on the flanks of Henderson Dome, and Zagorski (1991) inferred that natural fractures enhance gas production in the nearby Cooperstown gas field in Crawford and Venango Counties. However, the negative effect of increased risk of drilling sub-economic wells within the graben trend far outweighs this geologically favorable aspect. With past success ratios exceeding 90 percent for completion of gas wells, the current main concern within industry is not if a well will produce but if the well will be economic.

This limitation to expanding the productive trend of the Cataract/Medina Group sandstones has important implications for continued development of the Cataract/Medina and for delineating

Figure 1. Map showing study area, regional location, and extent of tight gas portion of Cataract/ Medina play.

the lateral extent of other major gas trends, such as the Ordovician and Cambrian, in the Appalachian Basin. Investigation of the limitations to development in the Cataract/Medina play and the technical barriers that must be overcome are the focus of this study.

Objectives

A two-pronged investigative strategy is necessary to extend development of the Cataract/ Medina Group reservoirs at and near Henderson Dome and similar reservoirs elsewhere in the Appalachian Basin. By using advanced technology, we are investigating how to (1) avoid drilling sub-economic wells by identifying fracture attributes in core samples and using geophysical methods so that high-conductivity fractured-reservoir sweet spots can be targeted.

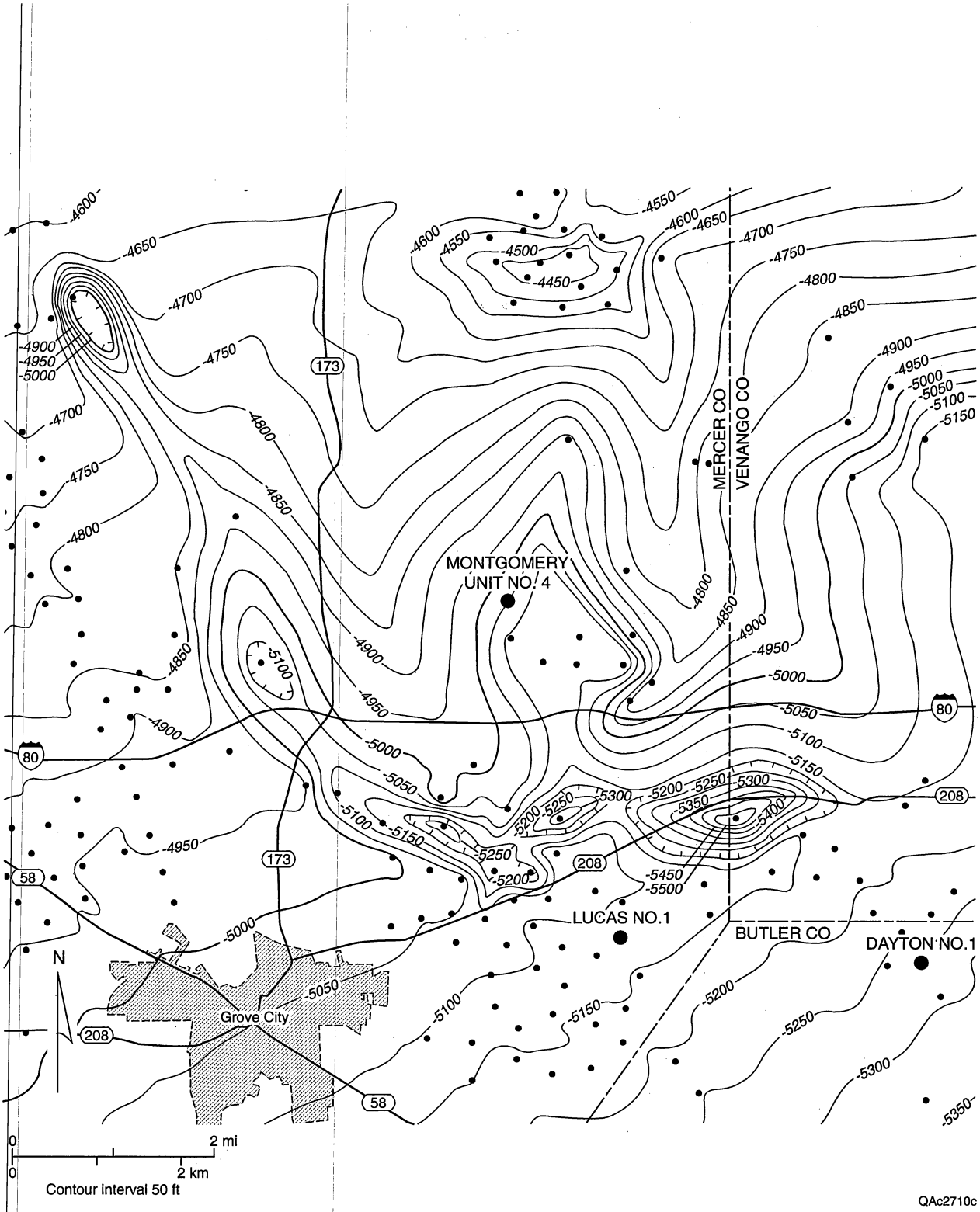

Figure 2. Map of structure on top of the Queenston Shale showing location of study wells (modified from Atlas Resources, 1997).

In this report, we present the initial (Phase 1) research results of the project. Phase 1 results fall into two distinct areas of investigation: (1) analysis of fractures in Cataract/Medina reservoir facies at and near Henderson Dome and (2) application of seismic techniques to enhance recovery in the same area. The specific Phase 1 objectives of the fracture-analysis part of the study were to determine the feasibility of measuring fracture size, conductivity, and orientation using microstructure-imaging and -scaling methods and formation borehole-imaging technology, and to apply the results to test wells. The objectives of the seismic part of the study were to investigate seismic technologies that can be used to detect and map fractured-sandstone reservoir facies in the Henderson Dome region, and to determine if these technologies can be integrated to allow effective 3-D seismic surveys to be conducted over this and other Appalachian prospects.

Selection of the Henderson Dome as the Study Area

Strategies for enhanced production from the low-permeability, fractured Cataract/Medina Group sandstones would benefit from cost-effective techniques that could delineate fractured zones associated with inferred regional-fault boundaries and intersections (see Geologic Setting). Evidence of faults and fractures is routinely detected by operators from well data and 2-D seismic profiles in the vicinity of Henderson Dome. For example, loss of coherency in a key regional seismic reflector (Ordovician Trenton Limestone) occurs domeward of the arcuate trend of fault-bounded grabens on the south and west flanks of Henderson Dome. The coherency loss is probably due to pervasive faulting and fracturing. Natural-gas shows were recorded in the fractured Trenton and underlying Black River Formations in a 1944-vintage Cambrian test located near the top of the Henderson Dome. Moreover, Atlas Resources, Inc. has identified 10 prospective areas within the disturbed region identified on 6 seismic lines where the Trenton event loses coherency close to inferred deep faulting. Low-cost microfracture analysis from cores, which was developed at the Bureau of Economic Geology, is ideally suited for determining fracture attributes (size, conductivity, and orientation) in the Cataract/Medina Group

sandstones. In addition, it may be possible for seismic-attribute analysis to identify Cataract/ Medina fracture trends in the Henderson Dome region. Natural-gas plays throughout the Appalachian Basin where surface seismic technologies will be applied will also benefit from improved techniques for near-surface velocity corrections that are necessary due to variations in glacial-till thickness.

Geologic Setting

The Lower Silurian strata in the Appalachian Basin are known by several stratigraphic names: the Clinton Group (Kentucky), the Clinton and Cataract Group (Ohio), and the Cataract Group (Ontario). In Pennsylvania and New York, equivalent rocks are included within the Medina Group (Piotrowski, 1981). Unfortunately, Cataract/Medina Group sandstones are widely known as "Clinton" by Appalachian operators as a result of miscorrelations that occurred during the early development of the gas play (McCormac and others, 1996). The Medina and Cataract Groups are subdivided as follows (in ascending order): Whirlpool Sandstone, Cabot Head Shale, Grimsby Sandstone, and Thorold Sandstone (figs. 3 and 4). In the Henderson Dome region, the gas-producing units are the Whirlpool, Grimsby, and Thorold. Drillers in the producing area commonly refer to the Grimsby and Thorold Sandstones as the White Clinton and Red Clinton sandstones, and the Stray Clinton sandstones, respectively (fig. 3). The Whirlpool unconformably overlies the Upper Ordovician Queenston Shale, and the top of the Medina Group (Thorold Sandstone) is also marked by a hiatal depositional surface (fig. 3).

Although regionally within the Appalachian Basin the Whirlpool Sandstone is divided into three major lithofacies (sandstone, calcareous shale, and dolostone), the sandstones facies dominates in Pennsylvania, New York, and Ontario (Coogan, 1991). In these areas, the sandstone is inferred to have originated as a transgressive marine sheet sand (Martini, 1971; Kearney, 1983). The lower part of the Whirlpool in Pennsylvania records a braided-river environment of deposition, whereas the upper part is interpreted as marine wave-dominated nearshore deposits

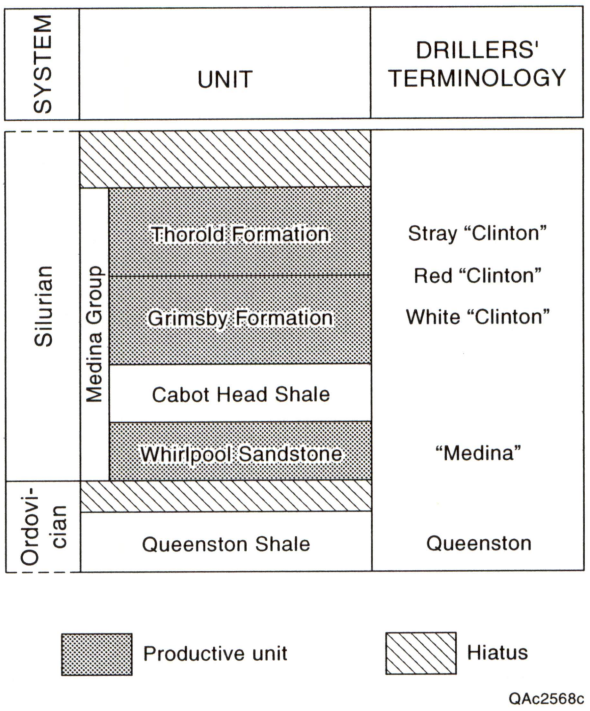

Figure 3. Generalized stratigraphic column of Silurian strata in west-central Pennsylvania.

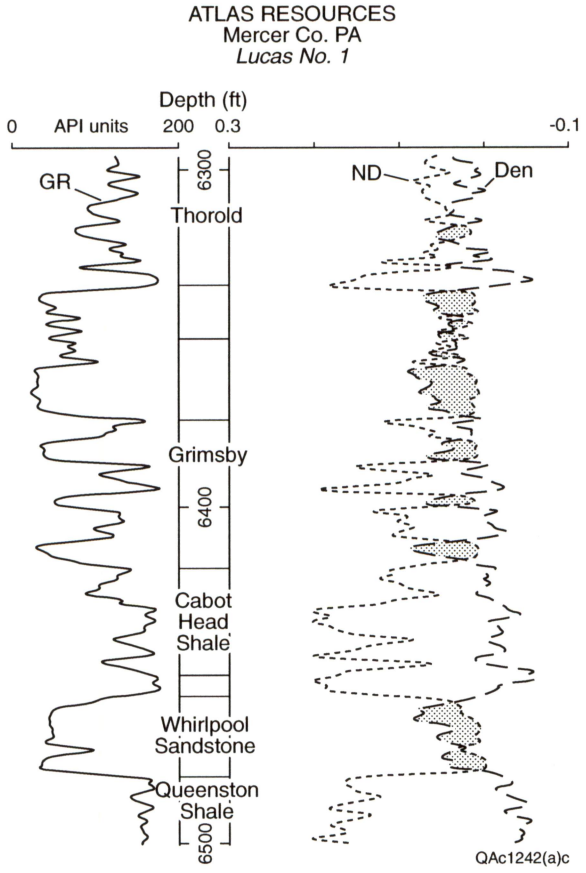

Figure 4. Representative well log of the study area (Atlas Lucas No. 1 well).

(Zagorski, 1991; Cheel and Middleton, 1993). Overlying Grimsby and Thorold reservoir sandstones (Stray, Red, and White Clinton) were deposited in a complex deltaic to shallow-marine environment during an overall regressive depositional stage (Overbey and Henniger, 1971).

The Cataract/ Medina Group play occurs on the northwest flank of the Appalachian Basin in northeast Kentucky, east Ohio, northwest Pennsylvania, west New York, and southeast Ontario. Throughout the play, the trapping mechanism is primarily stratigraphic, although subtle structure also has considerable influence on gas production in some fields (McCormac and others, 1996). Structures identified in the Henderson Dome area record basement-involved faulting along SW-NE structures such as the Rome Trough that roughly parallel the basin trend as well as cross-strike discontinuities related to the Taconian Orogeny. Wrench faulting is probably the source of the subtle local structural patterns. The basement faults were probably reactivated during the Appalachian Orogeny, and again during the opening of the Atlantic Ocean basin in the Late Triassic/Early Jurassic. A mantle hot spot may have existed near the study area during the Late Triassic/Early Jurassic (Crough and others, 1980; Parrish and Lavin, 1982) that could be related to the emplacement of two kimberlite pipes near the study area. An arcuate graben trend has been detected in the subsurface near Henderson Dome (Atlas Resources, 1997). Major vertical displacements are not observed on faults here, but compartmentalization of the reservoir is likely, as deduced from production data. Fracturing associated with the faulting is probably a control on local reservoir quality in the Henderson Dome area, both in terms of the fracture density and fracture porosity and permeability.

PART 1: FRACTURE ANALYSIS

The main objective in this part of the study was to characterize natural fractures and assess their role in reservoir performance. We used a new analytical approach that is based on using microfractures (defined as having lengths of microns to millimeters) as proxies for the larger natural fractures that influence reservoir behavior (Laubach and Milliken, 1996; Laubach, 1997; Marrett and Laubach, 1997). Microfractures are useful guides to large fractures because they are far more common than large fractures and therefore can be used even where large fractures are not encountered by the wellbore. This method is also useful where the attributes of large fractures are inadequately determined by geophysical well logging methods. An example of this is enhanced interpretation of borehole image logs. Imaging tools can detect large fractures that intersect the wellbore, but in many cases they cannot discriminate between natural and drilling-induced fractures (Laubach and others, 1988) or between open fractures and fractures that have merely experienced erosion of mineral fill near the wellbore (Clift and others, 1998). We show that with small rock samples from zones with ambiguous image-log responses, microfracture observations can help provide a more robust interpretation of the image log.

In this report, we describe the physical and diagenetic attributes of natural microfractures in three wells in the Cataract/Medina Group in the Henderson Dome study area (fig. 2). Our fracture-characterization procedure begins with analysis of sidewall cores and borehole image logs; use of scanning electron microscopy, cathodoluminescence, and conventional petrographic analysis of thin sections; and predictive scaling analysis of fracture populations. A major accomplishment of the study was the development of a new method to orient drilled sidewall cores that allows microfracture orientations to be obtained. Finally, an aim of this study was to determine if independent fracture information could be collected from wells to calibrate and test seismic methods for natural-fracture characterization.

The microfracture analysis methods we used are capable of providing three basic types of information about large fractures. Microfracture orientation can be used to infer the strike of

large fractures (Laubach, 1997). The timing relations of fracture opening and cement precipitation can be used to assess the degree of mineral fill in fractures and therefore fracture conductivity (Laubach and Milliken, 1996). Microfracture-size distributions can be used to predict the size distribution of large fractures (Marrett and others, 1998), and therefore they can provide a measure of the intensity of fracture development. All of these approaches are experimental; both the practical utility and empirical success (or failure) of the methods and the theoretical basis for their applicability were research issues in this project. This study also marked the first test of these methods in the Appalachian Basin. Other applications of this approach have mostly been in younger basins having less complex burial histories; therefore, this study area provides a good test of the method's applicability in areas having protracted and potentially complex loading histories. Subsurface fractures in such areas are generally difficult to assess using conventional techniques.

Data for the analyses in our study are from 27 sidewall cores from two Cataract/Medina wells, one in Mercer County and one in Butler County (table 1). Samples from the Atlas Dayton No. 1 and Atlas Lucas No. 1 wells have been examined in the greatest detail. We also had access to borehole image logs from two of the three wells. We interpreted wireline logs from the Atlas Dayton No. 1 and Atlas Lucas No. 1 wells, and Schlumberger independently analyzed the Atlas Montgomery No. 4 log on a work station.

Fracture Sampling Method

Sidewall Coring

Fracture information was obtained from drilled sidewall cores. Because fracture analysis from sidewall cores is a new method, and because a key element of our study was devising a method to obtain oriented sidewall cores, we begin our description of results with an account of the sidewall-coring research.

Table 1. Ranking of sidewall-core-orientation attributes from Atlas Lucas No. 1 well.

Sidewall core depth (ft)	Core top (rank)	Bedding (rank)	Borehole end curvature (rank)	Lip	Plume (rank)	Initiation point (rank)	Natural fracture (rank)	Sedimentary structures (rank)	Scribe marking (rank)	Coring-induced fracture (rank)	Combined core (rank)	Core deviation (rank)	FMI azimuth (rank)	FMI core azimuth error (degrees)*	Deviation from normal to borehole (degrees)	Diagenetic features (rank)	
6,338	6	0	2	2	2	0	0	0	0	0	6	0	3	120	na	0	
6,342	6	0	2	0	0	0	3	1	0	0	8	2	4	120	2	2	
6,360	6	1	2	2	0	1	0	0	0	0	7	1	4	2.5	-9	2	
6,364	7	2	2	2	0	1	0	0	0	0	9	2	2	90	-6	0	
6,366	8	1	2	2	1	1	1	0	0	0	8	0	4	2.5	na	0	
6,371	-1	0	0	0	0	0	0	0	0	-1	-1	0	3	45	na	0	
6,381	10	1	2	3	2	1	2	0	0	-1	12	2	4	2.5	2	0	
6,386	3	2	2	0	0	0	0	0	0	-1	5	2	2	90	2	0	
6,386	10	2	2	3	2	1	0	0	0	0	13	3	3	2.5	0	1	
6,399	3	1	2	0	0	0	0	0	0	0	5	2	4	2.5	6	0	
6,412	8	1	2	3	1	1	0	0	0	0	9	1	4	2.5	-8	2	
6,462	7	1	2	3	0	1	0	0	0	0	8	1	4	2.5	8	0	
6,463	1	1	0	0	1	0	0	0	0	-1	1	0	4	2.5	na	0	
6,467	7	2	flat	3	1	1	0	1	0	-1	10	3	4	2.5	0	0	
6,477	6	2	2	2	0	0	0	0	0	0	8	2	4	2.5	-2	0	

*2.5 degrees assumed to be normal FMI error.

Our method for obtaining oriented sidewall cores involves examining the recovered core to determine the stratigraphic and geographic top of the core. Although this may seem a trivial step, we found it to be the key to successful core orientation. The second step is to measure the azimuth of the sidewall core by examining the trace of the sidewall-core hole visible on an image log run after the coring tool. A key part of this step is careful comparison of the recovered core with the image log.

Sidewall coring is a commercially available alternative to conventional full-wellbore (whole) cores. In our study, we used the Schlumberger Sidewall CoreDriller® tool. A wireline sonde carrying a small, rotary, diamond-studded bit and gamma-ray detector is lowered to the desired depth interval (fig. 5). The entire sonde is pressed against the borehole wall by a hydraulically powered shoe. The bit is then rotated perpendicular to the borehole wall, and drilling is commenced. The bit drills 5 cm into the borehole wall, and the Schlumberger device is abruptly rotated 7 degrees downward at the bit end (other devices have similar designs, but the exact direction, and to a lesser extent, the amount of rotation used for breakoff, must be known when applying our approach).

In the method we devised for orienting core, this rotation step in the operation of the sidewall device is critical. The rotation of the sidewall bit snaps the core off of the rock mass. With the device we used, this results in a crisp and reproducible pattern of breakage in the tough, fine-grained strata typical of Cataract/Medina sandstones. The fracture-surface features (arrest lines, plume structures, etc.) that result indicate the direction of fracture propagation. Together with information on the working of the tool (rotation direction), this information can be used to infer core tops, as described below.

Core is recovered inside a free-rotating core barrel and subsequently is dropped borehole-end up into a receiving cylinder. A marker disc that is used to identify the core is dropped on top of it. Cores and partial cores are thus stored sequentially from the bottom of the cylinder, with one disc separating each core from the next. Figure 6 shows cores as they appear when the receiving cylinder is first opened after tripping out. By counting disks, and comparing them with

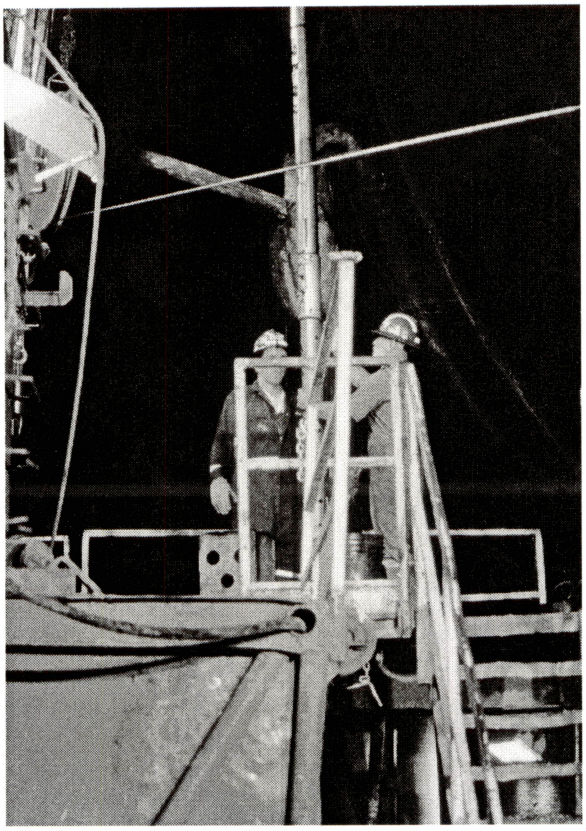

QAc2707c

Figure 5. Schlumberger Sidewall CoreDriller® tool tripping into the Atlas Lucas No. 1 well.

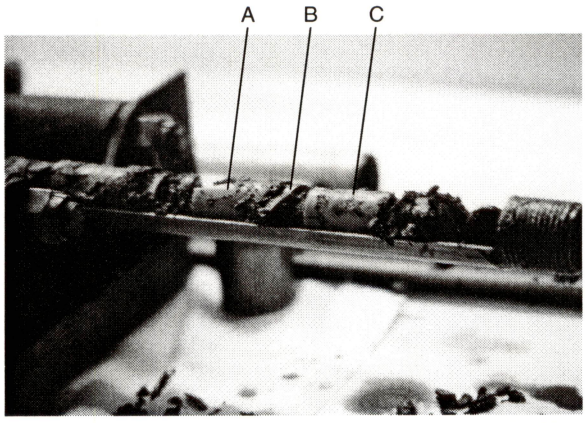

QAc2704c

Figure 6. Retrieved sidewall core as it appears when the receiving cylinder is first opened, Atlas Lucas No. 1 well. (a) Core from 6,381 ft depth. (b) Marker disc. (c) Core from 6,386 ft depth.

a list of the depths cored, each core can be matched to its approximate recovery depth. Even if no core is retrieved at a particular depth, the marker disc is present to account for the failed attempt. A typical sidewall core is 21 mm in diameter and 4-6 cm long. No markings from which orientation can be obtained are made on the sidewall core itself during drilling.

Sidewall coring must be followed by microresistivity logging or other image logging to allow precise determination of depths of azimuth of the core. The sidewall tool has a gamma-ray detector, which allows sample depths to be selected fairly accurately, although because the coring device is a wireline tool, bouncing can affect vertical placement. Currently available sidewall coring devices do not directly measure core azimuth, although inclusion of a magnetometer should be possible.

In this study, the borehole wall was imaged using Schlumberger's Formation Microimager® (FMI) log, but any borehole imaging tool (including borehole televiewer logs and varieties of caliper log that have excellent circumferential wellbore coverage) should work equally well for obtaining sidewall core azimuth orientation. The FMI tools give very precise measurements of resistivity between eight pads carrying probes pressed firmly against the wellbore surface. The FMI device only measures resistivity a few millimeters into the borehole face and produces an image of the inner surface of the borehole wall. Depending on borehole diameter and logging conditions, 60 to 100 percent of the borehole wall is imaged. Horizontal, planar features appear as straight, horizontal lines. Dipping planar features appear as partial to full sine waves, the amplitude of which indicates the steepness of dip (fig. 7).

In hard-copy output, different scales are typically used for the vertical and horizontal dimensions of image logs. Images used in this study have a pronounced horizontal exaggeration, so that the circular holes left by core removal appear as oblate ellipses (fig. 8). Thick mud cake can produce poor-quality images, as can borehole rugosity, excessive logging speeds, and extreme vertical deviation. Without access to digital logs and a workstation equipped to view and analyze them, we were restricted to interpretation of hard-copy logs. Such interpretation is difficult and less precise than digital-image analysis in the determination of fracture strikes and

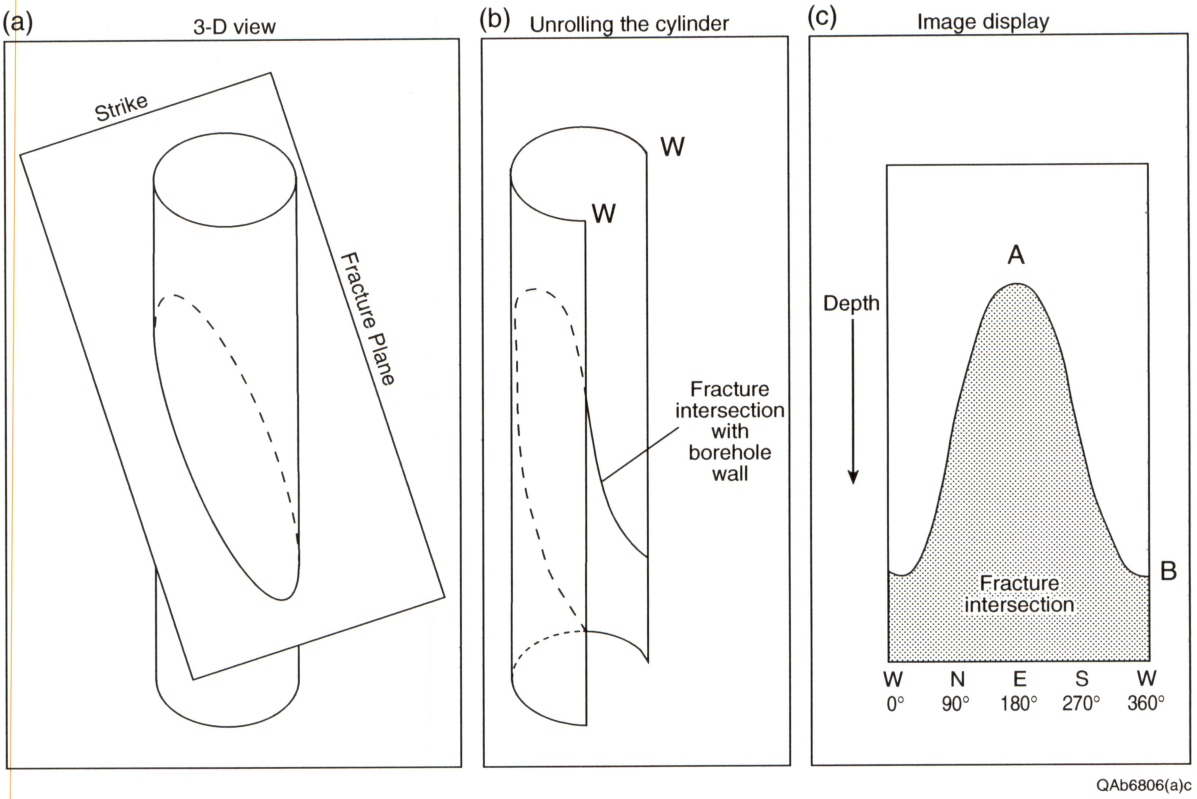

Figure 7. Illustration showing the appearance of a planar feature (fault, fracture, or bedding) on an image log. From Hammes (1997).

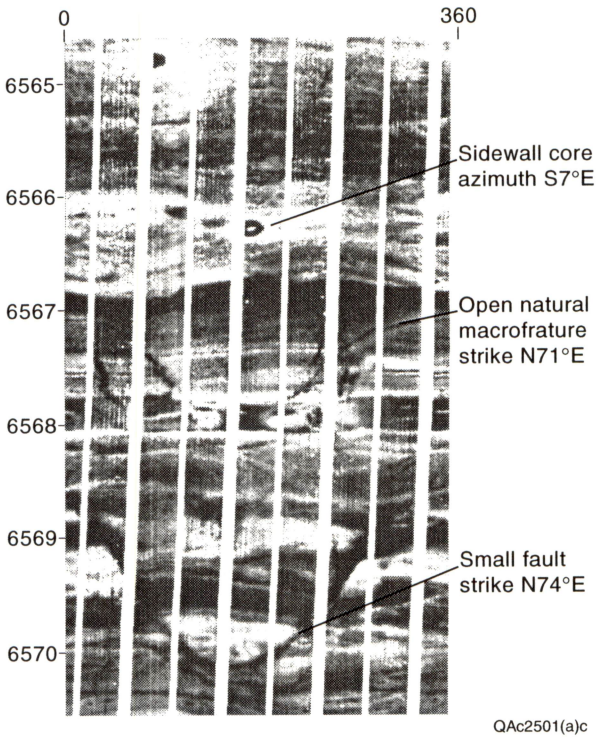

Figure 8. A portion of the FMI log of the Atlas Dayton No. 1 well, showing a failed coring attempt (at 6,564.8 ft); a successful coring attempt; a small fault; and a conductive, non-vertical macrofracture. Both coring attempts targeted a depth of 6,568 ft.

apertures. Log descriptions for the Atlas Lucas No. 1 and Atlas Dayton No. 1 wells are included in appendix 1. We did not have access to an image log from the Atlas Montgomery No. 4 well in Phase I.

Sidewall Core Azimuth

Once the sidewall cores are collected, the cores must be analyzed to determine the top of the core, and the cores and image logs are examined to measure core azimuth. The image log reveals the precise depths and azimuths at which cores were drilled. It also allows examination of the near-core environment for lithologic and core-hole details that are helpful for determining the top of the core.

Since image logs provide an oriented map of the borehole wall and because sidewall-core holes filled with conductive drilling mud are large compared to the features these logs are designed to detect, in many cases measuring the azimuth of sidewall core holes merely involves measuring the orientation of the center of the dark circle (or ellipse, where images are not corrected for vertical exaggeration) created by the hole on the image log. Ambiguities can, however, be introduced by coring operations.

For example, determining the azimuth from which a core has been retrieved is ambiguous if two coring attempts are made at the same depth. A failed attempt at coring and a successful one leave essentially identical indications on an image log. It is not possible to determine during drilling at exactly which depth a core has been drilled because Sidewall CoreDriller® is a wireline tool. Any small amount of recoil or bouncing on the cable can cause the driller to core a location as much as 1 m from the target interval. Tight gas sandstones are typically very hard and tough, with the presence of natural fractures being an additional complication. Some fractures are weakly cemented, making the likelihood of obtaining an intact core on the first try uncertain. We monitored coring operations on site in our study, and in 11 out of 26 cases, the drillers had to make multiple attempts prior to obtaining indications that they had a satisfactory sample from a

given depth interval. In two cases, the cores actually retrieved were too short for use in conventional permeability and porosity determinations. We were able to use information from the image log (other than the appearance of the hole itself) to refine the azimuths of most of the duplicate cores. In four cases, certain determination of core azimuth was not possible. These results show that a careful protocol for coring should be established with the coring crew prior to coring operations.

A final adjustment must be made to the azimuth obtained from the imaging log. The sidewall drill does not typically recover samples perpendicular to the borehole wall. Realizing that this deviation would need to be considered when determining the core's azimuth orientation, we developed a way to measure and rank the deviation. It is uncertain whether deviation is a result of the circular shape in the borehole or a skewed seating of the sonde when the hydraulic shoe presses it against the borehole wall. In no case did the deviation exceed 12 degrees from perpendicular to the borehole wall. In some cores, the alignment of the core axis is not constant. This is caused by the operator "backing out" the bit when the drilling rate drops off due to accumulated fine cuttings. This accumulation of fine, tough cuttings is apparently characteristic of the Cataract/Medina Group. Over 50 percent of coring attempts in this study required backing out, most resulting in no core retrieval. In cases where a single deviation angle cannot be determined, such as that shown in figure 9, where the core axis changes orientation along the core, the core may not be used for orientation purposes with good accuracy. The measurement of azimuth deviation is a simple procedure when performed on intact core, but it becomes complicated, and sometimes impossible, when performed on core reconstructed after preparation for permeability and porosity testing.

Even when the sidewall core log shows that coring was successful, the entire core may not remain in the barrel as it is pulled from the hole if a fracture was intercepted. In two cases, this resulted in only a short (2-3 cm) core section, too small for conventional permeability and porosity determinations. These samples may also be unsuitable for sidewall core orientation, although they can be used for microfracture-quality studies.

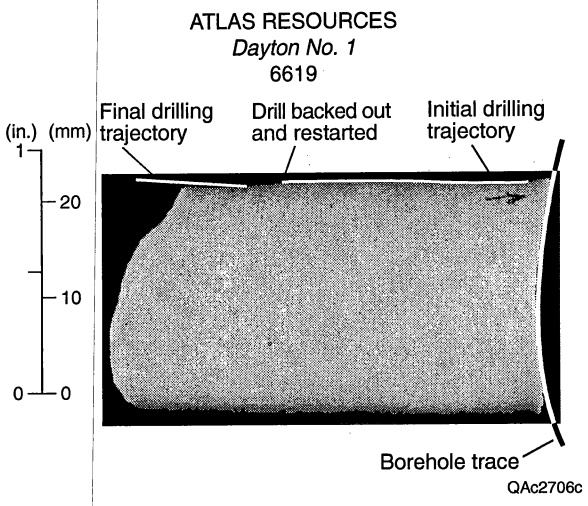

Figure 9. An example of a core for which deviation cannot be determined. The drill was backed out and reinserted, which changed azimuth orientation. The uniaxial concavity composing the borehole trace is also shown.

Sidewall Core Tops

Having obtained the azimuth of the core, we still had to determine the facing direction (top direction) of the small (21-mm-diameter) core. The task is similar to that of deciphering the facing direction of strata revealed in a quarry wall by looking at only one 21-mm circular area. All of the most common facing indicators, such as asymmetric depositional features like cross beds, are typically much larger than the sample available. Only one of 27 cores we examined held a usable sedimentary facing indicator.

With currently deployed sidewall coring devices, no markings from which orientation can be obtained are made on the sidewall core itself during drilling. Scribes or other types of markers could in principle be added to the devices, although care must be used to insure that such markings do not interfere with or complicate permeability and porosity testing on the recovered cores. However, even without sedimentary facing evidence or a scribe line on the core, a substantial portion of retrieved sidewall cores can be uniquely oriented in vertical facing by using fracture-surface marks on the cores and through careful examination of evidence from the image logs.

To determine which direction was vertically up when the core was in the well, we began by observing the core drilling at the Atlas Lucas No. 1 well and analyzed the mechanical working of the coring device (fig. 10). This was done to assess the potential of using the surface morphology of the broken end of the core as a top indicator. The morphology of such surfaces, and what it can tell about the forces that caused the fracture, have been widely studied (Kulander and others, 1990, and many others). We then examined the cores as soon as the receiving cylinder was opened and marked the borehole-remnant end of each core. Because the coring device always drops a core borehole-end up into the receiving cylinder, this was readily determine on-site. The collected cores were packed individually and hand-carried for laboratory analysis.

Examination of this first group of cores made it clear that the borehole-remnant end of a core could be determined with 100 percent certainty.

All fragments of each core sample were cleaned and photographed. We had determined, in our mechanical examination of the breakoff operation of Schlumberger's device, that the formation end should be a mixed mode I-II fracture surface resulting from forces such as those shown in figure 11. Using oblique lighting and magnification, the end of the core that had broken from the formation (formation end) was examined carefully for morphological clues to the direction of propagation of the fracture. We hypothesized that there should be an initiation point, or dimple, that would occur near the bottom, a projecting lip that would occur at top center, and horizontal arrest marks with little curvature. All of these features were observed in the group of cores studied. Several other features were observed and their causes determined. These features are represented in a single idealized sidewall core in figure 12. In a few samples, inclined bedding was observed; the dip direction of the beds could be seen in the FMI log. In all cases examined, the morphological indicators were in agreement with the bedding orientation (fig. 13). In another case, shown in figure 14, one of the vagaries of wireline core drilling provided us with a sample that had its orientation indicator built in, in the form of a nick made by a prior, failed coring attempt. The shape of the core and its image on the FMI log established the core top; and its formation-end morphological indicators were in agreement.

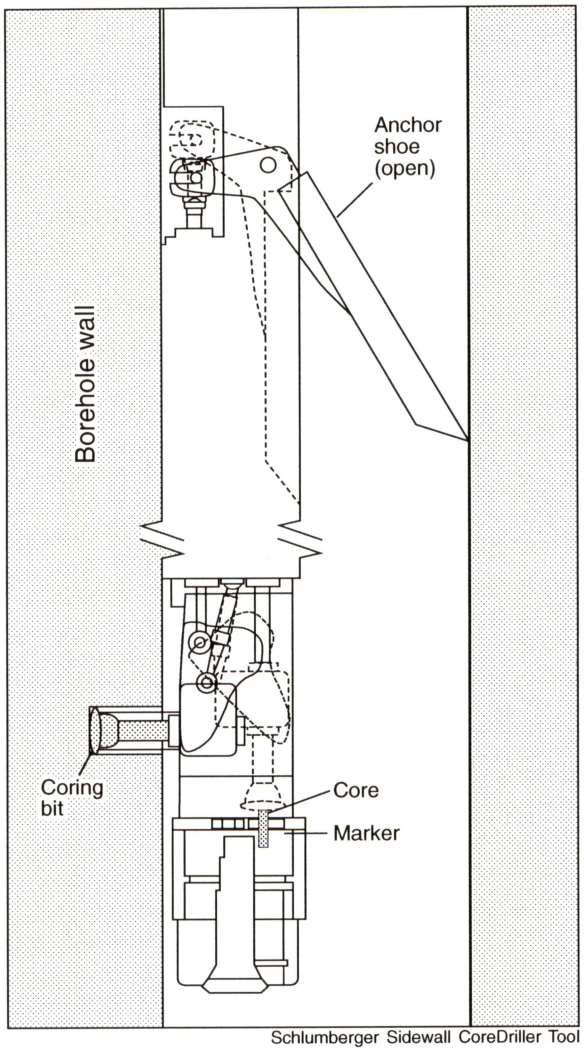

Figure 10. Schematic diagram of the Schlumberger Sidewall CoreDriller® tool, showing its deployment in the wellbore, position of the drill during coring, and collection of core and marker in the receiving cylinder.

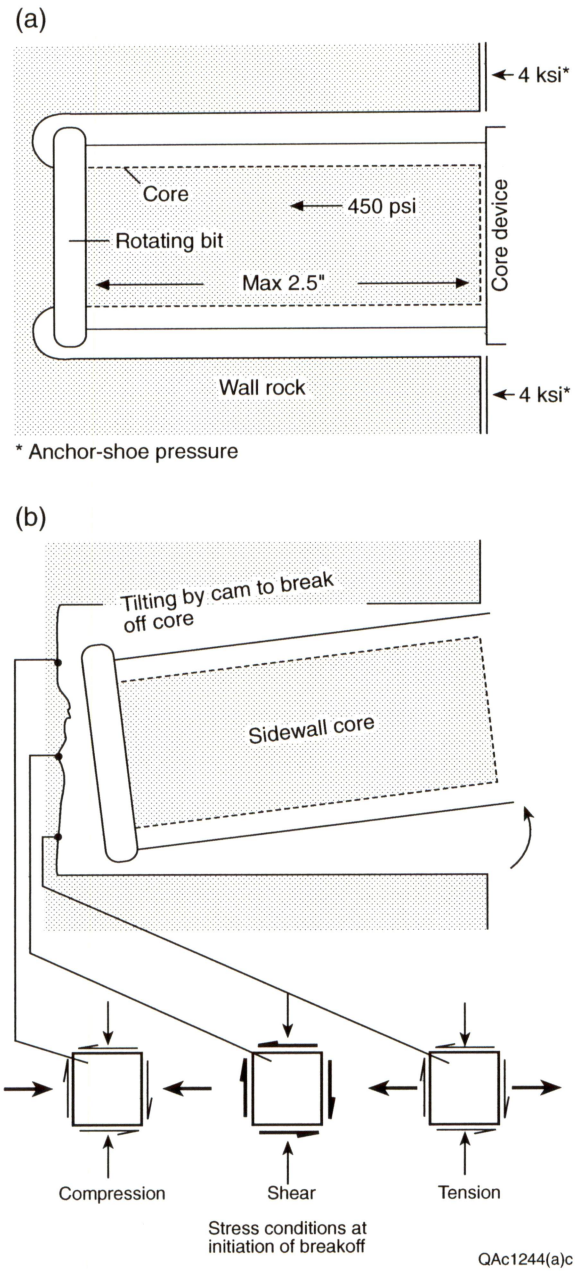

Figure 11. Local stresses during drilling and initiation of breakoff.

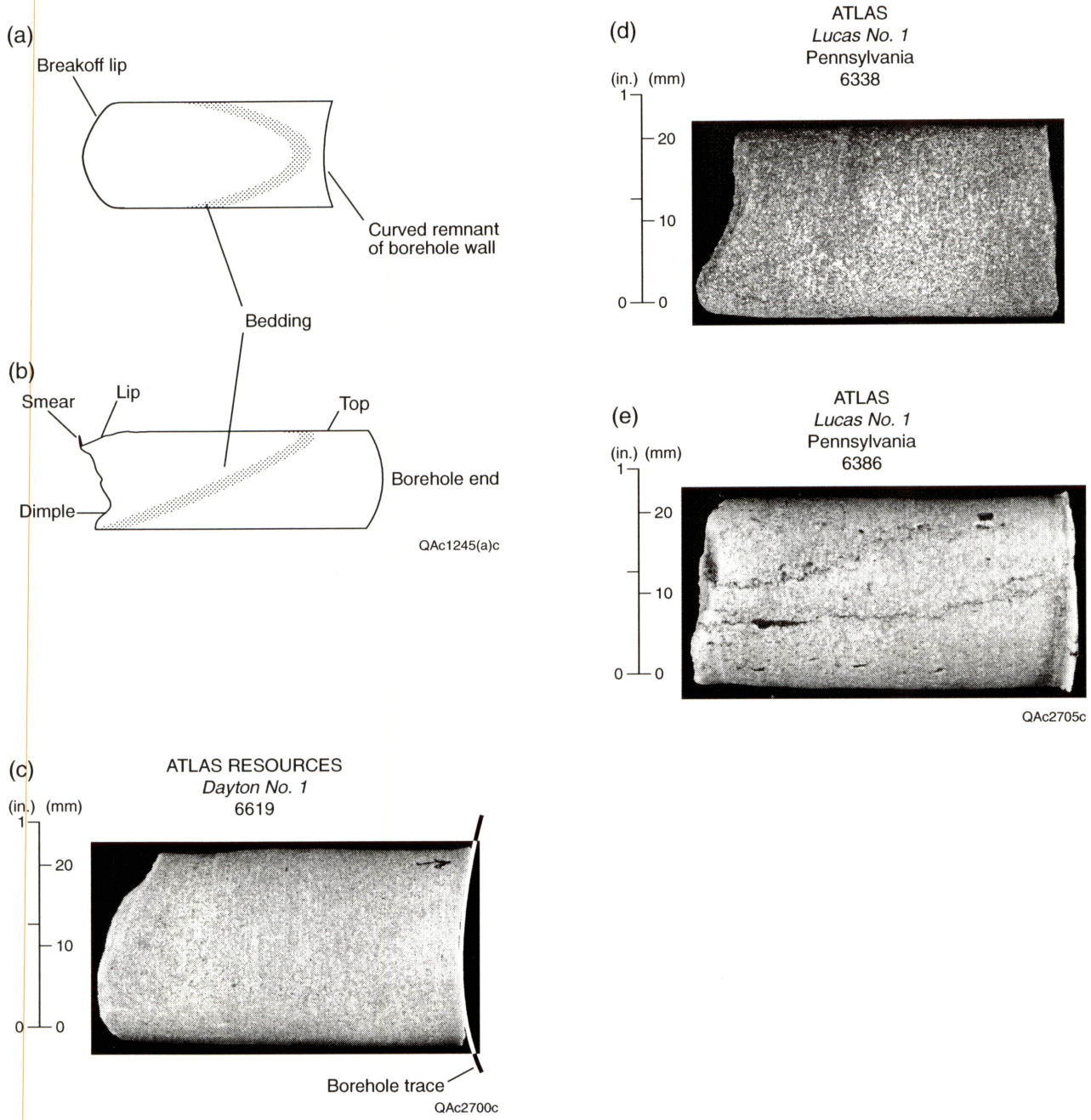

Figure 12. Schematic representation and photographs of features desirable for orientation of sidewall core. Initially dominant tension in the lower portion of the core forms a dimple (b). Plume and subhorizontal arrest marks (not shown) are formed by upward propagation, and the lip (b, c) and smear (b, d, e) are related to initially high compression followed by shear in the upper portion of the core. The downward curving zone on top of the lip is formed by the still-rotating bit.

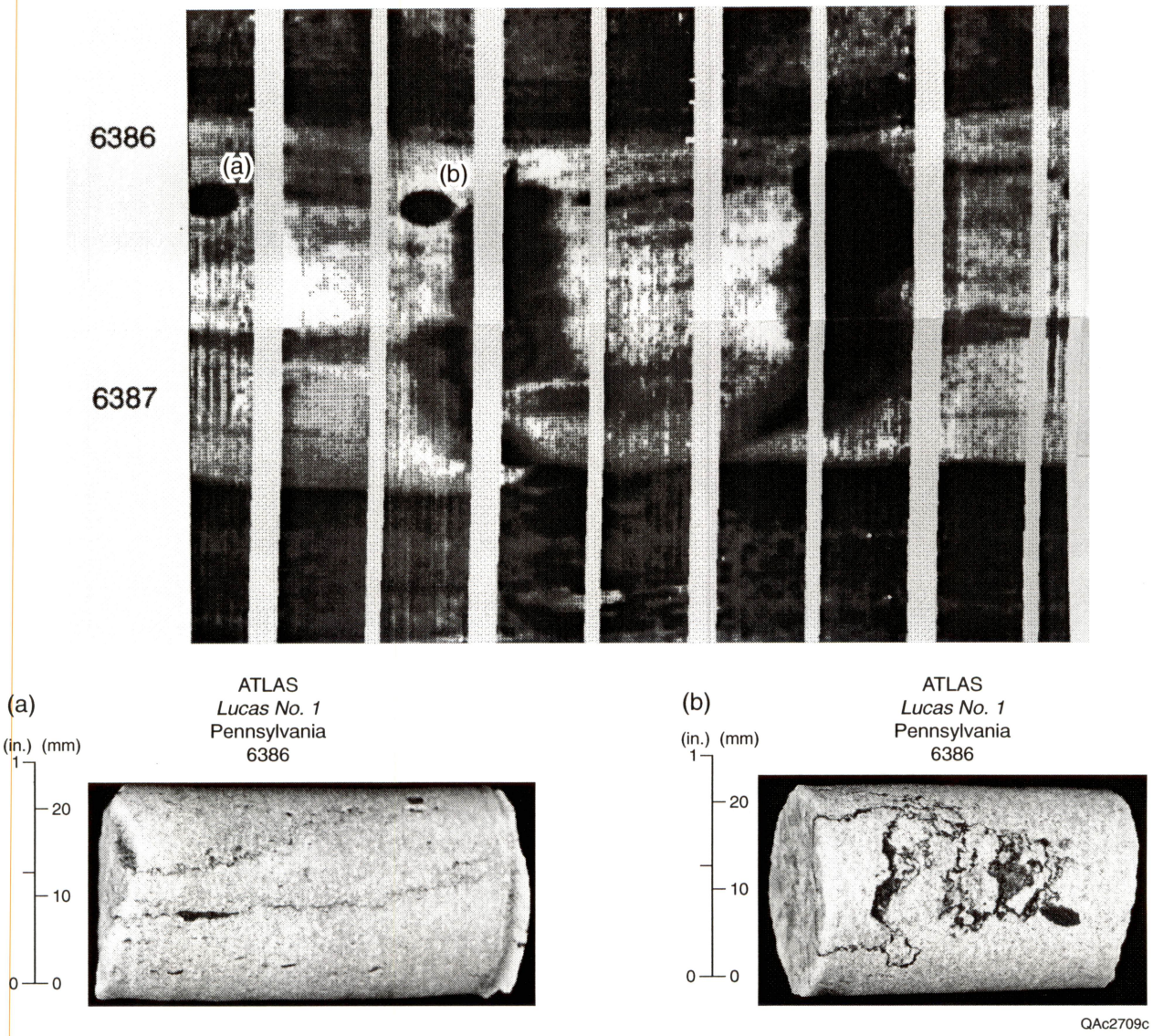

Figure 13. Use of inclined bedding in determination of core top. (a, b) Sidewall cores, showing well-developed black shale partings. (b) FMI log shows dip of bedding at locations of sidewall cores a and b. (c) Worm's-eye view of a truncated ripple, with only the top preserved. (d) End view of core showing ripple remnant and reconstruction of ripple.

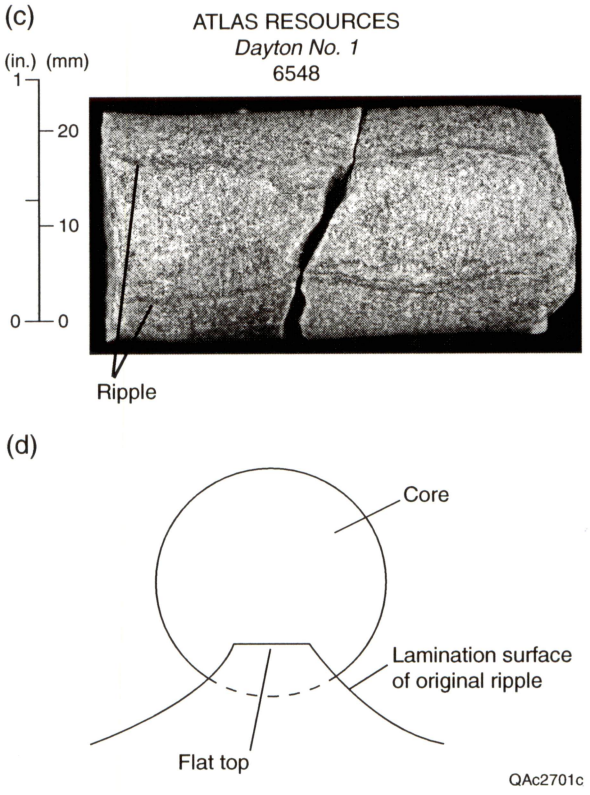

Figure 13 (cont.).

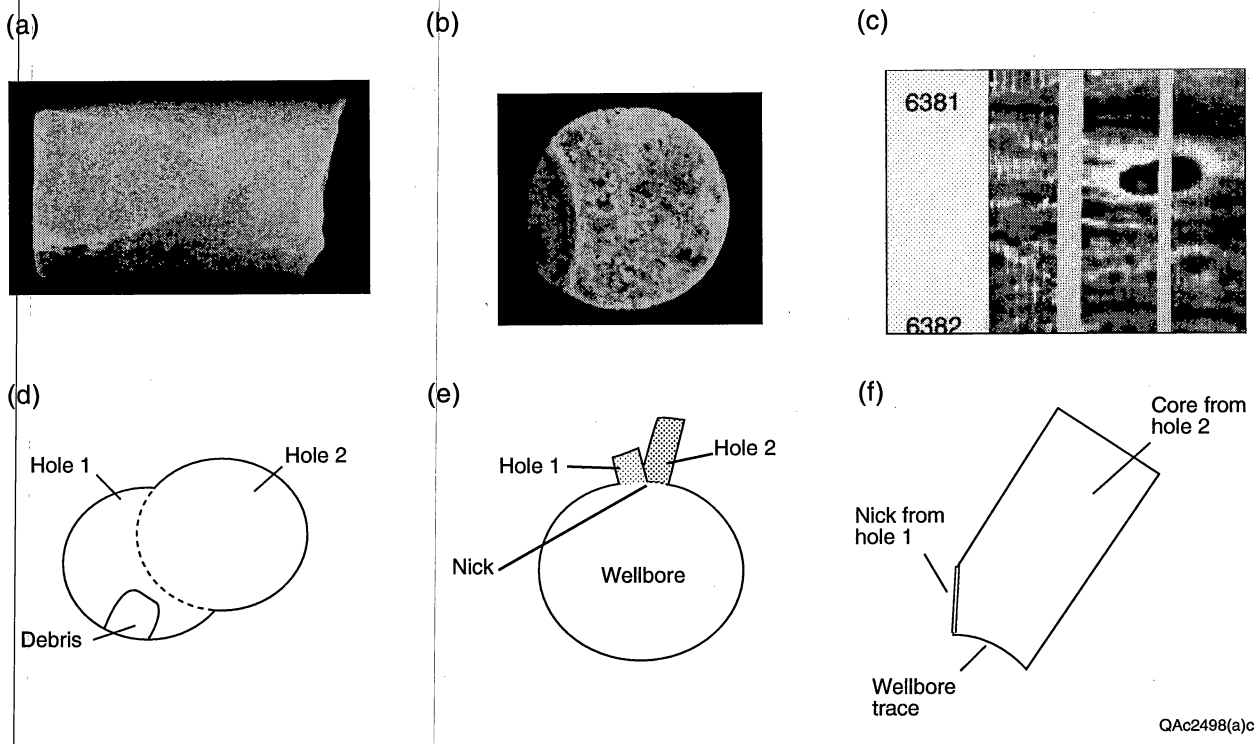

Figure 14. Orientation of sidewall core when coring is achieved on a second attempt and envelopes a portion of the volume removed during the failed first attempt. (a) Appearance of the nick along-core. (b) Appearance of nick at borehole end. (c) Core and attempted core on FMI, showing location of retrieved core.

Drilling-induced fractures similar to disc fractures (Kulander and others, 1990) seen in whole cores were observed in several of the sidewall core samples. These render the cores nonorientable unless they contain inclined beds that can be seen in the image log. Cores with natural macrofractures are rarely recovered because the cores containing them are usually highly fragmented. When a natural macrofracture is observed in a recovered core and on the image log, the core is oriented for practical purposes (although ambiguity in core top may remain). Furthermore, even if a sampled macrofracture cannot be oriented, observations of type, timing, and degree of fracture fill may be of great utility. In our study, we retrieved one core that contained part of a large fracture, and it gave macroscale confirmation of some of our microscopic observations.

We offer a cautionary note at this point. Only the operation of the Schlumberger device has been analyzed and related to formation-end morphology in this study. If the devices of other service companies accomplish breakoff in a different mechanical manner, the relation of fracture-surface features to core tops may differ from that using the Schlumberger device. However, if the samples are collected by a single rotation to snap off cores, then knowledge of the specific rotation direction for the tool should be sufficient to adapt the technique that we describe to the new tool. This should be applicable to any break-off method that involves a single abrupt motion and that does not induce torsion.

Ranking Core Orientation

Not all of the desirable features for finding core tops were evident in every Cataract/Medina core. Therefore, we developed a semi-quantitative ranking system that was tested by multiple examiners to achieve a repeatable method of assessing the certainty of the tops determination. Table 1 is a spreadsheet presentation of this ranking system applied to cores from the Atlas Lucas No. 1 well. The same analysis was done on the samples from the Atlas Dayton No. 1 well, and the results of both are depicted in figures 15 and 16.

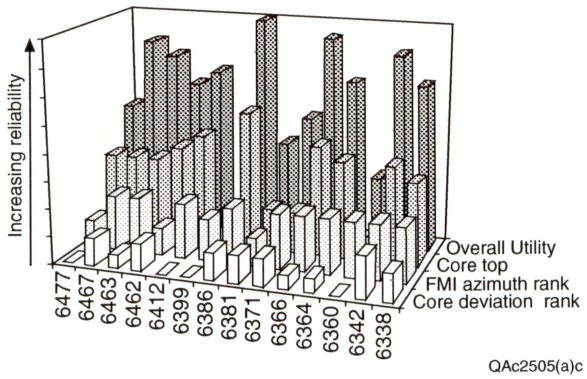

Figure 15. Results of the semi-quantitative ranking scheme for reliability of sidewall core orientation, Atlas Lucas No. 1 well. Core-top rank represents degree of certainty in the in-situ up orientation. Core-top rank represents the degree of certainty of the in situ vertically up orientation. Combined core rank evaluates this top certainty in conjunction with the core's azimuthal certainty. Overall utility incorporates the combined core rank with diagenetic features of potential value.

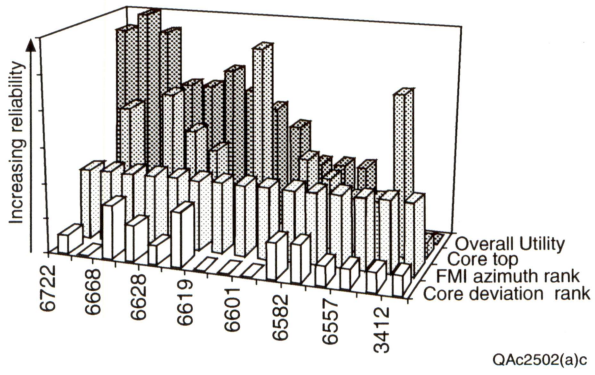

Figure 16. Results of the semi-quantitative ranking scheme for reliability of sidewall core orientation, Atlas Dayton No. 1 well. Core-top rank represents the degree of certainty of the in situ vertically up orientation. Combined core rank evaluates this top certainty in conjunction with the core's azimuthal certainty. Overall utility incorporates the combined core rank with diagenetic features of potential value.

Although semi-quantitative at this point in development, the core-orientation ranking scheme can be further developed to yield quantitative measures of error in azimuth and vertical tops. This ranking system considers our degree of confidence in determining the orientation of the core as well as our preliminary estimation of its potential utility in microfracture analysis and diagenetic study. In our study of the Atlas Lucas No. 1 and Atlas Dayton No. 1 wells, we used the core-orientation ranking system to focus on the nine samples with the most reliable orientation. We are preparing a manual for sidewall-core examination that details the application of this system to cores selected for microfracture-orientation studies.

Faults and Macrofractures on Image Logs and in Core

Large-aperture fractures and faults are evident on FMI logs from all three study wells. Most of the fractures are subvertical. It has proven difficult to discriminate natural from drilling-induced subvertical fractures using only a borehole image (Nelson and others, 1987; Kulander and others, 1990; Laubach, 1992; Clift and others, 1998; Olson and others, 1998). A comprehensive listing of all those identified from the FMI logs, with their manually measured orientations are included as appendix 1. In the Atlas Dayton No. 1 well, we were able to retrieve two samples proximal to small faults. One is shown in figure 17. From the same well, we retrieved cores proximal to four vertical fractures, three of which we were able to conclusively identify as drilling-induced as a result of examining the fracture in the retrieved core. From the Atlas Lucas No. 1 well, one of the short cores (6,342 ft depth) intercepted a subvertical natural fracture of substantial aperture, partially filled with anhydrite over euhedral quartz overgrowths, from which we retrieved one fracture face. On the FMI log, the trace of this fracture is visible, but faint, indicating its partially mineral filled character. Two other cores from this well intercepted very small aperture macrofractures that proved to be natural and are not distinguishable on the FMI log. Only one core from the Atlas Lucas No. 1 well intercepted a drilling-induced fracture, and this subvertical fracture is easily visible on the FMI log.

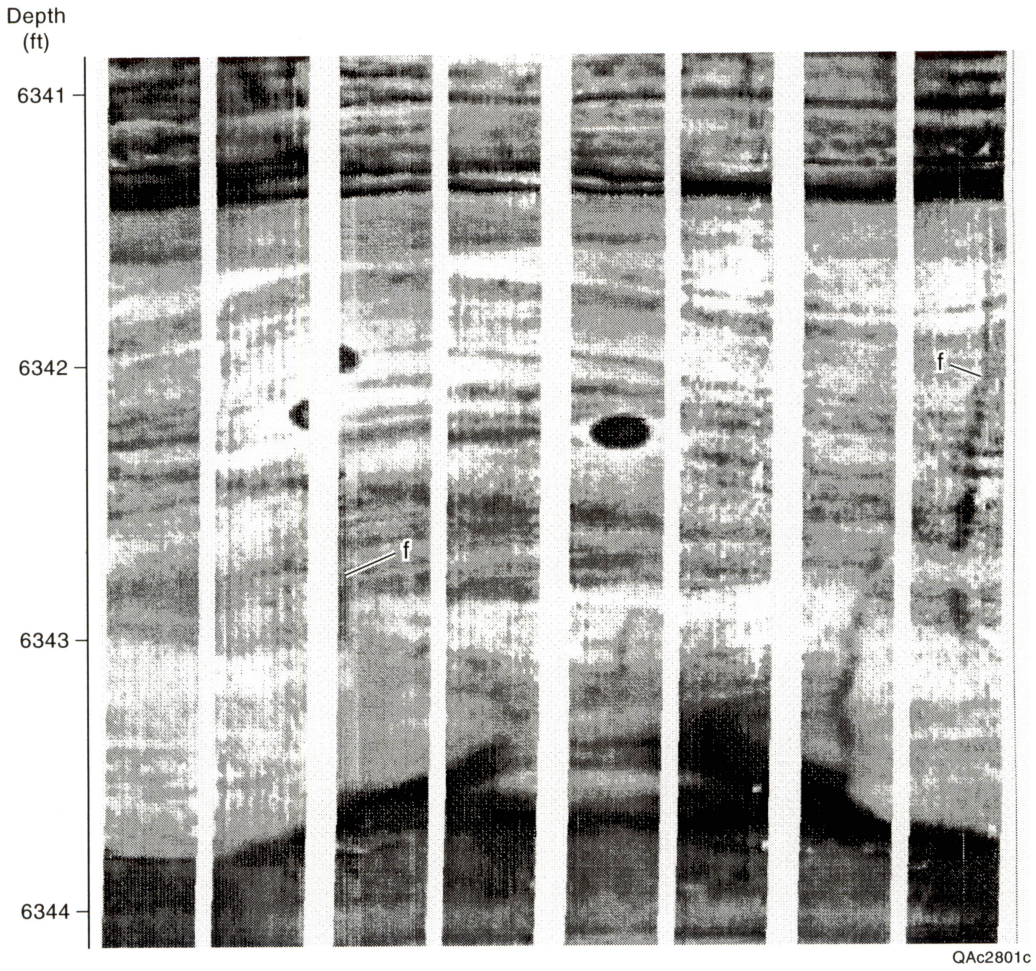

Figure 17. A portion of the FMI log of the Atlas Lucas No. 1 well showing a retrieved core that intercepted a natural fracture partially filled with quartz and anhydrite. The fracture is faint and strikes N46W.

Of the faults seen in the two logs, all are small with regard to visible vertical displacements. Some have a normal component to displacement, whereas others show a reverse component. In no case is horizontal displacement absent, and slight rotation is common. The character of the fault surfaces is not consistent with soft-sediment deformation or large displacements. The overall impression received is of distributed response to strike-slip strains.

Fracture-Attribute Measurement

Methods

The primary purpose in developing a method for determining the orientation of sidewall cores was to provide oriented thin sections for microfracture-population studies. Most microfractures in quartz sandstones are filled, or partially filled with quartz cement (Laubach, 1988; Milliken, 1994). Quartz-lined microfractures are not normally visible using optical petrographic methods. When they can be detected, they present themselves as tabular clusters of fluid inclusions. It is not possible to measure fracture-morphology parameters such as length, aperture (width of opening), or spacing by this type of examination (fig. 18), and orientation measurements may have great uncertainties (Laubach, 1989, 1997; Laubach and Milliken, 1996). However, authigenic and detrital quartz, which crystallized at different temperatures and contain contrasting trace-element compositions, exhibit varying absolute brightness in luminescence, as well as different color spectra, under electron-beam bombardment (fig. 19). These contrasts can be detected using conventional or Scanning Electron Microscope-based cathodoluminescence (scanned CL) detectors (Sipple, 1968; Zinkernagel, 1978; Yacobi and Holt, 1990; Walker and Burley, 1991; Hogg and others, 1992; Olson and others, 1998). However, scanned CL analysis is more rapid, clear, and accurate, and is the only practical method for imaging relatively large sample areas, as is required for orientation and scaling analysis (Laubach, 1997). We used scanned CL methods to study the microfracture populations in the Cataract/Medina Group samples.

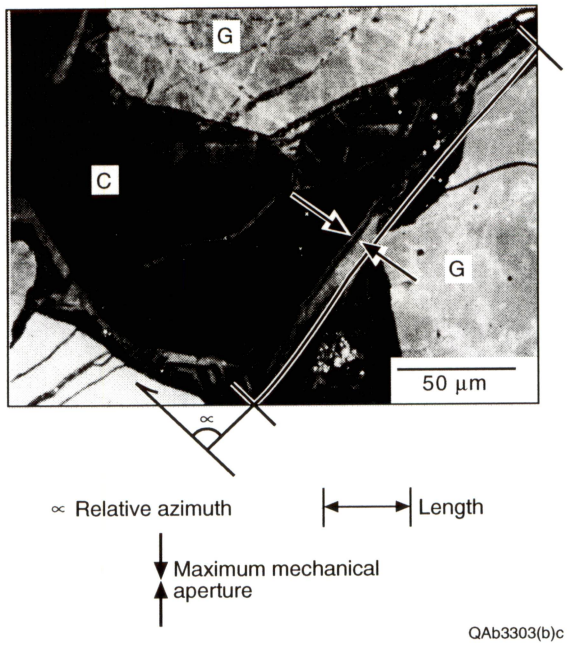

Figure 18. Measurement of fracture attributes. Apparent aperture is the width of the fracture opening measured in the horizontal plane. Length is measured from end to end in the horizontal plane. Azimuth is measured from a convenient reference and is mathematically related to magnetic north.

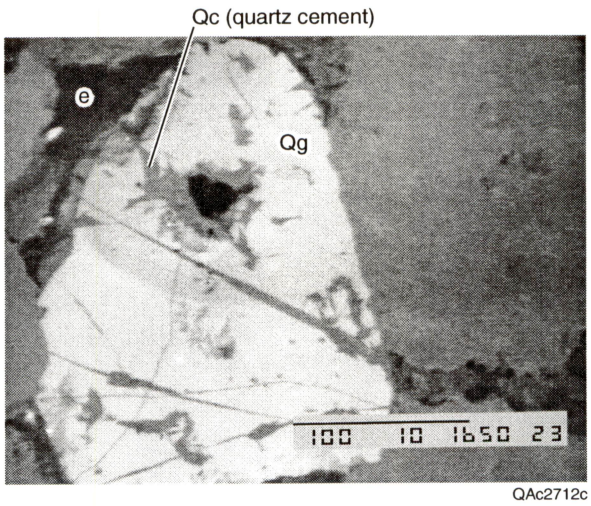

Figure 19. Quartz grain with quartz cement, Atlas Lucas No. 1 well (6,338 ft). The grain (Qg) is quartz of high-temperature origin, the fracture-filling quartz cement (Qc) is of low-temperature authigenic origin. Epoxy resin (e) fills open pore space and is dark in CL. Note the solutional attack to which some of these fractures were subjected, as evidenced by rough, widened segments of the walls. Scale bar is 100 µ long.

Oriented thin sections from the sidewall cores with the highest orientation rankings were analyzed and photographed using scanned CL and standard petrographic techniques. Laubach (1997) established a classification system for relating microfracture morphology to probability of postlithification tectonic origin. In this study, the utility of this method of examination has been rigorously applied to thin sections made from plugs drilled from whole core, as well as thin sections from outcrops. The first step in interpreting scanned CL images to measure fracture-orientation trends is to categorize the microfractures, since not all are reliable guides to the strike of large fractures (Laubach, 1997). We separate microfractures that have shapes that are consistent with their formation in a regional stress field and a relatively mechanically homogeneous rock (category I) from those that we infer are caused by grain-to-grain contact stresses (category II) and microfractures that are inherited from the source rocks of detrital grains (category III). The categories and types of fractures that are classified in this study are detailed in figure 20. All samples examined in Laubach (1997) are much younger than the Silurian Cataract/ Medina strata examined in this study. Moreover, in contrast to the sandstones sampled in this study, which are very fine to fine grained, the sandstones examined in the previous study are fine to medium grained. Thus, the results of this project extend the previously known application of this methodology in mode of sampling (sidewall core), in age of strata, and in the texture of sandstones.

One thin section each from the Atlas Dayton No. 1 and Atlas Lucas No. 1 wells was selected for initial intensive observation. From scanned CL photographs of each of these two thin sections, we physically assembled large (3.15×10^6 μ^2) mosaics composed of 30 to 40 individual photographs. We then determined the classification of each microfracture and manually measured its attributes. For each mosaic, orientation populations were studied by linearly length-weighting the population and analyzing the resultant distribution by category and type. An example of the population orientation analysis is presented in figure 21. Scanlines produce optimal results when oriented perpendicular to the strike of the fracture set being studied. Based on these analyses, we selected trends for scanline imaging of the remaining thin sections in each

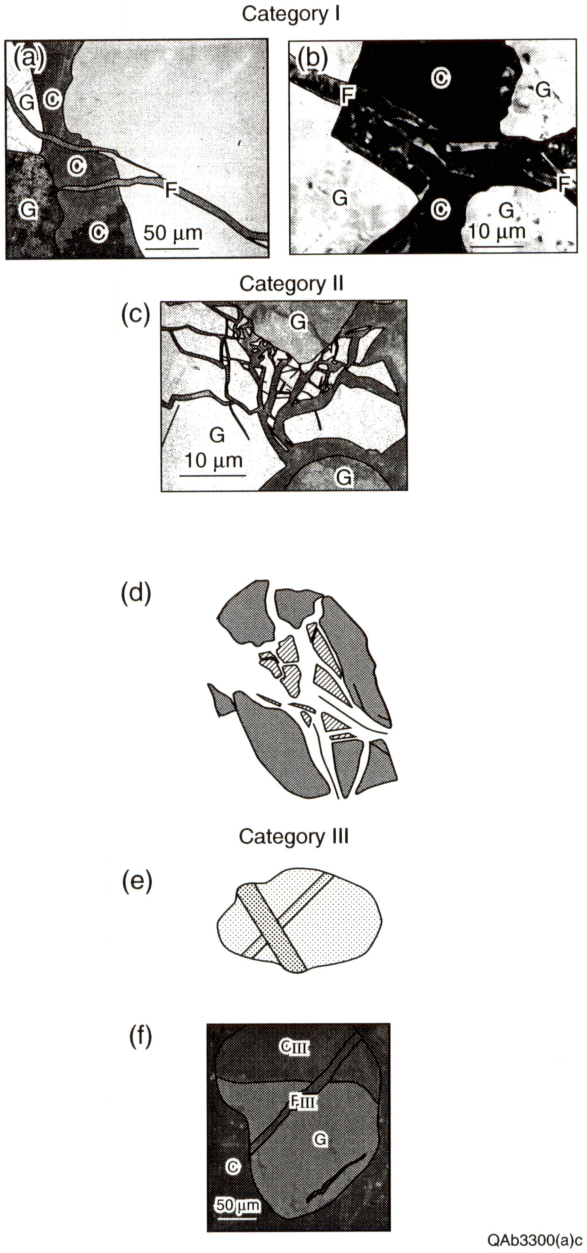

Figure 20. Patterns of microfractures in horizontal section traced from scanned CL photographs. G=grain, C=cement, F= fracture. Parts a-c illustrate category I fractures; parts d and e show category II fractures; parts f and g record category III fractures. (a) Tapering profiles near end of transcement (Ia) fractures. (b) Segmented fracture cutting cement. (c) Network of fractures at grain to grain contact due to interpenetration. (d) Biaxial extension and dilation. (e) Inherited fractures contained entirely within a single grain. (f) Grain with both inherited fracture and inherited cement. Samples are from the Travis Peak, Fall River, and Canyon Formations.

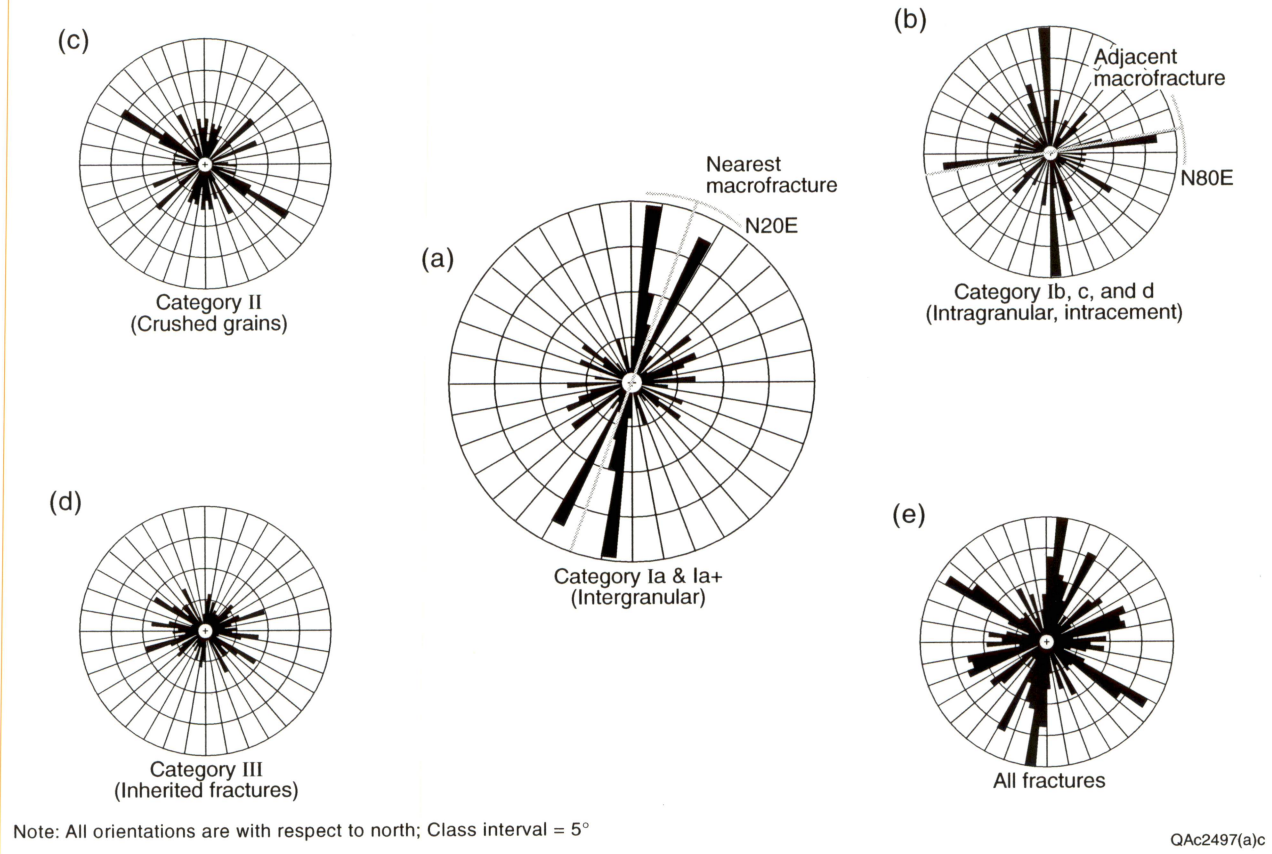

Figure 21. Orientation analysis of microfracture population and subsets from the Atlas Lucas No. 1 well (6,386 ft). Reference is to magnetic north. (a) Types Ia and Ia+ only. (b) Types Ib, c, and d. (c) Category II. (d) Category III. (e) All fracture categories.

well. Photographs were taken along a single scanline on each thin section. We assembled the photographs into a linear collage, classifying and measuring each microfracture. For all thin sections studied, pore-occluding cements were also imaged using scanned CL and secondary-electron-imaging techniques. Such imaging is helpful in distinguishing cements that are opaque to transmitted light and in determining relative timing of cementation events.

Diagenetic analysis is used in assessment of fracture quality. We measured cement compositions and cement volumes from thin sections prepared from the Atlas Dayton No. 1 and Atlas Lucas No. 1 wells, as well as from a suite of outcrop samples collected from the Cataract/ Medina Group outcrops of western New York.

Fracture Orientation

Microfracture analysis indicates the existence of multiple fracture sets fractures in the cored Medina intervals. The single most prominent set strikes N85W, the next most dominant strikes N20E, and the third distinct set strikes N30W. In the Atlas Dayton No. 1 well, the N75W trend is dominant, with the N20E trend only tertiary, whereas in the Atlas Lucas No. 1 well the N20E set is dominant, with the N85W trend secondary. These results are based on a total of 2,225 microfractures, 1,175 microfractures observed in 4 sidewall cores in the Atlas Dayton No. 1 well and 1,050 microfractures in 4 sidewall cores in the Atlas Lucas No. 1 well. The depths of the samples and principal orientations of the microfractures are shown in figure 22, which also depicts regional-scale fractures in the basin. In all, about 2.07×10^7 μ^2 of rock was imaged with scanned CL to obtain this result. These results are compatible with the orientations of some of the fractures visible on image logs in these wells.

Examples of microfractures and cement textures from the Cataract/Medina samples are shown in figures 23 and 24. Microfractures photographed in our previous studies are typically opening-mode fractures with little or no evidence of shear offset, although a fair proportion (about 30 percent) of the microfractures seen in the Medina are mixed-mode, with offset, many

occurring in en-echelon arrays. They are mostly filled with dark (non-luminescent) authigenic cement, although locally, residual microfracture porosity is present, and a late generation of cement bright in CL is observed in many samples. Subtle textural features are commonly visible within the microfracture fill. Mostly, these textures reflect crystal growth into fracture pore space. Some textures appear to have resulted from processes of repeated cracking and fracture sealing ("crack-seal structure"). Such textures are common in large fractures in quartz-cemented rocks (Laubach, 1988, 1997) and indicate that at least some of the quartz cement in the rock was precipitating when fractures were opening. Quartz cement is also conveyed by microfractures to points of precipitation on the grain surfaces at the fracture opening. This timing relationship is also consistent with the widespread occurrence of quartz as the primary and only phase in very thin Cataract/Medina microfractures.

Scaling of fracture sizes is discussed in a following section. In general, microfracture lengths range from 5 μ to hundreds of microns, and apertures from 0.5 μ to 40 μ. The lower aperture size limit represents a limit of resolution, not an absolute limit of size. The upper aperture limit represents our informal definition of microfracture.

Although the distinction between categories (and, therefore, origins) of microfractures is straightforward for many fractures, in most samples there are a large number of microfractures for which the distinction is challenging to make. This arises partly because in most samples there is a range of microfracture sizes, and the large majority of microfractures tend to be of the smallest sizes and hence are the most difficult to image clearly and to categorize. This variation in size (and, indirectly, suitability for determining strike) is reflected in the recorded fracture-size distribution and in the classification of fractures into subcategories (types) in our microfracture classification scheme. In appendix 2, the size range and classification of all the fractures is listed.

Another distinction that can be made using scanned CL is crosscutting relations among fractures. In this suite of samples, it is possible to recognize crosscutting relations that suggest that the N20E fracture set is older that the N85W set based on this criterion (fig. 25).

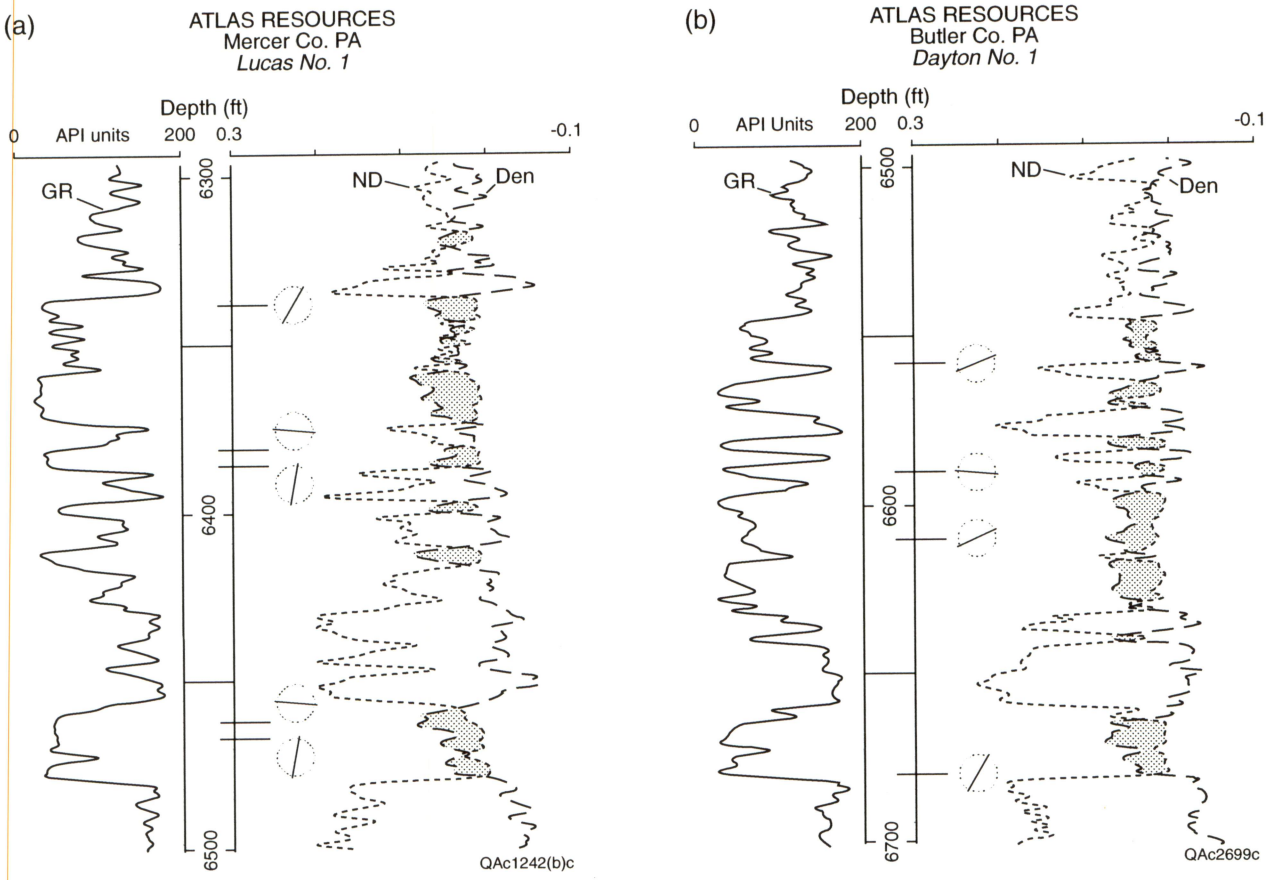

Figure 22. Principal orientations of microfractures. Orientation distributions are linearly length-weighted by category and depth interval. (a) Atlas Lucas No. 1 well. (b) Atlas Dayton No. 1 well. (c) Pattern of regional scale fractures in the Appalachian Basin. Study area is lightly stippled. After Engelder (1985).

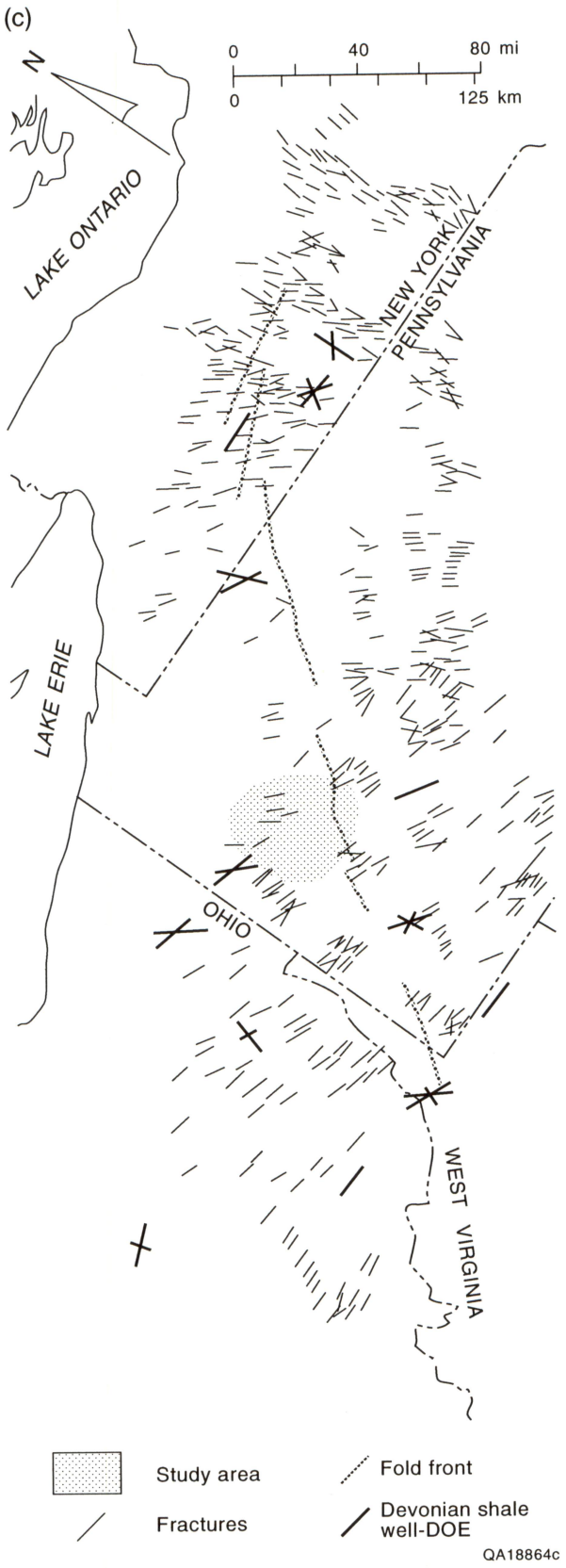

Figure 22 (cont.).

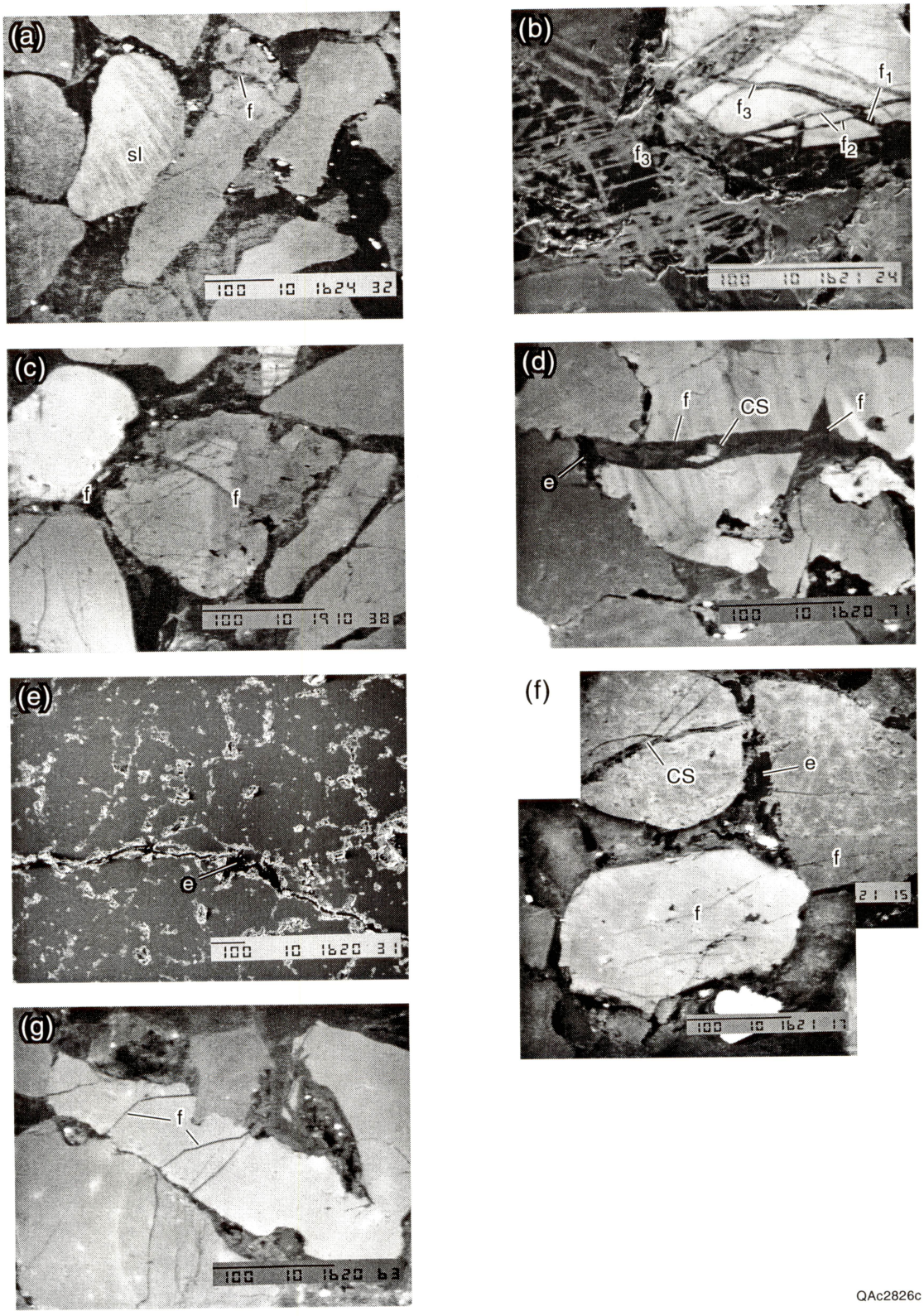
(a)
f
sl
100 10 1624 32
(b)
f1
f3
f2
f3
100 10 1621 24
(c)
f
f
100 10 1910 38
(d)
f
CS
f
e
100 10 1620 31
(e)
e
100 10 1620 31
(f)
CS
e
f
f
21 15
100 10 1621 17
(g)
f
100 10 1620 63

QAc2826c

Figure 23. Microfractures from Medina Group sandstones viewed in CL. Scale bars in microns. Qg=quartz grain, Qc=quartz cement, f=fracture, e=epoxy in open porosity, sl=stress lamellae, CS=crack-seal texture. (a) Fracture cutting grain and early cement, stress lamellae, Atlas Lucas No. 1 well (6,386 ft). (b) Early fractures filled with dark cement (f_1), cross-cut by later fractures (f_2) filled with dark cement, and third generation (f_3) of fractures filled with bright cement, Atlas Dayton No. 1 well (6,568 ft). (c) Partially open microfracture, filled with bright cement, and with definite shear offset, Thorold Sandstone outcrop sample. (d) Sutured interpenetrating grains and cement, parallel to nearby macrofracture. (e) Secondary electron image (SEI) of macrofracture with quartz bridges and open porosity, Atlas Dayton No. 1 well (6,568 ft). (f) Small-aperture Category Ia+ fracture, crack-seal texture in Category Ia fracture, quartz bridging, and epoxy in open porosity, Atlas Dayton No. 1 well (6,568 ft). (g) Fractures perpendicular to sutured grain boundary, Atlas Dayton No. 1 well (6,568 ft).

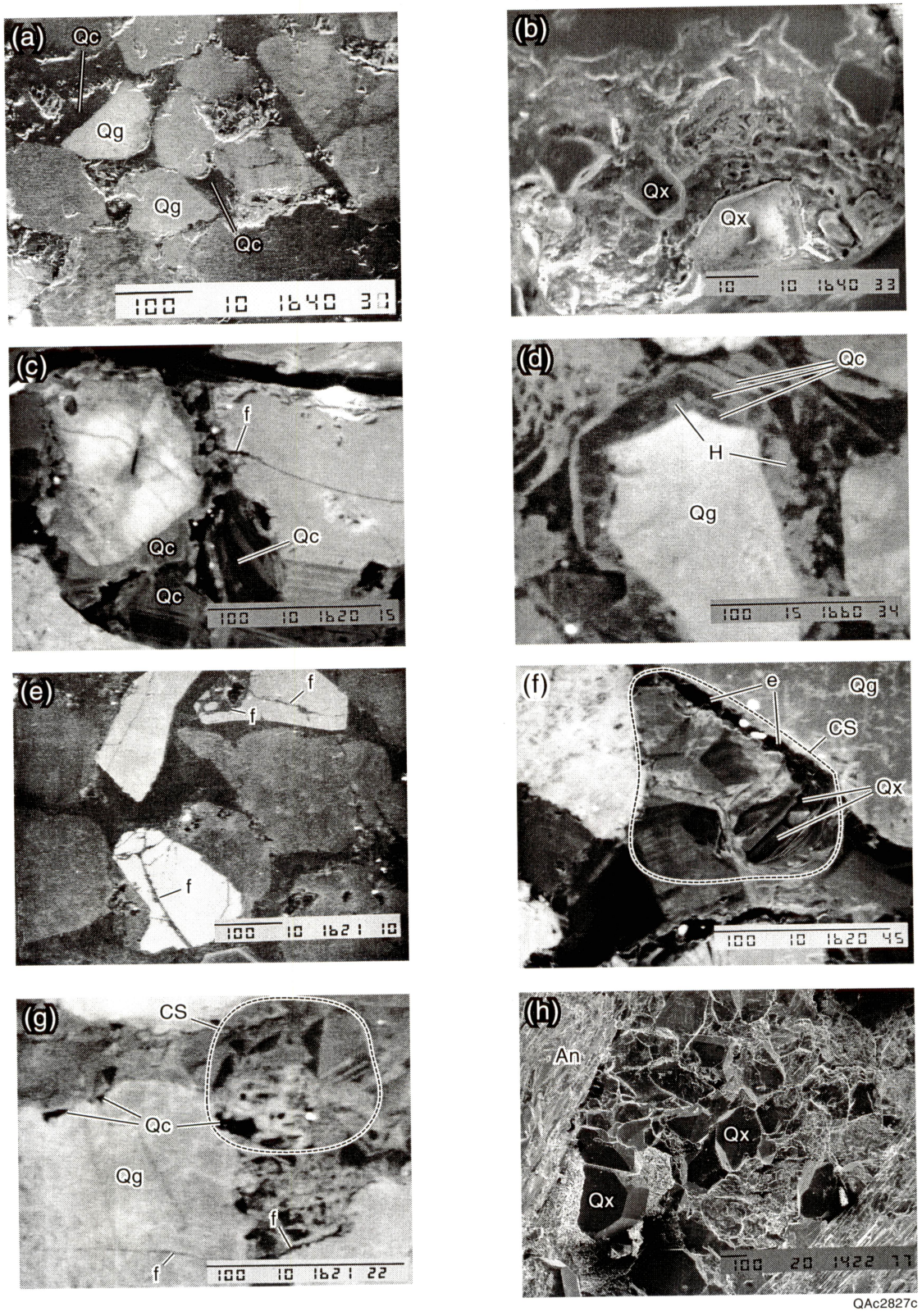
(a)
Qc
Qg
Qg
Qc
100 10 1640 30
(b)
Qx
Qx
10 10 1640 33
(c)
f
Qc
Qc
Qc
100 10 1620 15
(d)
Qc
H
Qg
100 15 1660 34
(e)
f
f
f
100 10 1621 10
(f)
e
Qg
CS
Qx
100 10 1620 45
(g)
CS
Qc
Qg
f
f
100 10 1621 22
(h)
An
Qx
Qx
100 20 1422 11

QAc2827c

Figure 24. Cements and microfractures from the Medina Group sandstones viewed in CL, secondary electron imaging (SEI), and SEI/CL. Scale bars in microns. Qg=quartz grain, Qc=quartz cement, Qx=quartz crystal, CS=crack-seal texture, e=epoxy in open porosity, f=microfracture, H=hematite cement, An=anhydrite cement. (a) SEI/CL double exposure showing relief at optical "grain" boundaries, actual grain boundaries, and angular shapes of original grains, Upper Whirlpool Formation, Atlas Lucas No. 1 well (6,462 ft). (b) Euhedral quartz crystal lining an open primary pore, Upper Whirlpool Formation, Atlas Lucas No. 1 well (6,462 ft). (c) Zoned quartz cement partially filling and bridging pores, and microfracture connecting to open pore, Atlas Dayton No. 1 well (6,568 ft). (d) Euhedral quartz cement on high-temperature quartz grain. Sequence of cementation: thin early layer of dark, low-temperature quartz; hematite; and additional quartz, Lower Whirlpool Formation, Atlas Lucas No. 1 well (6,467 ft). (e) Solutionally widened quartz-cemented fractures, Atlas Dayton No. 1 well (6,568 ft). (f) SEI/CL double exposure showing crack-seal texture in cement, euhedral quartz crystals growing into open pore space preserved by quartz bridging, Atlas Dayton No. 1 well (6,568 ft). (g) Category Ia fracture, zoned cement with crack-seal texture. Note thin, discontinuous coating of dark, low-temperature quartz cement on large quartz grain, Atlas Dayton No. 1 well (6,568 ft). (h) SEI of mineralized natural fracture. Note euhedral quartz crystals, partially covered by later anhydrite. Traces of clay containing rare earth elements occur along cleavage surfaces in the anhydrite, Atlas Lucas No. 1 well (6,342 ft).

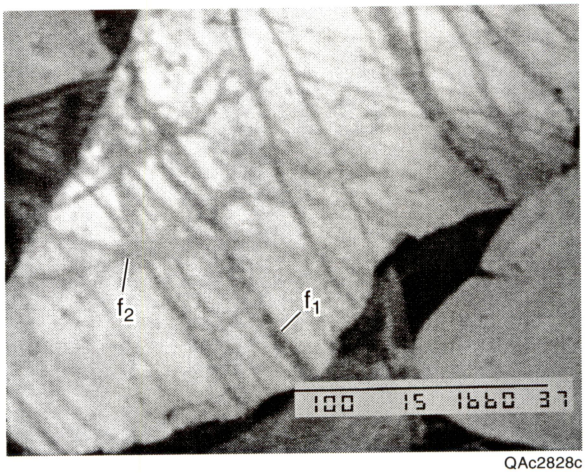

Figure 25. Scanned CL photograph of cross-cutting fracture swarms seen in the lower Whirlpool Sandstone in the Atlas Dayton No. 1 well. The older, dark-cemented set is clearly cross-cut by a younger set of bright-cemented fractures. The older set trends 280 degrees, and the younger, 10 degrees.

Microfracture data can be used to help interpret image logs. These tools can detect large fractures that intersect the wellbore, but in many cases they cannot discriminate between natural and drilling-induced fractures (Laubach and others, 1988) or between open fractures and fractures that have merely experienced erosion of mineral fill near the wellbore (Clift and others, 1998). Several of the samples obtained in this study were from intervals where image logs detected macroscopic fractures in the wellbore. Where the orientations of microfractures and large fractures are congruent, there is increased confidence that the large fractures on the image log are natural. Also, as previously discussed, several of the sidewall cores record intersected fractures imaged by the FMI log and were used to discriminate between natural and drilling-induced fractures. Macrofractures could be natural and also differ in strike from the microfractures if, for example, the fractures were of different ages. This shows that with small

rock samples from zones with ambiguous image-log responses, microfracture observations can help provide a more confident interpretation of the image log. But perhaps the best application of microstructures to calibrating image-log fracture interpretation is determining whether fractures are likely to be open or mineral filled, as described in the next section.

Fracture-Quality Analysis

We analyzed fracture quality in samples from three wells and from several outcrop localities. The complex diagenetic and tectonic history of the Cataract/Medina Group in the Henderson Dome area is clearly revealed in the results of our analyses. A range of authigenic cements are present, and microfractures suggest at least two episodes of fracture formation.

The goals of the petrographic study are to identify detrital and authigenic mineralogy, determine diagenetic history, and identify microfractures and the timing of cement precipitation relative to fracture opening. The samples we examined are from cores and outcrops.

Petrographic Methods

Composition of the sandstones in five outcrop samples and in nine sidewall core samples was determined by standard thin-section petrography. Thin sections were made from samples cut perpendicular and parallel to bedding. Pore space was impregnated with blue-colored epoxy. Thin sections were prepared for use in CL studies and are approximately twice as thick as those prepared for typical petrographic analysis in order to minimize fracturing due to sample preparation. The outcrop and oriented sidewall-core thin sections were not stained for feldspar or carbonate grains. A total of at least 200 points were counted on each thin section to determine composition. Grain size and roundness were estimated by comparison to standard images. Table 2 presents results of point counts and an error analysis. Two outcrop thin sections (Medina 1-1 and Thorold 1-2) and one sidewall core (from which two thin sections were made) were counted twice to check for consistency. Differences between estimates from repeated analyses

Table 2. Cement and porosity data for the Atlas Lucas No. 1 and Atlas Dayton No. 1 sidewall-core samples and outcrop samples.

Atlas Lucas No.1

Depth (ft)	Quartz (%)	Ferroan dolomite and calcite (%)	Anhydrite (%)	Clay (%)	Hematite (%)	Total postkinematic cement (%)	Primary porosity (%)	Secondary porosity (%)	Total porosity (%)	Degradation index
6,338	10.5	0	0.5	0	10	0.5	5.5	0.5	6.0	7.7
6,342	20.0	8.0	0	0		8.0			1.0	88.9
6,360	17.0	0	2.0	0		2.0			7.0	22.2
6,364	21.0	0	1.0	5.0		6.0			2.0	75.0
6,366	22.0	0	0	0		0			5.0	0
6,381b	25.0	0	3.0	0	0	3.0	3.0	0	3.0	50.0
6,381c	20.5	2.0	0	0	0	2.0	5.0	0.5	5.5	26.7
6,386-1	20.0	0	0	4.0	0	4.0			1.5	72.7
6,386-2	27.6	0	0	0		0	3.0	0.5	3.5	0
6,399	17.0	12.0	0	2.0		14.0			0	100.0
6,412	17.0	4.0	0	2.0		6.0			6.0	50.0
6,462	15.0	0	0.5	0	0	0.5	6.5	0.5	7.0	6.7
6,463	11.0	0	0	0.5		0.5			10.0	4.8
6,467	20.0	0	0	0.5	0	0.5	2.5	1.5	4.0	11.1
6,477	19.0	7.0	5.0	0		12.0			0.5	96.0

Atlas Dayton No.1

Depth (ft)	Quartz (%)	Ferroan dolomite and calcite (%)	Anhydrite (%)	Clay (%)	Hematite (%)	Total postkinematic cement (%)	Primary porosity (%)	Secondary porosity (%)	Total porosity (%)	Degradation index
6,548	17.0	0	6.0	4.0		10.0			0	100.0
6,568	23.5	0	0	0	0	0	3.5	0.5	4.0	0
6,582	15.0	0.5	0	7.0		7.5			0.5	93.8
6,590	29.5	0	0	1.5	0	1.5	0	0.5	0.5	75.0
6,601	17.0	0	0.5	0.5		1.0			6.0	14.3
6,612	11.0	1.0		12.0	0.5	13.0	2.5	1.0	3.5	78.8
6,619	15.0	0	0	8.0		8.0			0	100.0
6,623	20.0	0	0	6.0		6.0			0.5	92.3
6,628	18.0	2.0	0	8.0		10.0			0.5	95.2
6,641	20.0	7.0	0	7.0		14.0			0	100.0
6,668	19.0	0.5	0	4.0		4.5			0	100.0
6,680	9.5	0.5	9.0	2.5	0	12.0	2.5	0.5	3.0	80.0

Outcrop samples

Formation and sample name	Quartz (%)	Ferroan dolomite and calcite (%)	Anhydrite (%)	Clay (%)	Hematite (%)	Total postkinematic cement (%)	Primary porosity (%)	Secondary porosity (%)	Total porosity (%)	Degradation index
Grimsby, Medina 1-1	17.0	1.0	0	0	4.5	1.0	8.0	2.5	10.5	8.7
Grimsby, Medina 1-1	20.0	0	0	0	4.5	0	7.0	3.5	10.5	0
Grimsby, Medina 1-2	13.0	7.0	0	0	0.5	7.0	6.0	3.5	9.5	42.4
Thorold 1-1	15.9	10.9	0	0	0	10.9	7.0	1.5	8.5	56.2
Thorold 1-2	18.4	6.5	0	0	0.5	6.5	7.0	2.0	9.0	41.9
Thorold 1-2										
U. Whirlpool, M-1c										
Thorold T-8										
Thorold T-6										

Error analysis*

Formation and location	Quartz (%)	Ferroan dolomite and calcite (%)	Hematite (%)	Total porosity (%)
Medina1-1	±2.5	±2.0	±<1.5	±2.0

* Estimated from nomograph in Folk (1974, p. 155).

are well within the error limit, except for the differences between the two estimates of calcite cement in the Thorold 1-2, which are at the threshold of being significant.

A suite of conventional thin sections, stained for carbonates and feldspars, have been prepared from the remaining sidewall cores. These thin sections are described in a following section, along with the method used in their examination.

Sandstone Texture and Composition

The Cataract/Medina samples viewed so far in this study are in the upper range of very fine grained (88 to 125 μ; 3.5 to 3.0 ϕ) sandstones and are well to very well sorted (sorting index of 0.35). The median grain size of one Thorold sample likewise is in the upper range of very fine grained (88 to 125 μ; 3.5 to 3 ϕ) sandstone but is only moderately well to well sorted (sorting index of 0.50). Detrital grains in the Thorold sample varied from lower very fine grained (62 to 88 μ; 4.0 to 3.5 ϕ) to upper fine grained (177 to 250 μ; 2.5 to 2.0 ϕ). Grains in both Medina and Thorold samples typically are subangular to subrounded. There is no evidence of welding or interpenetration of grains or of spreading of grains owing to cement growth.

Point-count data from each of the thin sections are given in table 2. Quartz is the predominant detrital grain. Orthoclase and microcline are more abundant than plagioclase, as previously reported (Dutton and others, 1993, p. 27). Very little plagioclase is identified in these unstained thin sections, although a few albite grains are recognizable by their twinning. In addition, detrital grains include trace amounts of tourmaline and zircon.

Table 3 compares present (postdiagenesis) and original (prediagenesis) composition of framework grains. If some detrital feldspar has been dissolved and replaced by calcite in secondary pores, as discussed below, the original composition of these subarkosic sandstones might have been $Q_{84}F_{16}R_0$ to $Q_{89}F_{11}R_0$. These ratios are consistent with previous reports that typical Cataract/Medina sandstones include 2 to 21 percent feldspar (Dutton and others, 1993, p. 27). The postdiagenetic Medina 1-2 and Thorold 1-2 samples would be classified as quartz arenites (quartz ≥ 95 percent), whereas the Medina 1-1 is still a subarkose.

Table 3. Framework grain composition for the Atlas Lucas No. 1 and Atlas Dayton No. 1 sidewall-core samples and outcrop samples.

Atlas Lucas No.1

Depth (ft)	Quartz (%)	Plagioclase (%)	Orthoclase (%)	Microcline (%)	Metamorphic and plutonic rock fragments (%)	Sedimentary rock fragments-chert (%)	Sedimentary rock fragments-siltstone (%)	Sedimentary rock fragments-shale (%)	Other framework grains (%)
6,338	70.0	0	2.0	0	1.0	0	0	0	0
6,342									
6,360									
6,364									
6,366									
6,381	64.0	0	3.5	0	0	0	0.5	0	1.0
6,386	61.8	0	5.5	0	0	0	0	1.5	0
6,399									
6,412									
6,462	70.5	0	3.5	0.5	0.5	0.5	0	0	2*
6,463									
6,467	65.0	0	5.5	0.5	1.5	0.5	1.0	0	1.5
6,477									

*Zircon and tourmaline

Atlas Dayton No.1

Depth (ft)	Quartz (%)	Plagioclase (%)	Orthoclase (%)	Microcline (%)	Metamorphic and plutonic rock fragments (%)	Sedimentary rock fragments-chert (%)	Sedimentary rock fragments-siltstone (%)	Sedimentary rock fragments-shale (%)	Other framework grains (%)
6,548									
6,568	71.0	0	0.5	0	0.5	0	0	0.5	0
6,582									
6,590	61.0	0	3.5	0	1.0	.	0.5	1.5	0.5†
6,601									
6,612	53.0	6.0	1.5	0	0	0	0	1.0	0.5
6,619									
6,623									
6,628									
6,641									
6,668									
6,680	62.5	0.5	2.5	0	0	0.5	0.0	1.0	1‡

†Zircon
‡Chlorite

Table 3 (cont.)

Outcrop samples

Formation and sample name	Quartz (%)	Plagioclase (%)	Orthoclase (%)	Microcline (%)	Sedimentary rock fragments-chert (%)	Clay clasts (%)	Heavy minerals (%)	Other framework grains (%)	Original FMCP	Present FMCP	Original QFR	Present QFR
Grimsby, Medina 1-1	61.5	0	3.0	1.0	0	0	1.0	0.5	$F_{71}M_0C_0P_{29}$	$F_{67}M_0C_{23}P_{10}$	$Q_{89}F_{11}R_0$	$Q_{94}F_6R_0$
Grimsby, Medina 1-1	59.5	1.0	3.0	0	0	0	1.0	0.5	$F_{69}M_0C_0P_{31}$	$F_{65}M_0C_{25}P_{10}$	$Q_{89}F_{11}R_0$	$Q_{94}F_6R_0$
Grimsby, Medina 1-2	66.0	0	2.0	0.5	0	0	1.5	0.0	$F_{79}M_0C_0P_{21}$	$F_{70}M_0C_{20}P_{10}$	$Q_{85}F_{15}R_0$	$Q_{96}F_4R_0$
Thorold 1-1												
Thorold 1-2	59.2	0	1.5	1.0	0	0	2.5	0.5	$F_{74}M_0C_0P_{26}$	$F_{65}M_0C_{27}P_8$	$Q_{84}F_{16}R_0$	$Q_{96}F_4R_0$
Thorold 1-2	61.2	0	3.0	0	0	0	1.5	0.0	$F_{72}M_0C_0P_{28}$	$F_{66}M_0C_{25}P_9$	$Q_{87}F_{13}R_0$	$Q_{95}F_5R_0$
U. Whirlpool, M-1c												
Thorold T-8												
Thorold T-6												

Error analysis[§]

Sample name	Quartz (%)	Plagioclase (%)	Orthoclase (%)	Microcline (%)	Sedimentary rock fragments-chert (%)	Clay clasts (%)	Heavy minerals (%)	Other framework grains (%)
Medina 1-1	±3.5	±0.5	±1.0	±0.5	±0.5	±0.5	±0.5	±0.5

§ Estimated from nomograph in Folk (1974, p. 155).

Framework grains compose approximately 65 to 70 percent of the present (postdiagenesis) sample volume, whereas 20 to 27 percent consists of authigenic cement, and 8 to 10 percent is pore space (table 3). Predominant cements include hematite, quartz, and calcite. Relative volumes of these cements as determined by point count are shown in figure 26. Hematite cement occurs as coatings on detrital grains and also, to a small extent, in secondary pores. Quartz cement forms as overgrowths on detrital quartz. Calcite cement fills both primary and secondary pores. Secondary porosity makes up 18 to 37 percent of total pore space and is apparently derived from the leaching or dissolution of detrital feldspar grains. There is negligible clay matrix. Clay matrix is observable in the Thorold 1-2 sample and helps define bedding, but its volume is estimated at $<1\pm0.5$ percent.

Table 3 estimates the original volume of framework grains by adding back all secondary porosity and calcite in secondary pores, assumed to represent the loss of original feldspar. Original porosity is back-calculated by adding back the volume of cement in primary pore space and subtracting secondary porosity. The estimated original porosity is 21 to 32 percent (table 3).

Diagenetic History

The main diagenetic events are inferred to be (in relative order of occurrence, earliest to latest):

(1) Precipitation of hematite or other ferric oxide cements as coatings on detrital grains;

(2) Precipitation of quartz cement as overgrowths on detrital quartz, especially on grains that lack a hematite coating;

(3) Fracture formation, which was contemporaneous with step 2;

(4) Dissolution of detrital feldspar grains;

(5) Precipitation of calcite in primary pore space as well as in secondary pores, especially as a cement replacing feldspar; and

(6) Possible dissolution of calcite and limited precipitation or redistribution of hematite in pore space, which might be an effect of outcrop weathering.

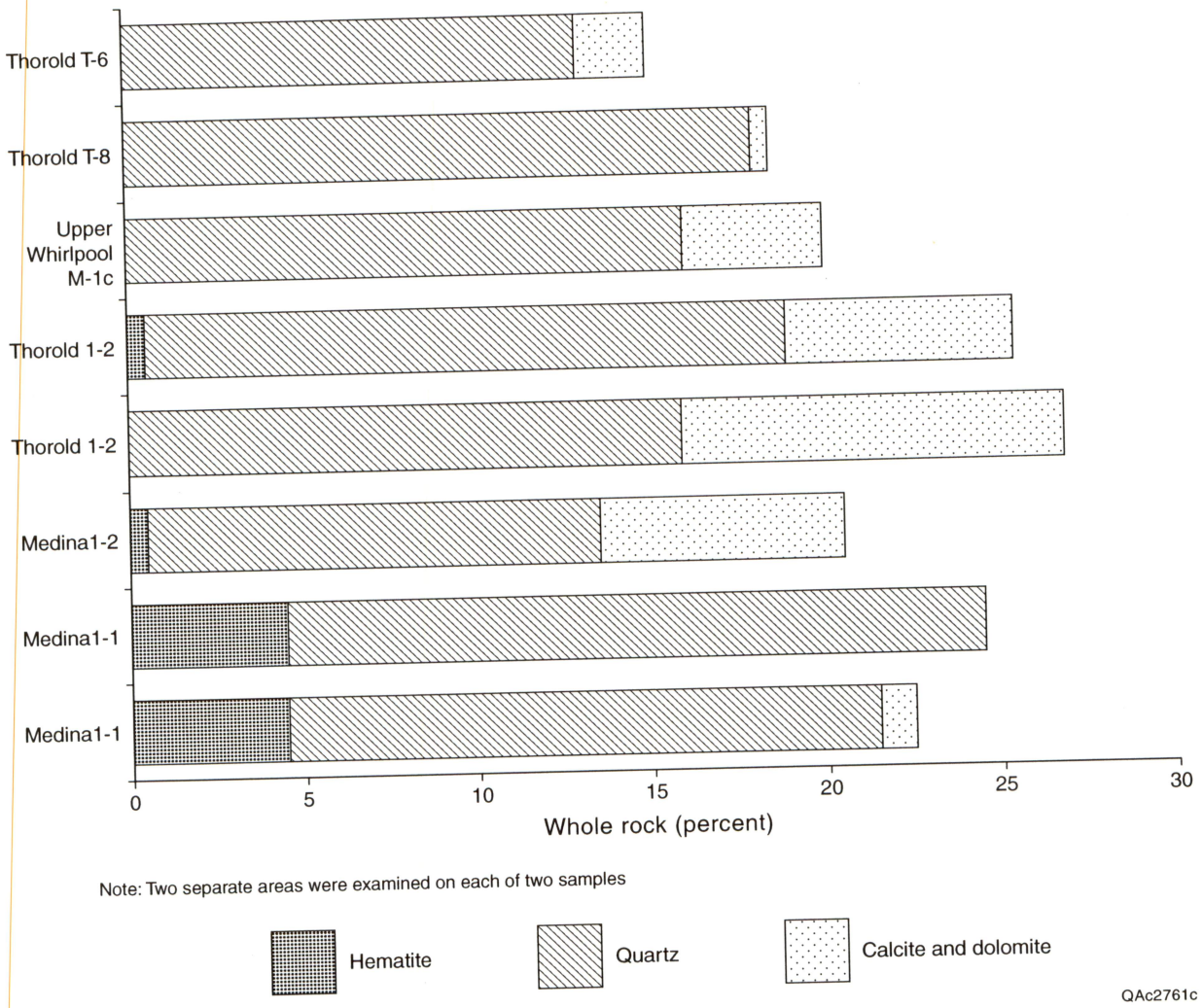

Figure 26. Compositional analysis of six Medina Group outcrop samples from western New York. Plot shows cements as a percent of total cement. Two samples have duplicate point-count measurements.

Calcite and some hematite are therefore postkinematic (that is, they precipitated after fractures opened) phases, and they are potential fracture-occluding phases.

Hematite coats occur in alternating linear bands with high and low concentrations, especially in the Medina 1-1 sample in which the bands are oblique to bedding, and to a lesser extent in the Medina 1-2 sample in which the hematite coats appear to define bedding. Grain coating by hematite ranges from discontinuous spheres to relatively thick continuous coatings.

Quartz cementation can be extensive with little to no primary porosity remaining in zones or bands where hematite coatings are absent. In most cases, detrital and authigenic quartz could be distinguished by at least a subtle outline of the detrital grain. Most primary porosity remains where quartz grains have some hematite coating. Quartz cementation in the Thorold 1-2 sample appears more patchy than the banded or laminated pattern shown in the Medina samples.

Detrital feldspar grains in a given sample range from unaltered to slightly leached, and from highly vacuolized to completely dissolved. Many "ghosts" of feldspar grains within secondary pores can be recognized by an extremely thin residual fabric that includes suggestions of mineral cleavage. Feldspar dissolution is inferred to predate quartz cementation in outcrop samples. Although many secondary pores, some with traces of a feldspar grain remaining, are tightly bounded by the quartz cement overgrowths, possibly consistent with feldspar dissolution after quartz cementation, this relationship is more likely due to very late stage (near-surface) weathering of clay minerals after leached feldspars. Feldspars seem to have been dissolved rather than replaced by clay minerals.

There are a few examples of fluid-inclusion planes indicative of fracturing and microfracturing in these samples. Suggestive evidence includes linear or curvilinear vacuole traces that extend across two or more detrital grains and their associated authigenic cements. Whether the vacuoles contain gas or cement is uncertain. Such examples were too uncommon to allow confident correlation of trends. Some of the larger fractures in the thin sections clearly reflect a subsurface event (that is, they are mineral lined), although others might have been induced by the sample-preparation process. Fractures postdate dissolution of feldspar, as

evidenced by fractures commonly connecting through secondary pores. Most fractures curl around grains, but there are a few cases where grains are broken. In addition, two separate fractures in the Thorold 1-2 sample are locally plugged with calcite cement, strongly suggesting calcite was a postkinematic cement.

Calcite is more abundant in the Thorold outcrop sample than in the Medina outcrop samples. It usually is associated with the remains of feldspar and either partly or completely fills the secondary pores created by the dissolution of feldspar. According to Milliken and Land (1991), cited in Dutton (1993), dissolution of feldspar neutralizes acid pore water sufficiently to allow calcite precipitation. In the Thorold sample, the distribution of calcite cement in primary and secondary pores is patchy. As previously mentioned, calcite appears to be a postkinematic cement because it is found occluding parts of fractures.

Some hematite cement can be seen as obstructing fractures and partly filling secondary pores, but it could have broken off adjacent grains during sample preparation or might been affected by near-surface weathering. It seems most likely that this event occurred under near-surface conditions rather than late in the burial process. A return to oxygenated waters near the surface could either initiate further oxidation of ferric minerals or possibly remobilize or redistribute existing hematite.

In addition, the distribution of secondary porosity in the Thorold 1-2 sample is patchy, rather than distributed randomly or uniformly or in bands. It is possible that some of this secondary porosity was previously filled with calcite that replaced feldspar but that later dissolved in a patchy pattern, perhaps under outcrop or near-surface conditions.

Core Sample Petrography -Conventional and CL-Based

The conventional petrography of subsurface samples from the Atlas Dayton No. 1 and Atlas Lucas No. 1 wells are summarized in figure 27. Seven samples have also been analyzed from the Atlas Montgomery No. 4 (fig. 28). Stained thin sections were made from samples not selected

for CL examination, and the results from preliminary analyses are presented in figure 28. Grain sizes, as seen in CL, range from 20 μ to over 500 μ (fig. 23). None of the samples were moderately (or better) sorted. Large grains are subrounded to angular, whereas smaller grains are mostly angular to subangular. These textural observations differ from the petrographic observations due to increased definition of grain boundaries offered in CL (fig. 23). Cements and the timing of cements are similar to those seen petrographically in outcrop samples, with notable exceptions. The inferred paragenetic sequence is as follows:

(1) Precipitation of quartz cement (minor) as a grain overgrowth, and as euhedral crystals projecting into pores (especially evident in the upper Whirlpool, see figure 23);

(2) Precipitation of hematite or other ferric oxide cements as coatings on detrital grains and quartz overgrowths (especially evident in the upper Grimsby and Thorold Formations);

(3) Precipitation of quartz cement as overgrowths on detrital quartz, especially on grains that lack a hematite coating (fig. 23), and possible replacement of calcite by quartz;

(4) Fracture formation, which was contemporaneous with step 2;

(5) Dissolution of detrital feldspar grains, with contemporaneous replacement by illite and smectite (fig. 23);

(6) Precipitation of ferroan dolomite grading to calcite;

(7) Precipitation and relocation of anhydrite in primary pores; and

(8) Precipitation of clay minerals (mainly chlorite). Locally in the Atlas Montgomery No. 4, a late stage dissolution event is evident that mainly results in loss of carbonate cement.

Calcite occurs only as a trace constituent in the subsurface samples. Anhydrite and gypsum are absent from the outcrop samples. Some anhydrite in subsurface samples appears to have been syndepositional and preserves very large pores (fig. 29). Some quartz grains preserve solution-

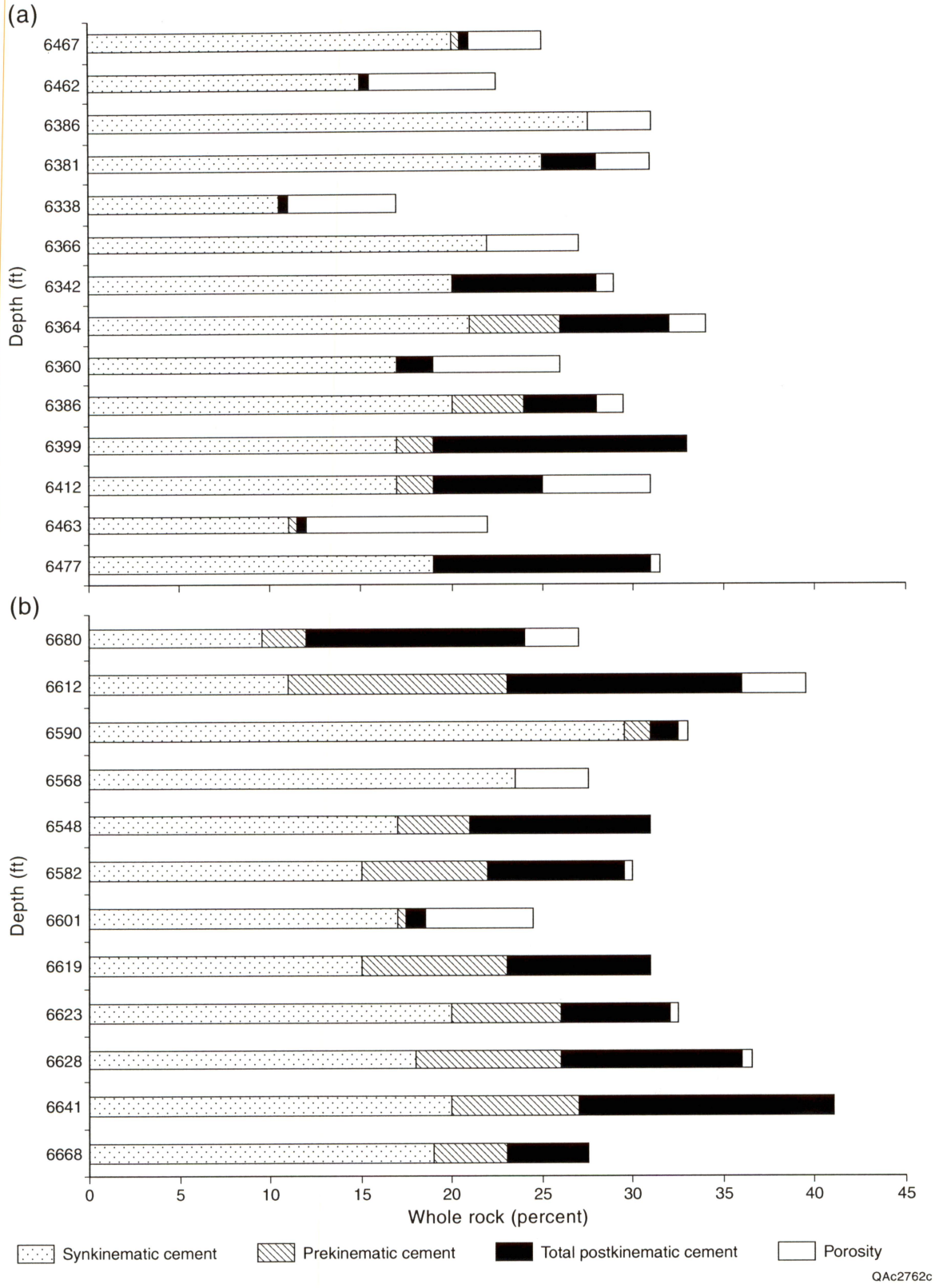

Figure 27. Key cement phases in the Atlas Lucas No. 1 (a) and Atlas Dayton No. 1 (b) wells, distinguished by their timing of precipitation relative to fracture opening and porosity. Cement volumes from petrographic point counts (200 points) and from visual estimates. Atlas Montgomery No. 4 samples have similar compositions.

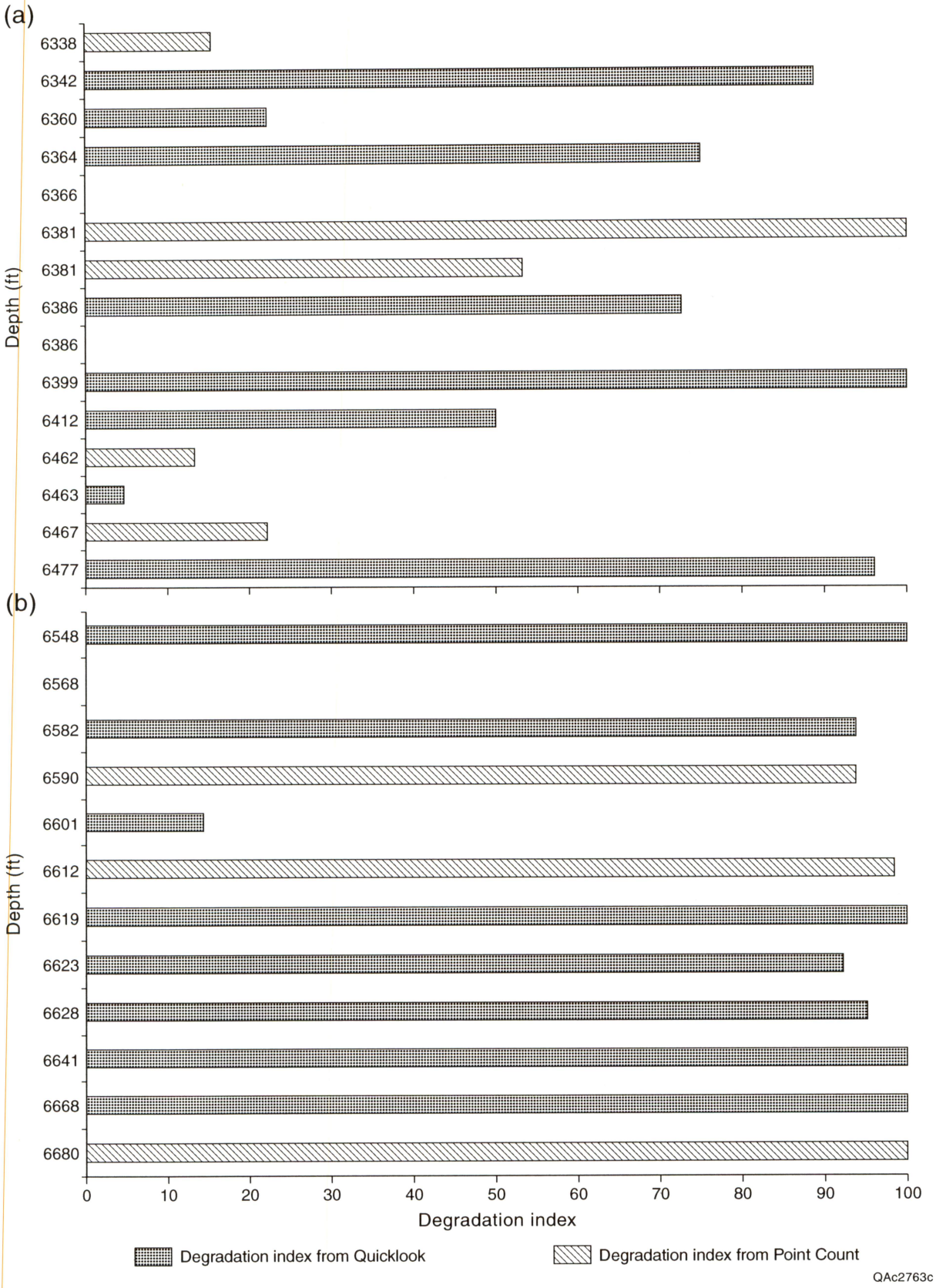
(a)
Depth (ft)
6338
6342
6360
6364
6366
6381
6381
6386
6386
6399
6412
6462
6463
6467
6477
(b)
Depth (ft)
6548
6568
6582
6590
6601
6612
6619
6623
6628
6641
6668
6680
0
10
20
30
40
50
60
70
80
90
100
Degradation index
Degradation index from Quicklook
Degradation index from Point Count
QAc2763c

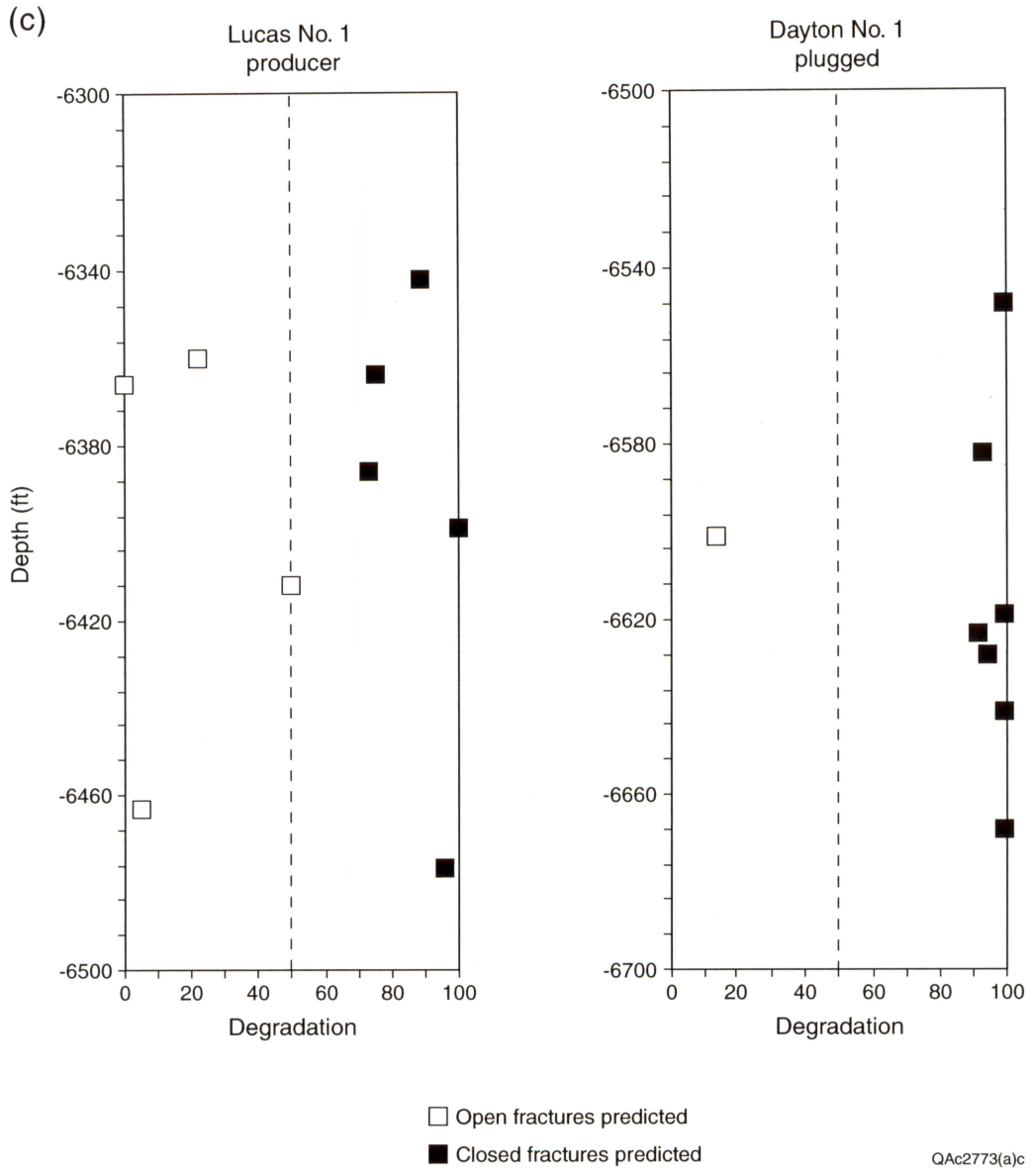

Figure 28. Degradation index plots for the Atlas Lucas No. 1 (a) and Atlas Dayton No. 1 (b) wells. Postkinematic cement/postkinematic cement plus total porosity. High values indicate that post-quartz cement porosity is largely infilled by postkinematic cement, suggesting that fracture porosity is also degraded (filled). Measurements of cement volume referred to as Quicklook are based on systematic visual estimates. Other measurements are based on point counts of 200 points per thin section. (c) Graphic displays of degradation index for the Atlas Lucas No. 1 and Atlas Dayton No. 1 wells.

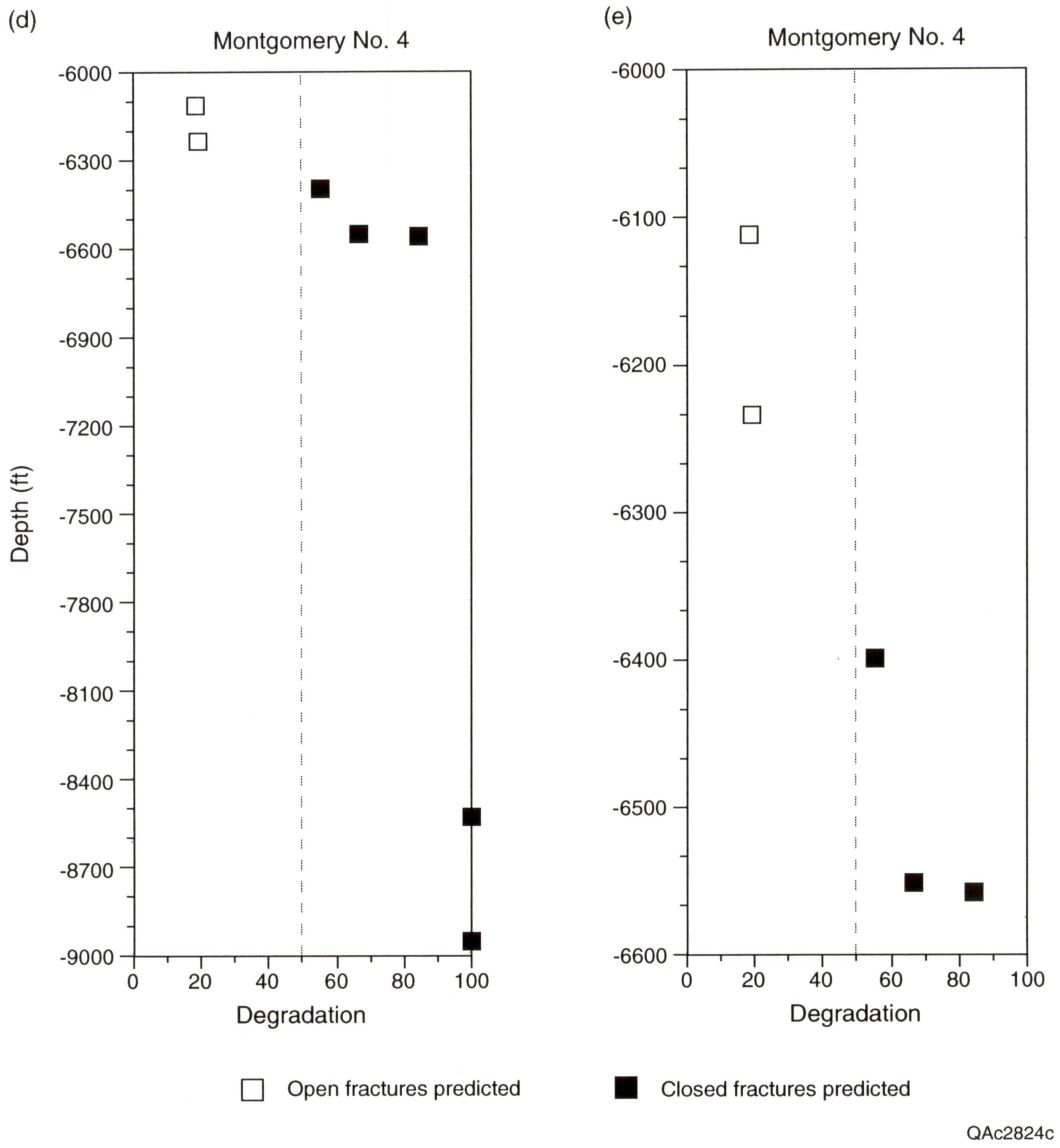
(d)
Montgomery No. 4
-6000
-6300
-6600
-6900
-7200
-7500
-7800
-8100
-8400
-8700
-9000
Depth (ft)
0
20
40
60
80
100
Degradation
(e)
Montgomery No. 4
-6000
-6100
-6200
-6300
-6400
-6500
-6600
0
20
40
60
80
100
Degradation
Open fractures predicted
Closed fractures predicted
QAc2824c

(f)

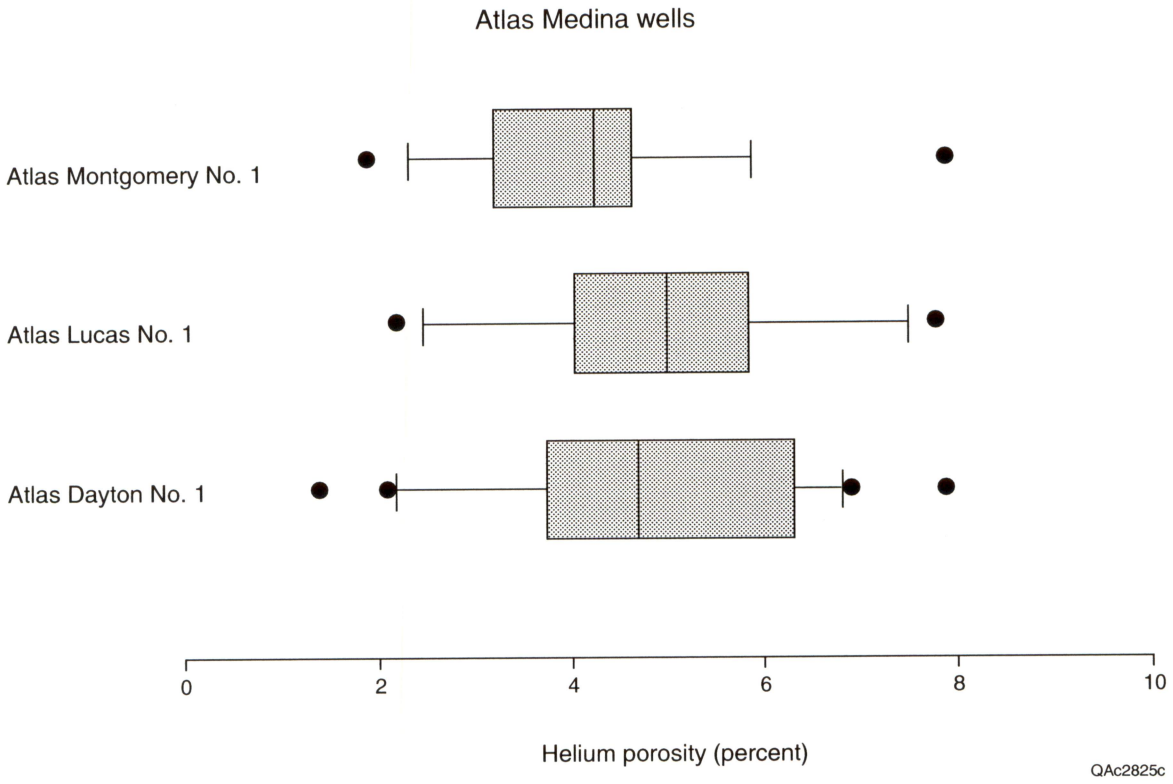

Figure 28 (cont.). (d) Degradation plot for selected samples, Atlas Montgomery No. 4 well. Deep samples are from the Trenton Group. These are the first indirect assessments of fracture quality in a carbonate rock. Sample from 8,950.5 ft contains a filled fracture as predicted by method. (e) Degradation index for siliciclastic interval of Atlas Montgomery No. 4 well. (f) Box plots of helium porosity data from three Atlas Resources, Inc., wells (Medina intervals only). Plots show median (vertical bar), 10th, 25th, 75th, and 90th percentiles as boxes with error bars. Plot shows that core porosity data for these three wells are indistinguishable.

widened fractures that are now filled with quartz cement, evidence of a period of attack by aggressive fluids, during which those fractures were open. This may be coincident with reduction of ferric iron in red shales observed along fractures. Quartz is largely contemporaneous with fracture opening (synkinematic), with the early cement mentioned in step 1 above occurring as a very thin coat. The main postkinematic phases are anhydrite, ferroan dolomite, and clay minerals (chlorite).

Fracture Quality Summary

The timing of fracture opening with respect to cement precipitation can be used to assess the degree of mineral fill in fractures and therefore fracture conductivity (Laubach and Milliken, 1996). These results from the Cataract/Medina study show that regional fractures are likely present in the Henderson Dome area and that these fractures are lined with quartz. Based on microstructure relations, we infer that postkinematic authigenesis, largely ferroan dolomite, calcite, anhydrite, and possibly clay minerals, is mainly responsible for fracture closure. The distribution of these cements is variable within the Atlas Lucas No. 1, Atlas Dayton No. 1, and Atlas Montgomery No. 4 core samples and in the outcrop samples. Although the variability cannot be predicted with our current understanding of the systematics of these minerals, their distribution can be accurately mapped using samples from sidewall core. This result means that a significant and highly variable factor controlling reservoir quality, namely the capability of fractures to conduct fluid, can now be mapped. Such maps could be used to identify targets for additional wells.

Tables 2 and 3 and figures 27 and 28 show compositional data from the Atlas Dayton No. 1, Atlas Lucas No. 1, and Atlas Montgomery No. 4 wells. Conventional porosity and permeability results are presented in figures 30 and 31. The most complete sample coverage is in the Atlas Lucas No. 1 and Atlas Dayton No. 1, and these wells are also most similar in other aspects of their geology. Conventional helium porosity data suggest that the Atlas Dayton No. 1 and Atlas

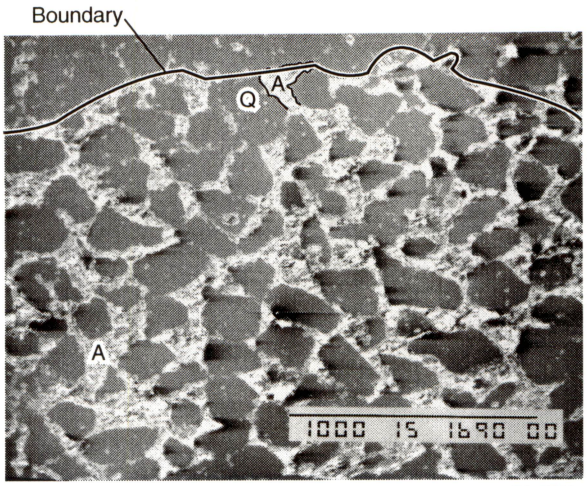

Figure 29. Region of large, anhydrite-filled pores typical of several depth intervals in the subsurface. Note lack of grain-to-grain contact. Few of the grains have quartz overgrowths, and very few have microfractures that are not inherited.

Lucas No. 1 wells have similar properties, but fracture-quality indicators (such as volume of postkinematic cement and proportion of porosity to postkinematic cement) tell another story. These indicators suggest that fractures in the Atlas Dayton No. 1 well are mainly mineral filled, whereas the Atlas Lucas No. 1 mainly has open fractures. The Atlas Montgomery No. 4 has indications of open fractures in the shallow part of the well, and closed fractures at depth in both the lower siliciclastic interval and in the Trenton. The reasoning behind this interpretation is as follows.

In the following paragraphs, we compare the Atlas Dayton No. 1 and the Atlas Lucas No. 1. Synkinematic quartz cement is the main porosity-occluding cement in both wells; it is present in about equal proportions in both wells. At the end of quartz cementation, porosities were reduced to uniformly low values of about 10 to 15 percent. At this time, we infer that the maximum fracture porosity likely existed in large regional Cataract/Medina fractures, based on an empirical model of fracture growth during synkinematic cementation that postulates that fracture opening

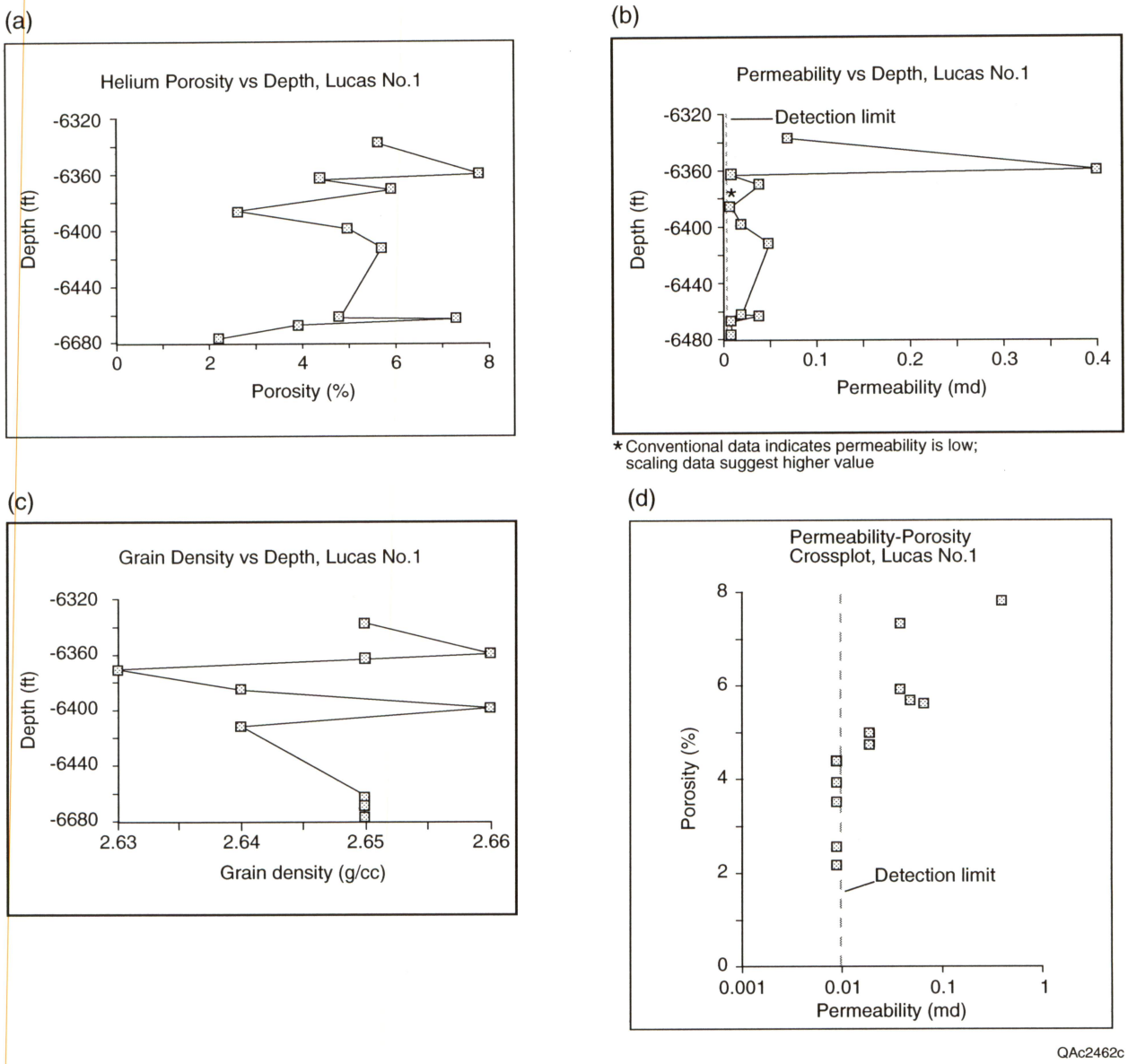

Figure 30. Data from OMNI Labs, Atlas Lucas No. 1 well sidewall cores. (a) Helium porosity vs. depth. Note error bars in relation to data values. (b) Plot of permeability vs. depth. Note that the detection limit is 0.01 md. Four samples have permeabilities lower than this and are shown as 0.009 md. (c) Grain density vs. depth. Note that the sample with the highest grain density also has the highest permeability. (d) Permeability–porosity semilog cross plot. No linearity is observable.

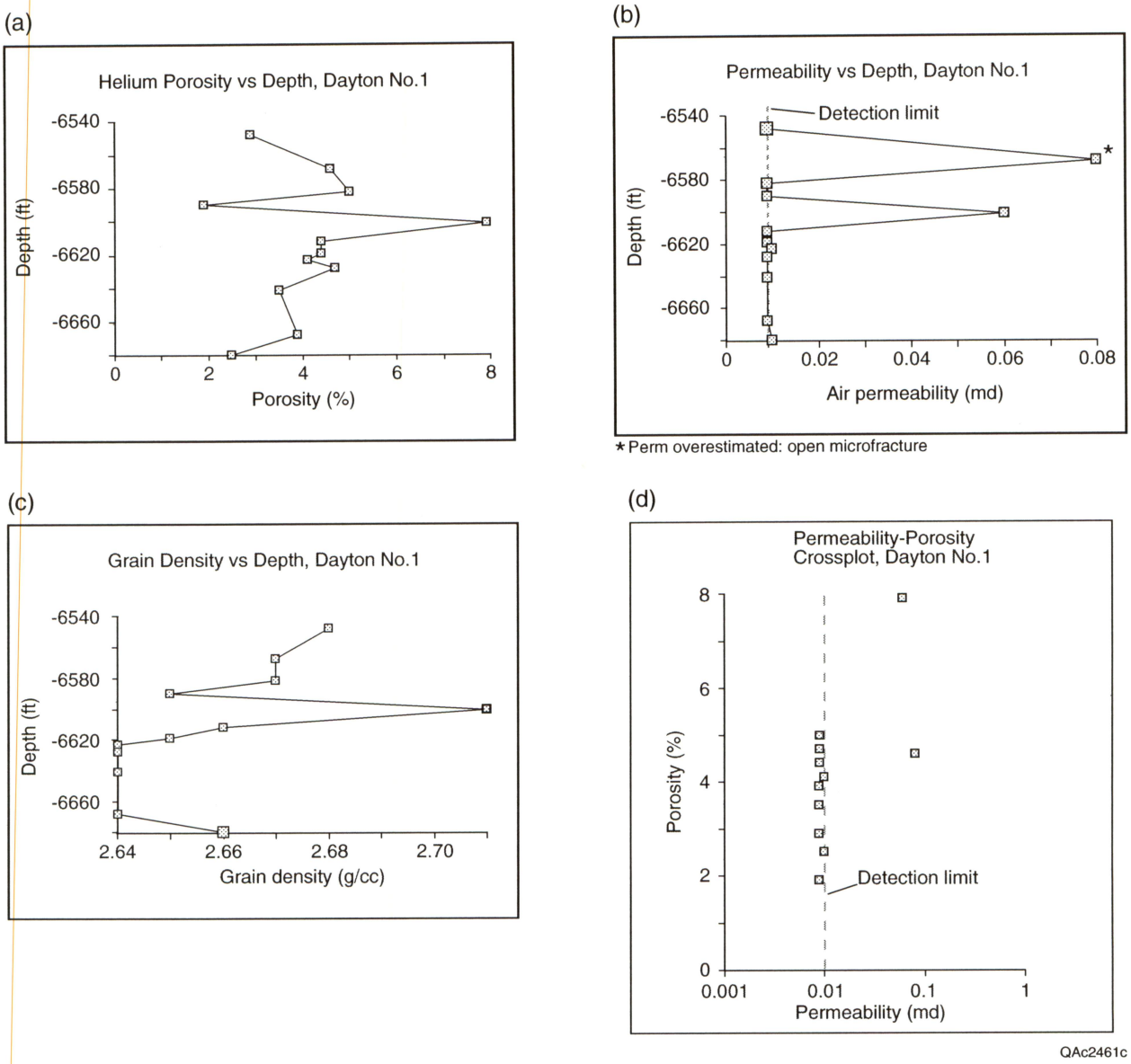

Figure 31. Data from OMNI Labs, Atlas Dayton No. 1 well sidewall cores. (a) Helium porosity vs. depth. Note error bars in relation to data values. (b) Plot of permeability vs. depth. Limit of detection is 0.01 md. Note that eight samples fall below this value and are plotted as 0.09 md. The sample showing the highest permeability has a small zone of large-diameter porosity, which did not significantly raise its overall porosity. (c) Grain density vs. depth. Again, the sample with the highest grain density exhibits the highest porosity (and high permeability). (d) Permeability-Porosity semilog crossplot. No linearity is observable.

exceeds fracture filling for fractures having apertures greater than about 1 mm (Laubach and Milliken, 1996; Marrett and Laubach, 1997; unpublished data). In this model, postkinematic cements are the cements mainly responsible for fracture occlusion. We imaged microfractures and macrofractures with apertures of 40 μ or less that remain partially open, proving this estimate to be conservative.

In all three wells, the main postkinematic cements are ferroan dolomite, anhydrite, and clay minerals. Petrographically, the timing of precipitation of these phases after quartz was identified based on overlapping and crosscutting relations; the timing of fracture formation was established by scanned CL analysis. Each of these postkinematic phases is present in varying amounts in the two wells. However, in the Atlas Dayton No. 1 and in the lower Atlas Montgomery No. 4 wells, most of the porosity that had existed after quartz cementation (and fracture formation) was filled with postkinematic cements. Because fractures are a variety of porosity, we conclude that fractures in this well are also filled. We predict that closed fractures in the Atlas Dayton No. 1 and the Atlas Montgomery No. 4 wells are lined with quartz but filled with ferroan dolomite, anhydrite, or clay minerals (or some combination of these phases) and open fractures in the Atlas Lucas No. 1 well (fig. 24) are quartz lined, and depending on where they are located, may have variable amounts of infilling postkinematic cement. Figure 24 shows euhedral quartz overgrowths on a fracture surface covered by late anhydrite from the Atlas Lucas No. 1 core at 6,342 ft. This partially open fracture is also visible on the FMI log. The identity and relative proportions of these expected minerals can be determined by inspection of figures 27 and 28.

Zones in the three wells that we predict would have the greatest probability of natural-fracture enhancement of permeability are readily visualized by reference to the normalized degradation index presented in figure 28. Intervals having high proportions of porosity to postkinematic cement plot to the left on these charts and represent best potential production. Those intervals that plot far to the right (high degradation index values) indicate unlikely production from fractures, most of which are assumed to be mineral filled. In the Atlas Lucas No. 1 well, zones of high natural fracture quality are predicted at about 6,338 ft, 6,360 ft,

6,366 ft, 6,386 ft, 6,420 ft, 6,462 ft, 6,463 ft, and 6,467 ft. In the Atlas Dayton No. 1 well, good fracture quality is only predicted near 6,568 ft, and 6,600 ft. Data are sparse for the Atlas Montgomery No. 4. Results indicate open fracture above 6,300 ft and closed fracure below, in the siliciclastic interval and in the Trenton Group. These predictions can be tested by comparison with (1) intervals that were perforated, (2) frac schedules, (3) post-stimulation production and (4) temperature logs. Overall, the Atlas Lucas No. 1 well has more favorable natural fracture quality than the Atlas Dayton No. 1 well. This difference is reflected in overall production response. The Atlas Lucas No. 1 is a producer (IP 120 MCFD, 80 to 90 MCFD sustained), whereas the Atlas Dayton No. 1 is a dry hole (plugged and abandoned). Production for the Atlas Montgomery No. 4 is reported to be comparable to the Atlas Lucas No. 1.

The variability of distribution of these postkinematic phases in the study wells suggests that this variability, and its spatial relationship to small faults, could contribute significantly to observed variations in producibility. Maps of the lateral and vertical distribution of these fracture-occluding phases would be an easily obtained guide to the location of potential productive regional fracture zones. Maps of postkinematic cement volumes would be powerful guides to infill drilling and could reveal the geologic controls on postkinematic cement distribution (for example, proximity to faults) that could greatly aid extrapolation of productive trends between well clusters.

We suspect, based on unpublished evidence from other areas and the high-temperature geochemistry of the late-stage ferroan carbonate minerals, that one possibility for the localization of these postkinematic cements is proximity to through-going (but possibly still fairly small) faults. Although speculative, the distribution of postkinematic cement halos around small faults in the vicinity of Henderson Dome could account for much of the observed fault-related variation in production, and could be important for predicting the seismic response (or variability in response) of these fault zones.

Fracture Scaling

A wide range of microfracture sizes is apparent in the samples that were analyzed. In order to adequately represent the distribution of these aperture and length sizes, we have applied power law scaling analyses to our data sets (table 4). Such analyses are powerful tools for revealing order in the apparent chaos of self-affine data. Our initial results indicate that such order exists in the data obtained from the study wells. Figures 32 and 33 show scaling results from the aggregate fracture population in each well by interval. The orderly appearance of the aperture and length data from the Atlas Dayton No. 1 well suggests proximity to large fractures and significant faults.

In order to apply scaling analyses to a set of tectonically related fractures, it is necessary to filter our aggregate fracture populations to extract specific fractures. This is accomplished by deleting categories progressively in reverse order of their tectonic significance, then selecting a small range of azimuths from the resulting set. Figure 34 shows the relationship of scaling behavior within a given thin section by fracture category.

Considering the entire population of microfractures imaged from the Medina, there is no clear mathematical relation between fracture length and aperture. This lack of clear relationship is also apparent in subsets of the population filtered to extract only fractures believed to be part of a single tectonically related set. Filtering extracted only Type Ia & Ia+ fractures (Laubach, 1997 classification scheme) with azimuths in a 30-degree range from a single thin section, a test similar to that used in field studies of macrofractures. In light of the fact that our current understanding of fracture mechanics in this type of geologic setting implies a linear relationship between aperture and length, this lack of obvious relationship is ground for fruitful study. Any further definition of relatedness would have to address the generations of cement filling of the fracture, which could be accomplished in the future using digital images and image processing. It is possible that these results indicate a complex multivariate or parametric relationship not currently addressed by linear elastic fracture mechanics (LEFM). It has become especially

Table 4. Results of scaling analysis for fractures detected in Atlas Lucas No. 1 and Atlas Dayton No. 1 sidewall-core samples.

Depth (ft)	Thin section number	Number of fractures mapped	Total area photographed (μ^2)	Average fracture density (μ^{-2})	Fracturosity (%)	Scaling parameters		Orientations (degrees)		
						Length parameter (e)	Aperture parameter (c)	Primary	Secondary	Tertiary
6,565	AD6568c	490	5.43×10^{6}	9.03×10^{-5}	2.01	2.5963	0.8519	77	82	47
6,588	AD6590c	194	4.64×10^{6}	4.18×10^{-5}	0.91	2.5888	1.7893	287	27	315
6,611	AD6612c(200)	200	1.17×10^{6}	1.71×10^{-4}	0.97	1.9694	1.2281	65	280	
6,611	AD6612c(350)	70	2.02×10^{6}	3.47×10^{-5}	1.83	2.3653	1.0781	65	280	287
6,678	AD6680c	221	1.12×10^{6}	1.98×10^{-4}	1.45	2.1628	1.6927	35	10	
6,338	AL6338c	72	1.60×10^{6}	4.51×10^{-5}	1.37	2.5699	0.8519	50	280	330
6,386	AL6386.2c	353	3.86×10^{6}	9.16×10^{-5}	1.56	1.9694	1.2281	10	300	75
6,381	AL6381c	133	1.37×10^{6}	9.71×10^{-5}	1.21	2.5888	1.4158	30	10	340
6,462	AL6462c	286	9.64×10^{5}	2.97×10^{-4}	1.02	3.4263	1.7084	95	70	330
6,467	AL6467c	206	3.15×10^{6}	6.55×10^{-5}	0.82	2.1628	1.6927	10	50	
	Totals	2,225	2.53×10^{7}	8.79×10^{-5}						

Atlas Lucas No. 1 (total) 1,050
Atlas Dayton No. 1 (total) 1,175

(a)

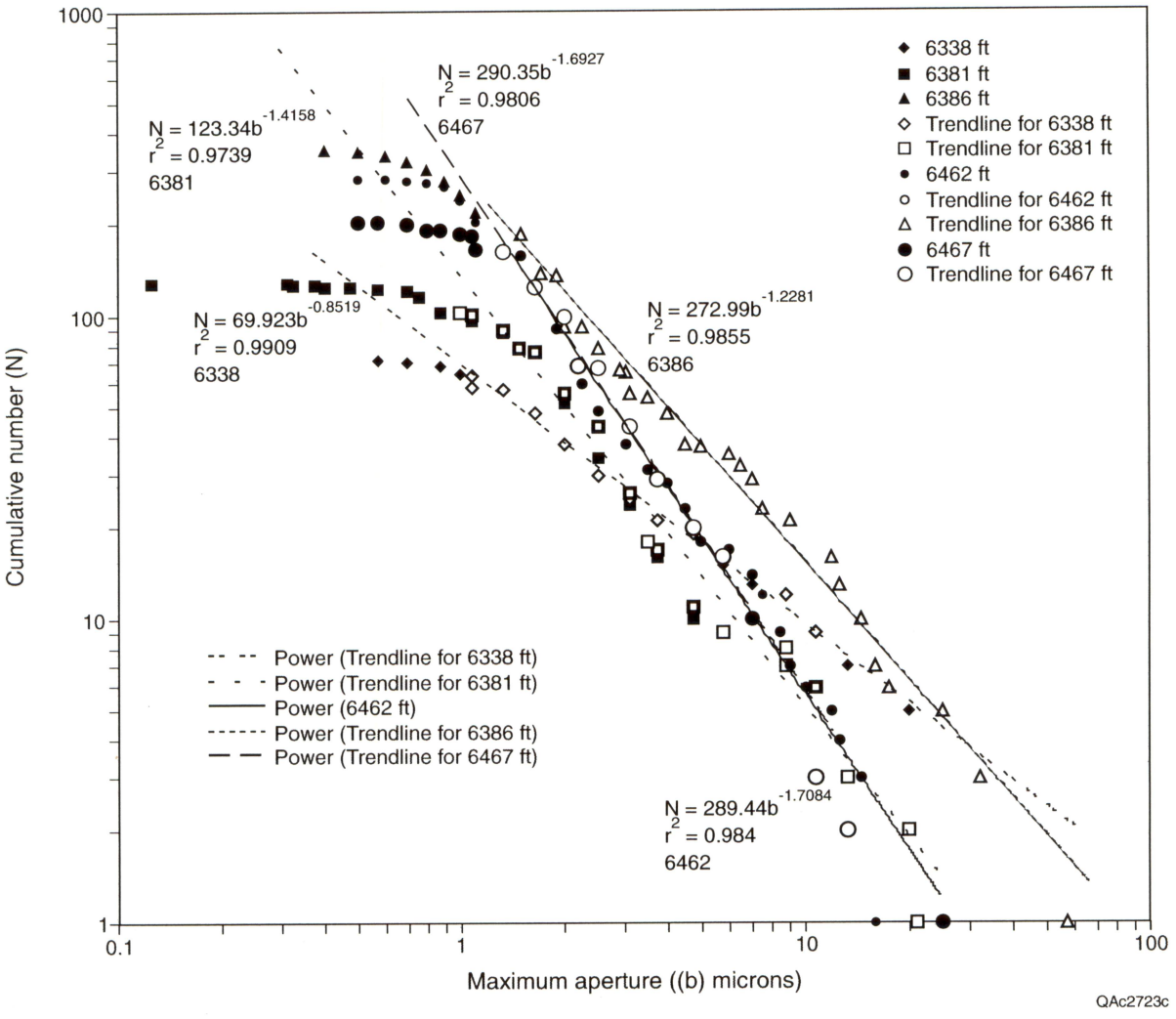

Figure 32. Fracture aperture scaling analyses, Atlas Lucas No.1 (a) and Atlas Dayton No. 1 (b) wells.

(b)

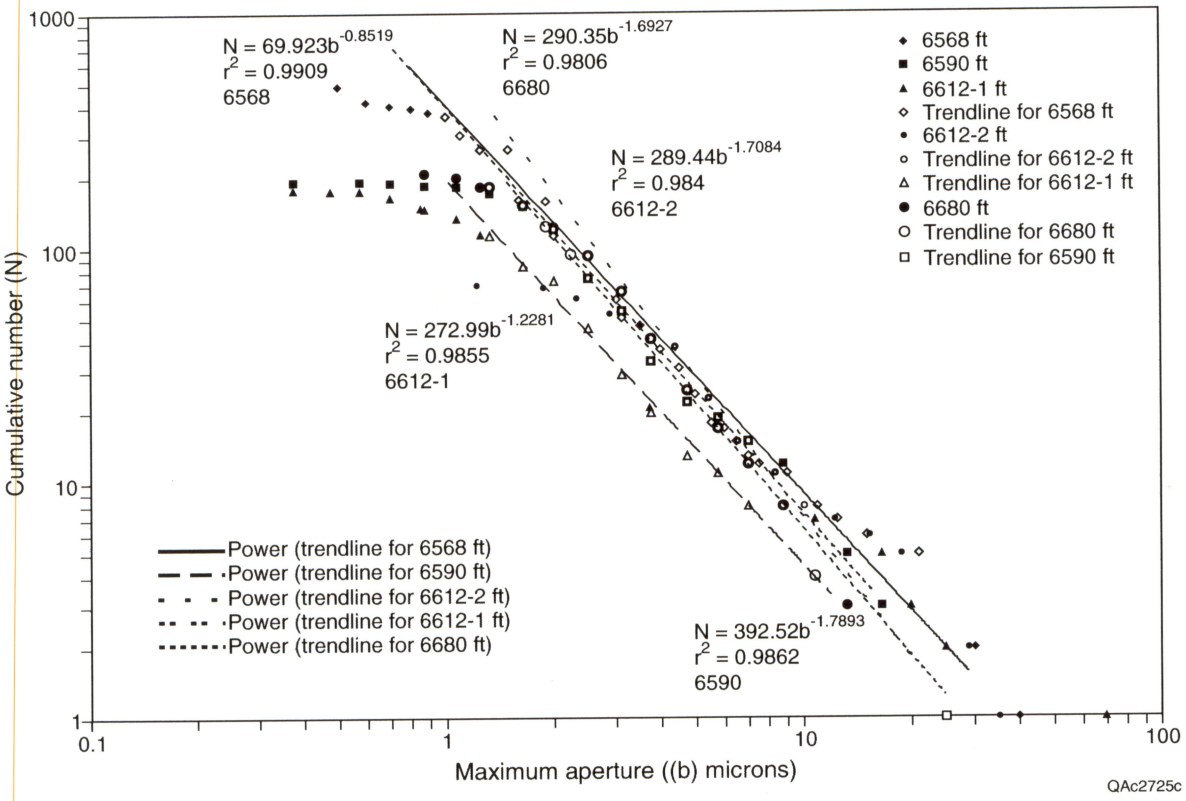

Figure 32 (cont.).

(a)

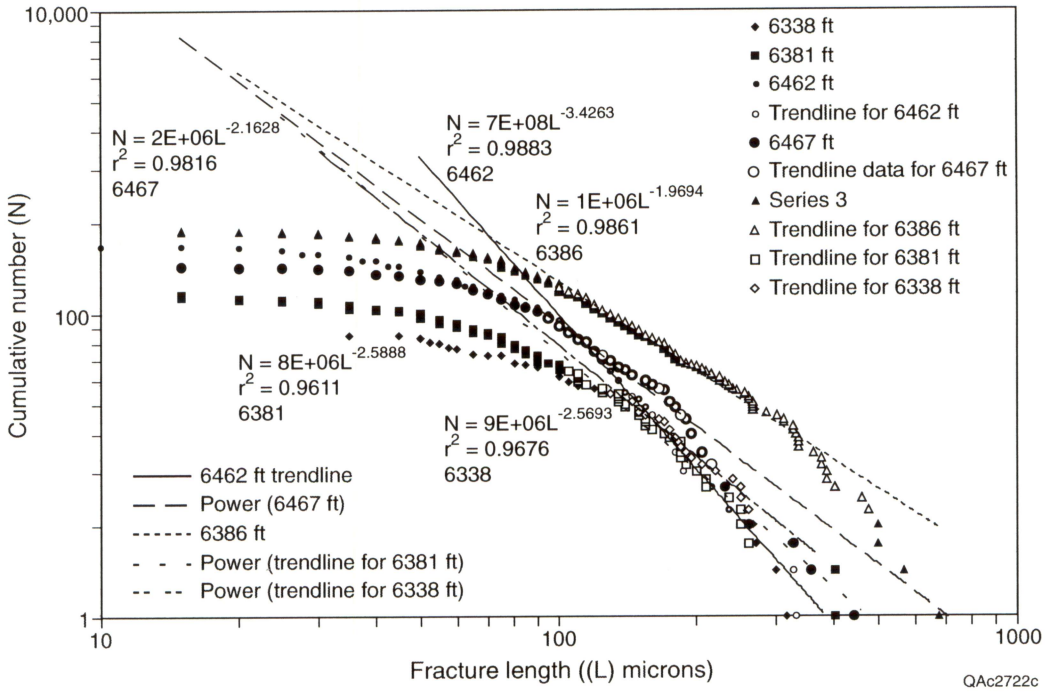

Figure 33. Fracture length scaling analyses, Atlas Lucas No. 1 (a) and Atlas Dayton No. 1 (b) wells.

(b)

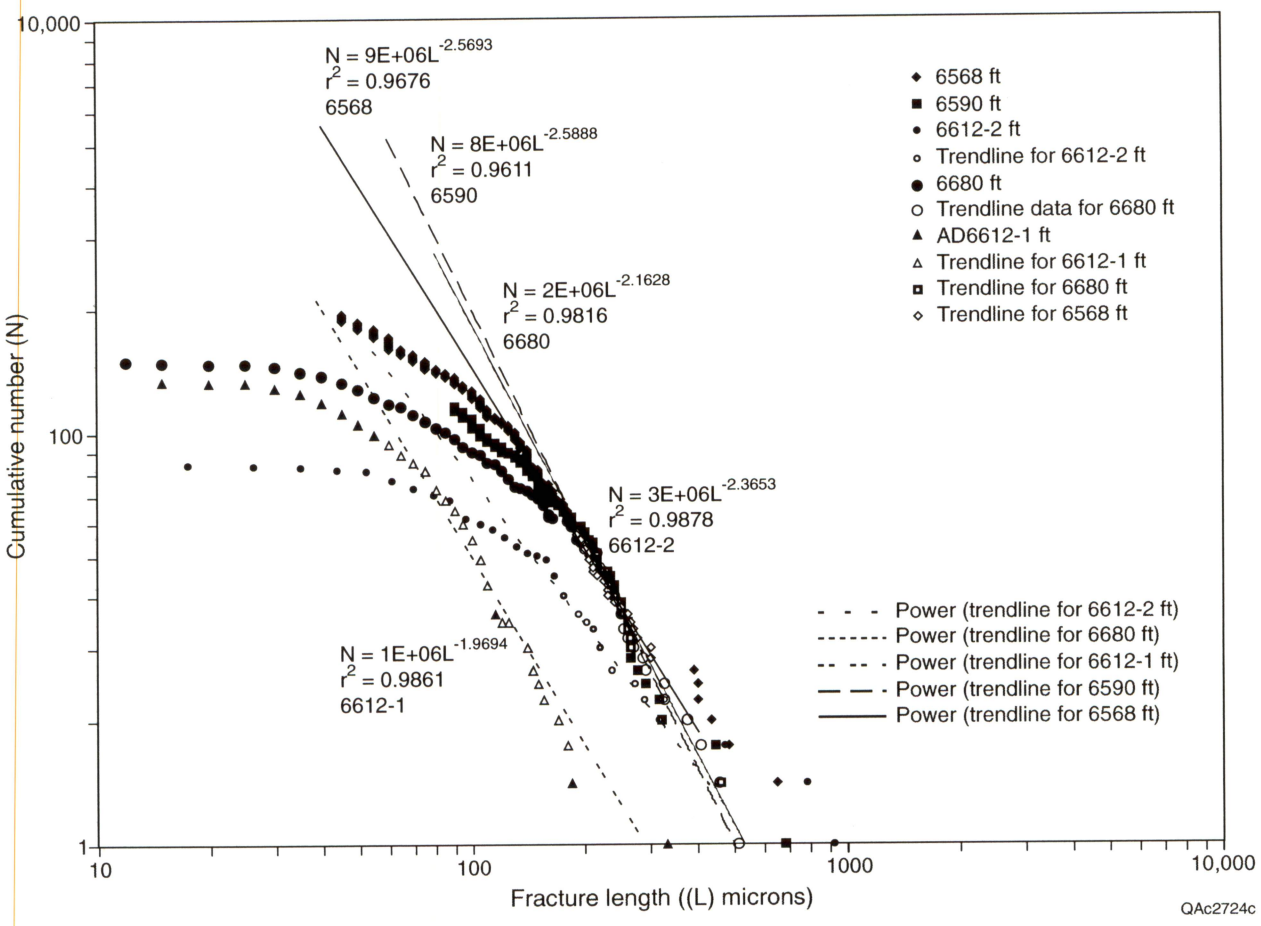

Figure 33 (cont.).

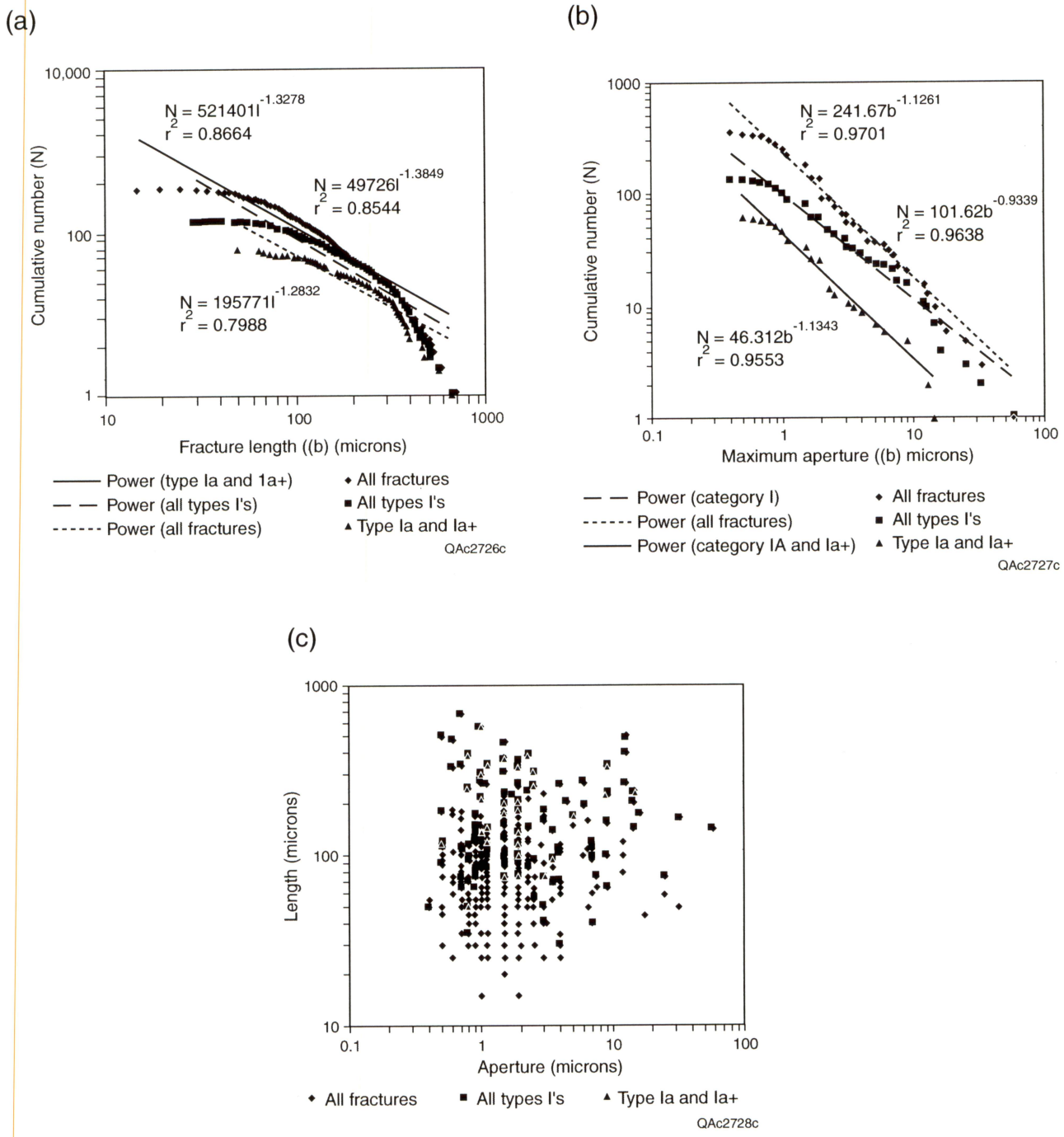

Figure 34. Scaling variation by category, Atlas Lucas No. 1 well, 6,386 ft depth. (a) Aperture scaling. (b) Length scaling. (c) Length vs. aperture plots.

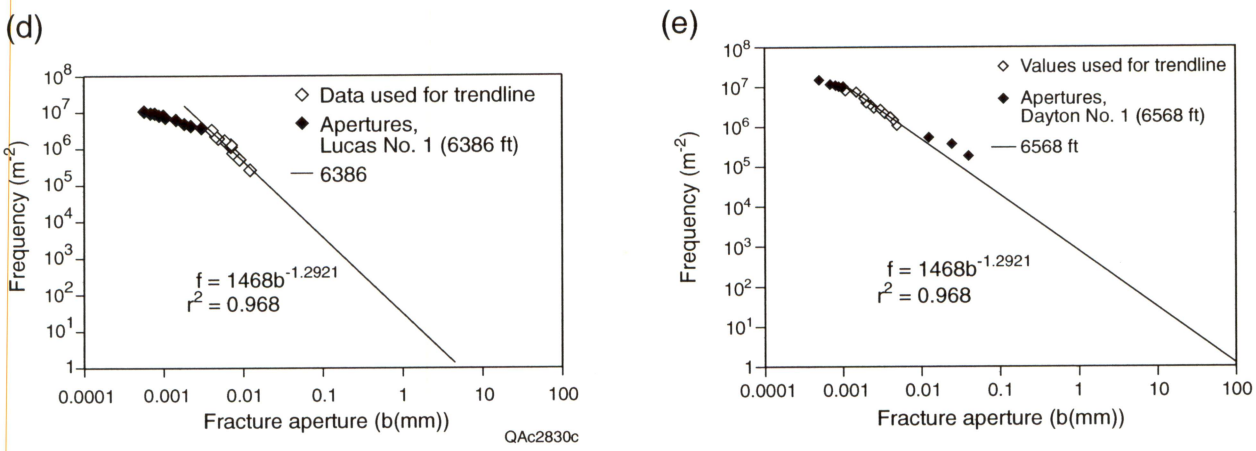

Figure 34 (cont.). (d) Aperture-frequency scaling data for the 6,386-ft interval, Atlas Lucas No. 1 well. Only Category I microfractures with strikes between due north and N30E are represented because they are inferred to have the highest probability of sharing a common tectonic genesis. (e) Aperture-frequency scaling data for the 6,568-ft interval, Atlas Dayton No. 1 well. Only Category I microfractures with strikes between N70E and N90E are represented because they are inferred to have the highest probability of sharing a common tectonic genesis.

evident that many fractures formed as the result of linking of smaller fractures. The energy expended in linking is not presently well accounted for in the LEFM equations but could well explain the observed lack of relationship between aperture and length.

Microfracture-size distributions can be used to predict the size distribution of large fractures (fig. 34) (Marrett and Laubach, 1997), and therefore they can provide a measure of the intensity of fracture development. Although the results of our study in the Medina are preliminary, they suggest that some parts of the microfracture population show power-law scaling. This is encouraging for applications that require upscaling to much larger fracture sizes, for the prediction of permeability enhancement and response in 2-D and 3-D seismic studies, particularly with regard to shear wave behavior (for example, Marrett, 1997). Figure 34d, e shows how microfracture population statistics can be used to predict the size distribution of large fractures on the interwell scale. Also, both our analyses of the FMI logs and the microfracture populations indicate the existence of two distinct generations of faulting/fracturing with different orientations and degrees of mineral fill.

CONCLUSIONS

The microfracture analysis methods we used provided information on the strike of large fractures, the degree of mineral fill in fractures (and, therefore, fracture conductivity), and the size distribution of large fractures. These attributes are difficult to assess using conventional techniques. In the Henderson Dome area, large quartz-lined regional fractures having N20E strikes, and a subsidiary set of fractures having N70W strikes, are prevalent. Some of these fractures have been filled with later ferroan dolomite and anhydrite, thus degrading fracture quality. The relative ages of these fracture sets has been determined. The location of zones of high fracture quality (intense fracture development with little or no mineral filling to occlude fracture conductivity) can be assessed from sidewall cores. Further mapping of fracture quality in the Henderson Dome area has good prospects for identifying natural-fracture-controlled, high-productivity zones (sweet spots).

The successful collection of microfracture-orientation, openness, and scaling data from the Atlas wells shows that fracture information can be collected from wells to calibrate and test seismic methods for natural-fracture characterization. Deployment of scaling methods applied to microfracture and production data, such as those described by Marrett (1997), could permit quantitative, independent fracture characterization at depths where seismic anomalies are present. An accomplishment of this study was the development of a new method to orient drilled sidewall cores. This should permit calibration of seismic methods, and fracture evaluation generally, to be carried out without the need to collect whole core in all intervals of interest. This will be needed for practical mapping of fracture attributes on the scale of the seismic volume.

PART 2: SEISMIC DETECTION OF FRACTURED ROCK

The objectives of the seismic portion of this research program were to investigate seismic technologies that can be used to detect and map fractured facies in Appalachian reservoirs, and to determine if these technologies can be integrated to allow effective 3-D seismic surveys to be done over Appalachian prospects. To detect fractured reservoir facies with seismic imaging technology, it is essential that the targeted reservoir system be illuminated with seismic shear (S) waves. Two approaches were followed to determine techniques that could be used to generate robust, downgoing S-waves over Henderson Dome in a Mercer County, Pennsylvania, prospect.

Approach 1 was to develop and test a new seismic explosive package that creates a downgoing wavefield that has a stronger S-wave component than does a conventional seismic explosive. The development of this new S-wave source technology is the most successful result achieved in the seismic research investigation because this source concept will allow Appalachian operators to generate seismic S-waves in prospect areas where conventional S-wave sources (specifically horizontal vibrators) cannot be used. The special packaging of directional, shaped-charge explosives developed in this research can be deployed in shallow shot holes if desired. The attractiveness of this source capability is that shallow shot holes (typically 10 ft deep) can be prepared with small portable drills that can be deployed across agricultural crops with minimal damage and can be operated in dense timber without having to remove trees.

Approach 2 was to analyze the amount of P-to-S converted-mode energy contained in downgoing wavefields generated by a standard P-wave seismic energy source. Converted-mode S-wave imaging is becoming a popular seismic technique, particularly in marine environments, and our objective was to determine if acceptable S-wave conversion occurred in the geologic section associated with the Henderson Dome in Mercer County, Pennsylvania. In this Appalachian study, a vertical wavetest analysis was done using 3-component vertical seismic profile (VSP) data generated by a vertical vibrator, a common seismic P-wave energy source. The amount of converted S-wave energy observed in this test was as great as that observed at

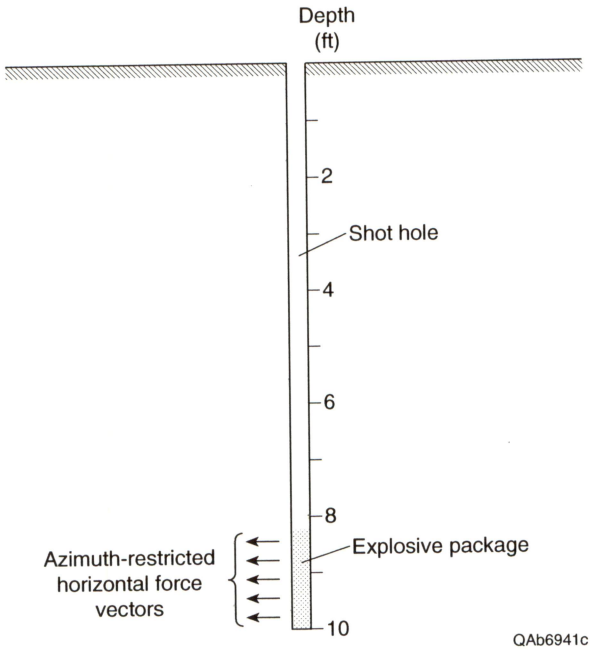

Figure 35. A fundamental need is to develop explosive packaging specifically for shear wave exploration. The packaging must be easily deployed in standard shot holes and must generate a robust, horizontally directed force vector that creates a horizontal impulse in a specific azimuth direction.

locations in West Texas and the Midcontinent where the Bureau of Economic Geology has done other converted-mode studies. We conclude that converted-mode imaging can be done in the Appalachian Basin, and the technique may be as effective for fracture detection as is the S-wave illumination approach provided by the special S-wave explosives package that was developed.

S-WAVE EXPLOSIVE SOURCE

To date, the bulk of S-wave seismic data acquisition has been done using vibrators that create horizontal force vectors on the ground surface by shaking their pads in a horizontal plane. Seismic vector-wavefield technology (S-wave imaging) cannot be used at some prospects until an alternate S-wave source technology is available because some horizontal vibrators cannot be phase-locked to create effective source arrays, others create too much surface damage to be used in some prospects, some may produce inconsistent wavelets from source point to source point, and none can be deployed in timbered areas where no tree clearing is allowed or where there is a large amount of rock outcrop across the prospect area.

One alternate S-wave source concept that offers promise is an explosive package that produces a horizontally directed force vector that can be oriented in a specific azimuth direction. To be commercially viable, this explosive packaging must be capable of being deployed in standard-diameter shot holes, as shown in figure 35. This diagram is drawn to scale to represent a 4-inch-diameter hole having a depth of 10 ft. Shot holes can be drilled with rock bits of various diameters, but the hole diameter rarely exceeds 5 inches. For reasons of economy, shot holes need to be as shallow as possible, yet they must be deep enough to ensure that there is an optimum transfer of explosive energy to the earth and that no rifling effect occurs at the surface. Shot holes will rarely be shallower than the 10-ft depth implied in figure 35; they may often be as deep as 20 to 60 ft or more to ensure that optimum energy coupling is achieved.

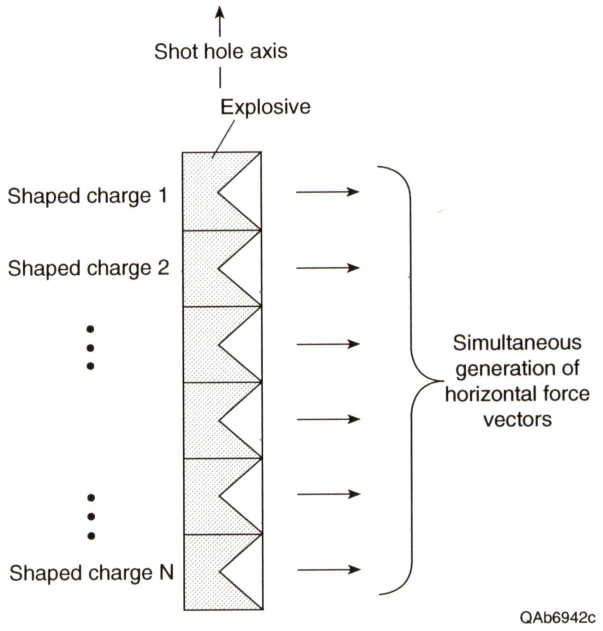

Figure 36. Shaped-charge concept. The objective is to assemble a stack of shaped charges that have a length less than the diameter of a shot hole into a package that allows all charges to be fired simultaneously to generate the required horizontally oriented force vector. This illustration is a section view of such a package being detonated in a shot hole.

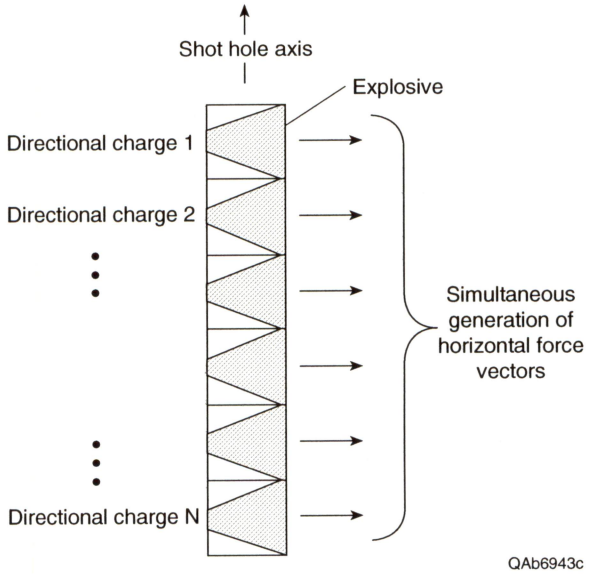

Figure 37. Directional charge concept. The objective is to assemble a stack of directional charges into a package that will fit in a shot hole. The charges must be horizontal in the hole and fire simultaneously to generate a robust, horizontally directed force vector. This diagram is a section view of a shot hole at the time of detonation.

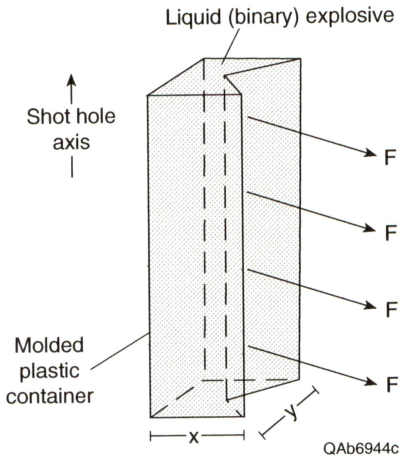

Figure 38. Binary liquid charge concept. The objective is to deploy a liquid binary explosive mixture in a plastic housing that is specially molded to create a horizontally directed, shaped-charge geometry in a small-diameter shot hole. The lateral dimensions x and y of the plastic container must be small enough to allow the package to be inserted into standard shot holes. Force vectors F must be horizontal and focused in a narrow azimuth aperture.

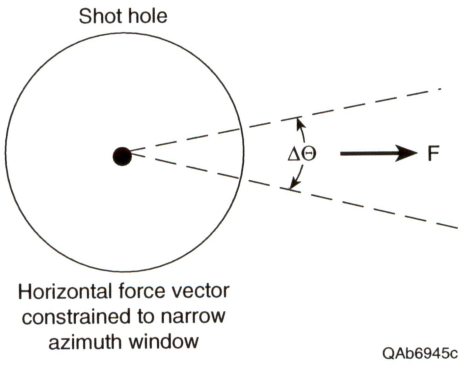

Figure 39. Top view of explosive package as seen looking down the shot hole. The output force vector must not only be horizontal, but it must also be oriented so that its impulse direction is constrained to be inside a narrow azimuth aperture $\Delta\theta$.

FUNDAMENTAL SOURCE REQUIREMENTS

The critical requirement of any explosive packaging used for seismic vector-wavefield imaging is that the output force vector must be capable of being oriented in a horizontal direction so that it creates a robust horizontal shear impulse to the earth. Any force vector component that is non-horizontal will produce an increased proportion of P-wave energy, which is not desirable. Packaging concepts that could be considered would be some type of vertical stack of shaped charges (fig. 36), a vertical stack of directional charges (fig. 37), or a liquid (binary) explosive in a container that is specially molded to create a horizontally directed shaped charge in small-diameter holes (fig. 38).

In addition to the requirement that the output force vector be horizontal, the force vector must also be oriented in a specific azimuth direction, as illustrated in figure 39. This requirement that the source should create an earth impulse that is oriented in a specific azimuth direction is critical to seismic vector-wavefield acquisition.

SHOT-HOLE DIAMETER

Shot holes can be drilled with a wide variety of bit sizes, with the maximum bit diameter being controlled by the power and size of the drill rig. Truck-mounted rigs can drill holes with a bit diameter as large as 12 or 15 inches; many buggy drills are limited to bits of 6-inch diameter or less; and light, portable drills often cannot use bits with a diameter larger than 4 inches.

Even though a wide range of shot-hole diameters can be drilled, there are economic constraints that cause large-diameter shot holes not to be practical. Drilling costs increase significantly when the bit size exceeds 4 3/4 inches. At this time (1998), competitive bids for shot-hole drilling and loading average $1.50 per foot in the United States if the bit size is 4 or 4 3/4 inches but increase to an average of about $2.50 per foot if a 6-inch diameter bit is used. This significant increase in cost (almost a factor of 2) is due primarily to the greater cost and shorter work life of 6-inch bits as compared with 4 3/4-inch (or 4-inch) bits.

Applying the philosophy, "keep the cost low so there will be wider commercial use," to the shot-hole requirements for any new S-wave explosive packaging leads to the decision that shot holes used for S-wave explosive sources should have a diameter of 4 or 4 3/4 inches.

EXPLOSIVE PACKAGING

Package Length

To make explosive S-wave sources more economically appealing to industry, shot-hole depths should be limited to 10 ft or less whenever possible. Thus, the idea of using a low-cost, disposable cardboard cylinder 10 ft long as an integral part of the explosive package is attractive. Such a package can be deployed easily and then azimuthally oriented in a 10-ft shot hole, which are two critical field operational requirements that must be done quickly and accurately to make explosive source technology attractive. The field tests done in this study used such 10-ft cylinders to orient the explosive in a selected direction, once it was placed at the base of the shot hole. Other orientation methods can be used in large-scale commercial use of the explosives. The explosive package itself should be no longer than 24 to 30 inches.

Package Diameter

Based on the economic requirement that a shot-hole diameter be either 4 or 4 3/4 inches, the diameter of the cylinder in which the explosives are packaged should be no larger than 3 inches. This package size will allow a shaped charge to be inserted inside the cylinder and still have a modest standoff distance between the charge and the shot-hole wall.

Standoff

Conventional thinking is that a shaped charge creates a narrower and deeper hole in a target and, by inference, a more directionally oriented force vector, if the standoff distance between the charge and the target (the shot-hole wall in this application) is on the order of 3 to 4 charge

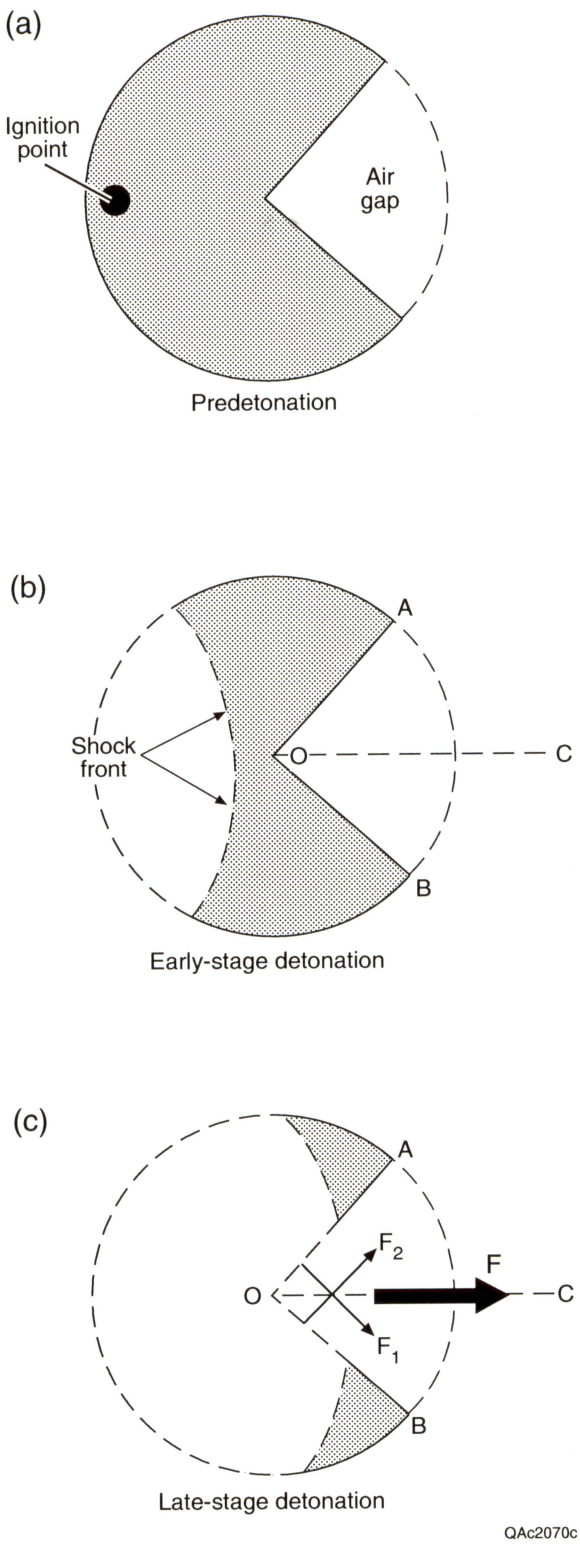

Figure 40. Vertical view looking down on the shaped charge that was developed in this project as it proceeds through various stages of detonation. The detonation front is created at an ignition point (a) that is directly opposite to the shaped notch BOA (b). As the shock front sweeps past the notch (c), it creates counter-opposed forces F_1 and F_2 that sum as vectors to create a strong horizontal force F. The shaped notch extends the full length of the cylindrical charge.

diameters (Austin Powder, personal communication, 1998). The shot hole and explosive package diameters proposed here do not create this ideal standoff geometry of 3 to 4 charge thicknesses. However, a standoff of 1.0 to 1.5 charge thicknesses can be created if the explosive package can be placed against the wall of the shot hole that is opposite to the point where the force vector is to be applied. This standoff geometry enhances the directionality of the output force and is a critical factor in ensuring that the explosive design creates a polarized source.

Package Durability

Once shot holes are loaded, it may be several weeks before the explosive can be detonated because of weather delays or logistical, permitting, and technical problems related to the deployment of the seismic crew. The explosive package must be engineered so that the various hostile conditions that exist in typical shot-hole environments do not adversely affect explosive behavior for a period of 2 to 3 months. For shaped charges, a key requirement would be that water never enter into the shaped-charge cavity, which would seriously degrade the energy output and would have unknown effects on the directionality of the output force vector. Downhole durability of the charges and of the explosive packaging is critical to the success of this new S-wave source technology.

Cavity Seal

One of the critical parameters of a shaped charge is the cavity that focuses the output force vector (fig. 40). The apex angle of a cavity ranges from 45° to 90° typically; a 90° angle is shown in figure 40. For a shaped charge to function properly, this cavity must be air filled. If water or soil fills the cavity, the focusing capability of the charge is impaired, and a properly polarized output force vector may not be generated. Thus, for a shaped charge to function properly in a shot hole, there must be a durable, waterproof seal completely around the shaped cavity.

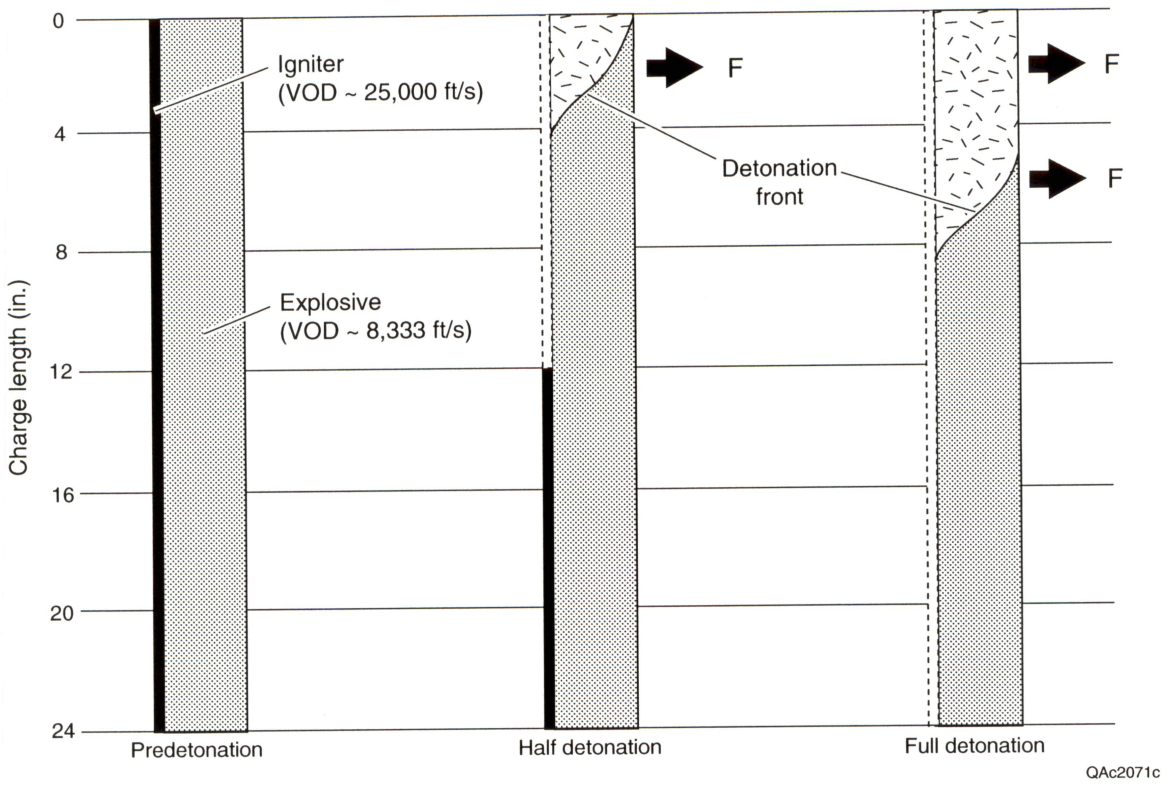

Figure 41. Side view of cylindrical shaped charge developed in this project at various stages of detonation. A high-velocity ignition cord extends the full length of the charge (left). The VOD in this ignition cord is three times greater than the VOD in the explosive, causing the detonation front in the explosive to lag the detonation in the ignition cord (center and right). The force vector F is the same force vector shown in figure 40.

Objective of Explosive Design Concept

Requiring an S-wave explosive package to fit in a 4-inch-diameter shot hole ensures that this new S-wave source technology will have the widest possible use because large shot-hole rigs capable of drilling large-diameter holes cannot be deployed in some prospect areas, for example in dense timber where no tree-clearing is allowed. In agricultural areas, there are certain calendar periods when landowners may consent to a small, portable drill rig being used in cultivated fields but will not approve the use of a large rig. Other examples could be cited, but the basic design objective is that by insisting that this S-wave source technology work in a 4-inch-diameter hole, then industry can make the transition from standard shot-hole seismic practice to new, vector-wavefield, shot-hole practice with minimal increase in cost and can also be assured that this S-wave explosive source technology can be used in most seismic-permitting conditions that will be encountered in the Appalachian Basin.

PHYSICS OF SHAPED CHARGES

The basic physics of the shaped charges that have been developed in this program is illustrated in figures 40 and 41. Figure 40 is a vertical view looking down on one of the cylindrical packages to show the interaction between the propagating shock front and the shaped-charge notch at various stages of detonation. In this perspective, the shock front begins to approximate a plane wave as it reaches the apex of the shaped-charge notch (fig. 40b).

As the quasi-plane wave sweeps past the notch (fig. 40c), it creates force vectors F_1 and F_2 that are normal to notch faces OA and OB, respectively. The components of F_1 and F_2 that are perpendicular to line OC cancel each other because they act in opposite directions. The components that are parallel to OC add constructively to create a strong horizontal force vector F oriented in the direction of line OC.

The behavior of the detonation front in a side view is depicted in figure 41. In this animation, the velocity of detonation (VOD) in the igniter cord is assumed to be three times

greater than the VOD in the explosive material, which is the VOD ratio used in the final explosive design developed in this study. The charge length of 24 inches is approximately the length of the final design package that was chosen. When the igniter cord has burned the full 24 inches, the detonation front has progress only 8 inches (full detonation panel; figure 41). The force vector F is the same vector shown in figure 40.

AUSTIN POWDER ALLIANCE

A technical alliance has been established between the Bureau of Economic Geology and Austin Powder, a major supplier of explosive products to the construction, mining, and seismic industries, to develop and test horizontal-vector explosive technology. In product planning, the basic packaging concept was agreed to be a cylindrical charge, 6 to 24 inches long, with a shaped notch extending the complete length of the explosive. Two explosive materials and package constructions were tested:

- A short, 6-inch cast of high-density, high-velocity pentolite (a mixture of pentaerythritol tetranitrate and trinitrotoluene), and
- A long, 24-inch plastic tube filled with low-density, low-velocity emulsion (the exact chemistry of this emulsion is proprietary to Austin Powder).

Photographs of these explosives will be shown later to clarify these word descriptions. The terms, high-velocity and low-velocity are relative, but in this report, *high-velocity* will be used to describe an explosive that has a VOD that exceeds 22,000 ft/s, and *low-velocity* will refer to explosives that have a VOD less than 12,000 ft/s.

VECTOR EXPLOSIVE CONCEPT NO. 1: CAST PENTOLITE

The first vector explosive concept fabricated by Austin Powder for this research investigation was a shaped charge of pentolite. Pentolite can have a range of bulk density and VOD values, depending on the percentages of pentaerythritol tetranitrate and trinitrotoluene used to

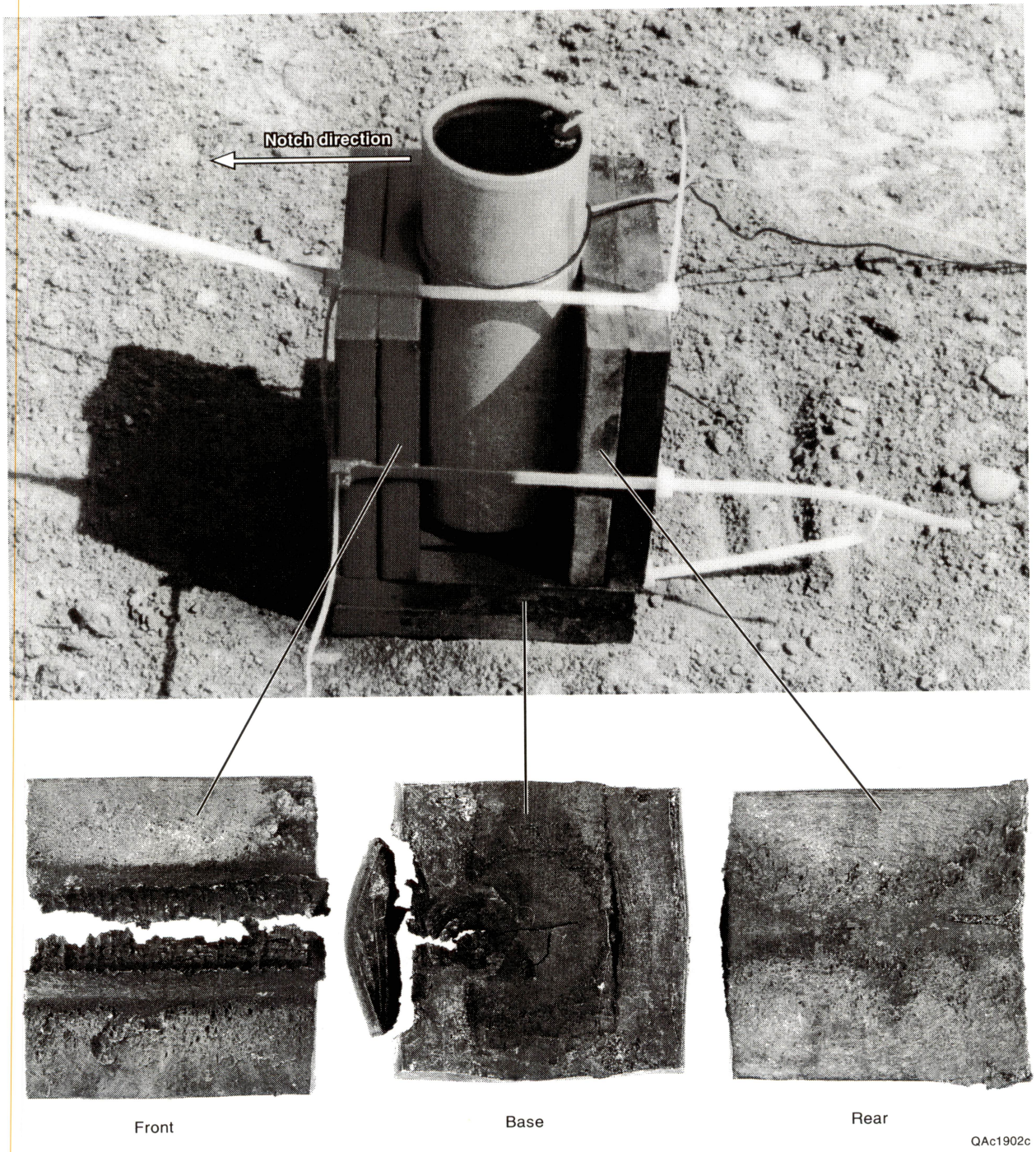

Figure 42. Deformation test demonstrating the directional force produced by a pentolite shaped charge. The shaped charge is surrounded by two layers of 0.5-inch steel plates (top). The deformation of the inner layer of plates (bottom) shows that the greatest force is in the direction that the shaped-charge notch faces. When such a charge is oriented vertically in a shot hole, the detonation will create a horizontally directed force vector.

fabricate the material. The particular formulation used for the vector-wavefield explosive had a bulk density of 1.6 gm/cm^3 (approximately) and a VOD of 23,000 ft/s (7,000 m/s).

Pentolite is a solid at room temperature. To fabricate the material as a shaped charge, it is melted in a steam-heated kettle and poured into molds. The molds used to fabricate the explosives used in this vector-wavefield testing program created explosive packages 6 inches long with a diameter of 1.5 inches. A photograph of one of these charges is shown in figure 42. Charges were made with three different angles, 45°, 60°, and 90°, in the longitudinal notch that extended the full length of the explosive package.

STEEL PLATE DEFORMATION TESTS OF DIRECTIONALITY

To demonstrate the horizontal directionality of the output force vector generated by the pentolite shaped charges, test charges were enclosed with 0.5-inch steel plates that were held in place with plastic tie strips. This encased charge was then buried about 2 ft deep in sand and detonated. Comparing the relative deformations for the steel plates that were in front of, in back of, and below the shaped charge notch provided a qualitative measure of the directionality of the output force vectors generated by the charge. An example of these steel-plate-deformation tests of directionality is shown in figure 42. In all tests, the plate in front of the shaped charge notch was more deformed that were any other plates, implying that the dominant force vector was oriented in the direction that the notch was facing. By deploying these cylindrical charges vertically in a shot hole with the shaped-charge notch facing in a selected horizontal direction, the charge should generate a horizontal-force vector in the direction that the notch is facing and create a stronger S-wave response than does a conventional seismic explosive.

FIELD TEST OF PENTOLITE SHAPED CHARGE

In preparation for the Appalachian Basin research, the pentolite-based shaped charge shown in figure 42 was first tested using a well of opportunity in Bee County, Texas. This test was

disappointing in that the S-wave content of the wavefield generated by the shaped charge was not significantly different from the S-wave component of the wavefield produced by a standard seismic charge. Conditions that perhaps contributed to this unexpected behavior of the shaped-charge explosive were (1) logistical constraints required that the shot hole be drilled with a 10-inch auger rather than a 4-inch drill bit and (2) these large-diameter holes could not be properly backfilled with the large, hardened clay clods produced by the auger in the soil conditions that existed at this site. The shortcomings of this test resulted in two decisions: to never deviate from standard size (4- to 5-inch-diameter) shot-hole drill bits, regardless of field logistical problems, and to design a new explosive package concept, which is described in the following section.

VECTOR EXPLOSIVE CONCEPT NO. 2: LOW-VELOCITY EMULSION

Two criteria dictated the design of the second vector-wavefield explosive package, these being (1) the package length should be increased to 2 ft or more and (2) the VOD of the explosive should be as low as possible. The logic behind these design criteria was that they would cause the explosion to create a force vector that was a better approximation of the force vector created by the pads of established S-wave seismic energy sources such as horizontal vibrators, Omnipulse units, and Aris vehicles. The width of the pads of these sources is of the order of 3 to 4 ft, thus the length of the explosive should be at least 2 ft. The impulse contact of the Omnipulse and Aris pads with the earth occurs over a time period of the order of a few milliseconds, thus the VOD of the explosive needs to be low to cause the explosive-force vector generated by the charge to be applied to the earth for the longest possible time interval.

These objectives resulted in a design that used a plastic shuck package that was 26 inches long and with a diameter of 3 inches. The explosive was a non-rigid emulsion having a VOD of approximately 9,000 ft/s. A 90° shaped-charge notch was created by taping a 26-inch length of plastic dry-wall corner strip to the interior of the plastic shuck before filling the shuck with the soft emulsion. A PETN igniter cord having a VOD of approximately 25,000 ft/s was inserted

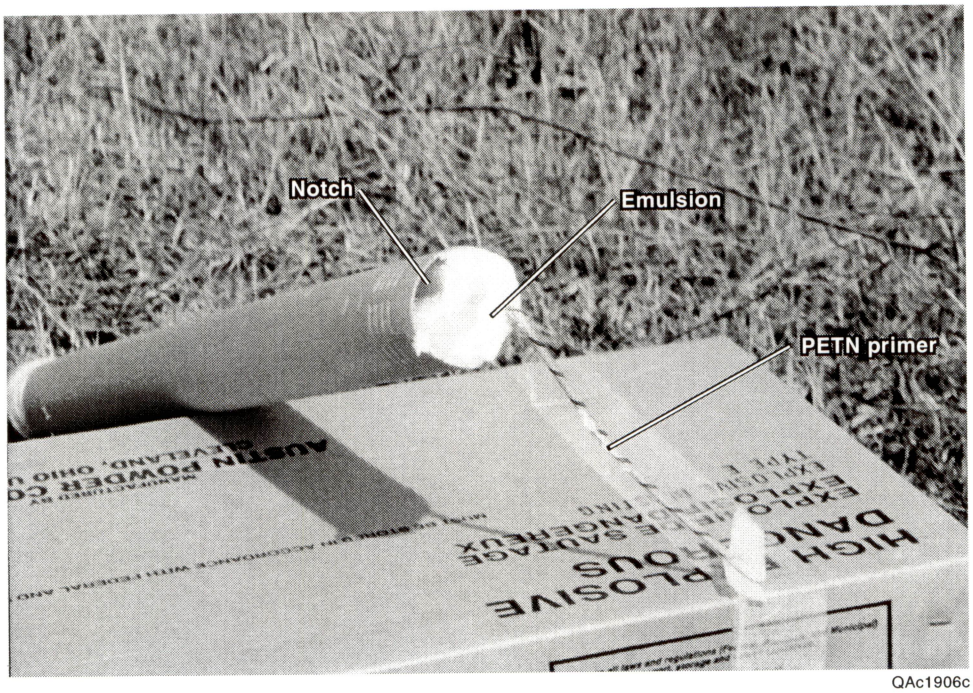

Figure 43. Low-velocity-emulsion shaped charge.

Figure 44. Low-velocity-emulsion shaped charge being prepared for detonation.

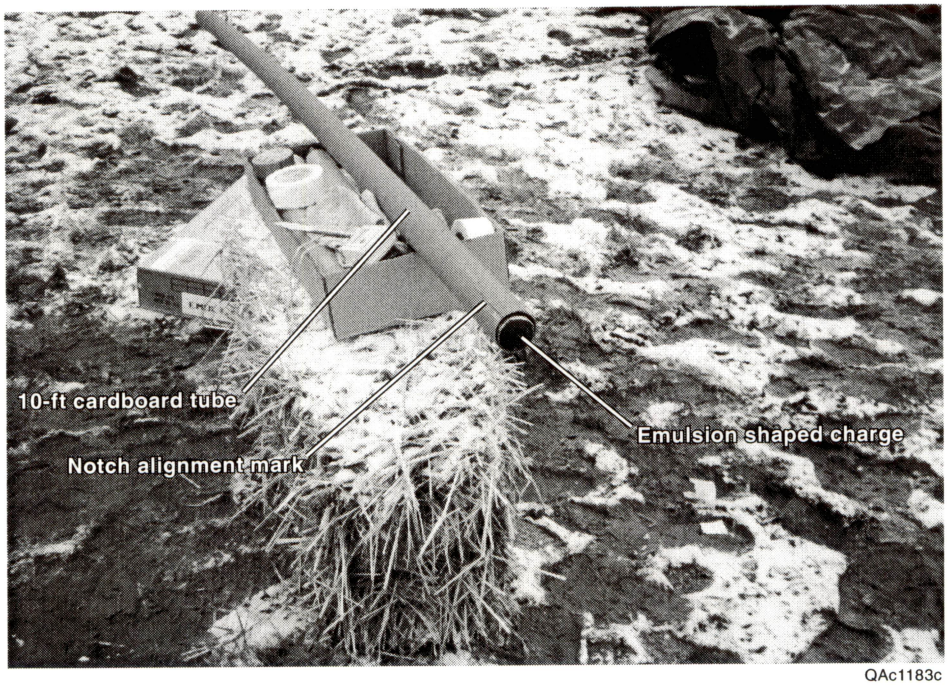

Figure 45. Low-velocity-emulsion shaped charge ready for shot-hole deployment.

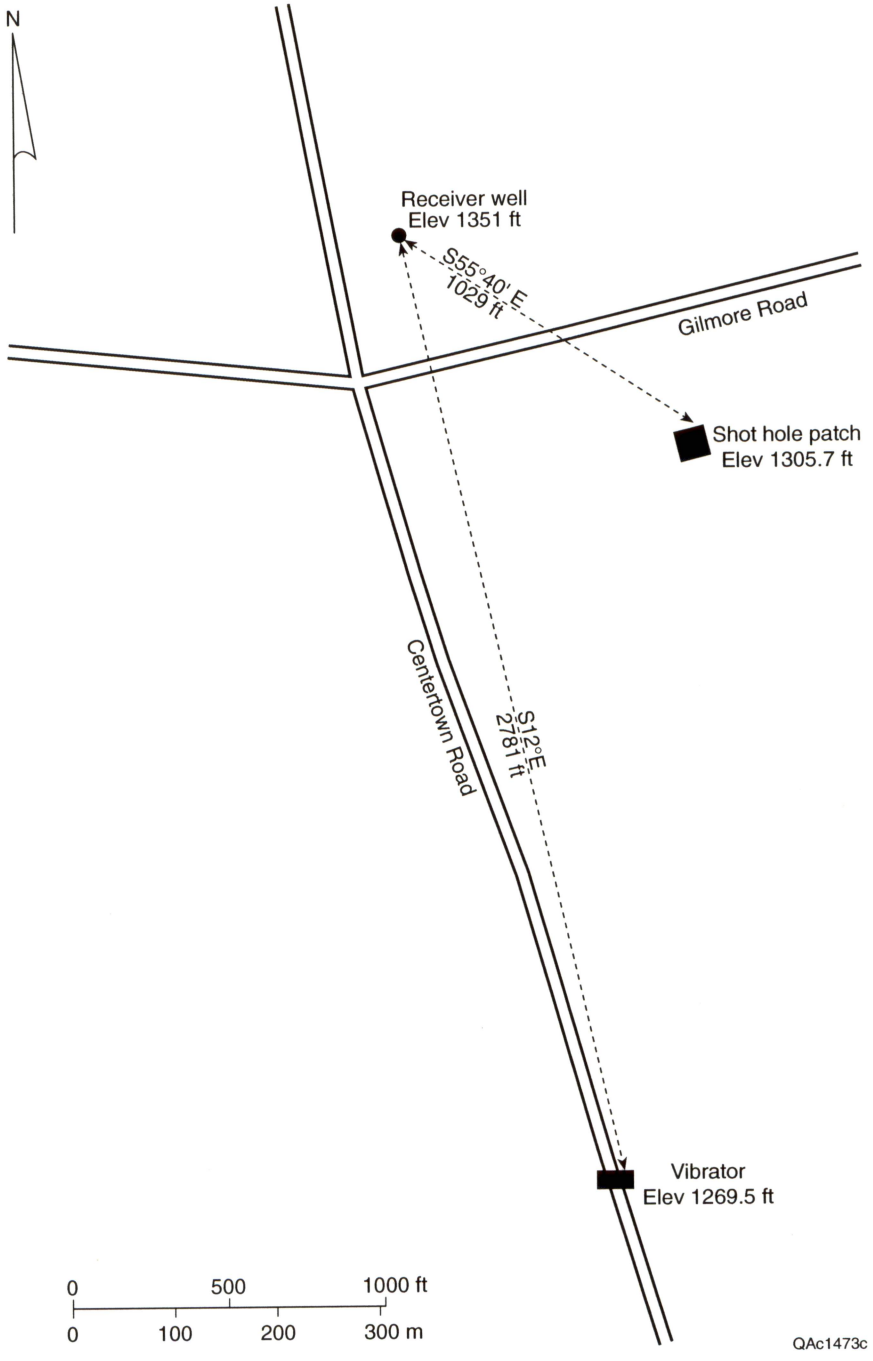

Figure 46. Wavetest geometry used to evaluate low-velocity-emulsion shaped charge. Downhole receivers were deployed in the VSP well; shaped charges were detonated in 10-ft shot holes inside the indicated shot hole patch.

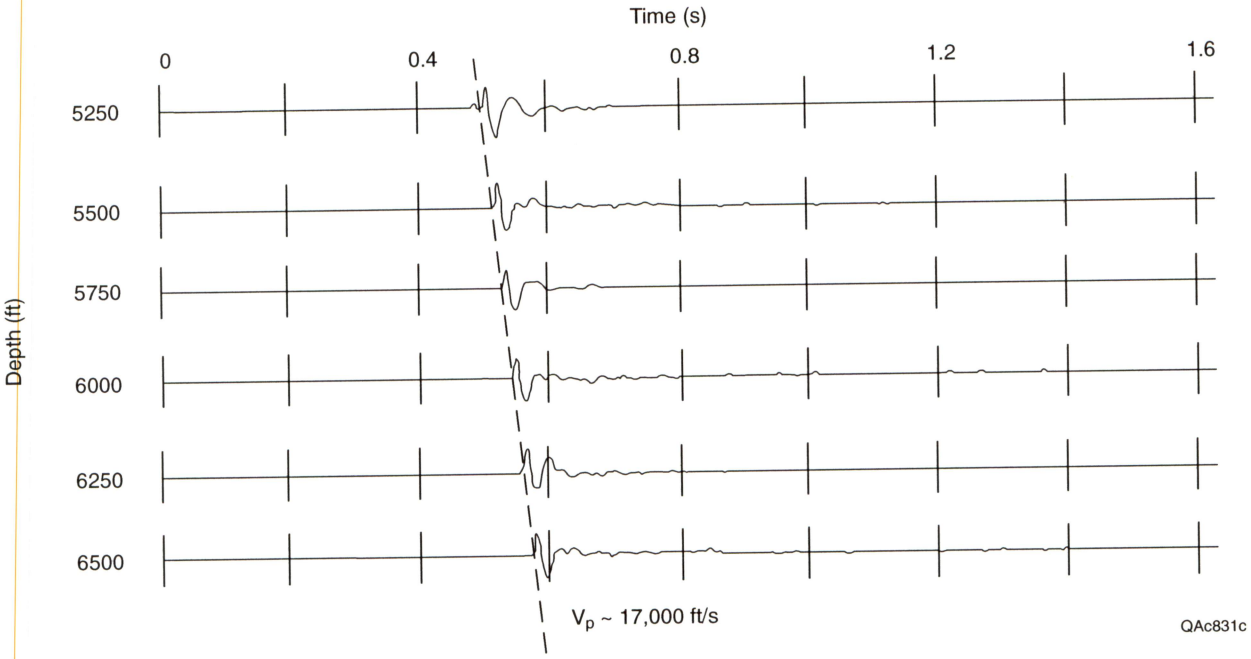

Figure 47. Shaped-charge wavefield recorded by vertically oriented downhole receivers.

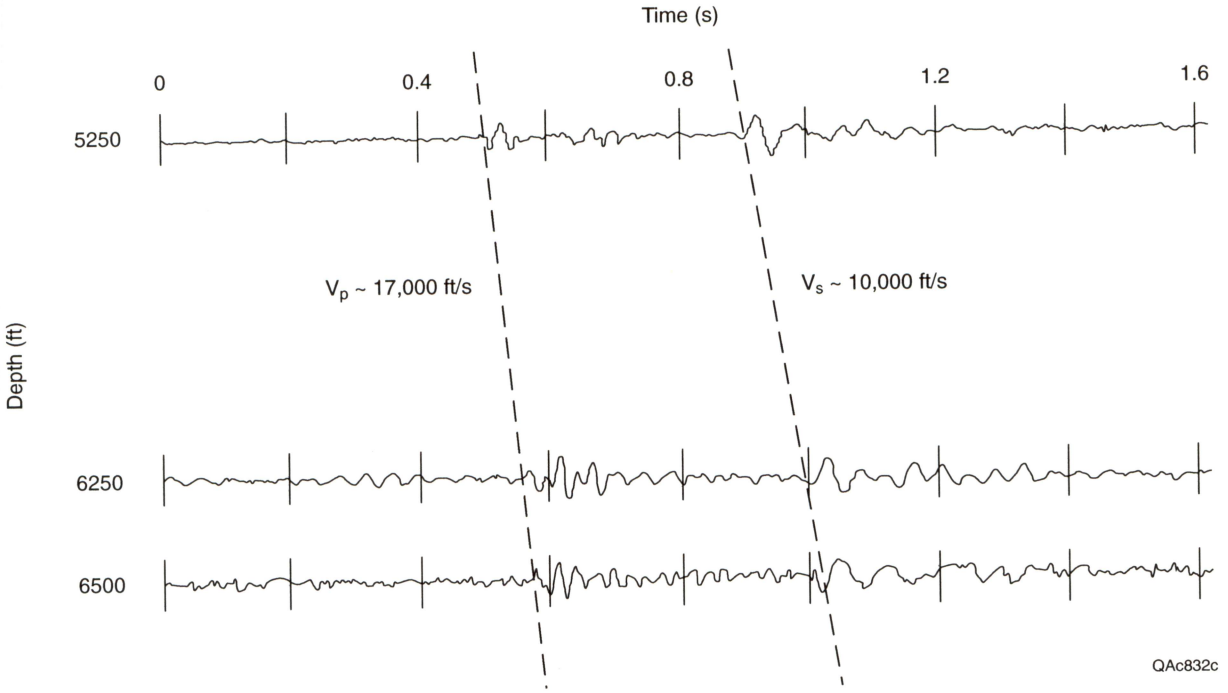

Figure 48. Shaped-charge wavefield recorded by horizontally oriented downhole receivers. Traces are omitted at receiver stations where horizontal receivers would not properly couple to the formation.

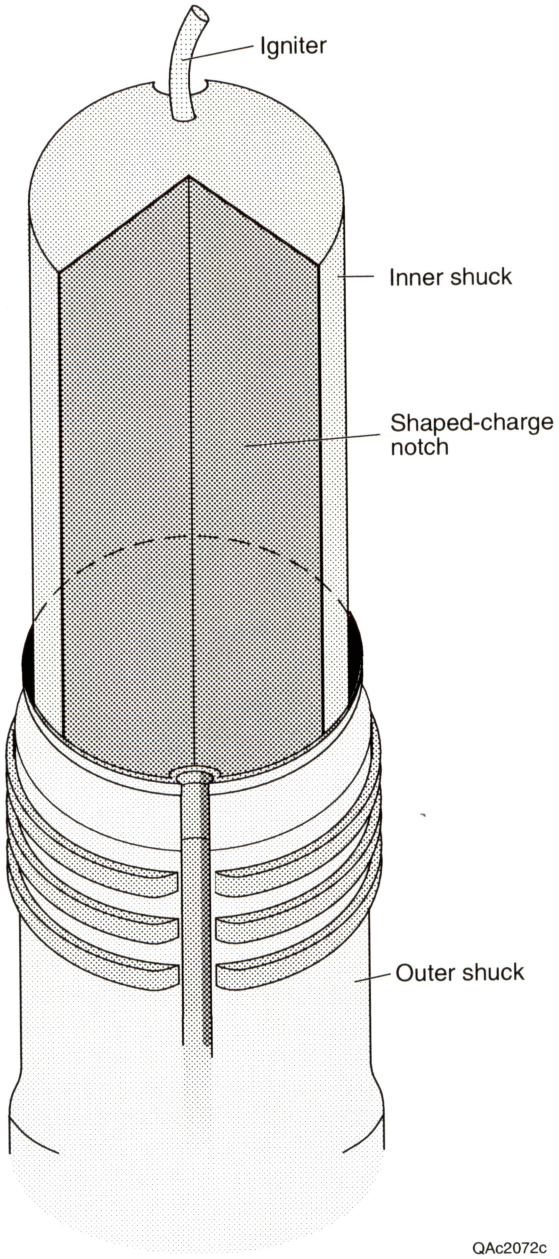

Figure 49. Final commercial package for the shaped-charge source. Two plastic shucks are required. The inner shuck has a full-length shaped-charge notch molded into its geometry. This inner shuck fits inside a smooth-walled shuck that ensures that no water or foreign matter intrudes into the shaped-charge notch.

along the complete length of the package at a circumference position directly opposite the shaped-charge notch (figures 40 and 41). Photographs of this package concept being assembled and deployed in the field are shown as figures 43 through 45.

VECTOR EXPLOSIVE TEST: MERCER COUNTY, PENNSYLVANIA

The photographs in figures 43 to 45 were taken during the testing of the low-velocity-emulsion shaped-charge package at the Atlas Montgomery No. 4 well in Mercer County, Pennsylvania, that was drilled by the industry partner, Atlas Resources, Inc. The field geometry involved in the test is illustrated in figure 46. The test well where vector-wavefield explosive data were recorded was the same well where VSP data were recorded to analyze converted-mode S-wave physics.

The key explosive-source data acquired in this test are illustrated in figures 47 and 48. The data in figure 47 were recorded with vertically oriented downhole geophones and show a robust P-wave first arrival. The data in figure 48 were recorded with horizontally oriented geophones and show a robust S-wave. The principal conclusion of the test results was that this second explosive package design was a more effective S-wave energy source than was the cast pentolite concept used in the first field test in Bee County, Texas.

COMMERCIAL PACKAGE DESIGN

The explosive packages shown in figures 43 to 45 are handmade products, not commercial, mass-produced units. Once the Mercer County test data confirmed that the package design was effective, Austin Powder commissioned the construction of a mold to make plastic shucks that would allow mass production of the shaped charges. This mold should be in operation in the fourth quarter of 1998.

The commercial version of the shaped-charge package will consist of two plastic shucks, one inserted inside the other (fig. 49). The inner shuck will have a full-length shaped notch

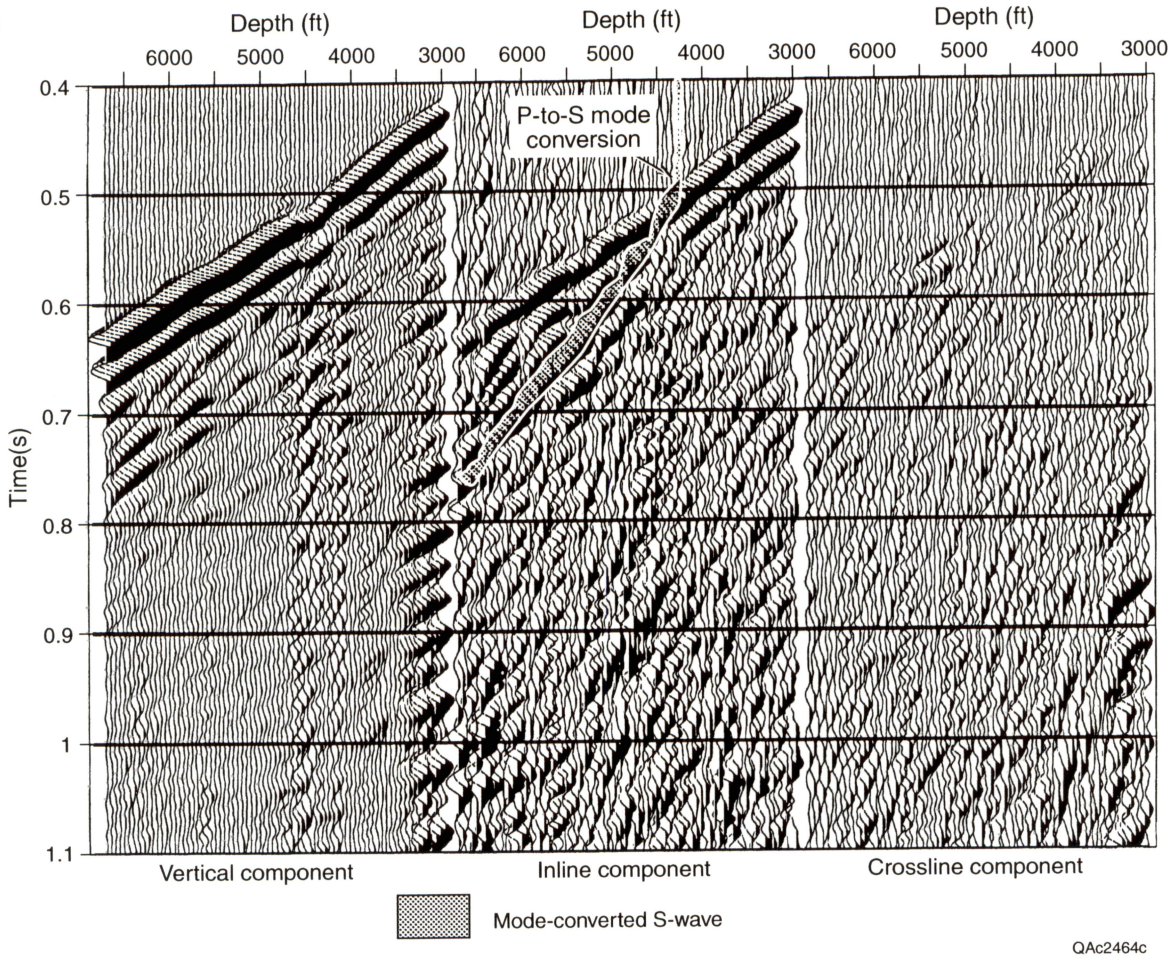

Figure 50. Downgoing VSP wavefield recorded in the Atlas Montgomery No. 4 well. The energy source was a vertical vibrator stationed 2,781 ft south of the well. A robust P-to-S conversion occurs at a depth of 4,300 ft. The downgoing S-wave produced by this mode conversion is highlighted in the panel that displays the inline-component data.

molded into the shuck wall. This notched shuck will then be inserted into the smooth-walled, cylindrical outer shuck. The purpose of the outer shuck is to keep water and shot hole backfill material out of the shaped-charge notch. The notch must be an air-filled space for the shaped charge to create an effective horizontal force vector.

CONVERTED-MODE SHEAR WAVE IMAGING

A method that is gaining acceptance as a means of illuminating reservoirs with seismic S-waves is to use seismic sources that generate robust P-waves, and then to cause these P-waves to generate downgoing S-waves via mode conversion at one or more formation boundaries positioned above the targeted reservoir. The result is that the reservoir is illuminated with both P and S waves, and both P and S wavefields reflect from the target. Both of these reflected wavefields (P and S) must be recorded at the surface with 3-component geophones rather than the vertical single-element geophones that are used to record P-wave reflection data.

One fundamental purpose for recording VSP data in the Atlas Montgomery No. 4 well was to determine if the P-to-S mode conversions that occur in Appalachian Basin rocks are of sufficient quality to cause mode-converted S-wave seismic imaging to be a recommended procedure over Appalachian Basin prospects. The energy source used to generate the downgoing P-waves in this VSP test was a vertical vibrator located approximately 2,800 ft south of the well (fig. 46). This source offset (2,800 ft) is small compared to source offsets that are used in surface-seismic profiling. Therefore, if P-to-S conversions occur for this short-offset geometry, even stronger mode conversions will occur for the long offset distances used in surface-based seismic profiling.

The 3-component VSP data recorded in the Atlas Montgomery No. 4 well are displayed as figure 50. Several robust P-to-S conversions occur starting at a depth of 4,300 ft, confirming that reservoirs below the Onondaga will be illuminated with S-waves. Thus S-wave imaging of fractured reservoirs at the Trenton, Medina, and Whirlpool levels can be accomplished in the

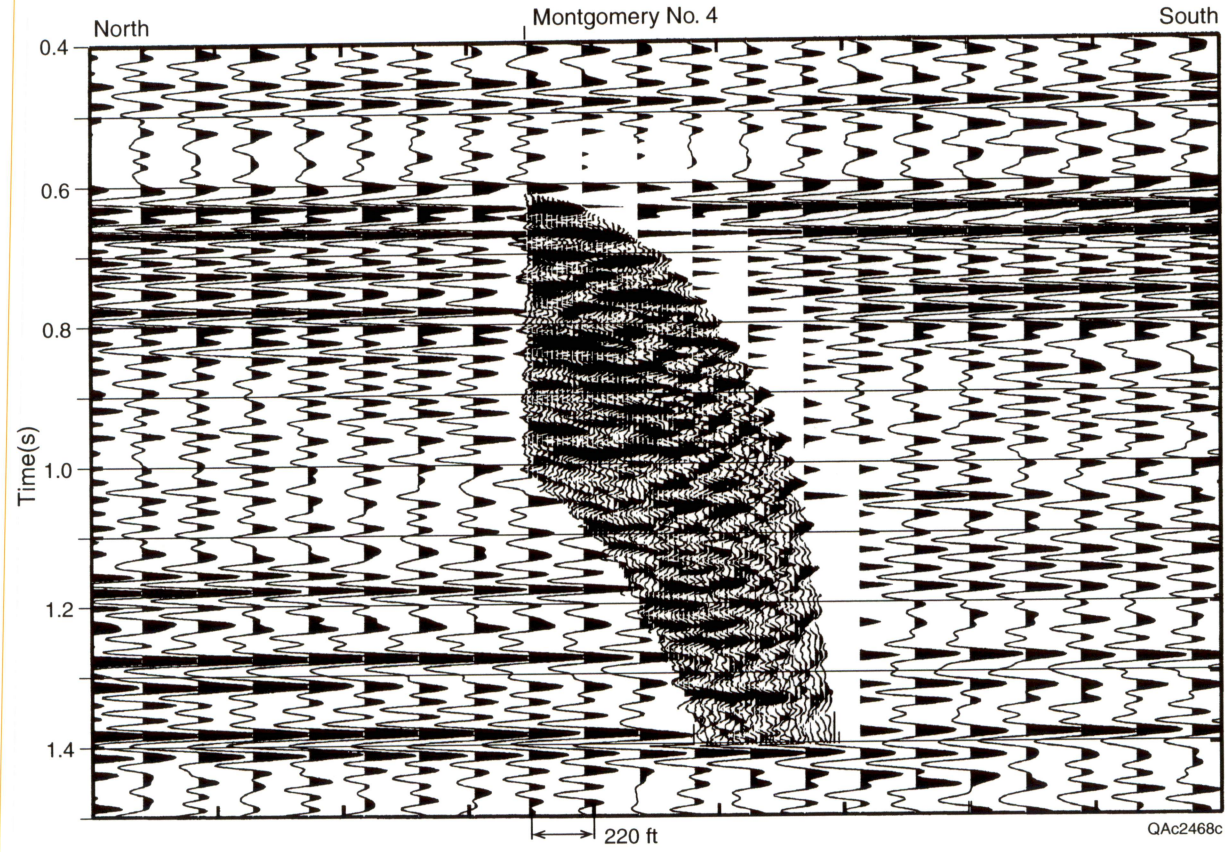

Figure 51. Comparison of VSP and surface-recorded P-wave seismic images at the Atlas Montgomery No. 4 well.

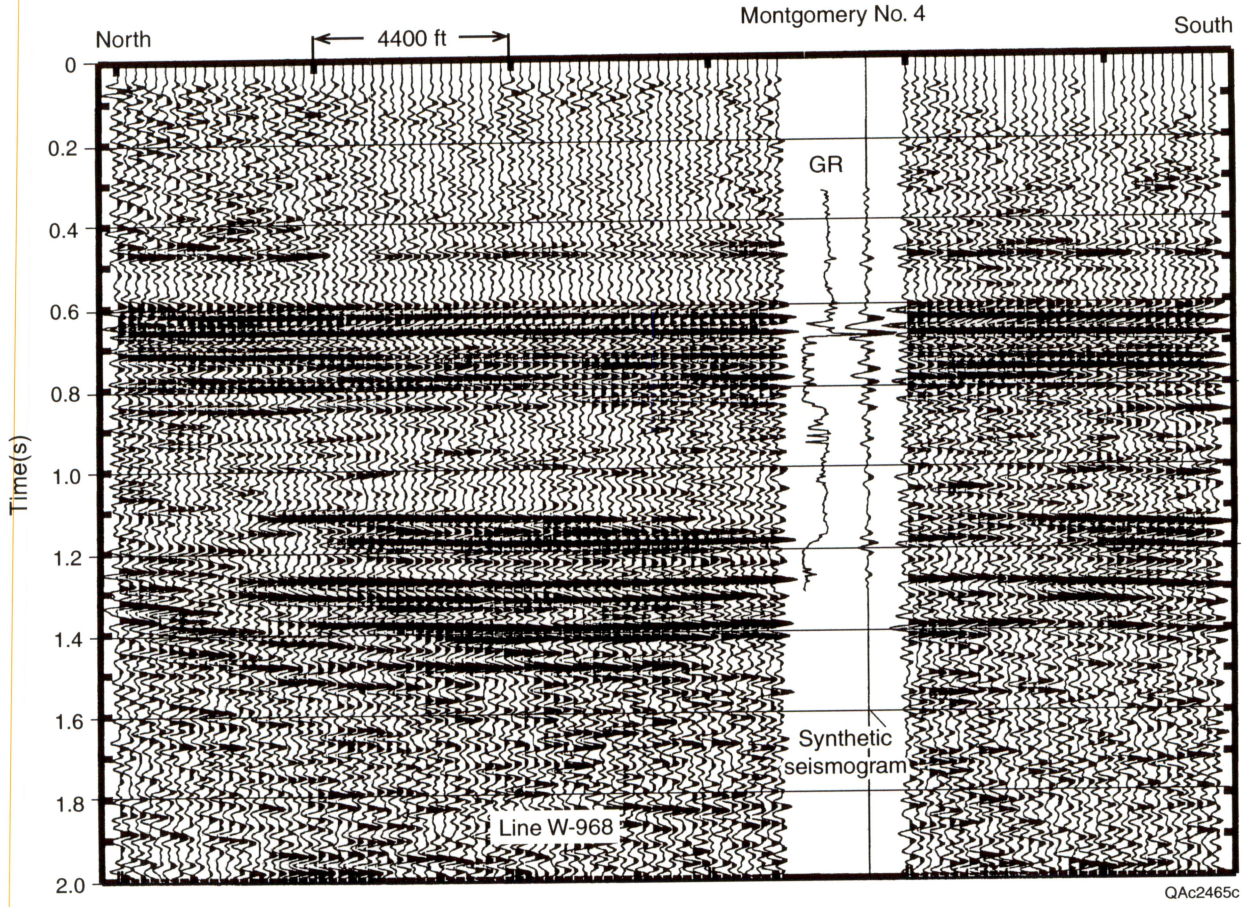

Figure 52. Comparison of synthetic seismogram and surface-recorded P-wave seismic image at the Atlas Montgomery No. 4 well.

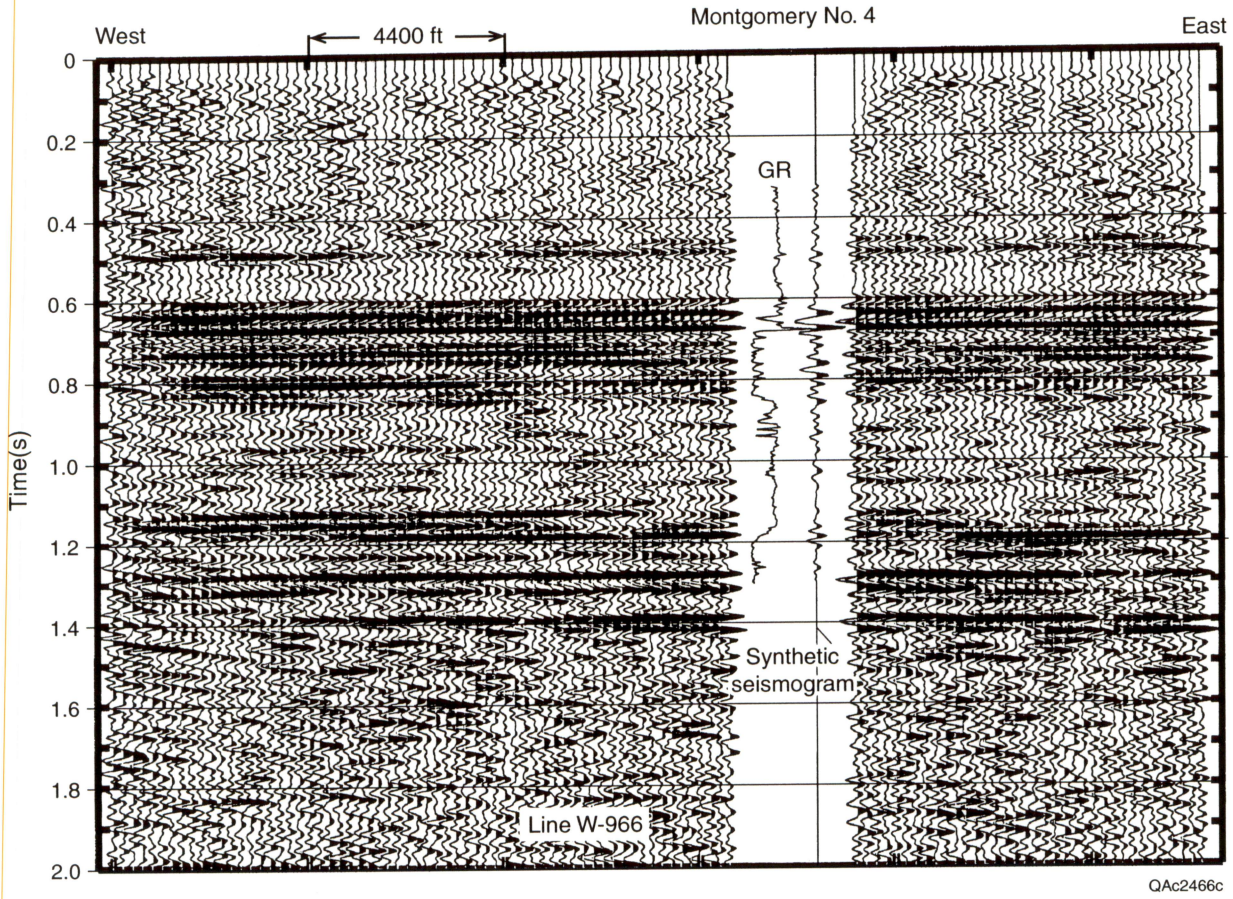

Figure 53. Comparison of synthetic seismogram and surface-recorded P-wave seismic image at the Atlas Montgomery No. 4 well.

Henderson Dome area by using standard seismic sources (explosives or vertical vibrators) and 3-component geophones. S-wave imaging of targets above these reservoir targets may also be possible, but the VSP data from the Atlas Montgomery No. 4 well imply that P-to-S mode conversions occurring above the Onondaga are relatively weak.

COMPARISON OF SURFACE-RECORDED P-WAVE SEISMIC DATA WITH VSP DATA AND SYNTHETIC SEISMOGRAM

Two 2-D P-wave seismic lines pass near the Atlas Montgomery No. 4 well. North-south line W-968 follows Centertown Road; east-west line W-966 follows Gilmore Road (fig. 46). A P-wave image extracted from the VSP data is compared with seismic profile W-968 in figure 51. The trace spacing in the high-resolution VSP image is 20 ft, whereas the trace spacing in the 2-D seismic profile is 220 ft. The VSP image implies that one or more faults may occur close to the receiver well; these fault indicators are associated with the disruptions in the VSP reflection events. In general, there is an acceptable correlation between the VSP image and the surface-recorded image.

A synthetic seismogram calculated from P-wave sonic-log data recorded in the Atlas Montgomery No. 4 well is compared with the two surface-recorded seismic profiles in figures 52 and 53. A gamma-ray log from the Atlas Montgomery No. 4 well is included in each display. This synthetic seismogram is also a reasonably good match with the surface-recorded P-wave seismic reflection character.

Subsurface stratigraphy can be inserted correctly into these P-wave surface-recorded seismic profiles using either the synthetic seismogram or the VSP image to correlate stratigraphic depth to P-wave image time. The synthetic seismogram option is the more economical approach as long as prospect evaluation is limited to P-wave seismic interpretation. The VSP calibration option will be necessary when prospect interpretation needs to be based on both P-wave and S-wave images.

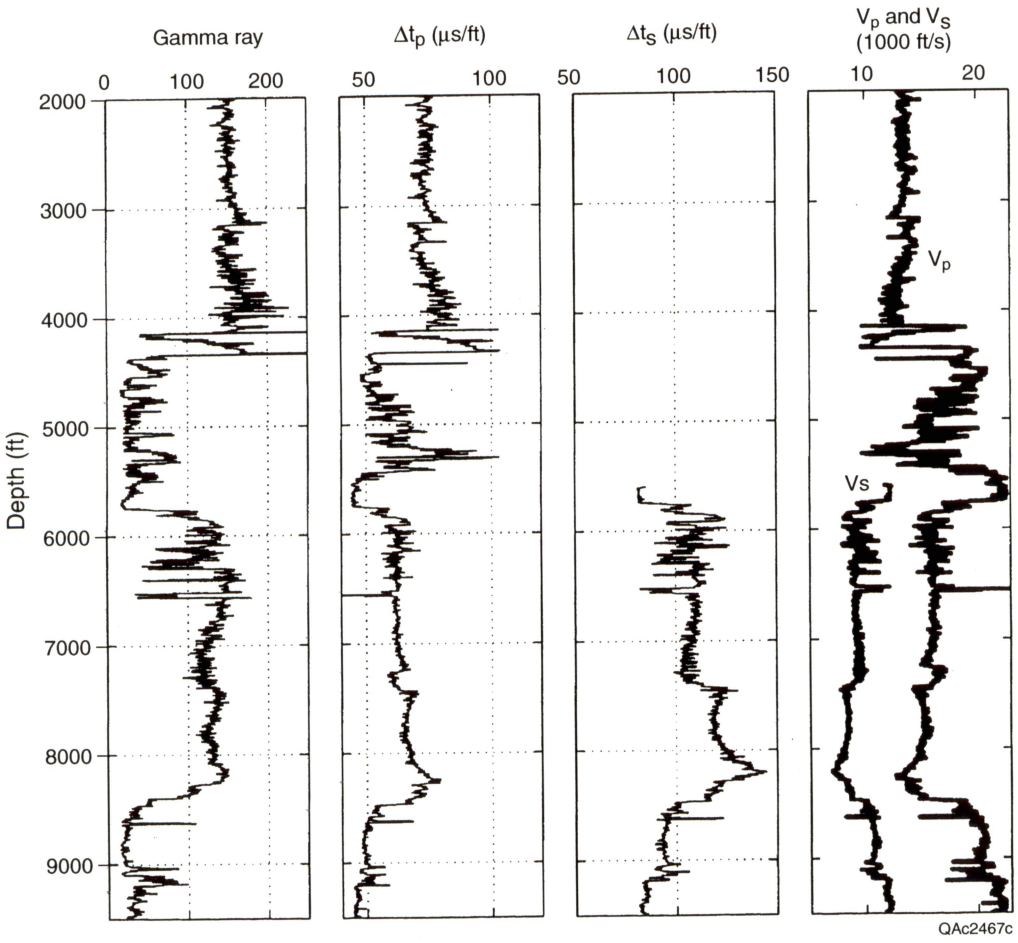

Figure 54. Comparison of well logs recorded in the Atlas Montgomery No. 4 well. The high degree of correlation between the gamma-ray curve and the Δt_p log implies that gamma-ray logs can be used as pseudo-sonic logs.

PSEUDO-SONIC LOGS

There is a good correlation between the gamma-ray log and the P-wave sonic log recorded in the Atlas Montgomery No. 4 well (fig. 54). The quality of the correlation is sufficient to permit gamma-ray logs to be substituted for sonic logs in wells where no sonic logs are recorded. The use of gamma-ray-based pseudo-sonic logs can be valuable in Appalachian Basin exploration, because Appalachian operators can use these pseudo-logs to calculate synthetic seismograms in older wells where no sonic logs exist. We do not recommend that gamma-ray logs be deliberately substituted for sonic logs in future drilling in the Appalachian Basin but that gamma-ray-based synthetic seismograms be used when there is no other recourse for acquiring sonic log data.

CONCLUSIONS

Appalachian operators should use seismic S-waves to detect and evaluate fractured reservoirs. The research performed in this study establishes two approaches that can be taken to create appropriate S-wave seismic data in the Appalachian Basin. One approach is to use the shaped-charge explosive package developed jointly by the Bureau of Economic Geology and Austin Powder. This S-wave explosive source will be a commercially available product by the first quarter of 1999. The second approach is to use a standard seismic source, such as a conventional shot hole explosive or a vertical vibrator, and to rely on P-to-S mode conversion to generate downgoing
S-waves that will illuminate fractured reservoirs. VSP data recorded in this research program demonstrate that robust S-waves are generated by P-to-S mode conversions over Henderson Dome and, by inference, the mode-converted technique should be considered as a viable S-wave imaging technique throughout the Appalachian Basin.

PRODUCTS AND CONCLUSIONS

Among the principal accomplishments of this project are two technology-transfer products that have clear commercial potential. One product is the methodology whereby microfractures observed in SEM images of thin sections cut from sidewall cores are used to create accurate models of the reservoir-scale macrofracture systems that control natural-gas production. The Bureau of Economic Geology is prepared to train service laboratories in the proper analysis procedures required to implement the method.

The second commercial product is the vector explosive package that generates seismic S-waves. Austin Powder is making a commercial mold to fabricate the special plastic shucks required for this explosive package and will be able to make large-quantity product runs of this new seismic energy source by the first quarter of 1999.

The practical results of this research are that Appalachian operators now have (1) a low-cost procedure, based on microfracture analysis of oriented sidewall cores, that can establish reliable fracture models for basin exploration, and (2) two seismic technologies (a new explosive source and converted-mode imaging) that can be used to detect and map fractured reservoir facies from the surface. All three of these technical developments now need to be practiced over selected Appalachian prospects to establish basin-specific case histories that can be circulated among local operators.

ACKNOWLEDGMENTS

Our thanks to Atlas Resources, Inc., for furnishing the sidewall cores, logs, and base map for the study. In particular, we want to thank Bob Heim. Thanks to Robert A. Sanchez for core photography and preparation, Robert M. Reed for assistance with SEM/CL imaging difficulties and interpretation, Sigrid J. Clift for instrument maintenance and lab management, Alan Dutton and Joy Griffin for point counts, David M. Stephens for photography and scanning, and Jennifer F. Hughes for graphic art, both under the direction of Joel L. Lardon, Senior Graphics

Illustrator. We are also grateful to Jim Simmons, Bureau of Economic Geology, and Doug Patchen, West Virginia Geological Survey, for their help. Thanks also to Susan Lloyd, who did the word processing and layout, and Nina Redmond and Lana Dieterich, who prepared the report for publication. Jamie H. Coggin designed the cover.

REFERENCES

Atlas Resources, 1997, Henderson Dome area: Field Demons Ration site; Mercer, Butler, and Venango Counties, Pennsylvania: unpublished structure-contour map, scale 1:24,000.

Cheel, R. J., and Middleton, G. V., 1993, Directional scours on a transgressive surface: examples from the Silurian Whirlpool of southern Ontario, Canada: Journal of Sedimentary Petrology, v. 63, no. 3, p. 392–397.

Clift S. J., Laubach, S. E., Abegg, F. E., Aslesen, K. S., Laroche, T. M., and Stanley, R. G., 1998, New core analysis methods applied to Permian sandstone, Pakenham (Wolfcamp) field, Terrell County, Texas (abs.): American Association of Petroleum Geologists Bulletin, v. 82, no. 3, p. 523–524.

Coogan, A. H., 1991, A fault-related model for the facies of the Lower Silurian Clinton sandstone interval in the subsurface of eastern Ohio: Northeastern Geology, v. 13, no. 2, p. 110–129.

Crough, S. T., Morgan, W. J., and Hargraves, R. B., 1980, Kimberlites, their relationship to mantle hot spots: Earth and Planetary Science Letters, v. 50, p. 260–274.

Dutton, S. P., 1993, Influence of provenance and burial history on diagenesis of Lower Cretaceous Frontier Formation sandstones, Green River Basin, Wyoming: Journal of Sedimentary Petrology, v. 63, no. 4, p. 665–677.

Dutton, S. P., Clift, S. J., Hamilton, D. S., Hamlin, H. S., Hentz, T. F., Howard, W. E., Akhter, M. S., and Laubach, S. E., 1993, Major low-permeability sandstone gas reservoirs in the continental United States: The University of Texas at Austin, Bureau of Economic Geology Report of Investigations No. 211, 221 p.

Englander, T., 1985, Loading paths to joint propagation during a tectonic cycle: an example from the Appalachian Plateau, U.S.A.: Journal of Structural geology, v. 7, p. 459–476.

Folk, R. L., 1974, Petrology of sedimentary rocks: Austin, Texas, Hemphill, 182 p.

Hammes, U., 1997, Electrical imaging catalog: microresistivity images and core photos from fractured, karsted, and brecciated carbonate rocks: The University of Texas at Austin, Bureau of Economic Geology Geological Circular 97-2, 40 p.

Hogg, A. J. C., Sellier, E., and Jourdan, A. J., 1992, Cathodoluminescence of quartz cements in Brent Group sandstones, Alwyn South, UK North Sea, *in* Morton, A. C., Haszeldine, R. S., Giles, M. R., and Browns, S., eds., Geology of the Brent Group: Geological Society Special Publication No. 61, p. 421–440.

Kearney, M. W., 1983, Subsurface geology of the Silurian Medina and Clinton Groups, New York State: M. S. thesis, Southern Methodist University, 119 p.

Kulander, B. R, Dean, S. L., and Ward, B. J., Jr., 1990, Fractured core analysis: interpretation, logging, and use of natural and induced fractures in core: American Association of Petroleum Geologists Methods in Exploration Series, No. 8, 88 p.

Laubach, S. E., 1988, Subsurface fractures and their relationship to stress history in East Texas Basin sandstone: Tectonophysics, v. 156, p. 37–49.

Laubach, S. E., 1989, Paleostress directions from the preferred orientation of closed microfractures (fluid-inclusion planes) in sandstone, East Texas Basin, U.S.A.: Journal of Structural Geology, v. 11, no. 5, p. 603–611.

Laubach, S. E., 1992, Fracture networks in selected Cretaceous sandstones of the Green River and San Juan Basins, Wyoming, New Mexico, and Colorado, *in* Schmoker, J. W., Coalson, E. B., and Brown, C. A., eds., Geological studies relevant to horizontal drilling in western North America: Rocky Mountain Association of Geologists, p. 61–74.

Laubach, S. E., 1997, A method to detect natural fracture strike in sandstones: American Association of Petroleum Geologists Bulletin, v. 81, no. 4., 604–623.

Laubach, S. E., Baumgardner, R. W., Monson, E. R., Hunt, E., and Meador, K. J., 1988, Fracture detection in low-permeability reservoir sandstone: a comparison of BHTV and FMS logs to core: Society of Petroleum Engineers, SPE Paper 18119, p. 129–139.

Laubach, S. E., and Milliken, K. L., 1996, New fracture characterization methods for siliciclastic rocks, *in* Aubertin, M., Hassani, F., and Mitri, H., eds., Rock mechanics: tools and techniques: A.A. Balkema, Rotterdam, p. 1209–1213.

Marrett, R., 1997, Permeability, porosity and shear-wave anisotropy from scaling of open fracture populations, *in* Hoak, T. E., Klawitter, A. L., and Blomquist, P. R., eds., Fractured reservoirs: characteristics and modeling guidebook: Rocky Mountain Association of Geologists, p. 217–226.

Marrett, R., and Laubach, S. E., 1997, Diagenetic controls on fracture permeability and sealing: International Journal of Rock Mechanics and Mining Science, v. 34, nos. 3–4, p. 409–415 (on CD-ROM).

Marrett, R., Laubach, S. E., Rossen, W., Olson, J., and Lake, L., 1998, Integration of new fracture observation, characterization, and fluid-flow modeling technology (abs.): American Association of Petroleum Geologists, 1998 Annual Convention, Extended Abstracts, p. A431.

Martini, I. P., 1971, Regional analysis of sedimentology of Medina Formation (Silurian), Ontario and New York: American Association of Petroleum Geologists Bulletin, v. 55, no. 8, p. 1249–1261.

McCormac, M. P., Mychkovsky, G. O., Opritza, S. T., Riley, R. A., Wolfe, M. E., Larsen, G. E., and Baranoski, M. T., 1996, Play Scm: Lower Silurian Cataract/Medina Group ("Clinton") sandstone play, *in* Roen, J. B., and Walker, B. J., eds., The atlas of major Appalachian gas plays: West Virginia Geological and Economic Survey Publication V-25, p. 156–163.

Milliken, K. L, and Land, L. S., 1991, Reverse weathering, the carbonate-feldspar system, and porosity evolution during burial of sandstones (abs.): American Association of Petroleum Geologists Bulletin, v. 75, p. 636.

Milliken, K. L., 1994, The widespread occurrence of healed microfractures in siliciclastic rocks: evidence from scanned cathodoluminescence imaging, *in* Nelson, P. P., and Laubach, S. E., eds., Rock mechanics: models and measurements, challenges from industry: Rotterdam, A. A. Balkema, p. 825–832.

Nelson, R. A., Lenox, L. C., and Ward, B. J., 1987, Oriented core: its use, error, and uncertainty: American Association of Petroleum Geologists Bulletin, v. 71, p. 357–368.

Olson, J. E., Hennings, P. H., and Laubach, S. E., 1998 (in review), Integrating wellbore data and geomechanical modeling for effective characterization of naturally fractured reservoirs: EUROCK 98.

Overbey, W. K., Jr., and Henniger, B. R., 1971, History, development, and geology of oil fields in Hocking and Perry Counties, Ohio: American Association of Petroleum Geologists Bulletin, v. 55, no. 2, p. 183–203.

Parrish, J. B., and Lavin, P. M., 1982, Tectonic model for kimberlite emplacement in the Appalachian Plateau of Pennsylvania: Geology, v. 10, p. 344–347.

Piotrowski, R. G., 1981, Geology and natural gas production of the Lower Silurian Medina Group and equivalent rock units in Pennsylvania: Pennsylvania Bureau of Topographic and Geologic Survey, Fourth Series, Mineral Resources Report M82, 21 p.

Sipple, R. F., 1968, Sandstone petrology: evidence from luminescence petrography: Journal of Sedimentary Petrology, v. 38, p. 530–554.

Walker, G., and Burley, S., 1991, Luminescence petrography and spectroscopic studies of diagenetic minerals, *in* Barker, C. E., and Kopp, O. C., eds., Luminescence microscopy, quantitative and qualitative aspects: Tulsa, Oklahoma, SEPM (Society for Sedimentary Geology), p. 83–96.

Yacobi, B. G., and Holt, D. B., 1990, Cathodoluminescence microscopy of inorganic solids: New York, Plenum, 292 p.

Zagorski, W. A., 1991, Model of local and regional traps in the Lower Silurian Medina Sandstone Group Cooperstown gas field, Crawford and Venango Counties, Pennsylvania: M. S. thesis, University of Pittsburgh, 131 p.

Zinkernagel, U., 1978, Cathodoluminescence in quartz and its application to sandstone petrology: Contributions to Sedimentology, v. 8, 69 p.

Appendix 1. Miscellaneous notes from descriptions of Atlas Lucas No. 1 and Atlas Dayton No. 1 FMI logs.

Atlas Lucas No. 1

Depth (ft) from	To	Comments
5,359.0	6,366.0	Possible small faults-need high resolution copy of FMI for this region
5,934.0		Top of log
5,942.0	5,851.0	Karst
5,953.0	5,957.0	Karst
5,982.0	6,011.5	Thinly bedded
6,011.5		Thin shale
6,012.0	6,039.0	Thinly bedded with moderate shaly layers, ripples, many truncated
6,021.0		Ripple laminations, thinly bedded, highly resistive
6,039.0	6,052.0	Larger ripples/dunes; dip toward 180 degrees at top of sequence, amplitude of ripples increasing downward
6,043.0		Unconformity
6,047.0		Breccia
6,052.0	6,068.0	Transition back to thinly bedded, no ripples, very clean
6,068.0	6,095.8	Thinly bedded, with ripples, bioturbated, very tight material
6,068.0		Vuggy porosity in carbonate
6,095.8		Unconformity
6,096.0		Carbonate with chert nodules, thin shale more common toward base of section
6,096.8	6,146.0	Karsted carbonate with chert lenses, size of features increasing downward
6,146.0	6,208.0	Shale with sparse lenses of very tight material
6,146.0		Unconformity
6,146.1		Shale
6,201.3		Thin horizontal bed of very tight material, repeated at intervals downsection (ls)
6,208.0	6,228.0	Mostly shale
6,228.0	6,239.0	Flysh, more sand
6,229.2		Conformable stratal boundary, base of shale section
6,242.5	6,247.5	Fracture, N54E, vertical, tight
6,247.7		Thin horizontal bed of very tight material
6,252.4		Thin tight bed (ls)
6,255.0	6,256.0	Thinly bedded
6,257.0	6,262.0	Thinly bedded
6,264.0		Salt water (laterolog)
6,265.0		Thin gas-bearing unit
6,266.5		Vertical burrows
6,273.0	6,275.0	Vuggy porosity
6,280.0		Large truncated sand body, draped with mud, gas
6,281.0		Bioturbated
6,284.0		Fracture with conflicting dip from traces on opposite sides of hole, approximate strike N80W
6,288.5	6,295.0	Smeared FMI, large rugosity in caliper
6,290.0		Large rugosity in caliper, well bore enlarged
6,317.5		Fracture, N66E, 56NW, tightly mineralized
6,319.0	6,320.8	Tabular crossbeds, dip north
6,320.8		Unconformity
6,335.5	6,344.0	Ss, large ripples upper portion of sequence shaly, API almost zero
6,335.5		Unconformity, top of interval with liesegang bands
6,338.0		This is our core, azimuth 099
6,338.5		Still has some material visible in the hole, unsuccessful, azimuth 190
6,340.8		Fracture, N77E

Atlas Lucas No. 1 (cont.)

Depth (ft) from	To	Comments
6,341.4	6,343.8	Massive ss
6,341.5	6,343.8	The mineralized fracture that intersects our core labeled AL6342, N60W, 70SW
6,342.0		Distinct bedding, dipping to 340; this is the core fragment with the mineralized surface, azimuth 080
6,342.1		Distinct bedding, dipping to 341, core azimuth 190
6,342.8		Fracture, N50W, subvertical, partially open
6,343.8		Fracture, N68W, 56NE, synsedimentary, tight
6,345.0	6,346.0	Horizontal burrows
6,345.0		Horizontal burrows
6,347.0	6,353.0	Crossbeds and dipping beds
6,352.0		Two small normal faults, x-cutting, synsedimentary, N77E and N48W
6,356.0		Deformed bedding and breccia, probably with gouge, probable strike-slip fault, N87W, 69SW, gas
6,364.1		Core, azimuth 100
6,364.5		Unsuccessful core, azimuth 180
6,365.0	6,367.0	Clean sand, deep invasion, bedding and fracture porosity, fracture N86W, probably no gas
6,366.5		Core, azimuth 160
6,369.3	6,373.2	Gas
6,371.3		Core, azimuth 160
6,371.5		Core azimuth 090
6,380.0	6,387.3	Massive ss
6,381.3		Core with nick, azimuth 090
6,382.3		Nick, failed attempt
6,384.0	6,386.0	Partially bed bounded fracture, N40E, vertical
6,386.0	6,387.0	Bed-bounded fracture, N20E, subvertical
6,386.1		Core, azimuth 011
6,386.2		Core, azimuth 099, fractures N72W, very open, possible fracture N20E, mineralized
6,399.5		Bedding, dips toward 300, core, azimuth 244
6,400.0	6,410.0	Thinly bedded
6,400.0		Fracture, N59W, top of shale
6,409.0		Tight fracture, N9W, 67NE
6,411.0	6,414.3	Multiple, parallel fractures, N71E
6,411.0	6,418.0	Massive ss
6,412.0		Bedding dips toward 300, core azimuth 160
6,420.0	6,445.0	Thinly bedded flysch
6,445.0	6,447.6	Region of thicker beds
6,447.5		Top of Cabot Head Shale
6,448.0		Concretion
6,453.5		Old, mineralized fracture, N29W, 60NE
6,462.3		Core, azimuth 271
6,463.5		Core, azimuth 240
6,467.5		Core, azimuth 175
6,476.4	6,477.2	Gas, flow along bedding plane
6,477.2		Core, azimuth 100, massive ss
6,480.2		Top of Queenston shale
6,485.0	6,485.7	Fracture N40E, 71 SE
6,490.1		Core, azimuth 280, Queenston shale
6,490.2		Core, azimuth 280

Atlas Dayton No. 1

Depth (ft) from	To	Comments
3,412.0		No FMI information
6,130.0		FMI log begins at 6130 ft; the image is very noisy, but bedding is visible and is horizontal
6,142.0	6,144.5	
6,147.3	6,157.5	Vuggy porosity (karsted ls), many small dark ovoid shapes 20 -50 mm major axis
6,164.0		Bedding dips NE
6,172.5	6,176.3	Karst, larger dark ovoids, 60mm on major axis, high resistivity, possible oil
6,191.0		Bedding-plane porosity, gas
6,209.0	6,215.0	Ripples visible, current from SE
6,217.0	6,228.0	Shale interbeds, salt water
6,221.0		N58E
6,228.0	6,232.0	Ripples, noisy section
6,232.0		Beds dip NNE
6,240.0		Top of thin-bedded interval with shale
6,263.0		Top of sub-vertical fractures, strike N59E
6,269.7		Top of massive bed 1.5 ft thick
6,271.3		Top of thin-bedded interval, cherty dolomite
6,281.0	6,283.0	Chert nodules
6,303.0	6,336.0	Vuggy dolomite with nodular chert
6,318.0		Fracture N85E, 67SE
6,320.0	6,325.0	Subvertical fracture N39E, 84SE
6,333.0	6,338.0	Fracture N56E, 84NW
6,338.0	6,342.0	Crossbedding
6,342.0		N30W, 40NE bedding
6,347.0		Liesegang bands
6,353.0	6,361.0	Vertical fracture, N62E
6,364.0		Bedding dips N30W, 40NE
6,366.0		Breccia or conglomerate, large clasts (up to 3")
6,368.0	6,372.0	Gas
6,378.0		Series of bed-bounded fractures N60E, 60SE (some borehole ellipticity here, also significant drift)
6,386.0	6,390.0	Ripple laminations
6,395.0		Fault, N43W, 60SW
6,407.0		Top of shale sequence, fracture N28W
6,415.0		Sand lens N40W, borehole ellipticity significant
6,442.0	6,448.0	Thin-bedded, gas conducted by vertical fractures
6,448.5	6,450.0	Fractures N22W, thin-bedded, gas conducted by vertical fractures
6,452.0		Fractures, N22W and N68E, N68E are older and partially mineralized, N22 are younger and mostly open
6,464.0		Fractures N60E
6,476.0		Fractures N20W
6,481.0		Fracture N66E, 40SE, significant borehole ellipticity
6,482.0		Fracture N66E
6,512.0	6,515.0	Fractures N20E, 71SE
6,517.0	6,518.6	Group of reverse faults, N72E, SE, gas
6,518.0	6,523.0	Bedding, N50E, 55SE
6,519.0		Angular unconformity, dips south
6,526.0	6,561.0	Discontinuous, commonly bed-bounded, subvertical fractures
6,534.5		Syn-sedimentary fault

Atlas Dayton No. 1 (cont.)

Depth (ft) from	To	Comments
6,538.8	6539 .8	Fault, displacement is normal, 4" slight counterclockwise rotation of the footwall, gas directly above it
6,544.0		First cores look like three attempts at 350 (6544.5), 035 (6545.1), and 080 (6544.4), fractures, N70E
6,553.7	6,554.8	Large ripple with many laminated layers visible
6,555.4		Red shale core with green altered mineralization along fracture, azimuth 110. A fracture visible on FMI, N74E, 70SE
6,557.0	6,559.0	Fracture traces are anastomosing
6,564.8		Corehole at 085, beds horizontal, this is the site of core labeled 6568, another core attempt at 200 at 6566'. Beds dip shallowly to the east (maximum 20 degrees), and core is along strike
6,567.0	6,569.0	Two faults with visible vertical offset, older is N71E, 70 NW, is probably syn-sedimentary and is mostly mineralized, younger is N76E, 52SE, post-lithification and mostly open, both show small normal vertical slip
6,572.0	6,574.0	Another small fault with the same geometry as those just above it, but opposite kinematics, post-lithification
6,579.0		A core hole, azimuth 305
6,580.4		Another core hole, azimuth 245, almost in the direction of dip of laminations in a clearly laminated ss, this is the 6582' core, both cores are near the top of an interval with significant borehole ellipticity and drift
6,586.0	6,590.0	Another faulted region, the fault surface is N80E, 65NW, the kinematic sense here is normal, vertical displacement approximately 0.4 ft with possible slight rotation of the hanging wall counterclockwise
6,586.8		Core hole in an unlaminated region, azimuth 110
6,588.0	6,591.0	Vertical fracture, strike N60E
6,588.2		Core hole, azimuth 160 in a clearly laminated region, making it my bet for the 6590 core
6,593.0	6,594.0	Fault, N51E 80SE, brecciation/gouge visible, vertical displacement unknown from this information, but apparently multiple feet, post-lithification
6,596.0	6,608.0	Discontinuous vertical fractures with tips ultimately curving to parallel a planar fault with normal displacement, N48E, 86SE
6,610.4		Corehole for sample 6612 is immediately adjacent to a vertical fracture similar to the one described above, azimuth 250
6,613.7	6,614.8	Fault with very small normal displacement, N50E, 70SE, and the vertical fracture above it shows a similar pattern of tip curvature parallel to the fault, these fractures are propagating ahead of the drill bit
6,614.7	6,625.0	Vertical fractures, multiple
6,617.2		Corehole for sample 6619, azimuth 040, bedding is almost horizontal
6,621.3		Corehole for sample 6623, azimuth 245, almost parallel to dip of bedding
6,626.2		Corehole for sample 6628, azimuth 130, multiple fractures nearby of uncertain origin
6,639.2		Corehole, azimuth 310
6,640.5		Corehole for sample 6641, azimuth 130, parallel to dip direction
6,640.6	6,658.2	Cabot Head shale, borehole ellipticity high, vertical fractures striking N10E and N85E, some N39W (old, mineralized, very tight)
6,666.1		Corehole for sample 6668, azimuth 260
6,677.9		Corehole for sample 6680, azimuth 020
6,680.0		Top of Queenston shale, fractures strike 060, and are irregular in form
6,720.0		Corehole for sample 6722, azimuth 110

Appendix 2. Microfracture survey data from the Atlas Dayton No. 1 and Atlas Lucas No. 1 wells.

Atlas Dayton No. 1

Formation: Thorold
Depth: 6,566 ft
Image ID: AD6568 mosaic no. 1
View: Uphole
Azimuth reference: 85°
Area imaged: 5.43×10^6 μ²

Fracture		Strike (degrees)		Length		Maximum aperture		
Number	Category	Recorded	True	Image (mm)	Fracture (μ)	Image (mm)	Fracture (μ)	Area (μ²)
1	Ia+	21	64	55	275	1	5	687.5
2	Ia+	36	49	27	135	1	5	337.5
3	Ib	114	331	12	60	0.5	2.5	75
4	Ia+	20	65	87	435	0.6	3	652.5
5	Ib	146	299	17	85	0.25	1.25	53.125
6	Ia+	23	62	32	160	0.8	4	320
7	Ic	9	76	11	55	0.3	1.5	41.25
8	Id	30	55	25	125	0.3	1.5	93.75
9	Ic	103	342	19	95	0.7	3.5	166.25
10	Ib	27	58	11	55	0.7	3.5	96.25
11	Ib	27	58	12	60	1.1	5.5	165
12	Ib	27	58	6	30	0.8	4	60
13	Ib	226	219	7	35	1	5	87.5
14	Ia	56	29	48	240	0.2	1	120
15	Ib	26	59	3	15	0.4	2	15
16	Ib	68	17	15	75	0.4	2	75
17	Ib	22	63	15	75	0.5	2.5	93.75
18	Ib	120	325	31	155	0.4	2	155
19	Ic	125	320	14	70	0.2	1	35
20	Ia	125	320	26	130	0.2	1	65
21	Ia	137	308	17	85	1	5	212.5
22	Ic	116	329	21	105	0.4	2	105
23	Ic	116	329	22	110	0.3	1.5	82.5
24	Ic	140	305	19	95	0.3	1.5	71.25
25	Ia+	165	280	33	165	0.5	2.5	206.25
26	Ia+	157	288	30	150	0.4	2	150
27	II	162	283	7	35	0.3	1.5	26.25
28	Ib	162	283	37	185	0.2	1	92.5
29	Ia+	30	55	28	140	1	5	350
30	II	22	63	21	105	0.3	1.5	78.75
31	Ib	1	84	28	140	0.2	1	70
32	II	60	25	9	45	0.2	1	22.5
33	Ia+	168	277	46	230	0.2	1	115
34	Ia+	168	277	46	230	0.4	2	230
35	II	82	3	24	120	0.2	1	60
36	II	41	44	5	25	0.2	1	12.5
37	III	157	288	16	80	2.5	12.5	500
38	Ia+	85	0	80	400	5	25	5000
39	II	158	287	9	45	0.2	1	22.5
40	Ic	160	285	18	90	0.3	1.5	67.5
41	Ic	152	293	24	120	0.6	3	180
42	Ic	6	79	8	40	0.1	0.5	10
43	Ic	158	287	27	135	0.3	1.5	101.25

Appendix 2 (cont.)

Fracture		Strike (degrees)		Length		Maximum aperture		
Number	Category	Recorded	True	Image (mm)	Fracture (μ)	Image (mm)	Fracture (μ)	Area (μ^2)
44	Ic	30	55	30	150	0.1	0.5	37.5
45	Ic	108	337	18	90	0.1	0.5	22.5
46	Ic	86	359	26	130	0.1	0.5	32.5
47	Ic	86	359	37	185	0.1	0.5	46.25
48	Ic	40	45	39	195	0.1	0.5	48.75
49	Ic	172	273	38	190	0.1	0.5	47.5
50	Ia+	121	324	25	125	3	15	937.5
51	Ic	73	12	37	185	0.1	0.5	46.25
52	Ic	0	85	12	60	0.1	0.5	15
53	Ic	119	326	10	50	0.1	0.5	12.5
54	II	82	3	23	115	1	5	287.5
55	Ib	157	288	19	95	0.2	1	47.5
56	II	46	39	9	45	0.1	0.5	11.25
57	II	46	39	8	40	0.1	0.5	10
58	II	56	29	9	45	0.1	0.5	11.25
59	II	59	26	6	30	0.1	0.5	7.5
60	Ib	176	269	30	150	0.2	1	75
61	Ib	176	269	14	70	0.2	1	35
62	Ib	176	269	7	35	0.2	1	17.5
63	Ib	178	267	40	200	0.2	1	100
64	II	172	273	42	210	0.1	0.5	52.5
65	Ic	150	295	21	105	0.3	1.5	78.75
66	II	142	303	7	35	0.1	0.5	8.75
67	II	113	332	8	40	0.1	0.5	10
68	II	170	275	8	40	0.1	0.5	10
69	II	143	302	8	40	0.1	0.5	10
70	II	180	265	7	35	0.1	0.5	8.75
71	II	180	265	5	25	0.1	0.5	6.25
72	II	142	303	6	30	0.1	0.5	7.5
73	Ic	176	269	5	25	0.2	1	12.5
74	Ia	174	271	28	140	0.5	2.5	175
75	Ic	21	64	19	95	0.1	0.5	23.75
76	Ia+	27	58	42	210	0.1	0.5	52.5
77	II	27	58	4	20	0.1	0.5	5
78	II	67	18	5	25	0.2	1	12.5
79	II	18	67	14	70	0.1	0.5	17.5
80	Ic	34	51	40	200	0.4	2	200
81	Ia	39	46	41	205	0.2	1	102.5
82	Ic	175	270	29	145	0.2	1	72.5
83	Ic	144	301	22	110	0.1	0.5	27.5
84	II	156	289	9	45	0.1	0.5	11.25
85	II	45	40	16	80	0.1	0.5	20
86	II	156	289	7	35	0.1	0.5	8.75
87	II	149	296	9	45	0.1	0.5	11.25
88	II	32	53	13	65	0.3	1.5	48.75
89	II	75	10	8	40	0.45	2.25	45
90	Ib	172	273	8	40	0.3	1.5	30
91	II	72	13	6	30	0.22	1.1	16.5
92	II	72	13	5	25	0.8	4	50
93	II	160	285	11	55	0.7	3.5	96.25
94	II	90	355	8	40	0.45	2.25	45
95	II	145	300	11	55	0.38	1.9	52.25
96	II	99	346	7	35	0.5	2.5	43.75
97	II	94	351	5	25	0.45	2.25	28.125

Appendix 2 (cont.)

Fracture		Strike (degrees)		Length		Maximum aperture		
Number	Category	Recorded	True	Image (mm)	Fracture (μ)	Image (mm)	Fracture (μ)	Area (μ^2)
98	Ia+	16	69	60	300	0.18	0.9	135
99	II	81	4	10	50	0.22	1.1	27.5
100	II	172	273	8	40	0.22	1.1	22
101	II	81	4	17	85	0.6	3	127.5
102	Ia+	25	60	46	230	0.38	1.9	218.5
103	Ia+	18	67	28	140	0.22	1.1	77
104	Ia	21	64	32	160	0.38	1.9	152
105	Ia	20	65	25	125	0.38	1.9	118.75
106	Ia	20	65	36	180	0.45	2.25	202.5
107	Ia	22	63	16	80	0.18	0.9	36
108	Ia+	119	326	6	30	0.5	2.5	37.5
109	II	10	75	6	30	0.38	1.9	28.5
110	II	1	84	18	90	0.6	3	135
111	Ia+	20	65	60	300	0.5	2.5	375
112	Id	145	300	11	55	0.45	2.25	61.875
113	Ia+	32	53	54	270	0.9	4.5	607.5
114	II	100	345	12	60	0.38	1.9	57
115	II	103	342	15	75	1.3	6.5	243.75
116	II	101	344	15	75	1.2	6	225
117	II	4	81	5	25	0.7	3.5	43.75
118	II	101	344	8	40	0.9	4.5	90
119	II	165	280	5	25	0.38	1.9	23.75
120	II	29	56	5	25	0.38	1.9	23.75
121	Id	173	272	12	60	0.3	1.5	45
122	Id	180	265	23	115	0.3	1.5	86.25
123	Id	180	265	12	60	0.3	1.5	45
124	Id	4	81	20	100	0.3	1.5	75
125	Id	4	81	38	190	0.45	2.25	213.75
126	Id	152	293	21	105	0.22	1.1	57.75
127	Ic	81	4	9	45	6	30	675
128	Ia+	9	76	53	265	2.2	11	1457.5
129	Ic	120	325	11	55	0.3	1.5	41.25
130	Ic	102	343	7	35	0.2	1	17.5
131	Ic	96	349	5	25	0.2	1	12.5
132	Ic	103	342	10	50	0.1	0.5	12.5
133	Ic	108	337	12	60	0.7	3.5	105
134	Ic	108	337	7	35	0.9	4.5	78.75
135	Ic	180	265	4	20	0.6	3	30
136	Ic	4	81	5	25	0.9	4.5	56.25
137	III	73	12	33	165	4.2	21	1732.5
138	Ia	73	12	33	165	0.22	1.1	90.75
139	Ic	74	11	21	105	0.22	1.1	57.75
140	Id	120	325	8	40	0.2	1	20
141	Ic	125	320	25	125	0.3	1.5	93.75
142	Id	103	342	8	40	0.6	3	60
143	III	112	333	8	40	0.6	3	60
144	Ic	178	267	21	105	0.18	0.9	47.25
145	III	162	283	12	60	0.2	1	30
146	III	162	283	13	65	0.3	1.5	48.75
147	Id	73	12	16	80	0.3	1.5	60
148	Ia+	158	287	28	140	0.38	1.9	133
149	Id	102	343	9	45	0.2	1	22.5
150	Id	103	342	19	95	0.38	1.9	90.25
151	III	110	335	6	30	0.22	1.1	16.5

Appendix 2 (cont.)

Fracture		Strike (degrees)		Length		Maximum aperture		
Number	Category	Recorded	True	Image (mm)	Fracture (μ)	Image (mm)	Fracture (μ)	Area (μ^2)
152	Id	112	333	12	60	0.5	2.5	75
153	III	27	58	9	45	0.45	2.25	50.625
154	III	165	280	9	45	0.3	1.5	33.75
155	Ic	26	59	12	60	0.22	1.1	33
156	Ic	53	32	6	30	0.38	1.9	28.5
157	Ia+	120	325	33	165	0.3	1.5	123.75
158	Id	116	329	16	80	0.2	1	40
159	Id	3	82	6	30	0.14	0.7	10.5
160	Id	6	79	10	50	0.3	1.5	37.5
161	Ia+	4	81	15	75	0.3	1.5	56.25
162	Id	130	315	41	205	0.3	1.5	153.75
163	Id	124	321	36	180	0.14	0.7	63
164	Ia+	56	29	20	100	0.22	1.1	55
165	Id	138	307	12	60	0.3	1.5	45
166	Ib	4	81	8	40	0.8	4	80
167	Ib	180	265	15	75	0.5	2.5	93.75
168	Ib	7	78	11	55	0.3	1.5	41.25
169	Id	7	78	16	80	0.38	1.9	76
170	Id	7	78	15	75	0.38	1.9	71.25
171	Id	122	323	9	45	0.38	1.9	42.75
172	Id	156	289	14	70	0.16	0.8	28
173	Ia+	58	27	5	25	0.14	0.7	8.75
174	Id	110	335	8	40	0.3	1.5	30
175	Id	10	75	10	50	0.1	0.5	12.5
176	II	170	275	10	50	0.62	3.1	77.5
177	II	90	355	3	15	0.45	2.25	16.875
178	II	5	80	7	35	0.8	4	70
179	II	62	23	50	250	0.1	0.5	62.5
180	Ic	106	339	13	65	0.1	0.5	16.25
181	III	97	348	11	55	0.38	1.9	52.25
182	III	44	41	17	85	0.22	1.1	46.75
183	Id	156	289	4	20	0.3	1.5	15
184	III	13	72	80	400	0.38	1.9	380
185	Ia+	11	74	36	180	0.38	1.9	171
186	Id	175	270	15	75	0.22	1.1	41.25
187	Ib	79	6	14	70	0.5	2.5	87.5
188	Id	105	340	21	105	0.3	1.5	78.75
189	Ic	68	17	32	160	0.3	1.5	120
190	Ib	53	32	26	130	0.2	1	65
191	Id	150	295	23	115	0.1	0.5	28.75
192	Id	76	9	18	90	0.5	2.5	112.5
193	Ib	30	55	22	110	0.38	1.9	104.5
194	III	131	314	25	125	0.2	1	62.5
195	III	131	314	12	60	0.2	1	30
196	III	105	340	11	55	0.1	0.5	13.75
197	III	174	271	5	25	0.1	0.5	6.25
198	III	105	340	3	15	0.1	0.5	3.75
199	III	96	349	19	95	0.1	0.5	23.75
200	Ia+	10	75	25	125	0.14	0.7	43.75
201	Id	162	283	20	100	0.12	0.6	30
202	Id	112	333	11	55	0.16	0.8	22
203	III	175	270	10	50	0.1	0.5	12.5
204	III	170	275	11	55	0.2	1	27.5
205	Id	175	270	21	105	0.38	1.9	99.75

Appendix 2 (cont.)

Fracture		Strike (degrees)		Length		Maximum aperture		
Number	Category	Recorded	True	Image (mm)	Fracture (μ)	Image (mm)	Fracture (μ)	Area (μ^2)
206	Id	128	317	20	100	0.3	1.5	75
207	III	65	20	9	45	0.6	3	67.5
208	Id	24	61	18	90	0.45	2.25	101.25
209	Id	34	51	8	40	0.3	1.5	30
210	III	15	70	18	90	0.9	4.5	202.5
211	III	134	311	4	20	0.3	1.5	15
212	III	130	315	5	25	0.4	2	25
213	III	26	59	28	140	0.45	2.25	157.5
214	Id	42	43	19	95	0.3	1.5	71.25
215	Id	70	15	17	85	0.38	1.9	80.75
216	Id	20	65	6	30	0.22	1.1	16.5
217	Id	175	270	8	40	0.2	1	20
218	III	117	328	34	170	0.22	1.1	93.5
219	II	20	65	7	35	0.2	1	17.5
220	II	160	285	7	35	0.3	1.5	26.25
221	Ia	161	284	9	45	0.3	1.5	33.75
222	II	122	323	37	185	0.7	3.5	323.75
223	Id	132	313	9	45	0.3	1.5	33.75
224	Id	146	299	28	140	0.7	3.5	245
225	Id	1	84	20	100	0.7	3.5	175
226	Id	24	61	25	125	0.2	1	62.5
227	Id	83	2	10	50	0.1	0.5	12.5
228	Id	125	320	38	190	0.16	0.8	76
229	Ia+	63	22	27	135	0.1	0.5	33.75
230	Ia	61	24	97	485	0.16	0.8	194
231	Id	121	324	32	160	1.8	9	720
232	II	128	317	15	75	0.8	4	150
233	III	125	320	6	30	0.3	1.5	22.5
234	III	30	55	10	50	0.2	1	25
235	II	128	317	10	50	0.4	2	50
236	III	35	50	6	30	0.4	2	30
237	Ia+	2	83	21	105	0.16	0.8	42
238	Ic	90	355	4	20	0.4	2	20
239	Ic	57	28	7	35	0.4	2	35
240	Ic	62	23	12	60	0.18	0.9	27
241	Id	84	1	27	135	0.3	1.5	101.25
242	Ic	58	27	12	60	0.4	2	60
243	Id	54	31	14	70	0.4	2	70
244	Ia+	35	50	21	105	0.2	1	52.5
245	II	90	355	11	55	0.1	0.5	13.75
246	Ic	64	21	13	65	0.1	0.5	16.25
247	Ic	110	335	8	40	0.1	0.5	10
248	Ic	26	59	6	30	0.1	0.5	7.5
249	Ib	20	65	30	150	0.3	1.5	112.5
250	Ib	130	315	11	55	0.3	1.5	41.25
251	Ib	163	282	22	110	0.3	1.5	82.5
252	Ib	163	282	18	90	0.38	1.9	85.5
253	Ib	153	292	8	40	0.2	1	20
254	Id	22	63	12	60	0.3	1.5	45
255	Id	20	65	12	60	0.3	1.5	45
256	Ib	168	277	28	140	0.3	1.5	105
257	Id	72	13	16	80	0.1	0.5	20
258	Ia+	167	278	35	175	0.38	1.9	166.25
259	II	53	32	6	30	0.1	0.5	7.5

Appendix 2 (cont.)

Fracture		Strike (degrees)		Length		Maximum aperture		
Number	Category	Recorded	True	Image (mm)	Fracture (μ)	Image (mm)	Fracture (μ)	Area (μ^2)
260	II	42	43	13	65	0.1	0.5	16.25
261	II	37	48	11	55	0.1	0.5	13.75
262	II	40	45	13	65	0.1	0.5	16.25
263	II	153	292	9	45	0.1	0.5	11.25
264	II	142	303	9	45	0.1	0.5	11.25
265	II	156	289	9	45	0.1	0.5	11.25
266	II	40	45	10	50	0.1	0.5	12.5
267	II	40	45	10	50	0.1	0.5	12.5
268	II	40	45	12	60	0.1	0.5	15
269	II	110	335	28	140	0.3	1.5	105
270	II	127	318	40	200	0.4	2	200
271	Ia	18	67	30	150	0.22	1.1	82.5
272	Id	127	318	15	75	0.6	3	112.5
273	Ib	28	57	20	100	0.62	3.1	155
274	Id	20	65	12	60	0.3	1.5	45
275	Id	130	315	20	100	0.38	1.9	95
276	Id	47	38	9	45	0.14	0.7	15.75
277	Id	37	48	28	140	0.22	1.1	77
278	Id	52	33	9	45	0.18	0.9	20.25
279	Id	140	305	13	65	0.2	1	32.5
280	Id	10	75	12	60	0.38	1.9	57
281	III	70	15	21	105	0.2	1	52.5
282	III	104	341	8	40	0.3	1.5	30
283	III	146	299	6	30	0.4	2	30
284	III	86	359	6	30	0.3	1.5	22.5
285	III	146	299	4	20	0.4	2	20
286	Id	105	340	6	30	0.3	1.5	22.5
287	Id	96	349	10	50	0.38	1.9	47.5
288	Id	95	350	35	175	0.2	1	87.5
289	Id	110	335	30	150	0.3	1.5	112.5
290	Id	108	337	26	130	0.22	1.1	71.5
291	Id	108	337	26	130	0.38	1.9	123.5
292	Id	90	355	17	85	0.5	2.5	106.25
293	Ia+	10	75	45	225	0.45	2.25	253.125
294	Ia+	25	60	9	45	0.22	1.1	24.75
295	Ia+	28	57	15	75	0.2	1	37.5
296	Ia+	100	345	27	135	0.32	1.6	108
297	Ia+	112	333	38	190	0.62	3.1	294.5
298	Id	106	339	14	70	0.4	2	70
299	Id	53	32	14	70	0.3	1.5	52.5
300	Ia+++	14	71	600	3000	8	40	60000
301	Id	158	287	7	35	0.3	1.5	26.25
302	Id	158	287	9	45	0.3	1.5	33.75
303	Id	158	287	12	60	0.3	1.5	45
304	Id	158	287	18	90	0.3	1.5	67.5
305	Id	145	300	14	70	0.3	1.5	52.5
306	Id	98	347	14	70	0.38	1.9	66.5
307	Id	10	75	6	30	0.38	1.9	28.5
308	Id	18	67	8	40	0.3	1.5	30
309	Id	15	70	10	50	0.3	1.5	37.5
310	Id	10	75	13	65	0.3	1.5	48.75
311	Ia+	17	68	34	170	0.32	1.6	136
312	Ia+	0	85	11	55	0.32	1.6	44
313	Id	178	267	27	135	0.3	1.5	101.25

Appendix 2 (cont.)

Fracture		Strike (degrees)		Length		Maximum aperture		
Number	Category	Recorded	True	Image (mm)	Fracture (μ)	Image (mm)	Fracture (μ)	Area (μ^2)
314	Id	24	61	30	150	0.3	1.5	112.5
315	Id	42	43	8	40	0.1	0.5	10
316	Id	30	55	22	110	0.2	1	55
317	Id	20	65	15	75	0.1	0.5	18.75
318	Id	82	3	14	70	0.5	2.5	87.5
319	Id	63	22	27	135	0.3	1.5	101.25
320	Id	74	11	33	165	0.38	1.9	156.75
321	Id	124	321	22	110	0.2	1	55
322	Id	43	42	29	145	0.2	1	72.5
323	Id	48	37	24	120	0.2	1	60
324	Id	14	71	21	105	0.2	1	52.5
325	II	160	285	8	40	0.2	1	20
326	II	162	283	9	45	0.3	1.5	33.75
327	II	161	284	9	45	0.3	1.5	33.75
328	II	80	5	8	40	0.3	1.5	30
329	Ia+	95	350	13	65	0.4	2	65
330	Id	0	85	8	40	0.3	1.5	30
331	Id	9	76	11	55	0.3	1.5	41.25
332	Id	0	85	8	40	0.3	1.5	30
333	Id	72	13	14	70	0.3	1.5	52.5
334	Id	2	83	37	185	0.3	1.5	138.75
335	Id	43	42	28	140	0.3	1.5	105
336	Id	70	15	18	90	0.3	1.5	67.5
337	Ia+	15	70	41	205	0.3	1.5	153.75
338	Ia+	73	12	28	140	0.22	1.1	77
339	Id	74	11	12	60	0.2	1	30
340	Id	108	337	7	35	0.3	1.5	26.25
341	Id	65	20	5	25	0.3	1.5	18.75
342	Id	174	271	27	135	0.22	1.1	74.25
343	Id	172	273	26	130	0.22	1.1	71.5
344	Id	172	273	17	85	0.45	2.25	95.625
345	Id	30	55	9	45	0.3	1.5	33.75
346	II	26	59	7	35	0.18	0.9	15.75
347	II	8	77	12	60	0.18	0.9	27
348	II	12	73	9	45	0.16	0.8	18
349	Id	42	43	22	110	0.18	0.9	49.5
350	Id	160	285	10	50	0.14	0.7	17.5
351	Id	55	30	12	60	0.12	0.6	18
352	Id	158	287	12	60	0.3	1.5	45
353	Id	159	286	14	70	0.12	0.6	21
354	Id	62	23	12	60	0.16	0.8	24
355	Id	11	74	12	60	0.16	0.8	24
356	Id	31	54	11	55	1.4	7	192.5
357	II	60	25	10	50	1.8	9	225
358	II	77	8	21	105	0.62	3.1	162.75
359	II	20	65	13	65	0.9	4.5	146.25
360	Id	20	65	20	100	0.1	0.5	25
361	Id	162	283	11	55	0.16	0.8	22
362	Id	174	271	18	90	0.16	0.8	36
363	Id	134	311	20	100	0.2	1	50
364	Ia+	85	0	28	140	0.38	1.9	133
365	Ia+	52	33	78	390	0.18	0.9	175.5
366	Id	33	52	43	215	0.12	0.6	64.5
367	Id	17	68	7	35	0.22	1.1	19.25

Appendix 2 (cont.)

Fracture		Strike (degrees)		Length		Maximum aperture		
Number	Category	Recorded	True	Image (mm)	Fracture (μ)	Image (mm)	Fracture (μ)	Area (μ^2)
368	Id	56	29	26	130	0.38	1.9	123.5
369	Id	158	287	11	55	0.3	1.5	41.25
370	Id	171	274	21	105	0.3	1.5	78.75
371	Id	2	83	11	55	0.22	1.1	30.25
372	Ia+	18	67	17	85	0.3	1.5	63.75
373	Id	138	307	20	100	0.4	2	100
374	Id	17	68	25	125	0.3	1.5	93.75
375	II	108	337	18	90	0.6	3	135
376	II	163	282	16	80	0.3	1.5	60
377	II	3	82	10	50	0.3	1.5	37.5
378	II	18	67	8	40	0.5	2.5	50
379	II	125	320	6	30	0.7	3.5	52.5
380	II	173	272	7	35	0.45	2.25	39.375
381	Id	76	9	20	100	0.4	2	100
382	Id	60	25	22	110	0.38	1.9	104.5
383	Id	3	82	22	110	0.4	2	110
384	Id	60	25	9	45	0.3	1.5	33.75
385	Id	166	279	6	30	0.22	1.1	16.5
386	II	20	65	9	45	0.4	2	45
387	Id	42	43	12	60	0.22	1.1	33
388	Id	3	82	9	45	0.3	1.5	33.75
389	Id	106	339	20	100	0.3	1.5	75
390	Id	96	349	22	110	0.38	1.9	104.5
391	II	110	335	9	45	0.22	1.1	24.75
392	II	152	293	18	90	0.4	2	90
393	Ic	135	310	7	35	0.38	1.9	33.25
394	Ic	158	287	11	55	0.22	1.1	30.25
395	Ic	164	281	11	55	0.2	1	27.5
396	Ic	166	279	10	50	0.16	0.8	20
397	Ic	100	345	19	95	0.12	0.6	28.5
398	III	100	345	10	50	0.2	1	25
399	Ic	5	80	8	40	0.45	2.25	45
400	Ia++	11	74	130	650	1.5	7.5	2437.5
401	III	11	74	18	90	0.14	0.7	31.5
402	III	47	38	18	90	0.18	0.9	40.5
403	II	38	47	14	70	0.3	1.5	52.5
404	Id	38	47	13	65	0.22	1.1	35.75
405	Ic	45	40	7	35	0.3	1.5	26.25
406	II	42	43	12	60	0.22	1.1	33
407	II	95	350	9	45	0.2	1	22.5
408	II	41	44	6	30	0.18	0.9	13.5
409	II	40	45	11	55	0.22	1.1	30.25
410	II	65	20	11	55	0.2	1	27.5
411	II	15	70	24	120	0.3	1.5	90
412	II	11	74	21	105	0.2	1	52.5
413	II	20	65	13	65	0.14	0.7	22.75
414	II	44	41	10	50	0.18	0.9	22.5
415	Ic	24	61	12	60	0.45	2.25	67.5
416	III	157	288	22	110	0.1	0.5	27.5
417	Ic	27	58	4	20	0.2	1	10
418	Ic	78	7	16	80	0.3	1.5	60
419	II	11	74	8	40	0.22	1.1	22
420	II	6	79	10	50	0.3	1.5	37.5
421	Ic	10	75	7	35	0.3	1.5	26.25

Appendix 2 (cont.)

Fracture		Strike (degrees)		Length		Maximum aperture		
Number	Category	Recorded	True	Image (mm)	Fracture (μ)	Image (mm)	Fracture (μ)	Area (μ^2)
422	Id	6	79	7	35	0.12	0.6	10.5
423	Id	6	79	10	50	0.14	0.7	17.5
424	Ic	1	84	28	140	0.16	0.8	56
425	Ic	5	80	28	140	0.38	1.9	133
426	III	58	27	13	65	0.3	1.5	48.75
427	Ic	99	346	19	95	0.2	1	47.5
428	Ic	131	314	12	60	0.38	1.9	57
429	Ic	80	5	23	115	0.4	2	115
430	Ic	2	83	42	210	0.2	1	105
431	II	8	77	30	150	0.1	0.5	37.5
432	Ic	10	75	35	175	0.1	0.5	43.75
433	II	100	345	12	60	0.1	0.5	15
434	Ic	44	41	30	150	0.1	0.5	37.5
435	Ic	94	351	26	130	0.1	0.5	32.5
436	Ic	75	10	21	105	0.38	1.9	99.75
437	Id	103	342	26	130	0.1	0.5	32.5
438	III	3	82	10	50	0.22	1.1	27.5
439	II	104	341	15	75	0.4	2	75
440	II	150	295	14	70	0.3	1.5	52.5
441	II	110	335	5	25	0.22	1.1	13.75
442	Ic	70	15	22	110	0.12	0.6	33
443	Ic	64	21	15	75	0.2	1	37.5
444	II	23	62	7	35	0.45	2.25	39.375
445	II	24	61	10	50	0.3	1.5	37.5
446	II	11	74	7	35	0.22	1.1	19.25
447	II	55	30	8	40	0.12	0.6	12
448	II	99	346	12	60	0.2	1	30
449	II	98	347	12	60	0.45	2.25	67.5
450	Id	139	306	26	130	0.3	1.5	97.5
451	Id	141	304	5	25	0.18	0.9	11.25
452	Id	140	305	3	15	0.12	0.6	4.5
453	Id	137	308	11	55	0.14	0.7	19.25
454	II	22	63	10	50	0.22	1.1	27.5
455	II	33	52	14	70	0.22	1.1	38.5
456	II	121	324	12	60	1.2	6	180
457	II	117	328	24	120	1.8	9	540
458	II	74	11	15	75	0.7	3.5	131.25
459	Id	174	271	15	75	0.9	4.5	168.75
460	Id	142	303	13	65	0.14	0.7	22.75
461	Id	99	346	18	90	0.14	0.7	31.5
462	II	98	347	10	50	0.14	0.7	17.5
463	II	99	346	9	45	0.14	0.7	15.75
464	II	119	326	6	30	0.14	0.7	10.5
465	II	90	355	5	25	0.16	0.8	10
466	Id	52	33	20	100	0.1	0.5	25
467	III	28	57	8	40	0.1	0.5	10
468	III	35	50	11	55	0.12	0.6	16.5
469	III	50	35	8	40	0.1	0.5	10
470	III	50	35	6	30	0.1	0.5	7.5
471	II	30	55	15	75	1.3	6.5	243.75
472	II	154	291	19	95	0.38	1.9	90.25
473	II	66	19	8	40	0.38	1.9	38
474	II	66	19	6	30	0.45	2.25	33.75
475	II	161	284	3	15	0.38	1.9	14.25

Fracture		Strike (degrees)		Length		Maximum aperture		
Number	Category	Recorded	True	Image (mm)	Fracture (μ)	Image (mm)	Fracture (μ)	Area (μ^2)
476	II	170	275	7	35	0.38	1.9	33.25
477	II	24	61	12	60	0.3	1.5	45
478	II	58	27	12	60	0.22	1.1	33
479	II	34	51	14	70	0.3	1.5	52.5
480	II	49	36	20	100	0.2	1	50
481	II	9	76	15	75	0.18	0.9	33.75
482	II	46	39	10	50	0.22	1.1	27.5
483	Ia	172	273	11	55	0.22	1.1	30.25
484	Ic	181	264	20	100	0.2	1	50
485	Ia	171	274	15	75	0.3	1.5	56.25
486	Ic	138	307	12	60	0.22	1.1	33
487	Ia	90	355	9	45	0.2	1	22.5
488	Id	90	355	8	40	0.2	1	20
489	Ia	90	355	6	30	0.2	1	15
490	Ia+	6	79	52	260	4.2	21	2730
					Total fracture area (μ^2):			**109,015.13**

Atlas Dayton No. 1

Formation: Grimsby
Depth: 6,588 ft
Image ID: AD6590c thin section
View: Uphole
Azimuth reference: 67°
Area imaged: 4.64×10^6 μ^2

Fracture		Strike (degrees)		Length		Maximum aperture		
Number	Category	Recorded	True	Image (mm)	Fracture (μ)	Image (mm)	Fracture (μ)	Area (μ^2)
1	IB	153	274	14	70	0.75	3.75	131.25
2	IB	128	299	14	70	0.62	3.1	108.5
3	IB	130	297	21	105	2.65	13.25	695.625
4	IB	130	297	20	100	0.95	4.75	237.5
5	III	17	50	10	50	1.75	8.75	218.75
6	IB	130	297	22	110	1.15	5.75	316.25
7	IB	133	294	14	70	0.62	3.1	108.5
8	IB	131	296	17	85	0.75	3.75	159.375
9	IC	87	340	20	100	0.265	1.325	66.25
10	IA+	176	251	30	150	0.62	3.1	232.5
11	IA	29	38	40	200	0.75	3.75	375
12	IA	156	271	35	175	0.33	1.65	144.375
13	IC	130	297	8	40	0.33	1.65	33
14	IC	130	297	11	55	0.265	1.325	36.4375
15	IC	121	306	9	45	0.4	2	45
16	ID	40	27	12	60	0.5	2.5	75
17	IA+	84	343	40	200	0.4	2	200
18	IA+	81	346	36	180	0.62	3.1	279
19	IA+	66	1	55	275	0.4	2	275
20	ID	72	355	25	125	0.33	1.65	103.125
21	IC	94	333	64	320	0.62	3.1	496
22	II	73	354	43	215	0.62	3.1	333.25
23	II	52	15	30	150	1.75	8.75	656.25
24	II	164	263	15	75	1.75	8.75	328.125
25	ID	52	15	11	55	0.4	2	55
26	IC	172	255	39	195	0.4	2	195
27	II	128	299	22	110	0.5	2.5	137.5
28	II	140	287	18	90	0.75	3.75	168.75
29	II	138	289	20	100	1.75	8.75	437.5
30	II	97	330	7	35	0.33	1.65	28.875
31	II	55	12	31	155	0.33	1.65	127.875
32	II	94	333	16	80	0.5	2.5	100
33	II	101	326	21	105	0.115	0.575	30.1875
34	II	101	326	24	120	0.265	1.325	79.5
35	II	101	326	23	115	0.14	0.7	40.25
36	IC	69	358	28	140	0.33	1.65	115.5
37	IA	93	334	16	80	0.62	3.1	124
38	IA	57	10	15	75	0.4	2	75
39	IA	16	51	30	150	0.4	2	150
40	IB	39	28	24	120	0.4	2	120
41	ID	132	295	15	75	0.4	2	75
42	ID	144	283	25	125	0.5	2.5	156.25
43	IB	96	331	53	265	0.265	1.325	175.5625

Appendix 2 (cont.)

Fracture		Strike (degrees)		Length		Maximum aperture		
Number	Category	Recorded	True	Image (mm)	Fracture (μ)	Image (mm)	Fracture (μ)	Area (μ^2)
44	II	41	26	18	90	0.4	2	90
45	IC	41	26	53	265	0.4	2	265
46	IC	39	28	48	240	0.4	2	240
47	IA	34	33	21	105	0.265	1.325	69.5625
48	II	60	7	15	75	0.4	2	75
49	II	55	12	7	35	0.62	3.1	54.25
50	II	140	287	30	150	0.5	2.5	187.5
51	II	169	258	21	105	1.15	5.75	301.875
52	IA+	45	22	89	445	0.5	2.5	556.25
53	IA	103	324	19	95	0.5	2.5	118.75
54	IA	90	337	28	140	0.33	1.65	115.5
55	IB	12	55	15	75	0.5	2.5	93.75
56	IC	133	294	52	260	0.95	4.75	617.5
57	ID	143	284	43	215	3.3	16.5	1773.75
58	IC	70	357	16	80	0.4	2	80
59	IC	150	277	20	100	0.62	3.1	155
60	IB	65	2	10	50	0.33	1.65	41.25
61	IA	52	15	63	315	1.4	7	1102.5
62	ID	152	275	34	170	0.62	3.1	263.5
63	ID	41	26	20	100	0.95	4.75	237.5
64	IB	80	347	17	85	0.62	3.1	131.75
65	IC	62	5	19	95	0.215	1.075	51.0625
66	IA	148	279	24	120	0.4	2	120
67	IB	14	53	37	185	0.33	1.65	152.625
68	ID	52	15	39	195	0.62	3.1	302.25
69	ID	112	315	18	90	0.33	1.65	74.25
70	ID	24	43	20	100	0.33	1.65	82.5
71	IB	32	35	21	105	0.33	1.65	86.625
72	ID	66	1	13	65	0.33	1.65	53.625
73	IA+	143	284	92	460	0.4	2	460
74	ID	152	275	19	95	0.265	1.325	62.9375
75	ID	90	337	11	55	0.215	1.075	29.5625
76	IC	335	92	21	105	1.15	5.75	301.875
77	IC	50	17	26	130	0.33	1.65	107.25
78	IB	120	307	29	145	0.175	0.875	63.4375
79	IA	95	332	42	210	0.62	3.1	325.5
80	IB	106	321	17	85	0.33	1.65	70.125
81	IB	91	336	15	75	0.265	1.325	49.6875
82	IB	128	299	9	45	0.5	2.5	56.25
83	ID	68	359	20	100	0.4	2	100
84	IA	55	12	27	135	0.4	2	135
85	IC	112	315	30	150	0.4	2	150
86	IB	65	2	31	155	0.5	2.5	193.75
87	IA	80	347	22	110	0.215	1.075	59.125
88	ID	179	248	13	65	0.33	1.65	53.625
89	ID	179	248	9	45	0.33	1.65	37.125
90	ID	179	248	23	115	0.265	1.325	76.1875
91	ID	179	248	34	170	0.265	1.325	112.625
92	ID	179	248	19	95	0.4	2	95
93	IB	174	253	41	205	0.5	2.5	256.25
94	IB	134	293	40	200	1.75	8.75	875
95	III	103	324	19	95	0.33	1.65	78.375
96	III	125	302	20	100	0.265	1.325	66.25
97	IB	67	0	14	70	0.33	1.65	57.75

Appendix 2 (cont.)

Fracture		Strike (degrees)		Length		Maximum aperture		
Number	Category	Recorded	True	Image (mm)	Fracture (μ)	Image (mm)	Fracture (μ)	Area (μ^2)
98	IB	159	268	18	90	1.75	8.75	393.75
99	ID	87	340	20	100	0.75	3.75	187.5
100	ID	87	340	22	110	0.33	1.65	90.75
101	ID	88	339	21	105	0.33	1.65	86.625
102	ID	81	346	23	115	0.265	1.325	76.1875
103	III	138	289	8.5	42.5	0.5	2.5	53.125
104	IB	116	311	8	40	0.75	3.75	75
105	IB	40	27	7	35	0.4	2	35
106	IA	40	27	10	50	0.4	2	50
107	IC	75	352	47	235	0.62	3.1	364.25
108	IC	78	349	23	115	0.265	1.325	76.1875
109	ID	118	309	42	210	0.75	3.75	393.75
110	IB	15	52	58	290	0.215	1.075	155.875
111	IB	164	263	37	185	1.4	7	647.5
112	IC	128	299	21	105	0.4	2	105
113	ID	42	25	13	65	0.75	3.75	121.875
114	II	156	271	20	100	1.75	8.75	437.5
115	ID	76	351	21	105	0.265	1.325	69.5625
116	ID	78	349	18	90	0.215	1.075	48.375
117	IC	87	340	27	135	0.4	2	135
118	IC	70	357	43	215	5	25	2687.5
119	ID	135	292	14	70	0.4	2	70
120	ID	130	297	48	240	2.65	13.25	1590
121	IC	65	2	37	185	0.265	1.325	122.5625
122	IC	159	268	31	155	0.14	0.7	54.25
123	IB	38	29	43	215	0.5	2.5	268.75
124	ID	30	37	53	265	0.4	2	265
125	ID	21	46	50	250	0.4	2	250
126	ID	16	51	19	95	0.4	2	95
127	ID	63	4	42	210	0.14	0.7	73.5
128	ID	53	14	48	240	0.175	0.875	105
129	IA+	138	289	137	685	3.3	16.5	5651.25
130	IB	72	355	27	135	0.175	0.875	59.0625
131	IA	72	355	29	145	0.265	1.325	96.0625
132	IA	140	287	26	130	0.4	2	130
133	IA	140	287	11	55	0.33	1.65	45.375
134	IC	36	31	32	160	1.4	7	560
135	IC	40	27	10	50	0.14	0.7	17.5
136	ID	22	45	14	70	0.215	1.075	37.625
137	ID	34	33	30	150	0.215	1.075	80.625
138	IB	78	349	24	120	0.5	2.5	150
139	ID	5	62	18	90	0.5	2.5	112.5
140	IB	154	273	28	140	0.33	1.65	115.5
141	IB	158	269	33	165	0.4	2	165
142	IB	146	281	35	175	0.62	3.1	271.25
143	IB	140	287	35	175	0.5	2.5	218.75
144	IB	165	262	20	100	0.4	2	100
145	II	148	279	15	75	0.33	1.65	61.875
146	IA	134	293	26	130	0.5	2.5	162.5
147	IB	38	29	19	95	0.4	2	95
148	IB	38	29	9	45	0.265	1.325	29.8125
149	IB	38	29	17	85	0.4	2	85
150	IB	38	29	17	85	0.75	3.75	159.375
151	IB	101	326	27	135	0.62	3.1	209.25

Appendix 2 (cont.)

Fracture		Strike (degrees)		Length		Maximum aperture		
Number	Category	Recorded	True	Image (mm)	Fracture (μ)	Image (mm)	Fracture (μ)	Area (μ^2)
152	II	114	313	9	45	0.265	1.325	29.8125
153	ID	132	295	5	25	0.5	2.5	31.25
154	ID	122	305	18	90	0.4	2	90
155	ID	156	271	27	135	0.265	1.325	89.4375
156	ID	155	272	33	165	0.175	0.875	72.1875
157	ID	155	272	10	50	0.62	3.1	77.5
158	ID	165	262	15	75	0.33	1.65	61.875
159	IB	143	284	12	60	0.33	1.65	49.5
160	IB	158	269	22	110	0.62	3.1	170.5
161	IB	4	63	24	120	0.33	1.65	99
162	IA	163	264	32	160	0.4	2	160
163	IA	194	233	52	260	0.75	3.75	487.5
164	ID	141	286	29	145	0.14	0.7	50.75
165	ID	180	247	47	235	0.5	2.5	293.75
166	ID	165	262	37	185	0.265	1.325	122.5625
167	ID	155	272	43	215	0.4	2	215
168	ID	117	310	13	65	0.4	2	65
169	ID	156	271	50	250	0.4	2	250
170	ID	156	271	19	95	0.4	2	95
171	ID	174	253	10	50	0.75	3.75	93.75
172	ID	175	252	8	40	0.62	3.1	62
173	IB	32	35	21	105	0.5	2.5	131.25
174	IB	32	35	7	35	0.4	2	35
175	ID	122	305	12	60	0.33	1.65	49.5
176	IB	90	337	15	75	0.4	2	75
177	ID	90	337	16	80	0.62	3.1	124
178	ID	90	337	12	60	0.33	1.65	49.5
179	ID	31	36	17	85	0.215	1.075	45.6875
180	IB	33	34	33	165	0.4	2	165
181	IA	92	335	19	95	0.4	2	95
182	IB	116	311	18	90	0.5	2.5	112.5
183	IA+	136	291	51	255	0.4	2	255
184	IA	31	36	30	150	0.4	2	150
185	IB	136	291	23	115	0.4	2	115
186	II	90	337	46	230	0.215	1.075	123.625
187	IA	26	41	28	140	0.265	1.325	92.75
188	IB	121	306	15	75	1.15	5.75	215.625
189	IA	90	337	8	40	0.62	3.1	62
190	ID	75	352	30	150	0.265	1.325	99.375
191		73	354	28	140	0.215	1.075	75.25
192		73	354	20	100	0.115	0.575	28.75
193		119	308	28	140	0.075	0.375	26.25
194		90	337	6	30	0.215	1.075	16.125
						Total fracture area (μ^2):		**42,017.88**

Atlas Dayton No. 1

Formation: Grimsby
Depth: 6,610.5 ft
Image ID: AD6612 scanline no. 1
View: Downhole
Azimuth reference: 24°
Area imaged: 1.17×10^6 μ^2

Fracture		Strike (degrees)		Length		Maximum aperture		
Number	Category	Recorded	True	Image (mm)	Fracture (μ)	Image (mm)	Fracture (μ)	Area (μ^2)
1	ID	149	173	7	35	0.62	3.1	54.25
2	IC	43	67	7	35	0.14	0.7	12.25
3	IC	57	81	13	65	0.4	2	65
4	IA	81	105	18	90	0.33	1.65	74.25
5	IC	100	124	12	60	0.4	2	60
6	IC	81	105	21	105	3.3	16.5	866.25
7	IC	88	112	20	100	0.215	1.075	53.75
8	IC	40	64	7	35	0.115	0.575	10.0625
9	IA	31	55	19	95	0.95	4.75	225.625
10	IC	161	185	21	105	2.15	10.75	564.375
11	IA	36	60	15	75	0.5	2.5	93.75
12	IB	36	60	22	110	0.265	1.325	72.875
13	IB	81	105	10	50	0.115	0.575	14.375
14	IB	46	70	9	45	14	70	1575
15	IA+	59	83	31	155	0.33	1.65	127.875
16	II	106	130	7	35	0.33	1.65	28.875
17	II	163	187	3	15	0.745	3.725	27.9375
18	S	125	149	66	330	0.4	2	330
19	III	53	77	8	40	0.215	1.075	21.5
20	IA	34	58	16	80	1.4	7	280
21	ID	9	33	11	55	0.265	1.325	36.4375
22	ID	77	101	12	60	0.265	1.325	39.75
23	ID	5	29	15	75	0.215	1.075	40.3125
24	ID	62	86	5	25	0.115	0.575	7.1875
25	IA	102	126	18	90	0.5	2.5	112.5
26	III	6	30	14	70	0.25	1.25	43.75
27	III	174	198	12	60	2.15	10.75	322.5
28	S	66	90	36	180	0.265	1.325	119.25
29	IA	45	69	37	185	0.5	2.5	231.25
30	IA	75	99	11	55	0.4	2	55
31	ID	80	104	22	110	0.14	0.7	38.5
32	IA	80	104	5	25	0.14	0.7	8.75
33	II	130	154	4	20	0.265	1.325	13.25
34	II	178	202	5	25	0.4	2	25
35	II	82	106	5	25	0.4	2	25
36	IB	100	124	13	65	0.4	2	65
37	IB	76	100	9	45	0.62	3.1	69.75
38	IC	84	108	19	95	0.33	1.65	78.375
39	IB	56	80	21	105	0.115	0.575	30.1875
40	IA	6	30	13	65	0.265	1.325	43.0625
41	IB	100	124	11	55	0.215	1.075	29.5625
42	ID	148	172	7	35	0.4	2	35
43	ID	4	28	5	25	0.5	2.5	31.25

Fracture		Strike (degrees)		Length		Maximum aperture		
Number	Category	Recorded	True	Image (mm)	Fracture (μ)	Image (mm)	Fracture (μ)	Area (μ^2)
44	IA	84	108	9	45	0.4	2	45
45	IB	60	84	15	75	0.215	1.075	40.3125
46	ID	154	178	10	50	0.5	2.5	62.5
47	ID	154	178	11	55	0.265	1.325	36.4375
48	ID	154	178	10	50	0.265	1.325	33.125
49	II	25	49	1	5	0.4	2	5
50	II	154	178	6	30	0.215	1.075	16.125
51	IA	43	67	13	65	0.5	2.5	81.25
52	IB	15	39	9	45	0.265	1.325	29.8125
53	IA	75	99	21	105	1.15	5.75	301.875
54	IB	37	61	12	60	0.14	0.7	21
55	IB	172	196	10	50	0.4	2	50
56	IB	43	67	10	50	0.5	2.5	62.5
57	IB	43	67	8	40	0.4	2	40
58	IA	85	109	17	85	0.4	2	85
59	IB	10	34	20	100	0.14	0.7	35
60	IB	54	78	12	60	0.215	1.075	32.25
61	IA	162	186	20	100	0.75	3.75	187.5
62	II	16	40	8	40	0.75	3.75	75
63	II	175	199	8	40	1.15	5.75	115
64	II	175	199	6	30	0.4	2	30
65	II	61	85	7	35	0.215	1.075	18.8125
66	II	136	160	8	40	0.4	2	40
67	II	150	174	6	30	0.265	1.325	19.875
68	II	52	76	13	65	0.33	1.65	53.625
69	IA	49	73	18	90	0.265	1.325	59.625
70	II	44	68	17	85	0.14	0.7	29.75
71	II	10	34	9	45	0.175	0.875	19.6875
72	II	9	33	8	40	0.14	0.7	14
73	II	100	124	6	30	0.75	3.75	56.25
74	II	6	30	6	30	0.095	0.475	7.125
75	II	6	30	7	35	0.175	0.875	15.3125
76	ID	28	52	6	30	0.175	0.875	13.125
77	IA	40	64	23	115	0.115	0.575	33.0625
78	IA	41	65	30	150	0.175	0.875	65.625
79	II	64	88	7	35	0.14	0.7	12.25
80	IA	63	87	17	85	0.75	3.75	159.375
81	IA	128	152	19	95	0.14	0.7	33.25
82	IA	140	164	11	55	0.4	2	55
83	IB	142	166	11	55	0.14	0.7	19.25
84	IA	38	62	20	100	0.265	1.325	66.25
85	ID	20	44	6	30	0.33	1.65	24.75
86	IC	12	36	9	45	0.5	2.5	56.25
87	IC	80	104	11	55	0.17	0.85	23.375
88	IC	42	66	21	105	0.215	1.075	56.4375
89	IC	40	64	14	70	0.215	1.075	37.625
90	IC	40	64	15	75	0.4	2	75
91	IC	67	91	15	75	0.95	4.75	178.125
92	IA	67	91	9	45	0.215	1.075	24.1875
93	II	57	81	9	45	0.215	1.075	24.1875
94	IB	35	59	29	145	0.5	2.5	181.25
95	II	50	74	20	100	0.62	3.1	155
96	IB	50	74	16	80	0.265	1.325	53
97	ID	35	59	10	50	0.215	1.075	26.875

Appendix 2 (cont.)

Fracture		Strike (degrees)		Length		Maximum aperture		
Number	Category	Recorded	True	Image (mm)	Fracture (μ)	Image (mm)	Fracture (μ)	Area (μ^2)
98	ID	49	73	7	35	0.14	0.7	12.25
99	ID	0	24	3	15	0.5	2.5	18.75
100	ID	50	74	7	35	0.4	2	35
101	IA	73	97	17	85	0.4	2	85
102	IA	21	45	15	75	0.5	2.5	93.75
103	ID	170	194	25	125	0.33	1.65	103.125
104	IB	173	197	22	110	0.215	1.075	59.125
105	ID	46	70	9	45	0.265	1.325	29.8125
106	ID	46	70	8	40	0.175	0.875	17.5
107	ID	56	80	8	40	0.62	3.1	62
108	II	128	152	6	30	0.62	3.1	46.5
109	II	120	144	4	20	0.4	2	20
110	IA	58	82	19	95	0.175	0.875	41.5625
111	IA	53	77	15	75	0.14	0.7	26.25
112	IA	56	80	16	80	0.14	0.7	28
113	IA	46	70	10	50	0.115	0.575	14.375
114	IA	46	70	14	70	0.115	0.575	20.125
115	IB	102	126	11	55	0.62	3.1	85.25
116	IA+	74	98	34	170	0.14	0.7	59.5
117	IB	54	78	9	45	0.175	0.875	19.6875
118	IA	45	69	15	75	0.175	0.875	32.8125
119	IB	54	78	11	55	0.4	2	55
120	S	30	54	16	80	0.5	2.5	20
121	IA	53	77	18	90	5	25	225
122	IA	133	157	28	140	4	20	280
123	IB	27	51	10	50	0.33	1.65	8.25
124	IB	27	51	7	35	0.5	2.5	8.75
125	ID	113	137	12	60	0.265	1.325	7.95
126	IB	44	68	21	105	0.175	0.875	9.1875
127	IB	83	107	15	75	0.75	3.75	28.125
128	IB	145	169	16	80	3.3	16.5	132
129	IA	122	146	10	50	0.265	1.325	6.625
130	IA	121	145	10	50	0.265	1.325	6.625
131	IA	15	39	7	35	0.4	2	7
132	ID	37	61	15	75	0.75	3.75	28.125
133	ID	177	201	12	60	0.265	1.325	7.95
134	ID	96	120	8	40	0.215	1.075	4.3
135	ID	90	114	9	45	0.14	0.7	3.15
136	IC	26	50	22	110	0.4	2	22
137	IC	122	146	7	35	0.33	1.65	5.775
138	IC	157	181	7	35	0.4	2	7
139	IC	0	24	25	125	0.4	2	25
140	ID	158	182	13	65	0.215	1.075	6.9875
141	ID	141	165	7	35	0.265	1.325	4.6375
142	ID	105	129	8	40	0.5	2.5	10
143	IA	40	64	20	100	0.265	1.325	13.25
144	IA	50	74	19	95	0.075	0.375	3.5625
145	IA	68	92	18	90	0.265	1.325	11.925
146	IC	40	64	10	50	0.265	1.325	6.625
147	IC	32	56	3	15	0.33	1.65	2.475
148	IC	42	66	28	140	0.265	1.325	18.55
149	IA	35	59	24	120	0.115	0.575	6.9
150	IB	20	44	10	50	0.14	0.7	3.5
151	IB	46	70	13	65	0.115	0.575	3.7375

Appendix 2 (cont.)

Fracture		Strike (degrees)		Length		Maximum aperture		
Number	Category	Recorded	True	Image (mm)	Fracture (μ)	Image (mm)	Fracture (μ)	Area (μ^2)
152	IA	46	70	22	110	0.62	3.1	34.1
153	IA	8	32	19	95	0.115	0.575	5.4625
154	ID	1	25	5	25	0.14	0.7	1.75
155	II	170	194	8	40	0.175	0.875	3.5
156	IB	56	80	18	90	0.62	3.1	27.9
157	ID	39	63	12	60	0.265	1.325	7.95
158	IB	166	190	16	80	0.175	0.875	7
159	IB	166	190	12	60	0.5	2.5	15
160	II	93	117	15	75	1.15	5.75	43.125
161	ID	77	101	7	35	0.75	3.75	13.125
162	IB	90	114	15	75	0.265	1.325	9.9375
163	II	42	66	8	40	0.215	1.075	4.3
164	ID	32	56	17	85	0.175	0.875	7.4375
165	ID	93	117	14	70	0.265	1.325	9.275
166	IA	60	84	14	70	0.095	0.475	3.325
167	II	37	61	6	30	0.215	1.075	3.225
168	II	35	59	9	45	0.265	1.325	5.9625
169	II	15	39	9	45	0.33	1.65	7.425
170	II	135	159	12	60	0.5	2.5	15
171	II	53	77	9	45	0.175	0.875	3.9375
172	II	15	39	11	55	0.4	2	11
173	II	93	117	9	45	0.265	1.325	5.9625
174	II	32	56	8	40	0.4	2	8
175	II	127	151	8	40	0.265	1.325	5.3
176	IB	54	78	5	25	0.265	1.325	3.3125
177	IB	75	99	8	40	0.5	2.5	10
178	ID	18	42	14	70	0.215	1.075	7.525
					Total fracture area (μ^2):			**11,330.80**

Atlas Dayton No. 1

Formation: Grimsby
Depth: 6,610.5 ft
Image ID: AD6612 scanline no. 2A
View: Downhole
Azimuth reference: 287°
Area imaged: 3.55×10^5 μ^2

Fracture		Strike (degrees)		Length		Maximum aperture		
Number	Category	Recorded	True	Image (mm)	Fracture (μ)	Image (mm)	Fracture (μ)	Area (μ^2)
178	ID	137	64	14	70	0.215	1.075	7.525
179	ID	118	45	12	60	0.5	2.5	15
180	ID	118	45	17	85	0.62	3.1	26.35
181	IB	162	89	6	30	0.33	1.65	4.95
182	IB	163	90	9	45	0.265	1.325	5.9625
183	II	34	321	8	40	0.4	2	8
184	IA	7	294	28	140	2.15	10.75	150.5
185	IB	145	72	30	150	0.14	0.7	10.5
186	IB	170	97	7	35	0.33	1.65	5.775
187	S	34	321	10	50	1.75	8.75	43.75
188	IA	169	96	16	80	0.215	1.075	8.6
189	IA	143	70	11	55	0.215	1.075	5.9125
190	ID	73	360	5	25	0.265	1.325	3.3125
191	ID	130	57	13	65	0.5	2.5	16.25
192	ID	138	65	20	100	0.4	2	20
193	ID	161	88	22	110	0.175	0.875	9.625
194	ID	133	60	9	45	0.175	0.875	3.9375
195	ID	164	91	10	50	1.4	7	35
196	ID	166	93	18	90	1.15	5.75	51.75
197	IA	172	99	16	80	1.15	5.75	46
198	II	0	287	8	40	0.62	3.1	12.4
199	II	129	56	8	40	0.215	1.075	4.3
200	II	141	68	3	15	0.215	1.075	1.6125
					Total fracture area (μ^2)			**497.0125**

Atlas Dayton No. 1

Formation: Grimsby
Depth: 6,610.5 ft
Image ID: AD6612 scanline no. 2
View: Downhole
Azimuth reference: 287°
Area imaged: 2.02×10^6 μ^2

Fracture		Strike (degrees)		Length		Maximum aperture		
Number	Category	Recorded	True	Image (mm)	Fracture (μ)	Image (mm)	Fracture (μ)	Area (μ^2)
1	II	67	354	13	113.75	2.15	18.81	1069.96
2	IA+	135	62	105	918.75	0.62	5.43	2492.11
3	ID	170	97	18	157.5	0.5	4.38	344.53
4	IB	106	33	33	288.75	0.95	8.31	1200.12
5	IB	3	290	19	166.25	0.5	4.38	363.67
6	IC	86	13	5	43.75	0.62	5.43	118.67
7	IB	100	27	15	131.25	0.5	4.38	287.11
8	IC	105	32	10	87.5	0.33	2.89	126.33
9	IC	156	83	18	157.5	0.4	3.50	275.63
10	III	109	36	17	148.75	1.15	10.06	748.40
11	IA	109	36	14	122.5	0.4	3.50	214.38
12	ID	124	51	23	201.25	0.5	4.38	440.23
13	IA+	124	51	11	96.25	0.95	8.31	400.04
14	IA	152	79	9	78.75	0.5	4.38	172.27
15	IB	157	84	8	70	0.4	3.50	122.50
16	ID	0	287	12	105	0.5	4.38	229.69
17	ID	148	75	19	166.25	0.75	6.56	545.51
18	ID	140	67	13	113.75	0.215	1.88	107.00
19	ID	140	67	20	175	0.215	1.88	164.61
20	ID	140	67	6	52.5	0.265	2.32	60.87
21	ID	136	63	10	87.5	0.265	2.32	101.45
22	ID	136	63	6	52.5	0.33	2.89	75.80
23	IC	44	331	16	140	1.4	12.25	857.50
24	IA	17	304	36	315	0.62	5.43	854.44
25	IA	60	347	31	271.25	0.215	1.88	255.14
26	ID	73	360	10	87.5	0.265	2.32	101.45
27	ID	128	55	12	105	0.75	6.56	344.53
28	ID	10	297	10	87.5	0.75	6.56	287.11
29	ID	85	12	4	35	0.5	4.38	76.56
30	ID	100	27	7	61.25	0.265	2.32	71.01
31	ID	136	63	8	70	0.95	8.31	290.94
32	ID	136	63	2	17.5	0.4	3.50	30.63
33	ID	136	63	3	26.25	0.5	4.38	57.42
34	IB	134	61	7	61.25	0.5	4.38	133.98
35	IB	134	61	6	52.5	0.33	2.89	75.80
36	IA	124	51	27	236.25	0.62	5.43	640.83
37	IA	131	58	54	472.5	0.4	3.50	826.88
38	IB	48	335	13	113.75	0.62	5.43	308.55
39	IB	48	335	6	52.5	0.5	4.38	114.84
40	IA	75	2	19	166.25	0.4	3.50	290.94
41	IB	129	56	9	78.75	0.75	6.56	258.40
42	IB	114	41	4	35	0.5	4.38	76.56
43	II	114	41	7	61.25	4	35.00	1071.88

Appendix 2 (cont.)

Fracture		Strike (degrees)		Length		Maximum aperture		
Number	Category	Recorded	True	Image (mm)	Fracture (μ)	Image (mm)	Fracture (μ)	Area (μ^2)
44	II	126	53	7	61.25	0.265	2.32	71.01
45	IC	49	336	6	52.5	0.5	4.38	114.84
46	IC	129	56	11	96.25	0.5	4.38	210.55
47	ID	166	93	22	192.5	0.33	2.89	277.92
48	ID	168	95	24	210	0.4	3.50	367.50
49	IC	110	37	8	70	0.265	2.32	81.16
50	IC	124	51	24	210	0.33	2.89	303.19
51	II	142	69	8	70	0.215	1.88	65.84
52	II	145	72	7	61.25	0.14	1.23	37.52
53	II	160	87	10	87.5	0.5	4.38	191.41
54	II	87	14	20	175	0.265	2.32	202.89
55	II	130	57	14	122.5	0.4	3.50	214.38
56	II	90	17	19	166.25	2.15	18.81	1563.79
57	II	160	87	14	122.5	1.75	15.31	937.89
58	II	1	288	25	218.75	2.15	18.81	2057.62
59	II	142	69	89	778.75	3.3	28.88	11243.20
60	II	141	68	10	87.5	0.62	5.43	237.34
61	II	156	83	10	87.5	0.4	3.50	153.13
62	II	155	82	18	157.5	0.5	4.38	344.53
63	II	140	67	25	218.75	0.62	5.43	593.36
64	II	145	72	20	175	0.14	1.23	107.19
65	II	145	72	18	157.5	0.265	2.32	182.60
66	II	146	73	10	87.5	0.215	1.88	82.30
67	II	155	82	10	87.5	0.265	2.32	101.45
68	II	148	75	9	78.75	0.215	1.88	74.07
69	II	49	336	15	131.25	0.62	5.43	356.02
70	IA	161	88	6	52.5	0.33	2.89	75.80
					Total fracture area (μ^2)			**36934.71**

Atlas Dayton No. 1

Formation: L. Whirlpool
Depth: 6,677.9 ft
Image ID: AD6680c scanline no. 1
View: Downhole
Azimuth reference: 211°
Area imaged: 1.12×10^6 μ^2

Fracture		Strike (degrees)		Length		Maximum aperture		
Number	Category	Recorded	True	Image (mm)	Fracture (μ)	Image (mm)	Fracture (μ)	Area (μ^2)
1	IA+	90	301	37	185	0.95	4.75	439.375
2	IC	20	231	43	215	0.62	3.1	333.25
3	IA+	131	342	24	120	0.33	1.65	99
4	III	108	319	13	65	2.65	13.25	430.625
5	IA	128	339	26	130	0.95	4.75	308.75
6	ID	128	339	15	75	0.265	1.325	49.6875
7	II	175	26	6	30	0.4	2	30
8	IA	156	7	52	260	0.14	0.7	91
9	ID	16	227	11	55	0.265	1.325	36.4375
10	IC	16	227	28	140	1.75	8.75	612.5
11	ID	2	213	7	35	0.33	1.65	28.875
12	ID	8	219	17	85	0.62	3.1	131.75
13	ID	16	227	29	145	0.75	3.75	271.875
14	ID	15	226	8	40	0.33	1.65	33
15	ID	17	228	11	55	0.265	1.325	36.4375
16	IB	174	25	31	155	1.15	5.75	445.625
17	ID	70	281	43	215	0.215	1.075	115.5625
18	IA	120	331	46	230	0.175	0.875	100.625
19	ID	14	225	13	65	0.4	2	65
20	ID	30	241	15	75	0.75	3.75	140.625
21	IA+	172	23	44	220	0.215	1.075	118.25
22	ID	0	211	9	45	0.265	1.325	29.8125
23	ID	135	346	13	65	0.265	1.325	43.0625
24	ID	0	211	11	55	0.215	1.075	29.5625
25	ID	46	257	11	55	0.215	1.075	29.5625
26	IC	158	9	19	95	0.115	0.575	27.3125
27	III	166	17	23	115	0.115	0.575	33.0625
28	IC	192	43	20	100	0.215	1.075	53.75
29	ID	203	54	9	45	0.75	3.75	84.375
30	III	0	211	15	75	0.5	2.5	93.75
31	IA	172	23	18	90	0.265	1.325	59.625
32	II	68	279	6	30	1.15	5.75	86.25
33	III	162	13	12	60	0.5	2.5	75
34	II	181	32	27	135	1.4	7	472.5
35	II	155	6	17	85	0.62	3.1	131.75
36	II	155	6	13	65	0.95	4.75	154.375
37	III	49	260	7	35	0.75	3.75	65.625
38	ID	153	4	10	50	1.4	7	175
39	ID	160	11	15	75	1.15	5.75	215.625
40	IB	23	234	9	45	0.33	1.65	37.125
41	III	50	261	6	30	0.75	3.75	56.25
42	ID	142	353	57	285	0.175	0.875	124.6875
43	IC	135	346	65	325	0.14	0.7	113.75

Appendix 2 (cont.)

Fracture		Strike (degrees)		Length		Maximum aperture		
Number	Category	Recorded	True	Image (mm)	Fracture (μ)	Image (mm)	Fracture (μ)	Area (μ^2)
44	III	140	351	24	120	0.175	0.875	52.5
45	IA+	55	266	49	245	0.62	3.1	379.75
46	IA+	154	5	48	240	0.62	3.1	372
47	IA+	0	211	102	510	1.75	8.75	2231.25
48	IA	179	30	11	55	0.62	3.1	85.25
49	IA	152	3	8	40	0.4	2	40
50	ID	76	287	15	75	2.65	13.25	496.875
51	III	167	18	14	70	0.265	1.325	46.375
52	III	45	256	14	70	0.33	1.65	57.75
53	ID	176	27	29	145	0.62	3.1	224.75
54	IC	48	259		0		0	0
55	IC	30	241	24	120	0.5	2.5	150
56	III	50	261	4	20	0.62	3.1	31
57	III	42	253	5	25	0.4	2	25
58	III	42	253	5	25	0.265	1.325	16.5625
59	IA	66	277	16	80	0.62	3.1	124
60	IC	58	269	21	105	0.4	2	105
61	III	124	335	10	50	0.5	2.5	62.5
62	ID	112	323	6	30	0.265	1.325	19.875
63	ID	106	317	5	25	0.4	2	25
64	ID	122	333	30	150	0.62	3.1	232.5
65	IA	161	12	58	290	0.5	2.5	362.5
66	IA+	130	341	23	115	0.75	3.75	215.625
67	IA	168	19	10	50	0.33	1.65	41.25
68	IA	60	271	8	40	0.62	3.1	62
69	II	60	271	6	30	0.5	2.5	37.5
70	II	166	17	4	20	0.5	2.5	25
71	II	154	5	3	15	0.4	2	15
72	IB	36	247	19	95	0.62	3.1	147.25
73	IB	21	232	31	155	0.265	1.325	102.6875
74	IB	135	346	24	120	0.215	1.075	64.5
75	IA	160	11	21	105	0.4	2	105
76	II	143	354	9	45	0.75	3.75	84.375
77	II	70	281	3	15	0.62	3.1	23.25
78	IA	73	284	18	90	0.62	3.1	139.5
79	IA	60	271		0		0	0
80	IA+	0	211	11	55	0.5	2.5	68.75
81	IB	246	97	10	50	0.75	3.75	93.75
82	IB	178	29	7	35	0.33	1.65	28.875
83	ID	2	213	6	30	0.4	2	30
84	ID	110	321	21	105	0.5	2.5	131.25
85	IA	174	25	15	75	0.33	1.65	61.875
86	IB	63	274	47	235	0.4	2	235
87	IA	143	354	18	90	1.75	8.75	393.75
88	IA	28	239	18	90	0.5	2.5	112.5
89	IA	140	351	14	70	0.4	2	70
90	IA+	165	16	11	55	0.4	2	55
91	IB	153	4	32	160	1.4	7	560
92	III	86	297	20	100	2.65	13.25	662.5
93	III	25	236	5	25	0.5	2.5	12.5
94	III	25	236	17	85		0	0
95	III	74	285	8	40	0.95	4.75	23.75
96	III	75	286	18	90	0.33	1.65	8.25
97	III	24	235	12	60	0.95	4.75	23.75

Appendix 2 (cont.)

Fracture		Strike (degrees)		Length		Maximum aperture		
Number	Category	Recorded	True	Image (mm)	Fracture (μ)	Image (mm)	Fracture (μ)	Area (μ^2)
98	IB	170	21	45	225	1.15	5.75	28.75
99	III	150	1	40	200	0.62	3.1	15.5
100	III	3	214	36	180	0.4	2	10
101	III	74	285	13	65	0.75	3.75	18.75
102	III	158	9	9	45	0.265	1.325	6.625
103	III	170	21	13	65	0.33	1.65	8.25
104	III	67	278	15	75	0.14	0.7	3.5
105	III	26	237	9	45	0.33	1.65	8.25
106	III	95	306	13	65	0.14	0.7	3.5
107	III	71	282	14	70	0.175	0.875	4.375
108	III		211		0		**0**	**0**
109	III	118	329	25	125	0.62	3.1	15.5
110	IA	12	223	11	55	0.75	3.75	18.75
111	ID	51	262	8	40	0.5	2.5	12.5
112	ID	63	274	6	30	0.75	3.75	18.75
113	IA	140	351	21	105	0.4	2	10
114	IA	134	345	38	190	0.5	2.5	12.5
115	III	116	327	17	85	0.33	1.65	8.25
116	III	113	324	33	165	0.33	1.65	8.25
117	III	167	18	14	70	0.62	3.1	15.5
118	III	171	22	25	125	0.5	2.5	12.5
119	III	58	269	23	115	0.33	1.65	8.25
120	III	138	349	22	110	0.5	2.5	12.5
121	ID	89	300	21	105	0.215	1.075	5.375
122	ID	149	360	15	75	0.62	3.1	15.5
123	ID	40	251	6	30	0.4	2	10
124	IA	65	276	37	185	0.62	3.1	15.5
125	IB	55	266	37	185	0.215	1.075	5.375
126	ID	147	358	8	40	0.62	3.1	15.5
127	ID	2	213	7	35	0.14	0.7	3.5
128	ID	0	211	8	40	0.95	4.75	23.75
129	IB	160	11	37	185	0.25	1.25	6.25
130	IB	174	25	30	150	0.175	0.875	4.375
131	IA	110	321	9	45	0.5	2.5	12.5
132	III	150	1	14	70	0.5	2.5	12.5
133	IA	43	254	36	180	0.62	3.1	15.5
134	ID	16	227	23	115	0.33	1.65	8.25
135	IA	4	215	14	70	0.62	3.1	15.5
136	II	30	241	10	50	0.265	1.325	6.625
137	II	45	256	8	40	0.265	1.325	6.625
138	IA	10	221	8	40	0.14	0.7	3.5
139	IA	127	338	12	60	0.115	0.575	2.875
140	IB	126	337	17	85	0.265	1.325	6.625
141	IB	70	281	31	155	0.215	1.075	5.375
142	ID	11	222	20	100	0.115	0.575	2.875
143	IB	138	349	13	65	0.265	1.325	6.625
144	IA	0	211	28	140	0.5	2.5	12.5
145	IA	144	355	14	70	0.5	2.5	12.5
146	ID	0	211	7	35	0.265	1.325	6.625
147	ID	5	216	6	30	0.265	1.325	6.625
148	IA	50	261	7	35	0.14	0.7	3.5
149	ID	149	360	27	135	0.62	3.1	15.5
150	ID	130	341	11	55	0.4	2	10
151	ID	33	244	3	15	0.4	2	10

Appendix 2 (cont.)

Fracture		Strike (degrees)		Length		Maximum aperture		
Number	Category	Recorded	True	Image (mm)	Fracture (μ)	Image (mm)	Fracture (μ)	Area (μ^2)
152	IA	140	351	21	105	0.62	3.1	15.5
153	IA	144	355	6	30	0.75	3.75	18.75
154	ID	48	259	18	90	0.215	1.075	5.375
155	ID	43	254	9	45	0.265	1.325	6.625
156	ID	92	303	12	60	0.75	3.75	18.75
157	ID	86	297	10	50	0.4	2	10
158	ID	59	270	8	40	0.33	1.65	8.25
159	IA	132	343	9	45	0.4	2	10
160	IA++	115	326	91	455	1.15	5.75	28.75
161	IA	35	246	13	65	0.215	1.075	5.375
162	IA	21	232	19	95	0.265	1.325	6.625
163	IA	28	239	25	125	0.33	1.65	8.25
164	IA	5	216	25	125	0.33	1.65	8.25
165	IA	26	237	17	85	0.265	1.325	6.625
166	IA	25	236	6	30	0.215	1.075	5.375
167	IA	132	343	17	85	0.265	1.325	6.625
168	IA	124	335	10	50	0.265	1.325	6.625
169	IA	173	24	54	270	0.33	1.65	8.25
170	IA	198	49	47	235	0.265	1.325	6.625
171	IA	157	8	16	80	0.115	0.575	2.875
172	ID	174	25	8	40	0.4	2	10
173	IA	156	7	23	115	0.5	2.5	12.5
174	IA	25	236	11	55	0.265	1.325	6.625
175	ID	15	226	25	125	0.215	1.075	5.375
176	IA	50	261	43	215	0.215	1.075	5.375
177	ID	48	259	10	50	0.75	3.75	18.75
178	IA+	57	268	81	405	1.4	7	35
179	ID	76	287	8	40	0.5	2.5	12.5
180	IA	178	29	17	85	0.265	1.325	6.625
181	IB	140	351	75	375	0.4	2	10
182	IA+	90	301	19	95	0.33	1.65	8.25
183	IA+	43	254	39	195	1.75	8.75	43.75
184	II	115	326	6	30	0.5	2.5	12.5
185	II	0	211	8	40	0.4	2	10
186	IB	68	279	43	215	0.33	1.65	8.25
187	IB	178	29	46	230	0.4	2	10
188	ID	78	289	9	45	0.33	1.65	8.25
189	IB	158	9	16	80	0.215	1.075	5.375
190	ID	50	261	5	25	0.33	1.65	8.25
191	ID	96	307	16	80	0.265	1.325	6.625
192	II	14	225	13	65	0.62	3.1	15.5
193	ID	56	267	10	50	0.95	4.75	23.75
194	III	75	286	8	40	0.5	2.5	12.5
195	III	36	247	5	25	0.4	2	10
196	IA+	103	314	65	325	0.5	2.5	12.5
197	ID	0	211	7	35	0.95	4.75	23.75
198	IA+	11	222	18	90	0.75	3.75	18.75
199	ID	18	229	14	70	0.33	1.65	8.25
200	IB	46	257	19	95	0.215	1.075	5.375
201	IB	25	236	13	65	0.5	2.5	12.5
202	IA	104	315	32	160	0.33	1.65	8.25
203	II	26	237	10	50	2.15	10.75	53.75
204	II	108	319	10	50	0.75	3.75	18.75
205	IA	98	309	50	250	0.33	1.65	8.25

Appendix 2 (cont.)

Fracture		Strike (degrees)		Length		Maximum aperture		
Number	Category	Recorded	True	Image (mm)	Fracture (μ)	Image (mm)	Fracture (μ)	Area (μ^2)
206	IB	9	220	49	245	0.4	2	10
207	IB	150	1	9	45	0.265	1.325	6.625
208	IB	150	1	10	50	0.4	2	10
209	IA	153	4	6	30	0.33	1.65	8.25
210	IA	61	272	9	45	0.265	1.325	6.625
211	IB	30	241	10	50	0.215	1.075	5.375
212	IB	110	321	39	195	0.5	2.5	12.5
213	IB	50	261	51	255	0.33	1.65	8.25
214	IA+	176	27	50	250	0.4	2	10
215	IB	45	256	37	185	0.4	2	10
216	IB	45	256	30	150	0.265	1.325	6.625
217	IB		211		0		0	0
218	IB	8	219	30	150	0.5	2.5	12.5
219	IB	6	217	10	50	0.4	2	10
220	IB	4	215	21	105	0.215	1.075	5.375
221	IB	3	214	31	155	0.265	1.325	6.625
					Total fracture area (μ^2)			**16231.5625**

Atlas Lucas No. 1

Formation: Thorold
Depth: 6,338 ft
Image ID: AL6338c scanline no. 1
View: Downhole
Azimuth reference: 278°
Area imaged: 1.60×10^6 μ^2

Fracture		Strike (degrees)		Length		Maximum aperture		
Number	Category	Recorded	True	Image (mm)	Fracture (μ)	Image (mm)	Fracture (μ)	Area (μ^2)
1	IB	172	90	1.7	85	0.215	1.075	45.6875
2	IB	76	354	0.9	45	0.175	0.875	19.6875
3	ID	162	80	1.05	52.5	0.4	2	52.5
4	ID	358	276	0.9	45	0.33	1.65	37.125
5	IB	91	9	1.15	57.5	0.33	1.65	47.4375
6	ID	117	35	0.7	35	0.62	3.1	54.25
7	IB	76	354	1.1	55	0.4	2	55
8	ID	88	6	1	50	0.265	1.325	33.125
9	IC	51	329	2	100	0.115	0.575	28.75
10	IA+	35	313	3.7	185	0.62	3.1	286.75
11	ID	32	310	1.1	55	0.14	0.7	19.25
12	ID	157	75	1.3	65	0.2165	1.0825	35.18125
13	III	46	324	1.5	75	2.15	10.75	403.125
14	III	141	59	1.8	90	1.75	8.75	393.75
15	IB	62	340	4.8	240	0.4	2	240
16	ID	85	3	5.3	265	0.5	2.5	331.25
17	III	109	27	5	250	4	20	2500
18	III	7	285	1.2	60	1.75	8.75	262.5
19	IA	93	11	3.1	155	0.33	1.65	127.875
20	ID	166	84	1.8	90	0.215	1.075	48.375
21	ID	85	3	2	100	0.175	0.875	43.75
22	ID	9	287	5.95	297.5	0.14	0.7	104.125
23	IA	9	287	1.5	75	0.265	1.325	49.6875
24	IB	78	356	2.4	120	0.215	1.075	64.5
25	ID	56	334	1.5	75	0.75	3.75	140.625
26	ID	128	46	3.5	175	0.5	2.5	218.75
27	ID	57	335	2.1	105	0.62	3.1	162.75
28	ID	78	356	3.3	165	0.265	1.325	109.3125
29	IB	109	27	2	100	0.175	0.875	43.75
30	IA	157	75	1.8	90	0.33	1.65	74.25
31	IB	34	312	1.7	85	0.62	3.1	131.75
32	II	6	284	1.8	90	0.95	4.75	213.75
33	II	11	289	2.5	125	0.4	2	125
34	II	178	96	2.6	130	0.265	1.325	86.125
35	III	51	329	2.6	130	2.65	13.25	861.25
36	ID	17	295	5.2	260	1.4	7	910
37	III	16	294	3.6	180	4	20	1800
38	ID	118	36	3.8	190	0.33	1.65	156.75
39	ID	130	48	3.9	195	0.95	4.75	463.125
40	ID	33	311	3.5	175	0.265	1.325	115.9375
41	ID	45	323	1.4	70	1.15	5.75	201.25
42	IB	65	343	4.4	220	0.265	1.325	145.75
43	IB	72	350	2.6	130	0.175	0.875	56.875

Appendix 2 (cont.)

Fracture		Strike (degrees)		Length		Maximum aperture		
Number	Category	Recorded	True	Image (mm)	Fracture (μ)	Image (mm)	Fracture (μ)	Area (μ^2)
44	ID	83	1	0.9	45	0.33	1.65	37.125
45	III	100	18	5.4	270	4	20	2700
46	III	96	14	6.3	315	2.15	10.75	1693.125
47	III	104	22	3.65	182.5	0.75	3.75	342.1875
48	III	124	42	3.4	170	4	20	1700
49	III	99	17	1.5	75	4	20	750
50	III	153	71	1.8	90	0.33	1.65	74.25
51	III	153	71	1.1	55	0.4	2	55
52	IB	136	54	1	50	0.265	1.325	33.125
53	ID	151	69	1.2	60	0.33	1.65	49.5
54	III	164	82	1.1	55	0.265	1.325	36.4375
55	III	140	58	1.2	60	0.265	1.325	39.75
56	III	141	59	2.9	145	0.5	2.5	181.25
57	III	97	15	1	50	1.15	5.75	143.75
58	III	146	64	2.4	120	0.95	4.75	285
59	ID	23	301	1.6	80	0.215	1.075	43
60	IB	120	38	5	250	0.33	1.65	206.25
61	IA	114	32	4.1	205	0.95	4.75	486.875
62	IB	107	25	1	50	0.4	2	50
63	IA	89	7	3	150	0.5	2.5	187.5
64	ID	36	314	2.2	110	0.2	1	55
65	II	138	56	1.5	75	2.65	13.25	496.875
66	III	144	62	3.4	170	0.4	2	170
67	ID	25	303	1.2	60	1.75	8.75	262.5
68	IB	63	341	2.1	105	0.33	1.65	86.625
69	IB	99	17	2.9	145	0.5	2.5	181.25
70	IC	170	88	1.8	90	0.215	1.075	48.375
71	IB	172	90	2.9	145	0.4	2	145
72	IC	166	84	2.9	145	0.215	1.075	77.9375
					Total fracture area (μ^2)			**21918.36875**

Atlas Lucas No. 1

Formation: Grimsby
Depth: 6,381 ft
Image ID: AL6381c scanline no. 1
View: Uphole
Azimuth reference: 180°
Area imaged: 1.37×10^6 μ^2

Fracture		Strike (degrees)		Length		Maximum aperture		
Number	Category	Recorded	True	Image (mm)	Fracture (μ)	Image (mm)	Fracture (μ)	Area (μ^2)
1	Ia+	98	82	47	235	4.2	21	2467.5
2	Id	105	75	7	35	0.215	1.075	18.8125
3	Id	-4	184	13	65	0.075	0.375	12.1875
4	Ic	5	175	10	50	0.33	1.65	41.25
5	Id	-20	200	18	90	0.175	0.875	39.375
6	Id	-20	200	20	100	0.175	0.875	43.75
7	Id	-30	210	28	140	0.025	0.125	8.75
8	Ic	-62	242	27	135	0.215	1.075	72.5625
9	II	122	58	10	50	0.095	0.475	11.875
10	Ic	-15	195	15	75	0.062	0.31	11.625
11	III	-13	193	9	45	0.115	0.575	12.9375
12	Ia	106	74	13	65	0.5	2.5	81.25
13	Ia+	26	154	34	170	0.5	2.5	212.5
14	Ic	105	75	22	110	0.295	1.475	81.125
15	Ic	105	75	8	40	0.33	1.65	33
16	Ic	105	75	6	30	0.175	0.875	13.125
17	Ia	110	70	12	60	0.33	1.65	49.5
18	III	-35	215	16	80	0.4	2	80
19	III	100	80	7	35	0.215	1.075	18.8125
20	III	112	68	6	30	0.62	3.1	46.5
21	Id	-46	226	15	75	1.75	8.75	328.125
22	Id	-82	262	11	55	0.95	4.75	130.625
23	Id	-13	193	11	55	1.15	5.75	158.125
24	Ia+	-62	242	15	75	0.95	4.75	178.125
25	Ia	32	148	50	250	0.62	3.1	387.5
26	III	-35	215	17	85	0.175	0.875	37.1875
27	III	-25	205	10	50	0.5	2.5	62.5
28	III	-25	205	20	100	0.95	4.75	237.5
29	III	13	167	10	50	0.175	0.875	21.875
30	III	-20	200	6	30	0.175	0.875	13.125
31	III	-19	199	6	30	2.15	10.75	161.25
32	Ia+	-25	205	38	190	0.4	2	190
33	Ia+	-1	181	30	150	0.95	4.75	356.25
34	Ia+	74	106	30	150	0.5	2.5	187.5
35	Ia+	74	106	40	200	0.265	1.325	132.5
36	Ic	80	100	42	210	0.33	1.65	173.25
37	Id	-30	210	15	75	0.4	2	75
38	Id	85	95	16	80	0.215	1.075	43
39	III	12	168	4	20	0.62	3.1	31
40	III	-4	184	3	15	0.5	2.5	18.75

Appendix 2 (cont.)

Fracture		Strike (degrees)		Length		Maximum aperture		
Number	Category	Recorded	True	Image (mm)	Fracture (μ)	Image (mm)	Fracture (μ)	Area (μ^2)
41	III	51	129	27	135	0.265	1.325	89.4375
42	III	114	66	7	35	0.215	1.075	18.8125
43	Ia+	-45	225	30	150	2.65	13.25	993.75
44	Ia+	-43	223	18	90	0.2	1	45
45	III	31	149	4	20	0.5	2.5	25
46	III	31	149	6	30	0.265	1.325	19.875
47	III	31	149	11	55	0.33	1.65	45.375
48	III	31	149	14	70	0.33	1.65	57.75
49	Ib	114	66	10	50	0.5	2.5	62.5
50	Id	6	174	25	125	0.265	1.325	82.8125
51	III	106	74	5	25	0.62	3.1	38.75
52	III	0	180	3	15	0.75	3.75	28.125
53	Ic	97	83	25	125	0.175	0.875	54.6875
54	Ib	106	74	27	135	0.215	1.075	72.5625
55	Ib	106	74	11	55	0.215	1.075	29.5625
56	Ia+	94	86	22	110	0.5	2.5	137.5
57	Ib	91	89	17	85	0.265	1.325	56.3125
58	Id	117	63	21	105	0.14	0.7	36.75
59	Id	141	39	19	95	0.115	0.575	27.3125
60	Id	161	19	13	65	0.33	1.65	53.625
61	Ia	118	62	37	185	0.215	1.075	99.4375
62	Ia+	36	144	50	250	0.14	0.7	87.5
63	Ic	157	23	13	65	0.295	1.475	47.9375
64	Ia+	76	104	31	155	0.33	1.65	127.875
65	Ia+	46	134	37	185	0.33	1.65	152.625
66	Ia+	71	109	31	155	0.4	2	155
67	Ia	53	127	22	110	0.62	3.1	170.5
68	Ic	36	144	11	55	0.33	1.65	45.375
69	II	145	35	14	70	0.33	1.65	57.75
70	Id	134	46	16	80	0.175	0.875	35
71	Id	76	104	12	60	0.175	0.875	26.25
72	Ia+	34	146	18	90	0.75	3.75	168.75
73	Ia+	147	33	12	60	0.265	1.325	39.75
74	II	15	165	12	60	0.33	1.65	49.5
75	II	115	65	3	15	0.265	1.325	9.9375
76	II	95	85	31	155	0.215	1.075	83.3125
77	II	0	180	10	50	0.15	0.75	18.75
78	II	156	24	23	115	0.175	0.875	50.3125
79	II	59	121	18	90	0.4	2	90
80	II	135	45	10	50	0.14	0.7	17.5
81	II	50	130	6	30	0.065	0.325	4.875
82	II	164	16	22	110	0.4	2	110
83	Id	164	16	13	65	0.175	0.875	28.4375
84	Id	27	153	35	175	0.175	0.875	76.5625
85	III	157	23	15	75	0.14	0.7	26.25
86	Ib	165	15	7	35	0.33	1.65	28.875
87	Ia+	128	52	37	185	0.5	2.5	231.25
88	Id	144	36	10	50	0.5	2.5	62.5
89	?	154	26	10	50	0.01	0.05	1.25
90	?	154	26	24	120	0.01	0.05	3

Appendix 2 (cont.)

Fracture		Strike (degrees)		Length		Maximum aperture		
Number	Category	Recorded	True	Image (mm)	Fracture (μ)	Image (mm)	Fracture (μ)	Area (μ^2)
91	Id	127	53	15	75	0.7	3.5	131.25
92	Id	102	78	8	40	0.33	1.65	33
93	Ia+	55	125	80	400	0.4	2	400
94	Id	70	110	16	80	0.14	0.7	28
95	Ib	90	90	20	100	0.265	1.325	66.25
96	Ia+	55	125	80	400	0.75	3.75	750
97	Ia+	81	99	52	260	0.4	2	260
98	Id	148	32	20	100	0.5	2.5	125
99	III	19	161	7	35	0.75	3.75	65.625
100	III	149	31	25	125	0.265	1.325	82.8125
101	Ia+	92	88	37	185	0.4	2	185
102	III	64	116	7	35	0.215	1.075	18.8125
103	Id	85	95	22	110	0.4	2	110
104	Id	77	103	32	160	2.15	10.75	860
105	Id	148	32	15	75	0.62	3.1	116.25
106	Id	140	40	42	210	0.265	1.325	139.125
107	III	149	31	14	70	0.33	1.65	57.75
108	III	57	123	11	55	0.33	1.65	45.375
109	Ia+	135	45	5	25	0.215	1.075	13.4375
110	Id	153	27	22	110	2.15	10.75	591.25
111	Id	174	6	28	140	0.33	1.65	115.5
112	Id	168	12	20	100	0.215	1.075	53.75
113	Id	142	38	9	45	0.215	1.075	24.1875
114	Id	97	83	14	70	0.14	0.7	24.5
115	Id	72	108	17	85	0.62	3.1	131.75
116	III	94	86	3	15	0.4	2	15
117	Id	136	44	18	90	1.75	8.75	393.75
118	Id	109	71	27	135	0.265	1.325	89.4375
119	Id	35	145	18	90	0.33	1.65	74.25
120	Id	35	145	17	85	0.33	1.65	70.125
121	Id	132	48	11	55	0.5	2.5	68.75
122	Id	166	14	12	60	0.62	3.1	93
123	Id	166	14	3	15	0.5	2.5	18.75
124	II	111	69	12	60	4	20	600
125	Id	129	51	7	35	0.5	2.5	43.75
126	Id	129	51	3	15	0.62	3.1	23.25
127	III	55	125	5	25	0.33	1.65	20.625
128	III	144	36	10	50	0.4	2	50
129	III	145	35	7	35	0.62	3.1	54.25
130	III	145	35	9	45	0.4	2	45
131	Ia	-11	191	16	80	0.4	2	80
132	Id	-30	210	4	20	0.265	1.325	13.25
133	Id	-78	258	15	75	0.5	2.5	93.75
					Total fracture area (μ^2)			**16636.8**

Atlas Lucas No. 1

Formation: Grimsby
Depth: 6,386 ft
Image ID: AD6386.2c mosaic no. 2
View: Uphole
Azimuth reference: 276°
Area imaged: 3.86×10^6 μ^2

Fracture		Strike (degrees)		Length		Maximum aperture		
Number	Category	Recorded	True	Image (mm)	Fracture (μ)	Image (mm)	Fracture (μ)	Area (μ^2)
1	Ia	68	344	27	135	0.2	1	67.5
2	Ia	0	276	35	175	0.3	1.5	131.25
3	Ia	0	276	36	180	0.38	1.9	171
4	Ia	85	1	77	385	0.45	2.25	433.125
5	Ic	85	1	47	235	0.3	1.5	176.25
6	III	57	333	46	230	0.6	3	345
7	II	-15	261	14	70	0.45	2.25	78.75
8	Ib	82	358	51	255	0.38	1.9	242.25
9	Ia	25	301	40	200	0.38	1.9	190
10	Ia	-9	267	51	255	0.5	2.5	318.75
11	III	-52	224	14	70	0.12	0.6	21
12	III	-52	224	11	55	0.2	1	27.5
13	III	32	308	7	35	0.38	1.9	33.25
14	Ia	-65	211	42	210	0.38	1.9	199.5
15	Ia	-52	224	15	75	0.3	1.5	56.25
16	Ia	75	351	10	50	0.16	0.8	20
17	III	35	311	12	60	0.38	1.9	57
18	III	-78	198	10	50	0.18	0.9	22.5
19	III	-71	205	5	25	0.12	0.6	7.5
20	Ib	-30	246	8	40	1.4	7	140
21	III	0	276	6	30	0.4	2	30
22	III	27	303	10	50	0.2	1	25
23	Ib	50	326	15	75	0.3	1.5	56.25
24	Ib	22	298	20	100	0.16	0.8	40
25	Ib	22	298	33	165	6.4	32	2640
26	Ib	30	306	29	145	11.5	57.5	4168.75
27	III	80	356	7	35	0.38	1.9	33.25
28	Ia	37	313	47	235	2.9	14.5	1703.75
29	Ia	48	324	45	225	1.8	9	1012.5
30	Ic	56	332	37	185	0.6	3	277.5
31	Ic	45	321	10	50	0.6	3	75
32	Ia	56	332	24	120	0.22	1.1	66
33	III	60	336	13	65	0.22	1.1	35.75
34	III	-59	217	15	75	0.3	1.5	56.25
35	Ic	-5	271	36	180	0.1	0.5	45
36	Ic	-17	259	20	100	0.16	0.8	40
37	Ic	15	291	20	100	0.2	1	50
38	Ic	4	280	18	90	0.1	0.5	22.5
39	Ic	-10	266	7	35	0.16	0.8	14
40	III	-32	244	20	100	0.2	1	50
41	Ib	75	351	100	500	0.1	0.5	125
42	II	60	336	23	115	0.2	1	57.5
43	Ib	-80	196	45	225	0.3	1.5	168.75

Appendix 2 (cont.)

Fracture		Strike (degrees)		Length		Maximum aperture		
Number	Category	Recorded	True	Image (mm)	Fracture (μ)	Image (mm)	Fracture (μ)	Area (μ^2)
44	III	-18	258	20	100	0.38	1.9	95
45	III	-30	246	5	25	0.8	4	50
46	III	-91	185	9	45	3.5	17.5	393.75
47	s	-88	188	25	125	0.22	1.1	68.75
48	s	-90	186	22	110	0.3	1.5	82.5
49	Ib	-3	273	26	130	0.3	1.5	97.5
50	III	-25	251	7	35	0.3	1.5	26.25
51	III	-30	246	18	90	0.18	0.9	40.5
52	III	-51	225	5	25	0.12	0.6	7.5
53	Ib	-71	205	29	145	0.45	2.25	163.125
54	Ib	40	316	6	30	0.8	4	60
55	Ib	30	306	14	70	0.7	3.5	122.5
56	Ia	-67	209	40	200	0.3	1.5	150
57	Ia	-3	273	26	130	0.18	0.9	58.5
58	Ia	38	314	24	120	0.1	0.5	30
59	III	55	331	6	30	0.1	0.5	7.5
60	III	-15	261	23	115	0.14	0.7	40.25
61	III	-3	273	13	65	0.18	0.9	29.25
62	III	-23	253	16	80	0.14	0.7	28
63	Ia	-10	266	29	145	0.22	1.1	79.75
64	III	74	350	19	95	0.22	1.1	52.25
65	III	-75	201	11	55	0.18	0.9	24.75
66	III	-38	238	11	55	0.08	0.4	11
67	Id	24	300	20	100	0.3	1.5	75
68	Id	24	300	26	130	0.3	1.5	97.5
69	Ia	-25	251	15	75	0.62	3.1	116.25
70	III	6	282	11	55	0.16	0.8	22
71	III	63	339	5	25	0.3	1.5	18.75
72	III	48	324	8	40	0.16	0.8	16
73	III	1	277	18	90	0.6	3	135
74	III	4	280	17	85	0.2	1	42.5
75	Ib	104	20	41	205	0.9	4.5	461.25
76	Ic	27	303	48	240	0.45	2.25	270
77	Ic	30	306	53	265	0.38	1.9	251.75
78	Ia	-87	189	67	335	0.22	1.1	184.25
79	Ib	-87	189	15	75	1.5	7.5	281.25
80	III	-77	199	15	75	0.3	1.5	56.25
81	Ia	-18	258	62	310	0.5	2.5	387.5
82	III	-22	254	34	170	0.2	1	85
83	III	-67	209	15	75	0.2	1	37.5
84	Ia	-68	208	77	385	0.16	0.8	154
85	Ia	-93	183	113	565	0.2	1	282.5
86	Ia	30	306	43	215	0.2	1	107.5
87	Ia+	50	326	47	235	0.45	2.25	264.375
88	Ib	-46	230	23	115	0.1	0.5	28.75
89	III	2	278	34	170	0.6	3	255
90	Ib	10	286	28	140	0.7	3.5	245
91	III	-45	231	19	95	0.45	2.25	106.875
92	III	28	304	9	45	0.1	0.5	11.25
93	Ib	60	336	32	160	0.6	3	240
94	Ia	-55	221	19	95	0.7	3.5	166.25
95	III	85	1	11	55	0.45	2.25	61.875
96	III	1	277	8	40	0.38	1.9	38
97	III	-50	226	16	80	0.38	1.9	76

Appendix 2 (cont.)

Fracture		Strike (degrees)		Length		Maximum aperture		
Number	Category	Recorded	True	Image (mm)	Fracture (μ)	Image (mm)	Fracture (μ)	Area (μ^2)
98	III	60	336	10	50	0.5	2.5	62.5
99	III	43	319	34	170	0.38	1.9	161.5
100	Ia	-20	256	20	100	0.38	1.9	95
101	III	40	316	30	150	0.38	1.9	142.5
102	Ia	40	316	23	115	0.38	1.9	109.25
103	Ia	-88	188	65	325	0.38	1.9	308.75
104	Ia	-44	232	75	375	0.3	1.5	281.25
105	Ia	25	301	27	135	0.38	1.9	128.25
106	III	28	304	36	180	0.3	1.5	135
107	III	-23	253	22	110	1.3	6.5	357.5
108	Ib	75	351	16	80	2.4	12	480
109	Ib	20	296	11	55	0.5	2.5	68.75
110	III	-23	253	16	80	0.14	0.7	28
111	III	-88	188	15	75	0.14	0.7	26.25
112	III	-23	253	28	140	0.2	1	70
113	III	82	358	7	35	0.16	0.8	14
114	III	58	334	15	75	0.16	0.8	30
115	Ic	-74	202	15	75	0.18	0.9	33.75
116	III	-6	270	15	75	0.14	0.7	26.25
117	III	56	332	15	75	0.16	0.8	30
118	III	56	332	23	115	0.22	1.1	63.25
119	III	56	332	24	120	0.2	1	60
120	III	39	315	9	45	0.1	0.5	11.25
121	III	-62	214	9	45	0.16	0.8	18
122	III	-51	225	12	60	0.12	0.6	18
123	III	16	292	17	85	0.18	0.9	38.25
124	Ia	-29	247	60	300	0.2	1	150
125	III	-60	216	18	90	0.22	1.1	49.5
126	Ia	-70	206	49	245	0.16	0.8	98
127	II	-70	206	11	55	0.7	3.5	96.25
128	II	-55	221	27	135	0.18	0.9	60.75
129	Ib	80	356	18	90	0.3	1.5	67.5
130	III	-10	266	15	75	0.45	2.25	84.375
131	III	-10	266	9	45	0.3	1.5	33.75
132	Ib	-30	246	15	75	5	25	937.5
133	II	91	7	10	50	6.4	32	800
134	Ia	-30	246	66	330	1.8	9	1485
135	Ib	-29	247	35	175	3.2	16	1400
136	Ic	-29	247	20	100	0.22	1.1	55
137	Ia	-71	205	72	360	0.38	1.9	342
138	III	-45	231	25	125	0.45	2.25	140.625
139	III	7	283	24	120	0.45	2.25	135
140	III	7	283	27	135	0.22	1.1	74.25
141	III	7	283	21	105	0.18	0.9	47.25
142	III	-45	231	36	180	0.38	1.9	171
143	III	-24	252	20	100	0.1	0.5	25
144	III	72	348	10	50	0.1	0.5	12.5
145	III	-30	246	28	140	0.14	0.7	49
146	III	-42	234	35	175	0.12	0.6	52.5
147	III	-65	211	21	105	0.12	0.6	31.5
148	III	-2	274	25	125	0.38	1.9	118.75
149	III	-40	236	24	120	2.4	12	720
150	III	-21	255	10	50	0.45	2.25	56.25
151	III	-24	252	13	65	1.5	7.5	243.75

Appendix 2 (cont.)

Fracture		Strike (degrees)		Length		Maximum aperture		
Number	Category	Recorded	True	Image (mm)	Fracture (μ)	Image (mm)	Fracture (μ)	Area (μ^2)
152	III	-82	194	9	45	0.3	1.5	33.75
153	III	-31	245	10	50	0.38	1.9	47.5
154	Ib	-82	194	52	260	0.22	1.1	143
155	III	55	331	10	50	0.18	0.9	22.5
156	III	55	331	15	75	0.22	1.1	41.25
157	III	-49	227	33	165	0.14	0.7	57.75
158	III	-79	197	15	75	0.2	1	37.5
159	III	-90	186	15	75	0.14	0.7	26.25
160	Ib	-42	234	17	85	0.18	0.9	38.25
161	Ib	67	343	14	70	0.16	0.8	28
162	Ib	-27	249	24	120	0.18	0.9	54
163	Ib	67	343	31	155	0.3	1.5	116.25
164	Ib	-30	246	17	85	0.22	1.1	46.75
165	III	18	294	12	60	0.3	1.5	45
166	III	1	277	32	160	0.3	1.5	120
167	III	48	324	43	215	0.45	2.25	241.875
168	III	30	306	36	180	0.14	0.7	63
169	III	-20	256	15	75	0.12	0.6	22.5
170	III	10	286	18	90	0.3	1.5	67.5
171	Ib	10	286	10	50	0.08	0.4	10
172	IB	7	283	19	95	0.5	2.5	118.75
173	III	-15	261	28	140	0.22	1.1	77
174	III	15	291	12	60	0.38	1.9	57
175	III	-73	203	15	75	0.2	1	37.5
176	III	-48	228	22	110	0.3	1.5	82.5
177	III	-12	264	20	100	0.22	1.1	55
178	III	-58	218	37	185	0.12	0.6	55.5
179	III	-5	271	27	135	0.38	1.9	128.25
180	III	-90	186	17	85	0.14	0.7	29.75
181	III	65	341	17	85	0.38	1.9	80.75
182	III	-92	184	18	90	0.2	1	45
183	III	67	343	18	90	0.2	1	45
184	III	-65	211	13	65	0.22	1.1	35.75
185	II	-5	271	12	60	1.4	7	210
186	IB	-80	196	24	120	1.4	7	420
187	II	25	301	11	55	0.7	3.5	96.25
188	Ia+	-21	255	135	675	0.14	0.7	236.25
189	III	-79	197	10	50	0.22	1.1	27.5
190	III	-77	199	5	25	0.22	1.1	13.75
191	III	-76	200	10	50	0.3	1.5	37.5
192	Ib	-50	226	34	170	0.3	1.5	127.5
193	Ib	-10	266	31	155	1.8	9	697.5
194	III	-1	275	13	65	0.38	1.9	61.75
195	III	-37	239	17	85	0.18	0.9	38.25
196	III	-38	238	15	75	0.18	0.9	33.75
197	Ia+	-87	189	65	325	0.12	0.6	97.5
198	Ia+	31	307	75	375	0.3	1.5	281.25
199	III	-27	249	30	150	1	5	375
200	III	-10	266	32	160	1.3	6.5	520
201	III	-40	236	16	80	0.38	1.9	76
202	III	40	316	22	110	0.14	0.7	38.5
203	III	-70	206	23	115	0.16	0.8	46
204	III	45	321	15	75	0.38	1.9	71.25
205	III	45	321	8	40	0.6	3	60

Appendix 2 (cont.)

Fracture		Strike (degrees)		Length		Maximum aperture		
Number	Category	Recorded	True	Image (mm)	Fracture (μ)	Image (mm)	Fracture (μ)	Area (μ^2)
206	III	45	321	5	25	0.38	1.9	23.75
207	III	-25	251	11	55	0.38	1.9	52.25
208	III	-31	245	10	50	1.3	6.5	162.5
209	III	-31	245	6	30	0.18	0.9	13.5
210	Ia+	-78	198	52	260	0.8	4	520
211	III	-28	248	6	30	0.3	1.5	22.5
212	III	-82	194	10	50	0.38	1.9	47.5
213	II	67	343	12	60	5	25	750
214	Ib	28	304	29	145	2.9	14.5	1051.25
215	Ib	28	304	53	265	2.5	12.5	1656.25
216	Ib	28	304	41	205	2.9	14.5	1486.25
217	III	28	304	27	135	0.3	1.5	101.25
218	III	28	304	23	115	0.22	1.1	63.25
219	III	60	336	17	85	0.7	3.5	148.75
220	Ib	-50	226	100	500	2.5	12.5	3125
221	Ia	-69	207	34	170	1	5	425
222	Ia	-76	200	15	75	0.38	1.9	71.25
223	Ia	-82	194	13	65	1.8	9	292.5
224	Ia	-45	231	21	105	0.3	1.5	78.75
225	Ia	-45	231	45	225	0.34	1.7	191.25
226	III	4	280	12	60	0.2	1	30
227	Ia	-90	186	23	115	0.16	0.8	46
228	III	-92	184	10	50	0.14	0.7	17.5
229	III	-92	184	12	60	0.16	0.8	24
230	Ia	-40	236	38	190	0.38	1.9	180.5
231	Ib	55	331	30	150	0.2	1	75
232	III	37	313	12	60	0.22	1.1	33
233	Ib	-74	202	15	75	0.6	3	112.5
234	III	37	313	16	80	0.38	1.9	76
235	III	38	314	13	65	0.8	4	130
236	III	-78	198	20	100	0.14	0.7	35
237	III	12	288	25	125	0.22	1.1	68.75
238	III	-68	208	19	95	0.1	0.5	23.75
239	III	2	278	26	130	0.38	1.9	123.5
240	III	2	278	13	65	0.5	2.5	81.25
241	III	-90	186	8	40	0.3	1.5	30
242	III	31	307	19	95	0.3	1.5	71.25
243	III	31	307	23	115	0.58	2.9	166.75
244	III	31	307	3	15	0.2	1	7.5
245	III	31	307	4	20	0.3	1.5	15
246	Ib	90	6	19	95	1.4	7	332.5
247	Ib	56	332	20	100	1.8	9	450
248	III	-1	275	15	75	0.5	2.5	93.75
249	III	-72	204	11	55	0.18	0.9	24.75
250	Ia	-8	268	26	130	0.2	1	65
251	Ia	-9	267	16	80	0.18	0.9	36
252	III	-21	255	21	105	0.12	0.6	31.5
253	Ia	-72	204	14	70	0.8	4	140
254	Ia	-29	247	17	85	0.2	1	42.5
255	Ia	-22	254	53	265	1.2	6	795
256	Ia	-22	254	34	170	0.18	0.9	76.5
257	Ib	-22	254	18	90	0.38	1.9	85.5
258	Ib	24	300	15	75	0.14	0.7	26.25
259	Ia	22	298	13	65	0.18	0.9	29.25

Appendix 2 (cont.)

Fracture		Strike (degrees)		Length		Maximum aperture		
Number	Category	Recorded	True	Image (mm)	Fracture (μ)	Image (mm)	Fracture (μ)	Area (μ^2)
260	Ib	-85	191	21	105	0.8	4	210
261	III	-19	257	7	35	0.14	0.7	12.25
262	III	-22	254	11	55	0.14	0.7	19.25
263	III	-22	254	7	35	0.2	1	17.5
264	III	-87	189	7	35	0.8	4	70
265	III	-85	191	14	70	0.16	0.8	28
266	III	-83	193	17	85	0.3	1.5	63.75
267	III	-70	206	9	45	0.1	0.5	11.25
268	III	-25	251	8	40	0.3	1.5	30
269	III	-90	186	13	65	0.3	1.5	48.75
270	III	-50	226	26	130	0.38	1.9	123.5
271	III	-20	256	11	55	0.16	0.8	22
272	Ia	-74	202	23	115	0.22	1.1	63.25
273	Ia	80	356	28	140	0.18	0.9	63
274	III	80	356	14	70	0.22	1.1	38.5
275	Ib	30	306	22	110	0.14	0.7	38.5
276	Ib	30	306	30	150	0.2	1	75
277	III	30	306	15	75	0.1	0.5	18.75
278	Ia	-77	199	62	310	0.3	1.5	232.5
279	Ia	-70	206	57	285	0.2	1	142.5
280	Ia	-90	186	92	460	0.3	1.5	345
281	Ia	73	349	53	265	0.2	1	132.5
282	III	10	286	3	15	0.38	1.9	14.25
283	III	35	311	5	25	0.6	3	37.5
284	III	-90	186	4	20	0.3	1.5	15
285	Ia+	-83	193	80	400	2.5	12.5	2500
286	Ia+	-115	161	67	335	0.14	0.7	117.25
287	III	25	301	16	80	0.22	1.1	44
288	III	-90	186	7	35	0.38	1.9	33.25
289	Ib	-95	181	19	95	0.16	0.8	38
290	Ib	-95	181	32	160	0.3	1.5	120
291	III	-79	197	11	55	0.22	1.1	30.25
292	Ib	-115	161	20	100	0.16	0.8	40
293	Ib	-68	208	22	110	0.8	4	220
294	Ib	-95	181	39	195	1.2	6	585
295	III	-102	174	20	100	0.45	2.25	112.5
296	III	-95	181	24	120	0.38	1.9	114
297	III	0	276	6	30	0.22	1.1	16.5
298	III	-98	178	8	40	0.18	0.9	18
299	III	-98	178	8	40	0.3	1.5	30
300	III	-80	196	9	45	0.18	0.9	20.25
301	III	46	322	12	60	0.5	2.5	75
302	Ia+	-60	216	67	335	0.38	1.9	318.25
303	Ia+	-83	193	95	475	0.12	0.6	142.5
304	III	45	321	9	45	0.18	0.9	20.25
305	II	-12	264	20	100	0.18	0.9	45
306	III	-86	190	6	30	0.5	2.5	37.5
307	II	48	324	10	50	0.3	1.5	37.5
308	II	14	290	14	70	0.3	1.5	52.5
309	II	26	302	20	100	0.3	1.5	75
310	II	-97	179	23	115	0.8	4	230
311	II	-12	264	15	75	0.3	1.5	56.25
312	II	-18	258	10	50	0.45	2.25	56.25
313	II	22	298	7	35	0.22	1.1	19.25

Appendix 2 (cont.)

Fracture		Strike (degrees)		Length		Maximum aperture		
Number	Category	Recorded	True	Image (mm)	Fracture (μ)	Image (mm)	Fracture (μ)	Area (μ^2)
314	II	35	311	10	50	0.3	1.5	37.5
315	II	32	308	5	25	0.2	1	12.5
316	III	-87	189	14	70	0.14	0.7	24.5
317	III	22	298	25	125	0.3	1.5	93.75
318	III	28	304	15	75	0.22	1.1	41.25
319	III	28	304	30	150	0.3	1.5	112.5
320	III	-32	244	10	50	0.18	0.9	22.5
321	III	-96	180	17	85	0.18	0.9	38.25
322	III	28	304	15	75	0.5	2.5	93.75
323	Id	-19	257	30	150	0.18	0.9	67.5
324	III	28	304	12	60	1.4	7	210
325	II	6	282	20	100	2.4	12	600
326	III	42	318	8	40	0.62	3.1	62
327	III	28	304	5	25	0.22	1.1	13.75
328	Ia	-88	188	25	125	0.2	1	62.5
329	Id	-44	232	16	80	0.18	0.9	36
330	III	43	319	10	50	0.16	0.8	20
331	II	-20	256	12	60	0.2	1	30
332	Id	-87	189	8	40	0.6	3	60
333	II	52	328	10	50	0.38	1.9	47.5
334	II	-116	160	19	95	0.38	1.9	90.25
335	II	-98	178	20	100	1.2	6	300
336	II	-50	226	18	90	0.3	1.5	67.5
337	II	-57	219	7	35	0.16	0.8	14
338	II	-100	176	13	65	0.2	1	32.5
339	III	-10	266	24	120	0.1	0.5	30
340	III	20	296	10	50	0.22	1.1	27.5
341	III	-27	249	17	85	0.2	1	42.5
342	III	29	305	16	80	0.18	0.9	36
343	III	-100	176	6	30	0.16	0.8	12
344	III	-8	268	25	125	0.38	1.9	118.75
345	Ia	-91	185	13	65	0.14	0.7	22.75
346	II	-91	185	12	60	0.8	4	120
347	II	-26	250	6	30	0.22	1.1	16.5
348	Ib	-124	152	29	145	0.22	1.1	79.75
349	Id	9	285	22	110	0.22	1.1	60.5
350	Id	22	298	22	110	1.4	7	385
351	Id	22	298	21	105	0.22	1.1	57.75
352	III	-6	270	8	40	0.5	2.5	50
353	III	22	298	8	40	0.38	1.9	38
					Total fracture area (μ^2)			**60057.25**

Atlas Lucas No. 1

Formation: U. Whirlpool
Depth: 6,462.3 ft
Image ID: AL6462c scanline no. 1
View: Uphole
Azimuth reference: 271°
Area imaged: 9.64×10^5 μ^2

Fracture		Strike (degrees)		Length		Maximum aperture		
Number	Category	Recorded	True	Image (mm)	Fracture (μ)	Image (mm)	Fracture (μ)	Area (μ^2)
1	ID	157	68	21	105	0.9	4.5	236.25
2	ID	134	45	16	80	0.3	1.5	60
3	II	24	295	10	50	1.2	6	150
4	II	53	324	13	65	0.38	1.9	61.75
5	II	20	291	5	25	0.38	1.9	23.75
6	ID	173	84	4	20	0.22	1.1	11
7	ID	128	39	6	30	0.14	0.7	10.5
8	ID	176	87	11	55	0.3	1.5	41.25
9	II	31	302	8	40	0.18	0.9	18
10	ID	42	313	8	40	0.1	0.5	10
11	ID	42	313	4	20	0.16	0.8	8
12	ID	140	51	17	85	0.38	1.9	80.75
13	ID	103	14	18	90	0.18	0.9	40.5
14	ID	22	293	15	75	0.22	1.1	41.25
15	ID	33	304	14	70	0.22	1.1	38.5
16	IA	149	60	17	85	0.8	4	170
17	ID	12	283	24	120	0.5	2.5	150
18	ID	176	87	6	30	0.3	1.5	22.5
19	ID	176	87	7	35	0.3	1.5	26.25
20	II	9	280	9	45	0.38	1.9	42.75
21	II	125	36	10	50	0.22	1.1	27.5
22	ID	22	293	6	30	0.18	0.9	13.5
23	IA	26	297	37.5	187.5	0.3	1.5	140.63
24	IA	38	309	17	85	0.14	0.7	29.75
25	IB	162	73	31	155	2.9	14.5	1123.8
26	IB	90	1	15	75	0.38	1.9	71.25
27	IB	76	347	20	100	0.3	1.5	75
28	IB	162	73	30	150	0.22	1.1	82.5
29	ID	126	37	16	80	0.18	0.9	36
30	IA	177	88	20	100	1.8	9	450
31	IA	154	65	21	105	1.7	8.5	446.25
32	IA	80	351	15	75	1.4	7	262.5
33	IB	167	78	28	140	0.2	1	70
34	ID	174	85	8	40	0.2	1	20
35	ID	125	36	20	100	0.5	2.5	125
36	ID	51	322	19	95	0.45	2.25	106.88
37	IC	90	1	20	100	0.9	4.5	225
38	IA+	15	286	27	135	0.22	1.1	74.25
39	IA	154	65	33	165	0.22	1.1	90.75
40	ID	48	319	10	50	0.3	1.5	37.5
41	IA	46	317	34	170	1.4	7	595
42	IA	42	313	34	170	0.3	1.5	127.5
43	IA	66	337	20	100	0.18	0.9	45

Appendix 2 (cont.)

Fracture		Strike (degrees)		Length		Maximum aperture		
Number	Category	Recorded	True	Image (mm)	Fracture (μ)	Image (mm)	Fracture (μ)	Area (μ^2)
44	IA	70	341	18	90	0.18	0.9	40.5
45	IA	28	299	27	135	0.3	1.5	101.25
46	ID	100	11	9	45	0.22	1.1	24.75
47	ID	115	26	32	160	0.16	0.8	64
48	IA	171	82	10	50	0.5	2.5	62.5
49	IA	171	82	6	30	0.3	1.5	22.5
50	ID	90	1	6	30	0.22	1.1	16.5
51	ID	53	324	18	90	0.16	0.8	36
52	IA+	97	8	22	110	0.2	1	55
53	ID	88	359	23	115	0.3	1.5	86.25
54	ID	120	31	64	320	2.4	12	1920
55	IA	91	2	30	150	0.3	1.5	112.5
56	IA	111	22	9	45	0.9	4.5	101.25
57	IA	64	335	7.5	37.5	0.3	1.5	28.125
58	IA	104	15	30	150	0.2	1	75
59	IA	111	22	14	70	0.3	1.5	52.5
60	IB	64	335	12	60	0.3	1.5	45
61	IB	66	337	16	80	0.3	1.5	60
62	IB	160	71	34	170	0.45	2.25	191.25
63	IB	35	306	13	65	0.22	1.1	35.75
64	ID	60	331	12	60	0.2	1	30
65	ID	60	331	13	65	0.222	1.11	36.075
66	ID	60	331	12.5	62.5	0.2	1	31.25
67	ID	60	331	4	20	0.18	0.9	9
68	ID	67	338	10	50	0.38	1.9	47.5
69	ID	69	340	12	60	0.3	1.5	45
70	ID	73	344	13	65	0.3	1.5	48.75
71	ID	42	313	26	130	0.3	1.5	97.5
72	III	116	27	18	90	0.22	1.1	49.5
73	III	90	1	8	40	0.45	2.25	45
74	II	58	329	43	215	2.9	14.5	1558.8
75	ID	153	64	20	100	0.5	2.5	125
76	II	145	56	8	40	0.3	1.5	30
77	II	105	16	13	65	0.38	1.9	61.75
78	IA+	17	288	36	180	0.18	0.9	81
79	IA+	16	287	7	35	0.2	1	17.5
80	IA+	2	273	4	20	0.3	1.5	15
81	IA+	138	49	4	20	0.3	1.5	15
82	IB	95	6	12	60	0.38	1.9	57
83	ID	35	306	9	45	0.38	1.9	42.75
84	ID	71	342	19	95	0.8	4	190
85	IA	149	60	14	70	0.3	1.5	52.5
86	IA+	155	66	66	330	0.22	1.1	181.5
87	IA	156	67	65	325	0.38	1.9	308.75
88	ID	34	305	8	40	0.3	1.5	30
89	IA+	31	302	19	95	0.3	1.5	71.25
90	IA	14	285	20	100	0.2	1	50
91	IA	3	274	21	105	0.5	2.5	131.25
92	IA	160	71	26	130	0.22	1.1	71.5
93	IA	153	64	21	105	0.6	3	157.5
94	IA	155	66	18	90	0.3	1.5	67.5
95	IA	152	63	12	60	0.6	3	90
96	ID	44	315	19	95	0.22	1.1	52.25
97	IA	169	80	20	100	0.2	1	50

Appendix 2 (cont.)

Fracture		Strike (degrees)		Length		Maximum aperture		
Number	Category	Recorded	True	Image (mm)	Fracture (μ)	Image (mm)	Fracture (μ)	Area (μ^2)
98	ID	180	91	31	155	0.2	1	77.5
99	IA	15	286	25	125	0.22	1.1	68.75
100	IA	158	69	21	105	0.22	1.1	57.75
101	IA	180	91	23	115	0.3	1.5	86.25
102	IA	180	91	12	60	0.18	0.9	27
103	II	102	13	9	45	0.9	4.5	101.25
104	ID	158	69	12	60	0.45	2.25	67.5
105	ID	41	312	5.5	27.5	0.22	1.1	15.125
106	ID	11	282	16	80	0.18	0.9	36
107	ID	9	280	22	110	0.38	1.9	104.5
108	II	38	309	9	45	2	10	225
109	II	162	73	24	120	0.5	2.5	150
110	ID	52	323	7	35	0.3	1.5	26.25
111	IA+	5	276	22	110	0.3	1.5	82.5
112	ID	154	65	12	60	0.3	1.5	45
113	ID	136	47	25	125	0.7	3.5	218.75
114	IA	105	16	24	120	0.38	1.9	114
115	IB	127	38	27	135	0.3	1.5	101.25
116	IB	90	1	8.5	42.5	0.2	1	21.25
117	ID	142	53	5	25	0.3	1.5	18.75
118	IB	160	71	8	40	0.38	1.9	38
119	IB	165	76	25	125	0.18	0.9	56.25
120	IB	164	75	12	60	0.38	1.9	57
121	IB	165	76	18	90	0.18	0.9	40.5
122	IB	175	86	5	25	0.22	1.1	13.75
123	IB	159	70	25	125	0.38	1.9	118.75
124	ID	14	285	12	60	0.16	0.8	24
125	ID	114	25	6	30	0.2	1	15
126	ID	96	7	6	30	0.22	1.1	16.5
127	IA+	21	292	21	105	1.5	7.5	393.75
128	II	21	292	13	65	1	5	162.5
129	ID	90	1	9	45	0.6	3	67.5
130	ID	178	89	10	50	0.2	1	25
131	IA	73	344	16	80	1.2	6	240
132	IB	64	335	10	50	0.22	1.1	27.5
133	IB	150	61	24	120	0.3	1.5	90
134	IB	18	289	23	115	0.22	1.1	63.25
135	II	85	356	20	100	1.5	7.5	375
136	IB	120	31	19	95	0.3	1.5	71.25
137	III	46	317	12	60	0.22	1.1	33
138	III	5	276	20	100	0.38	1.9	95
139	III	33	304	9	45	0.5	2.5	56.25
140	IB	115	26	20	100	0.2	1	50
141	IB	116	27	20	100	0.3	1.5	75
142	IB	31	302	18	90	0.18	0.9	40.5
143	II	113	24	2	10	0.22	1.1	5.5
144	II	5	276	6	30	0.2	1	15
145	ID	24	295	23	115	0.6	3	172.5
146	II	171	82	19	95	0.7	3.5	166.25
147	IA	0	271	12	60	0.38	1.9	57
148	IA	0	271	27	135	0.2	1	67.5
149	III	29	300	6	30	0.16	0.8	12
150	IA+	36	307	8	40	0.2	1	20
151	IA	149	60	27	135	0.22	1.1	74.25

Appendix 2 (cont.)

Fracture		Strike (degrees)		Length		Maximum aperture		
Number	Category	Recorded	True	Image (mm)	Fracture (μ)	Image (mm)	Fracture (μ)	Area (μ^2)
152	IB	156	67	29	145	0.2	1	72.5
153	ID	55	326	8	40	0.45	2.25	45
154	ID	62	333	5	25	0.22	1.1	13.75
155	IB	84	355	28	140	0.14	0.7	49
156	ID	175	86	21	105	0.22	1.1	57.75
157	ID	7	278	10	50	0.3	1.5	37.5
158	IA	125	36	16	80	0.8	4	160
159	III	92	3	13	65	0.22	1.1	35.75
160	IB	138	49	10	50	0.16	0.8	20
161	IC	53	324	15	75	0.18	0.9	33.75
162	IB	155	66	13	65	0.3	1.5	48.75
163	IB	130	41	3	15	0.18	0.9	6.75
164	IA	41	312	7	35	0.3	1.5	26.25
165	IA+	163	74	3	15	0.2	1	7.5
166	IA+	163	74	4	20	0.14	0.7	7
167	IA+	70	341	19	95	0.12	0.6	28.5
168	IA	119	30	11	55	0.16	0.8	22
169	ID	134	45	21	105	0.18	0.9	47.25
170	IB	27	298	24	120	0.2	1	60
171	IA+	0	271	10	50	0.2	1	25
172	III	100	11	5	25	0.3	1.5	18.75
173	II	35	306	8	40	0.7	3.5	70
174	IA	158	69	10	50	0.45	2.25	56.25
175	II	24	295	4	20	0.2	1	10
176	IB	98	9	7	35	0.45	2.25	39.375
177	IB	170	81	9	45	0.38	1.9	42.75
178	IA	44	315	12	60	0.22	1.1	33
179	ID	18	289	5	25	0.18	0.9	11.25
180	IA+	0	271	42	210	0.3	1.5	157.5
181	IA+	2	273	16	80	0.22	1.1	44
182	IA+	2	273	37	185	0.14	0.7	64.75
183	IA+	178	89	9	45	0.9	4.5	101.25
184	IA+	178	89	9	45	0.5	2.5	56.25
185	ID	176	87	16	80	0.22	1.1	44
186	IA+	68	339	35	175	0.8	4	350
187	II	150	61	11	55	0.38	1.9	52.25
188	II	35	306	6	30	0.3	1.5	22.5
189	ID	82	353	37	185	0.3	1.5	138.75
190	II	148	59	3	15	0.22	1.1	8.25
191	II	148	59	3	15	0.22	1.1	8.25
192	II	148	59	3	15	0.22	1.1	8.25
193	IB	55	326	25	125	0.18	0.9	56.25
194	ID	93	4	20	100	0.38	1.9	95
195	IA	31	302	26	130	0.22	1.1	71.5
196	IB	0	271	47	235	2.5	12.5	1468.8
197	IA+	3	274	6	30	0.3	1.5	22.5
198	II	11	282	12	60	0.2	1	30
199	II	6	277	16	80	0.2	1	40
200	II	2	273		0		0	0
201	II	34	305	26	130	3.2	16	1040
202	IA	145	56		0		0	0
203	IB	160	71	19	95	0.18	0.9	42.75
204	IB	27	298	17	85	0.18	0.9	38.25
205	IA	115	26	13	65	0.3	1.5	48.75

Appendix 2 (cont.)

Fracture		Strike (degrees)		Length		Maximum aperture		
Number	Category	Recorded	True	Image (mm)	Fracture (μ)	Image (mm)	Fracture (μ)	Area (μ^2)
206	IA	177	88	19	95	0.3	1.5	71.25
207	ID	65	336	19	95	0.5	2.5	118.75
208	IA	64	335	31	155	0.38	1.9	147.25
209	III	18	289	14	70	0.18	0.9	31.5
210	IA	168	79	7	35	0.3	1.5	26.25
211	III	100	11	15	75	0.3	1.5	56.25
212	III	64	335	11	55	0.38	1.9	52.25
213	IA	171	82	8	40	0.3	1.5	30
214	IA	27	298	3	15	0.2	1	7.5
215	IA	131	42	18	90	0.3	1.5	67.5
216	IA	105	16	43	215	0.6	3	322.5
217	IA	9	280	25	125	0.38	1.9	118.75
218	IA	135	46	15	75	0.38	1.9	71.25
219	IA	52	323	9	45	0.45	2.25	50.625
220	S	45	316	17	85	0.2	1	42.5
221	IB	127	38	6	30	0.3	1.5	22.5
222	IB	127	38	8	40	0.2	1	20
223	IB	150	61	21	105	0.3	1.5	78.75
224	IA	20	291	16	80	0.3	1.5	60
225	IA+	45	316	7	35	0.2	1	17.5
226	IA	178	89	10	50	0.16	0.8	20
227	IA	0	271	11	55	0.3	1.5	41.25
228	IA	178	89	47	235	0.38	1.9	223.25
229	IA	95	6	34	170	0.45	2.25	191.25
230	IB	168	79	7	35	0.5	2.5	43.75
231	IA+	10	281	11	55	0.18	0.9	24.75
232	IA+	9	280	22	110	0.2	1	55
233	II	15	286	9	45	0.22	1.1	24.75
234	IB	4	275	23	115	0.38	1.9	109.25
235	ID	121	32	35	175	0.38	1.9	166.25
236	ID	138	49	25	125	0.3	1.5	93.75
237	II	72	343	10	50	0.22	1.1	27.5
238	II	59	330	13	65	0.3	1.5	48.75
239	II	44	315	15	75	0.18	0.9	33.75
240	III	128	39	11	55	1.2	6	165
241	IB	56	327	12	60	0.8	4	120
242	S	171	82	46	230	0.3	1.5	172.5
243	S	172	83	33	165	0.2	1	82.5
244	III	175	86	5	25	0.3	1.5	18.75
245	ID	175	86	5	25	0.22	1.1	13.75
246	ID	175	86	14	70	0.2	1	35
247	ID	55	326	13	65	0.38	1.9	61.75
248	III	78	349	5	25	0.38	1.9	23.75
249	IB	137	48	9	45	0.3	1.5	33.75
250	ID	49	320	23	115	0.38	1.9	109.25
251	ID	304	215		0		0	0
252	ID	58	329	16	80	0.3	1.5	60
253	ID	55	326	7	35	0.3	1.5	26.25
254	ID	163	74	5	25	0.2	1	12.5
255	ID	160	71	15	75	0.3	1.5	56.25
256	II	6	277	8	40	0.22	1.1	22
257	ID	88	359	9	45	0.2	1	22.5
258	ID	286	197	5	25	0.22	1.1	13.75
259	IC	176	87	5	25	0.22	1.1	13.75

Appendix 2 (cont.)

Fracture		Strike (degrees)		Length		Maximum aperture		
Number	Category	Recorded	True	Image (mm)	Fracture (μ)	Image (mm)	Fracture (μ)	Area (μ^2)
260	IB	304	215	10	50	0.3	1.5	37.5
261	II	24	295	10	50	0.6	3	75
262	IA	345	256	35	175	0.38	1.9	166.25
263	ID	358	269	22	110	0.2	1	55
264	IB	76	347	14	70	0.45	2.25	78.75
265	ID	297	208	4	20	0.3	1.5	15
266	ID	312	223	13	65	0.22	1.1	35.75
267	ID	314	225	14	70	0.3	1.5	52.5
268	IA+	357	268	25	125	0.14	0.7	43.75
269	IA+	5	276	26	130	0.3	1.5	97.5
270	ID	54	325	18	90	0.2	1	45
271	IA	331	242	7	35	0.22	1.1	19.25
272	II	40	311	3	15	0.2	1	7.5
273	IA+	90	1	22	110	0.18	0.9	49.5
274	II	6	277	8	40	0.2	1	20
275	ID	4	275	14	70	0.45	2.25	78.75
276	III	173	84	5	25	0.3	1.5	18.75
277	III	179	90	7	35	0.22	1.1	19.25
278	IA	346	257	8	40	0.18	0.9	18
279	III	177	88	7	35	0.18	0.9	15.75
280	III	176	87	5	25	0.2	1	12.5
281	III	316	227	5	25	0.22	1.1	13.75
282	II	58	329	8	40	0.6	3	60
284	III	144	55	27	135	1.7	8.5	573.75
285	III	152	63	23	115	0.5	2.5	143.75
286	III	136	47	25	125	1.5	7.5	468.75
					Total fracture area (μ^2)			**27971.6**

Atlas Lucas No. 1

Formation: Lower Whirlpool
Depth: 6,467.5 ft
Image ID: AL6467c scanline no. 1
View: Uphole
Azimuth reference: 283°
Area imaged: 3.15×10^6 μ^2

Number	Category	Recorded	True	Image (mm)	Fracture (μ)	Image (mm)	Fracture (μ)	Area (μ^2)
1	III	81	202	10	50	1.15	5.75	143.75
2	ID	95	188	26	130	0.95	4.75	308.75
3	ID	10	273	36	180	0.265	1.325	119.25
4	ID	57	226	15	75	0.4	2	75
5	ID	38	245	34	170	0.33	1.65	140.25
6	ID	38	245	20	100	0.265	1.325	66.25
7	IB	34	249	7	35	0.62	3.1	54.25
8	IA	10	273	19	95	0.5	2.5	118.75
9	IA	6	277	28	140	0.75	3.75	262.5
10	IA	4	279	17	85	0.5	2.5	106.25
11	IB	64	219	16	80	0.215	1.075	43
12	IB	176	107	22	110	0.14	0.7	38.5
13	IA	49	234	23	115	0.62	3.1	178.25
14	IC	37	246	12	60	0.265	1.325	39.75
15	IB	56	227	35	175	0.265	1.325	115.9375
16	IB	45	238	29	145	0.215	1.075	77.9375
17	IB	80	203	20	100	0.33	1.65	82.5
18	IB	81	202	7	35	0.215	1.075	18.8125
19	IC	135	148	20	100	0.44	2.2	110
20	IC	88	195	18	90	0.265	1.325	59.625
21	IA+	71	212	21	105	0.5	2.5	131.25
22	IB	20	263	8	40	0.62	3.1	62
23	ID	64	219	33	165	0.5	2.5	206.25
24	ID	54	229	28	140	0.5	2.5	175
25	ID	45	238	12	60	0.33	1.65	49.5
26	ID	44	239	17	85	0.175	0.875	37.1875
27	IC	82	201	22	110	0.14	0.7	38.5
28	IC	69	214	6	30	0.14	0.7	10.5
29	IC	30	253	17	85	0.4	2	85
30	IC	43	240	13	65	0.265	1.325	43.0625
31	IC	35	248	9	45	0.265	1.325	29.8125
32	IC	36	247	10	50	0.4	2	50
33	IC	149	134	16	80	0.265	1.325	53
34	IB	40	243	19	95	0.265	1.325	62.9375
35	IB	6	277	7	35	0.265	1.325	23.1875
36	IA+	118	165	65	325	0.4	2	325
37	IA	10	273	17	85	0.62	3.1	131.75
38	IB	122	161	43	215	0.75	3.75	403.125
39	IA+	129	154	4	20	1.15	5.75	57.5
40	ID	36	247	11	55	0.4	2	55
41	ID	30	253	10	50	0.215	1.075	26.875
42	IA	118	165	3	15	0.265	1.325	9.9375
43	IB	145	138	13	65	0.4	2	65
44	ID	4	279	32	160	0.33	1.65	132

Appendix 2 (cont.)

Number	Category	Recorded	True	Image (mm)	Fracture (μ)	Image (mm)	Fracture (μ)	Area (μ^2)
45	ID	45	238	21	105	0.265	1.325	69.5625
46	ID	41	242	19	95	0.33	1.65	78.375
47	IC	128	155	34	170	0.62	3.1	263.5
48	IC	160	123	13	65	0.14	0.7	22.75
49	IB	43	240	36	180	0.4	2	180
50	IA+	19	264	27	135	1.4	7	472.5
51	IB	137	146	6	30	0.75	3.75	56.25
52	IB	148	135	18	90	0.95	4.75	213.75
53	IB	14	269	18	90	0.265	1.325	59.625
54	IB	334	309	19	95	0.265	1.325	62.9375
55	IB	348	295	12	60	0.265	1.325	39.75
56	IA	107	176	71	355	0.33	1.65	292.875
57	IC	301	342	29	145	0.265	1.325	96.0625
58	IC	325	318	29	145	0.5	2.5	181.25
59	IA	80	203	31	155	2.65	13.25	1026.875
60	IC	325	318	12	60	0.215	1.075	32.25
61	IC	326	317	46	230	0.265	1.325	152.375
62	IC	318	325	17	85	0.62	3.1	131.75
63	IC	107	176		0	0	0	0
64	IC	324	319	25	125	0.265	1.325	82.8125
65	IC	335	308	14	70	0.215	1.075	37.625
66	IC	102	181	23	115	0.265	1.325	76.1875
67	IC	101	182	9	45	0.175	0.875	19.6875
68	IC	101	182	18	90	1.4	7	315
69	IC	101	182	11	55	0.215	1.075	29.5625
70	IC	108	175	34	170	0.62	3.1	263.5
71	IC	96	187	17	85	0.175	0.875	37.1875
72	IC	104	179	20	100	0.265	1.325	66.25
73	IC	97	186	43	215	0.5	2.5	268.75
74	IC	135	148	46	230	0.62	3.1	356.5
75	IC	100	183	31	155	0.4	2	155
76	IC	100	183	23	115	0.215	1.075	61.8125
77	IC	90	193	16	80	0.265	1.325	53
78	IB	5	278	26	130	1.4	7	455
79	IB	19	264	28	140	0.75	3.75	262.5
80	ID	46	237	18	90	0.215	1.075	48.375
81	ID	136	147	25	125	0.5	2.5	156.25
82	IA	14	269	23	115	0.33	1.65	94.875
83	IC	15	268	10	50	0.265	1.325	33.125
84	IA	38	245	15	75	0.4	2	75
85	ID	3	280	7	35	0.4	2	35
86	ID	38	245	12	60	0.62	3.1	93
87	ID	38	245	7	35	0.5	2.5	43.75
88	ID	26	257	7	35	0.4	2	35
89	IA	74	209	9	45	0.62	3.1	69.75
90	IA	135	148	32	160	1.15	5.75	460
91	IB	46	237	9	45	0.4	2	45
92	IB	63	220	12	60	0.33	1.65	49.5
93	IA	50	233	13	65	0.5	2.5	81.25
94	IB	58	225	13	65	0.4	2	65
95	IB	55	228	12	60	0.33	1.65	49.5
96	IB	12	271	7	35	0.4	2	35
97	ID	47	236	39	195	0.4	2	195
98	ID	105	178	21	105	0.33	1.65	86.625
99	ID	32	251	25	125	0.62	3.1	193.75

Appendix 2 (cont.)

Number	Category	Recorded	True	Image (mm)	Fracture (μ)	Image (mm)	Fracture (μ)	Area (μ^2)
100	II	72	211	11	55	0.95	4.75	130.625
101	II	109	174	12	60	1.15	5.75	172.5
102	IB	88	195	15	75	0.215	1.075	40.3125
103	III	40	243	34	170	1.4	7	595
104	ID	10	273	35	175	0.265	1.325	115.9375
105	IC	102	181	26	130	0.33	1.65	107.25
106	III	33	250	19	95	0.33	1.65	78.375
107	IB	70	213	14	70	0.33	1.65	57.75
108	ID	91	192	21	105	0.265	1.325	69.5625
109	ID	90	193	41	205	0.265	1.325	135.8125
110	ID	120	163	24	120	0.265	1.325	79.5
111	II	110	173	18	90	0.5	2.5	112.5
112	II	58	225	6	30	0.4	2	30
113	II	40	243	8	40	0.4	2	40
114	ID	2	281	13	65	0.5	2.5	81.25
115	ID	10	273	14	70	0.4	2	70
116	II	24	259	12	60	0.4	2	60
117	II	151	132	13	65	1.15	5.75	186.875
118	ID	20	263	6	30	0.215	1.075	16.125
119	ID	81	202	23	115	0.14	0.7	40.25
120	ID	76	207	9	45	0.175	0.875	19.6875
121	ID	75	208	15	75	0.265	1.325	49.6875
122	IB	95	188	20	100	0.4	2	100
123	IB	125	158	43	215	0.4	2	215
124	IB	102	181	39	195	0.75	3.75	365.625
125	IB	115	168	26	130	0.265	1.325	86.125
126	IB	115	168	52	260	0.5	2.5	325
127	IA	158	125	24	120	0.75	3.75	225
128	ID	132	151	25	125	0.5	2.5	156.25
129	ID	134	149	24	120	0.5	2.5	150
130	ID	133	150	22	110	0.33	1.65	90.75
131	ID	135	148	23	115	0.5	2.5	143.75
132	IA+	72	211	38	190	0.75	3.75	356.25
133	IB	76	207	38	190	0.5	2.5	237.5
134	IB	88	195	39	195	1.4	7	682.5
135	IB	5	278	34	170	0.33	1.65	140.25
136	IA	96	187	38	190	0.4	2	190
137	IB	85	198	16	80	0.75	3.75	150
138	IA+	83	200	23	115	0.62	3.1	178.25
139	IB	74	209	15	75	0.33	1.65	61.875
140	IB	76	207	15	75	0.175	0.875	32.8125
141	IA	46	237	19	95	0.5	2.5	118.75
142	IC	77	206	9	45	0.33	1.65	37.125
143	IV	73	210	9	45	0.4	2	45
144	IA+	71	212	19	95	0.33	1.65	78.375
145	IA+	148	135	46	230	0.265	1.325	152.375
146	ID	54	229	4	20	0.215	1.075	10.75
147	IB	78	205	13	65	0.4	2	65
148	IB	88	195	16	80	0.33	1.65	66
149	IB	76	207	15	75	0.5	2.5	93.75
150	IA	100	183	23	115	1.4	7	402.5
151	IA+	76	207	15	75	0.33	1.65	61.875
152	IB	156	127	8	40	0.215	1.075	21.5
153	ID	103	180	18	90	0.265	1.325	59.625
154	ID	101	182	37	185	0.215	1.075	99.4375

Appendix 2 (cont.)

Number	Category	Recorded	True	Image (mm)	Fracture (μ)	Image (mm)	Fracture (μ)	Area (μ^2)
155	ID	168	115	14	70	0.175	0.875	30.625
156	ID	28	255	8	40	0.115	0.575	11.5
157	ID	12	271	15	75	0.215	1.075	40.3125
158	II	354	289	11	55	0.115	0.575	15.8125
159	IA+	84	199	9	45	0.14	0.7	15.75
160	IB	354	289	20	100	0.62	3.1	155
161	IB	94	189	41	205	0.95	4.75	486.875
162	IB	9	274	14	70	0.5	2.5	87.5
163	IA	4	279	27	135	5	25	1687.5
164	IA+	340	303	36	180	0.33	1.65	148.5
165	II	120	163	14	70	0.265	1.325	46.375
166	IB	105	178	12	60	0.33	1.65	49.5
167	IB	110	173	12	60	0.5	2.5	75
168	IB	90	193	12	60	0.5	2.5	75
169	IB	340	303	18	90	0.33	1.65	74.25
170	IC	53	230	19	95	0.265	1.325	62.9375
171	III	25	258	14	70	0.5	2.5	87.5
172	III	72	211	12	60	0.75	3.75	112.5
173	IA	102	181	15	75	1.4	7	262.5
174	IA	24	259	26	130	0.215	1.075	69.875
175	IB	59	224	38	190	0.215	1.075	102.125
176	IA	124	159	11	55	0.5	2.5	68.75
177	IB	130	153	12	60	0.33	1.65	49.5
178	IB	115	168	21	105	0.4	2	105
179	ID	20	263	18	90	2.15	10.75	483.75
180	IA	72	211	12	60	0.4	2	60
181	IA	46	237		0		0	0
182	IA	98	185	19	95	0.4	2	95
183	IB	0	283	3	15	0.215	1.075	8.0625
184	IA	20	263	5	25	0.5	2.5	31.25
185	IB	0	283	14	70	0.265	1.325	46.375
186	IA	32	251	39	195	0.115	0.575	56.0625
187	ID	355	288	19	95	0.265	1.325	62.9375
188	ID	3	280	8	40	0.265	1.325	26.5
189	ID	0	283	7	35	0.33	1.65	28.875
190	ID	84	199	19	95	0.14	0.7	33.25
191	ID	90	193	7	35	0.33	1.65	28.875
192	ID	102	181	12	60	0.215	1.075	32.25
193	ID	44	239	7	35	0.215	1.075	18.8125
194	IA+	28	255	21	105	0.62	3.1	162.75
195	ID	8	275	5	25	0.265	1.325	16.5625
196	ID	8	275	6	30	0.265	1.325	19.875
197	IB	110	173	11	55	1.15	5.75	158.125
198	ID	110	173	10	50	0.4	2	50
199	IA	6	277	5	25	0.4	2	25
200	ID	10	273	19	95	0.14	0.7	33.25
201	IA	0	283	14	70	0.4	2	70
202	IA+	28	255	20	100	0.22	1.1	55
203	IA+	28	255	16	80	0.16	0.8	32
204	IA+	23	260	20	100	0.22	1.1	55
205	ID	40	243	21	105	0.1	0.5	26.25
206	IA+	52	231	88	440	0.2	1	220
207			283				0	0
					Total fracture area (μ^2)			**25684.25**